University of Nottingham
UK | CHINA | MALAYSIA

Application and Evaluation of Tip Enhanced Raman Spectroscopy in Pharmaceutical Analysis

by Georgios Papakostas MPharm MSc

Thesis submitted to the University of Nottingham for the degree of Doctor of Philosophy

Molecular Therapeutics and Formulation Division
School of Pharmacy
&
Nottingham Nanoscience Group
School of Physics and Astronomy

February 2022

Acknowledgements

I would like to express my deep gratitude to my supervisors Dr. Jonathan Burley, Prof. Ioan Notingher and Dr. Stephanie Brookes. Dr. Jonathan Burley you have been an inspiring guidance throughout this project, showing great patience, optimism, encouragement and the ability to explain and make things simpler in science. Prof. Ioan Notingher I thank you for your full support, providing me the freedom to delve into many aspects of this project, whilst pushing me to give my best in this work. Dr. Stephanie Brookes I deeply thank you for your constant support and interest you have shown in this project as well as help during the time spent in AstraZeneca.

Also, I wish to express my greatest appreciation to the people who have contributed as well as provided their input in various aspects of this work. From the National Physical Laboratory, I am extremely grateful to Dr. Naresh Kumar, Dr. Andrew Pollard, Dr. Elizabeth Legge and Dr. Dimitrios Tsikritsis for their massive aid in this work as well as technical support around TERS and Raman spectroscopy instrumentations and experiments. Also, I would like to thank Dr. Jonathan Booth, Dr. Kevin Treacher from AstraZeneca for their input in making this project more applicable in pharmaceutical science. The success of the Raman experiments would not have been possible with the invaluable help of Chris Corden, in the design and setup the project's instrument, alongside with the support of Radu, Nathan, Maria Giovanna and Zhiyu within the bio-photonics group for their technical support as well as the fun we had together over the past years.

I would like to extend my sincere thanks to the CDT management for giving me the opportunity to be part of this programme and especially to Dr. Claudia Matz for her warm support. Many thanks to everyone within the CDT, especially to Lorentzo and the rest of the CDT cohort Addie, Steven, Paula,

Issy, Ania and Valentina, for the help, unforgettable trips to conferences and the many moments we shared together in the last four years.

Last, I would like to thank the people who are special in my life. Mum, dad and Chris, thank you for always being there to support and encourage me, when I needed you the most. Also, thank you for showing interest in trying to grasp the concept of this work. Efi, thank you for loving and sharing your life with me. Thanks for your compassion and lifting me up from my lowest moments of this journey. Maria and Stuart, without you two I would have never gotten in the CDT programme and being part of this fascinating and turbulent "Odyssey". I am extremely grateful to you both for everything you have given me. To my grandmother, Chrysanthi Kokkia, who through very difficult times and against all odds migrated to Germany to support her family. You have inspired me patience, persistence and compassion to the people who matter in life the most. Therefore, I dedicate this thesis to you.

Declaration

I hereby declare that the work contained in this thesis titled "Application and Evaluation of Tip Enhanced Raman Spectroscopy in Pharmaceutical Analysis" is the result of my own work conducted at the University of Nottingham, AstraZeneca (Macclesfield) and the National Physical Laboratory between October 2017 and February 2022, with the guidance of my supervisors Dr. Jonathan Burley, Prof. Ioan Notingher, Dr. Stephanie Brookes and Dr. Andrew Pollard.

Abstract

Pharmaceutical analysis plays a crucial role in drug manufacturing, allowing the identification and exploration of the physio-chemical properties and interactions between active pharmaceutical ingredients (API) and excipients within a formulation. However, conventional microscopy instruments can be constrained in resolving chemical information below the micron-length scales. A newly arising nano-analytical technique is the Tip-Enhanced Raman Spectroscopy (TERS), which can obtain valuable spatio-chemical information from the sample of interest, at the length scales of tens of nanometres or less. TERS application has been reported on numerous carbon-based and biological samples, however to-date there are no records of TERS application on pharmaceutical formulations.

This thesis evaluates the application of TERS technique on individual pharmaceutical components or amorphous solid dispersions (ASDs). These include paracetamol, felodipine, nicotinamide, copovidone, polyvinyl alcohol (PVA) either alone or in combination as well as di-phenylalanine tubes. In these studies two microscopy systems were used to examine the samples of interest. One is the custom-built combined Atomic Force Microscopy - Confocal Raman Microscopy (AFM-CRM) system (located at the School of Physics and Astronomy - Chapter 2), equipped with silicon AFM probes and the second is the TERS system which is a combined AFM-CRM instrument of similar specifications (located at the National Physical Laboratory), equipped with Ag-coated TERS probes. Under the TERS equipment di-phenylalanine tubes were tested to evaluate the degree of signal enhancement and spatial resolution which can be obtained, followed by spectral evaluation of the ASDs, namely paracetamol/copovidone 50% w/w and felodipine/copovidone 50% w/w, in Ag-coated probe retracted and engaged positions (Chapter 3). With the intense photo-

luminescence background noise generated from the spectra in engaged probe position, two further studies were performed to identify the potential causes in individual pharmaceutical components (Chapters 4 and 5). In Chapter 4, each tested component was exposed under prolonged laser irradiation, with the AFM-CRM instrument, finding the threshold of sample photodegradation alongside with the association of photoluminescence occurrence in temperature rise. Moreover in Chapter 5, multiple spectra were acquired under the TERS instrument as a function to apex-to-focal spot distance across the XYZ directions, recording any changes in the spectra, including signal enhancement and sample photodegradation. After identifying paracetamol's properties to withstand prolounged laser irradiation and provide adequate signal enhancement, AFM, CRM and TERS maps were obtained from both systems (Chapter 6). Specifically, paracetamol/PVA 30% w/w 2D-printed microdot was interrogated under the probe, detecting nano-meter length inhomogeneities at the sample surface.

Under the tested bottom-illumination TERS instrument equipped with 532 nm incident light, most pharmaceutical components and formulations showed low TERS signal enhancement. In all studies, felodipine displayed photodegradation, whereas paracetamol demonstrated small enhancement beneath the probe apex. With limited signal enhancement, it was feasible to demonstrate qualitatively ASD inhomogeneity at the surface of the formulation.

Contents

Contents vi

List of Figures x

List of Tables xiv

Abbreviations xvi

1 Introduction 1
1.1 Oral formulations . . . 1
1.1.1 Background . . . 1
1.1.2 Amorphous solid dispersions . . . 3
1.2 Chemical characterisation of formulations . . . 7
1.2.1 Pharmaceutical analysis . . . 7
1.2.2 Vibrational spectroscopy . . . 8
1.2.2.1 Infrared spectroscopy . . . 9
1.2.2.2 Raman spectroscopy . . . 9
1.2.2.3 Raman microscopy . . . 11
1.2.2.3.1 Raman mapping . . . 13
1.2.2.3.2 Data analysis . . . 14
1.2.2.3.2.1 Data Pre-processing . . . 14
1.2.2.3.2.2 Data processing . . . 15
1.2.2.4 Surface-enhanced Raman spectroscopy . . . 15
1.2.2.4.1 Electromagnetic field enhancement . . . 16
1.2.2.4.2 Chemical enhancement . . . 17
1.2.2.4.3 SERS drawbacks . . . 18
1.2.3 Super-resolving microscopy techniques . . . 18
1.2.3.1 Scanning probe microscopy . . . 18
1.2.3.2 Atomic force microscopy . . . 19
1.2.3.3 AFM-IR . . . 21
1.3 Tip-Enhanced Raman Spectroscopy . . . 22
1.3.1 TERS concepts . . . 22
1.3.1.1 General principles . . . 24
1.3.1.2 Optical geometries . . . 25
1.3.1.3 Polarisation effect . . . 26
1.3.1.4 Probe preparation . . . 27
1.3.1.5 Spatial resolution . . . 29
1.3.2 TERS applications . . . 29

1.3.2.1 Carbon and other chemical investigations . . . 30
1.3.2.2 Biological investigations . . . 30
1.3.3 Motivation and aims of the work . . . 30

2 Instrumentation 33
2.1 Introduction . . . 33
2.2 Instrument design . . . 34
2.2.1 Combined AFM-CRM . . . 34
2.2.2 Atomic Force Microscopy (AFM) setup . . . 35
2.2.3 Confocal Raman microscopy (CRM) setup . . . 36
2.3 Software development . . . 37
2.3.1 Software design . . . 38
2.3.2 Software functionality . . . 40
2.4 Laser polarisation and laser-probe alignment . . . 41
2.4.1 Determining the radial polarisation of the laser spot . . . 42
2.4.2 Laser-probe co-alignment . . . 43
2.4.2.1 Apex detection via brightfield video recoding . 44
2.4.2.2 Co-alignment via scattered laser light . . . 44
2.4.2.3 Co-alignment via silicon probe Raman raster-scan 45
2.4.3 Calculation of laser spatial resolution . . . 46
2.4.3.1 Results and Discussion . . . 47
2.4.3.1.1 AFM measurements . . . 47
2.4.3.1.2 CRM measurements . . . 47
2.5 Summary . . . 48

3 TERS spatial resolution and signal enhancement evaluation on L,L-Diphenylalanine tubes and ASDs 51
3.1 Introduction . . . 51
3.2 Material and Methods . . . 53
3.2.1 Instrumentation & Measurements . . . 53
3.3 Results and Discussion . . . 55
3.3.1 Phe-Phe measurements . . . 55
3.3.1.1 AFM topography of Phe-Phe nanofibre . . . 55
3.3.1.2 Raman Spectra of Phe-Phe tube – TERS-active probe retracted . . . 55
3.3.1.3 Raman Spectra of Phe-Phe tube – TERS-active probe approached . . . 56
3.3.1.4 Phe-Phe tube sensitivity to laser irradiation– TERS-active probe retracted . . . 58
3.3.1.5 Line Intensity profiling of Phe-Phe tubes - TERS probe retracted & approached . . . 59
3.3.2 Paracetamol/copovidone 50% w/w spin-coated film . . . 64
3.3.2.1 Raman Spectra of paracetamol/copovidone sample – AFM Probe retracted . . . 64
3.3.2.2 Paracetamol/copovidone film sensitivity to laser irradiation- TERS-active probe retracted . . . 64

3.3.2.3 Raman Spectra of paracetamol/copovidone sample -AFM Probe approached 66
3.3.3 Felodipine/copovidone 50% w/w spin-coated film 67
3.3.3.1 Raman Spectra of felodipine/copovidone sample – AFM Probe retracted 67
3.3.3.2 Raman Spectra of felodipine/copovidone sample – AFM Probe approached 69
3.4 Conclusion 69

4 Laser sensitivity and Raman thermometry assessment of pharmaceutical components 72
4.1 Introduction 72
4.2 Material and Methods 75
4.2.1 Materials & Preparation method 75
4.2.2 Instrumentation & Raman Measurements 75
4.2.2.1 AFM-CRM 75
4.2.2.2 Horiba LabRAM 76
4.2.2.3 Irradiance investigation 76
4.2.2.4 Thermometry investigation 78
4.3 Results and Discussion 79
4.3.1 Laser sensitivity of Paracetamol 79
4.3.1.1 AFM-CRM measurements for paracetamol . . . 80
4.3.1.2 Horiba - LabRAM measurements for paracetamol 82
4.3.2 Laser sensitivity of Felodipine 84
4.3.2.1 AFM-CRM measurements for felodipine 85
4.3.2.2 Horiba - LabRAM measurements for felodipine 87
4.3.3 Laser sensitivity of Copovidone 88
4.3.3.1 AFM-CRM measurements for copovidone . . . 89
4.3.3.2 Horiba - LabRAM measurements for copovidone 90
4.3.4 Sample Temperature Evaluation 92
4.3.4.1 Sample Thermometry with AFM-CRM Raman instrument 93
4.3.4.2 Sample Thermometry with LabRAM Raman instrument 99
4.4 Conclusion 100

5 Sample integrity and signal enhancement evaluation based on focal point-to-probe distance 102
5.1 Introduction 102
5.2 Material and Methods 104
5.2.1 XY-Coordinate experimental setup 105
5.2.2 Z-Coordinate experimental setup 106
5.3 Results and Discussion 108
5.3.1 Paracetamol measurements 108
5.3.2 Felodipine measurements 111
5.3.3 Nicotinamide measurements 114
5.3.4 PVA measurements 117

5.4 Conclusion 120

6 AFM-CRM-TERS measurement on 2D-printed microdot ASD 122
6.1 Introduction 122
6.2 Material and Methods 123
6.2.1 Coverslip and sample preparation 123
6.2.2 2D inject printing 124
6.2.3 AFM-Raman measurements 125
6.2.4 TERS measurements 125
6.2.5 Computational preprocessing and analysis of data 126
6.3 Results and Discussion 127
6.3.1 AFM-CRM Instrument 127
6.3.1.1 AFM measurements 127
6.3.1.2 Raman measurements 129
6.3.2 TERS Instrument 133
6.3.2.1 AFM measurements 133
6.3.2.2 Raman measurements 134
6.4 Conclusion 139

7 Conclusions and Future Work 141

Bibliography 146

Appendices 186

A Supplementary information part-I 187

B Supplementary information part-II 189

C Supplementary information part-III 193

D Supplementary information part-IV 205

E Supplementary information part-V 213

List of Figures

1.1 The Biopharmaceutical Classification System (BCS). 2
1.2 The Developability Classification System (DCS). 4
1.3 Temperature and free energy correlation on single-component state. 6
1.4 Energy pyramid between crystalline and amorphous solid forms 7
1.5 Jablonski's diagram 11
1.6 Schematic of confocal Raman microscope 13
1.7 SERS schematic 16
1.8 SERS effect 17
1.9 Atomic force microscopy schematic 19
1.10 TERS optical geometries 26
1.11 Laser polarisations 27

2.1 AFM-CRM system photo images 34
2.2 AFM-CRM schematic 35
2.3 AFM-CRM schematic at the sample point of view 36
2.4 Model-View-Controller schematic 39
2.5 Software screenshot 40
2.6 Pseudo-coloured brightfield images of laser spot at different polarisations 43
2.7 Tip-retracted and approached brightfield images 44
2.8 Laser back-scattered AFM raster-scan image 45
2.9 Raman image and spectrum of silicon probe 46
2.10 AFM topography scan of SWCNT based on their height 48
2.11 Raman intensity map of SWCNT 49

3.1 Phe-Phe tube AFM map 56
3.2 Tip-retracted and approached Raman spectra of Phe-Phe tubes 57
3.3 10 minutes before and after of Phe-Phe tube laser burning . . . 59
3.4 Raman line scan of Phe-Phe tube with TERS probe retracted . 60
3.5 Raman line scan of Phe-Phe tube with TERS probe approached 62
3.6 Reference Raman spectra of paracetamol and copovidone 65
3.7 Paracetamol/copovidone 50% w/w 10 minute prolonged irradiation 66
3.8 Paracetamol/copovidone 50% w/w blend with TERS probe retracted and approached 67
3.9 Reference Raman spectra of felodipine and copovidone 68
3.10 Felodipine/copovidone 50% w/w blend with TERS probe retracted and approached 70

4.1 Image of Gaussian laser beam, with cross-sections 77
4.2 Reference paracetamol spectra across different NA and power intensities 81
4.3 Time series of Raman spectra of paracetamol on 1.45 NA objective 82
4.4 Time series of Raman spectra of paracetamol on 0.8 NA on objective 83
4.5 Reference felodipine across different NA and power intensities . 85
4.6 Time series of Raman spectra of felodipine on 1.45 NA objective 86
4.7 Time series of Raman spectra of felodipine on 0.8 NA objective 88
4.8 Time series of Raman spectra of Felodipine on 0.55 NA objective 89
4.9 Reference copovidone across different NA and power intensities . 91
4.10 Time series of Raman spectra of copovidone on 1.45 NA objective 92
4.11 Time series of Raman spectra of copovidone on 0.8 NA objective 93
4.12 Reference Raman spectra of paracetamol covering both Stokes and Anti-Stokes 95
4.13 Raman thermometry measurement of paracetamol, using 1.45 NA objective at 3 mW for 797 cm^1 band 96
4.14 Raman thermometry measurement of paracetamol, using 1.45 NA objective at 1.5 mW for 797 cm^1 band 98
4.15 Raman thermometry measurement of paracetamol, using 0.8 NA objective at 25 mW for 214.9 cm^1 band 100

5.1 Schematic diagram of TERS setup for focal point-probe XY-Axis co-alignment 105
5.2 Schematic diagram of TERS setup for focal point-probe Z-Axis raster-scan 107
5.3 Reference Raman spectrum of pure paracetamol 109
5.4 Hotspot Raman map of paracetamol 109
5.5 Z-scan Raman spectra of paracetamol 110
5.6 Reference Raman spectrum of pure felodipine 112
5.7 Hotspot Raman map of felodipine 112
5.8 Z-scan Raman spectra of felodipine 113
5.9 Reference Raman spectrum of pure nicotinamide 115
5.10 Hotspot Raman map of nicotinamide 115
5.11 Z-scan Raman spectra of nicotinamide 116
5.12 Reference Raman spectrum of pure PVA 118
5.13 Hotspot Raman map of PVA 118
5.14 Z-scan Raman spectra of PVA 119

6.1 Microdot brightfield image 127
6.2 AFM Height-Friction map from AFM-CRM instrument 128
6.3 AFM Friction-Adhesion map from AFM-CRM instrument . . . 128
6.4 Reference Raman spectra from AFM-CRM instrument 130
6.5 Confocal Raman maps from AFM-CRM instrument 132
6.6 AFM Friction map from TERS instrument 134
6.7 Reference Raman spectra from TERS instrument 135
6.8 Confocal Raman maps from TERS instrument 136
6.9 TERS Raman maps from TERS instrument 138

A.1 Radial polarisation distribution 188

B.1 Reference spectra of Di-Phenylalanine and Borosilicate glass . . 190
B.2 10 minutes before and after of Phe-Phe tube laser burning with probe retracted and 1 minute with probe engaged 190
B.3 Reference spectra of pure felodipine and copovidone materials as well as their 5% and 50% extrudate mixtures 191
B.4 Reference spectra of pure paracetamol 192
B.5 Reference spectra of Copovidone 192

C.1 Raman spectra time series of paracetamol for 0.55 NA objective 194
C.2 Raman spectra time series of copovidone for 0.55 NA objective . 195
C.3 Fitted intensity values of paracetamol at 3 mW for 797 cm^{-1}, with goodness of fits 196
C.4 Raman thermometry measurement of paracetamol, using 1.45 NA at 1.5 mW of laser power for 857.9 cm^1 band 197
C.5 Fitted intensity values of paracetamol at 3 mW for 857.9 cm^{-1}, with goodness of fits 198
C.6 Fitted intensity values of paracetamol at 1.5 mW for 797 cm^{-1}, with goodness of fits 199
C.7 Raman thermometry measurement of paracetamol, using 1.45 NA at 1.5 mW of laser power for 857.9 cm^1 band 200
C.8 Fitted intensity values of paracetamol at 1.5 mW for 857.9 cm^{-1}, with goodness of fits 201
C.9 Fitted intensity values of paracetamol at 25 mW for 214.9 cm^{-1}, with goodness of fits 202
C.10 Raman thermometry measurement of paracetamol, using 0.8 NA at 25 mW of laser power for 87 cm^1 band 203
C.11 Fitted intensity values of paracetamol at 25 mW for 89.4 cm^{-1}, with goodness of fits 204

D.1 Brightfield images of crystalline and molten Paracetamol 206
D.2 Brightfield images of crystalline and molten Felodipine 207
D.3 Brightfield images of crystalline and molten Nicotinamide 208
D.4 SERS-based background noise, generated by plasmon resonance 209
D.5 Brightfield of burned felodipine sample 210
D.6 Reference Raman spectrum of nicotinamide 211
D.7 Zoomed hotspot Raman map of nicotinamide 211
D.8 Reference Raman spectrum of polyvinyl alcohol 212

E.1 Raman spectra of pure paracetamol, alongside their forms . . . 214
E.2 Raman spectra of Paracetamol/PVA 30% w/w at different acquisition settings 215
E.3 Intensities and ESDs of Non-linear fitting curved, for Figure 6.5 216
E.4 Raw friction map from TERS instrument 217
E.5 Intensities and ESDs of Non-linear fitting curved, for Figure 6.8 218
E.6 Confocal Raman maps from TERS instrument with non-linear curve fittings 219

E.7 Intensities and ESDs of Non-linear fitting curved, for Figure 6.9 220
E.8 Confocal Raman maps from TERS instrument with non-linear curve fittings 221

List of Tables

4.1 Table of objectives, area beam, power intensities and irradiance applied on the samples 78
4.2 Table of laser intensities and irradiance on paracetamol 84
4.3 Table of laser intensities and irradiance on felodipine 90
4.4 Table of laser intensities and irradiance on copovidone 94
4.5 Table of laser intensities and irradiance on all samples 94

List of Equations

1.1	Abbe's lateral resolution equation	12
1.2	Abbe's axial resolution equation	12
1.3	Numerical Aperture equation	13
1.4	Hookes Law equation	20
3.1	Enhancement Contrast equation	54
3.2	Enhancement Factor equation	63
4.1	Irradiance equation	76
4.2	Area beam equation	77
4.3	Raman Thermometry equation	79
5.1	Enhancement Contrast equation	106

Abbreviations

AFM	Atomic Force Microscopy
ALS	Asymmetric Least Squares
APIs	Active Pharmaceutical Ingredients
ASD	Amorphous Solid Dispersions
BCS	Biopharmaceutical Classification System
CCD	Charged-Coupled Device
CRM	Confocal Raman Microscopy
CW	Continuous-Wave
DCS	Developability Classification System
EC	Enhancement Contrast
EF	Enhancement Factor
ESDs	Estimated Standard Deviations
FWHM	Full Width Half Maximum
HME	Hot-Melt Extrusion
IR	InfraRed
LSP	Localised Surface Plasmons
MVC	Model-View-Controller
NA	Numerical Aperture
NaN	Not a Number
Nd:YAG	Neodymium-doped Yttrium Aluminium Garnet
NIR	Near-InfraRed
Phe-Phe	L,L-DiPhenylalanine

PL	Photoluminescence
PVA	Polyvinyl Alcohol
SLAD	Solubility Limited Absorbable Dose
SN	Signal-to-Noise
SPM	Scanning Probe Microscopy
SPR	Surface Plasmon Resonance
STM	Scanning Tunnel Microscopy
SWCNT	Single-Wall Carbon Nanotubes
TERS	Tip-Enhanced Raman Scattering
UI	User Interface

Chapter 1

Introduction

1.1 Oral formulations

1.1.1 Background

Oral drug administration is known to be one of the most popular routes of drug delivery for the human body. This is based on the ease of use, limited sterility constraints during manufacturing, cost effectiveness, patient compliance, as well as flexibility in design of dosage forms [1–3]. To achieve the desired therapeutic effect, an oral formulation requires to cross a series of biological barriers after entry to the organism. This journey starts with the dissolution of the formulation in the gastrointestinal fluids, continues with the absorption through the gut mucosa into the hepatic portal vein and further bypass of the first pass hepatic metabolism, ending with the transport to the target tissue via systemic circulation [4]. In some instances, the medication may undergo physico-chemical changes at different stages of the gastrointestinal system which can affect its performance, especially during its dissolution in the gastric fluids [5, 6]. In order to obtain a clear view of the oral formulation and behaviour, the Active

Pharmaceutical Ingredients (APIs) have been classified into 4 groups, according to their degree of dissolution and solubilisation in aqueous medium as well as permeation through the intestinal tissue. For this, the Biopharmaceutical Classification System (BCS) was designed in 1995, as displayed in Figure 1.1 [7]. In brief, a BCS class 1 drug display high solubility and permeability perfor-

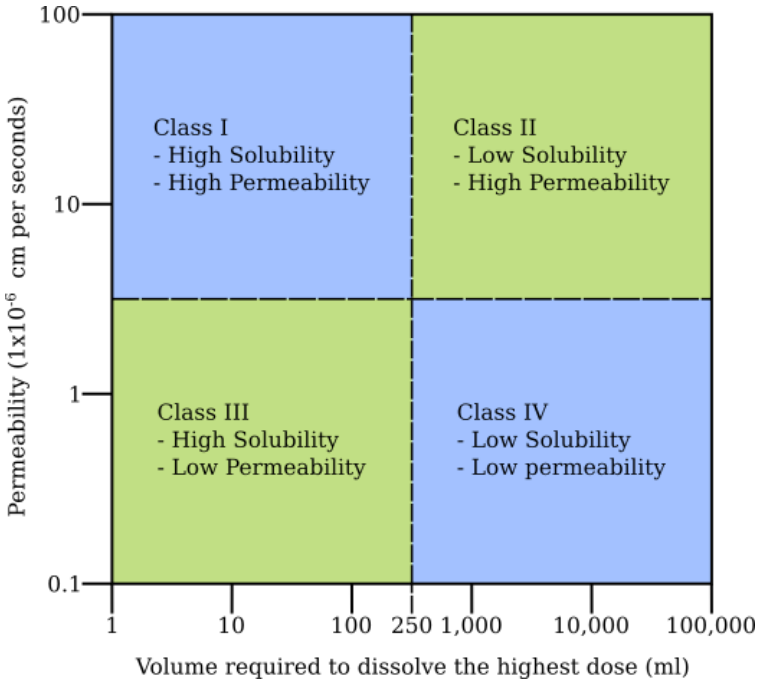

Figure 1.1: The Biopharmaceutical Classification System (BCS).

mance, a class 2 has low solubility and high permeability profile, class 3 shows high solubility and low permeability and class 4 display both low solubility and permeability. It is worth noting from the new chemical entities tested for market release, only a 5% belong to BCS class 1, making them the most attractive candidates to be pushed further into clinical trials. Whereas, 90% of the new entities have been categorised as poorly soluble, accumulating both class II and class IV substances [8]. Drug candidates, with limited solubility and/or dissolution rate can be very troublesome, as the uncontrollable and unpredictable solubilisation process may result in erratic and low bioavailability after their uptake.

Few years later, a revised version of the classification system has been published,

termed as the Developability Classification System (DCS), as displayed on 1.2. This system gives an emphasis on the addressing issues during drug development, rather than as an assurance in drug bio-equivalence. One of the main points DCS classifies formulations is based on the concept of Solubility Limited Absorbable Dose (SLAD) [9], where class II drugs have been divided into IIa (dissolution rate-limited) and IIb (solubility rate-limited). This division has been based on the concept that solubility and permeability are compensatory. Crystalline IIa drugs in standard solid oral dosage forms display complete oral absorption, even if saturation solubility is approached *in vivo*. This eliminates the need for complex solubilisation technologies for these types of compounds. However, their dissolution can be impacted by factors such as formulation particle size. Specifically, increased particulate size leads in reduction of particle surface area and further decrease of interaction with the gastrointestinal fluids, hence low dissolution-rate [10]. The opposite can be stated for the IIb compounds. Crystalline IIb drugs must be prepared in an already solubilised form, which presents the main challenge in drug formulation, as the crystalline structure within the formulation cannot solubilise enough. These outcomes generate great interest both in industry and academia to better understand the behaviour of crystalline structures, their physico-chemical properties and how such characteristics behave and interact with other compounds or influences from their micro-environment. This information will allow scientists to implement sophisticated formulation techniques that would improve aqueous solubility of BCS II and IV drugs.

1.1.2 Amorphous solid dispersions

Over the past decades, pharmaceutical industry has been consistently testing and utilising different routes to improve dissolution and oral absorption of

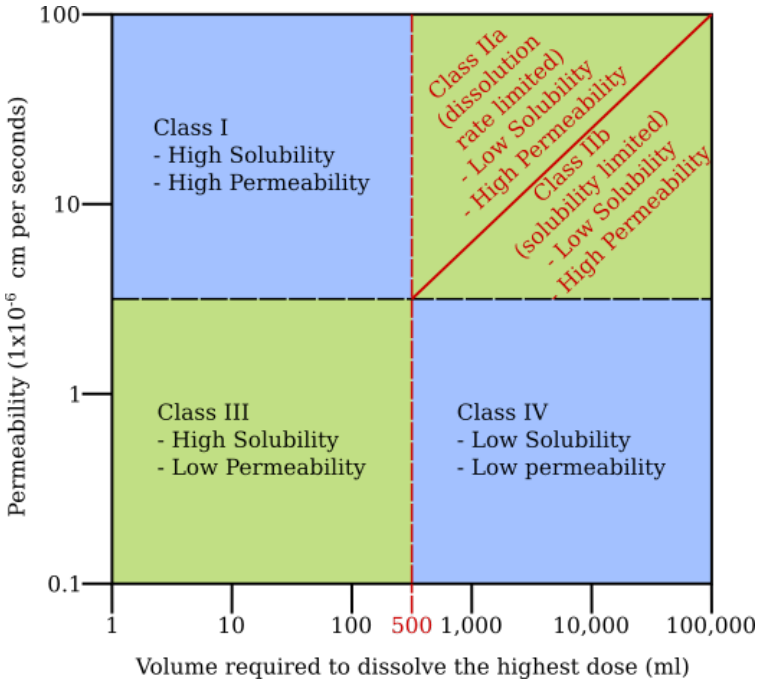

Figure 1.2: The Developability Classification System (DCS).

poorly-water-soluble drugs [11]. One popular route entails the chemical modification of the molecular structure, which involve synthesis of salts and co-crystals [12, 13]. With alterations to the structure of the drug however, this approach may lead to altered pharmacokinetic and pharmacodynamic properties [12] ending with unwanted pharmaceutical effects to the patient. Another interesting route is physical modification of the drug. By, increasing the contact surface area and decreasing particles size [14] micron to nano-ranged sized crystals are generated, with improved solubility performance. However, this method is effective only to particles which solubilise above 50 µg/ml [15]. Despite the chemical and physical alterations of an API, one very prominent route is the formulation approach. This entails the production of liquid or solid systems based on surfactant, lipid vehicles and carriers, respectively [16, 17]. Special attention has been given to polymeric Amorphous Solid Dispersions (ASD). Compared to crystalline compounds, these formulations gained popularity throughout the pharmaceutical research community, due to increased wettability, enhanced solubility, reduced particle size and high porosity [11, 18]. The main characteristic

feature of ASDs are the amorphous phase of the APIs in the system. They display an un-ordered intermolecular arrangement lacking their three-dimensional long-range crystalline structure [10, 19]. Their increased solubility is explained due to the higher energy state they exhibit compared to the crystalline solids. In Figure 1.3 [20] the classical free energy-temperature correlation is displayed. For a crystal when the temperature increases the free energy decreases significantly, converting spontaneously from solid to liquid state at melting temperature Tm. From this point there are two possible outcomes to the materials solid-state, depending on the speed of the cooling process. If the system is cooled at a slow rate below Tm, there is adequate time for crystal nucleation and growth, forming both short and long-range molecular ordering of the structure. Else, by rapidly decreasing the system temperature below Tm, the system enters a supercooled liquid state, where the molecules are mobile. Further cool-down of that system, below the glass transition temperature Tg, generates a free-energy increase in a distinct discontinuity. The system is said to enter a glassy state of high free energy compared to the crystalline counterpart.

As amorphous API solids exhibit a high energy state, they are also inherently less stable than crystals, and over time can convert to their thermodynamically stable crystalline form [10]. Furthermore, due to their increased molecular mobility to crystals, they demonstrate strong chemical reactivity with other molecules in their micro-environment, leading to chemical degradation [10]. In order to retard the crystallization process and prevent mobility, this is where the polymer molecules of the ASDs can be used. Polymers are structurally composed of repetitive units, known as monomers, forming long, carbon-backboned, molecular chains. When these chains are blended with the amorphous API down to a molecular level, crystal nucleation and growth can be hindered with hydrogen bonds [21–23] and/or by lipophilic attraction [24–26], forming numerous interchain or intra-chain crosslinks. As a result, the amorphous drugs

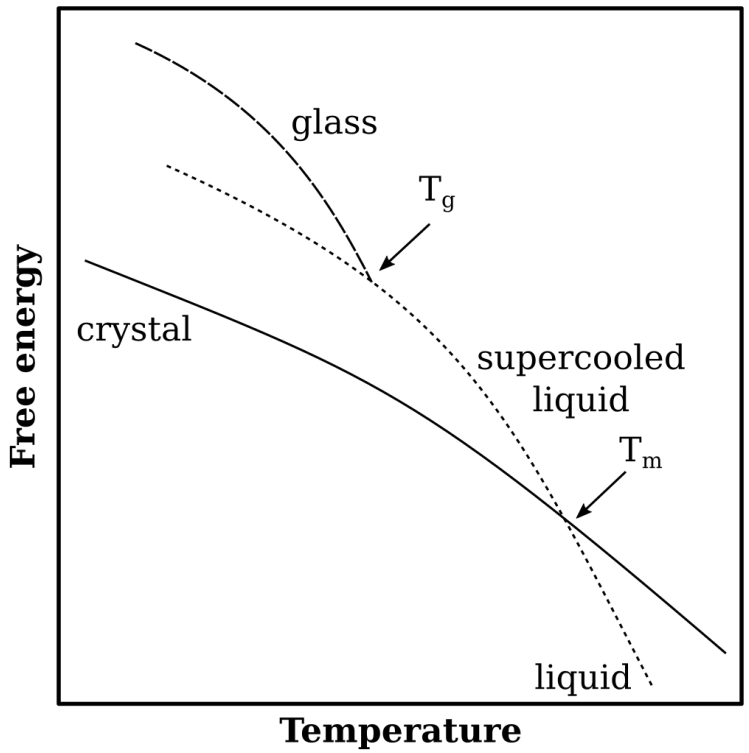

Figure 1.3: Temperature and free energy correlation on single-component state.

are entrapped, and hindered in mobility within those inter-molecular networks, reducing the formation rate of crystalline lattices. Amorphous solid-state systems contain adequate free energy to easily dissolve and solubilise in aqueous medium, whilst remaining relatively stable retarding the dissolution process [14, 27], as visualised in Figure 1.4. For the production of these types of formulations a series of ASD preparation methods have been established commercially and applied until today [28], such as Hot-Melt Extrusion (HME) [29, 30], spray drying [31, 32] or freeze-drying [33].

Regardless of the solubility enhancement of ASDs for poorly-soluble APIs provide, there are certain stability drawbacks to these types of formulation. Temperature, humidity [35], mechanical stress [36], as well as specific preparation methods [37–39] can affect the extent of matrix polymer mobilisation, drug crystallisation [34] as well as drug-polymer phase separation [40].

In addition, the API may also form different molecular arrangement of its crys-

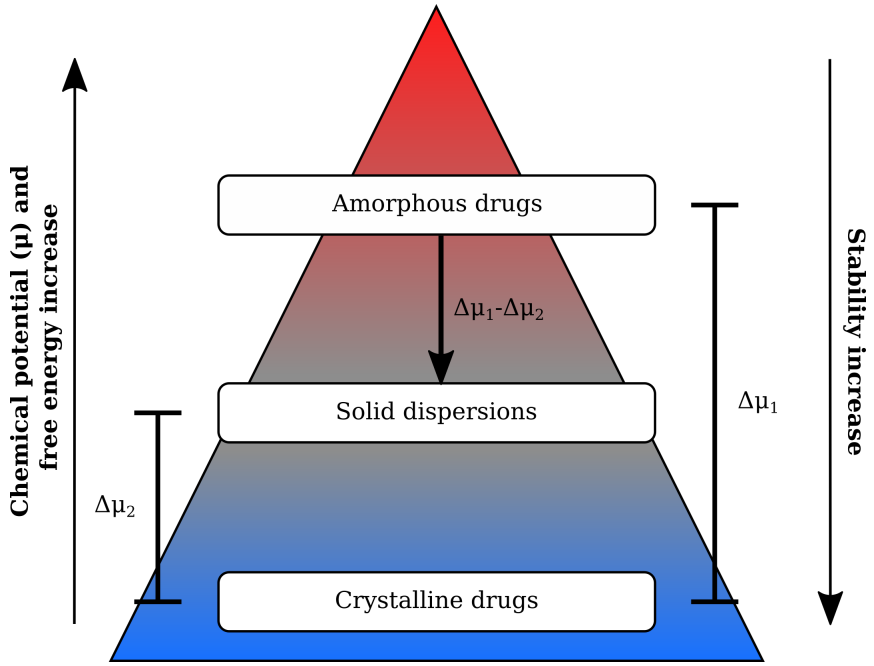

Figure 1.4: The energy pyramid of the crystalline, amorphous solid dispersion and amorphous form, with μ being the chemical potential (diagram not scalable) [34].

talline lattice, known as polymorphs. Different polymorphs of the same drug molecule, present different physical and chemical properties, with differing solubility, dissolution and stability effects compared to the desired crystalline form in a formulation [10]. As a result, changes in drug distribution and formulation homogeneity leads to variable dissolution rate and consequently to unwanted molecular bioavailability concentrations.

1.2 Chemical characterisation of formulations

1.2.1 Pharmaceutical analysis

For commercial ASD or even nanotechnology-driven pharmaceutical products to become released in the market it is vital to identify the causing factors which affect the stability and performance of these products. To address those issues,

pharmaceutical analysis plays a crucial role both in quality control as well as research and development in the field of pharmaceutics. Due to the complexity of the physico-chemical properties formulations present, multifaceted analytical methods are required to comprehensively characterise these materials, how they may interact with each other and how they might behave or perform in different environmental conditions, including *in vivo* [41]. Specifically, these methods are applied to provide answers to certain questions, such as identity of components, their amount in the formulation of interest, impurities, self life and more [42]. Depending on the nature of these questions, one must choose one or multiple suitable analytical techniques which will be able to provide adequate information to answer these questions. In particular, to physically characterise a ASD formulation, in terms of particulate dimensions and morphology, light microscopy [43], scanning electron microscopy [44, 45] or transmission electron microscopy [46] can be used. For thermometric-associated measurements differential scanning calorimetry [47] can be applied. However, these methods are limited or lack in chemical specificity. To complement with the obtained physical information, chemometric techniques can be implemented, which mainly fall under the field of spectroscopy. Spectroscopic methods are based on the concept of material interaction exposed under electric or magnetic radiation to a molecular or even atomic level. These range from fluorescence [48], infrared , near-infrared [49] or nuclear magnetic resonance [50]. Among these spectroscopies, one technique which gained great popularity over the recent years is Raman spectroscopy.

1.2.2 Vibrational spectroscopy

Light can interact with matter in various ways, including absorption, emission or scattering [51]. Light in the form of electromagnetic waves constitutes of very

small and discreet energy packages known as photons. These photons interact with molecules by transferring or gaining vibrational energy or by remaining intact. Here vibrational spectroscopy measures the transitions between molecular vibrational energy levels, by recording these changes in the form of recorded spectra.

1.2.2.1 Infrared spectroscopy

InfraRed (IR) spectroscopy relies on the absorption of the mid-IR (25 µm - 2.5 µm) and near-IR (2.5 µm - 800 nm) spectra range, where the transition between the molecular vibrational energy levels are recorded [51]. The basis of these transitions involves the change in dipole moment of the analyte molecule, by oscillating the distribution of the positive and negative partial charges between the atoms. Depending on the different functional groups in a molecule that undergo the transition in dipole moment, the drop in IR intensity, due to energy absorption, is recorded across the spectrum. This spectrum is then plotted against the inverse of the wavelength i.e. the wavenumber (cm^{-1})[52]. IR spectroscopy has been applied in a multitude of pharmaceutical studies. These were often associated with polymorph identification [53, 54], drug polymer interaction in ASD [55–57], even obtaining information about the content moisture of compounds such as powders, granules, pellets, tablets and capsules [58, 59].

1.2.2.2 Raman spectroscopy

The Raman effect was first been observed and reported by Sir C.V. Raman and Krishnan K.S. in 1928 [60, 61]. This effect is a two-photon inelastic light-scattering event. As shown in Jablonski's diagram in Figure 1.5, from the photon emission of a monochromatic light, a molecule is promoted to a vir-

tual excited state and further returns to the same or different levels of their vibrational ground state. In most cases, a photon undergo elastic scattering (Rayleigh), with no energy transfer to the sample molecule, which returns to its former ground state. From all the probabilities related to all processes of light-matter interaction, the Rayleigh scattering event has an approximate chance of occurrence of *ca.* $1{:}10^5$, for every meter of travel. There is also a small probability of *ca.* $1{:}10^7$ photons to inelastically scatter from the matter and either lose or obtain energy [62]. This is the Raman scattering phenomenon, in which the scattering could be red- shifted for the photon (Stokes scattering), returning the molecule to a higher vibrational ground level ($\nu{=}0 \rightarrow \nu{=}1$), or blue-shifted (Anti-Stokes scattering), with the molecule returning to a lower ground level ($\nu{=}1 \rightarrow \nu{=}0$). These processes are governed by Boltzmann distribution, defined by the relative population of energy states at a given temperature [63]. For a Raman event to occur, it is important to consider the polarisability of the analyte material. Polarisability refers to the ease of a molecular cloud becoming distorted by the electric field of an incoming photon and can be related to the elasticity of the electron cloud of the molecule. For instance, a C=C is a strong Raman active system, where the π electron cloud can be distorted with expansion and compression along the bond's axis. Raman active molecule give stronger Raman scattering signal [52]. Therefore, in pharmaceutical formulations analysed through Raman spectroscopy, stronger Raman signals are often detected from APIs due to the number of π-bonded electrons available compared to excipients, where mainly σ-bonds are available [64]. This distinction between APIs and excipients is a great asset in chemometric analysis of multi-component pharmaceutical products [65].

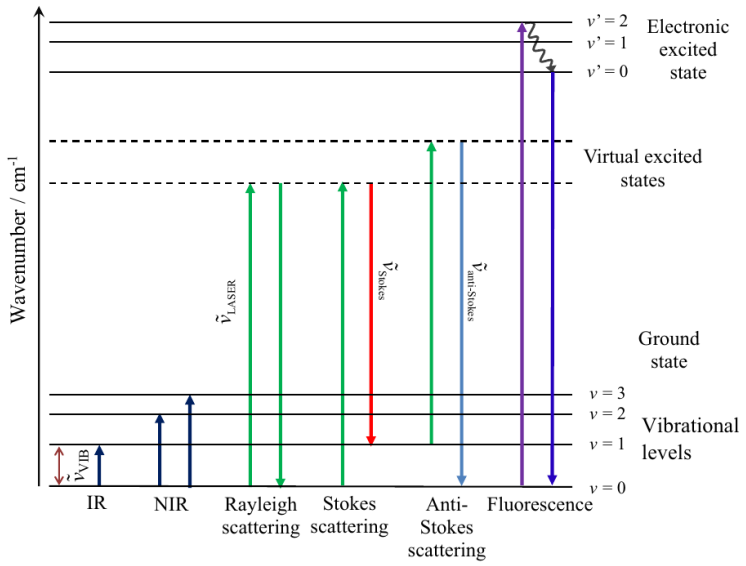

Figure 1.5: Jablonskis diagram [63]. Briefly, this illustration depicts the energy level changes in infrared (IR), Near-InfraRed (NIR) absorption, Raman and Rayleigh scattering and fluorescence. In Stokes scattering, the molecule gains energy from the laser photon (green) and thus the scattered photon (red) is at a lower energy. Whereas, in Anti-Stokes scattering, the photon gains energy from the molecule and the scattered photon (blue) is at higher energy.

1.2.2.3 Raman microscopy

Raman spectroscopy is often combined with optical microscopy in order to obtain spatially-associated chemical information of the sample of interest. As displayed on the schematic in Figure 1.6, a Raman microscope is equipped with an excitation laser of interest, which beam is directed with the help of set optics onto the sample's surface through the objective lens to produce Raman scattering [63]. The scattered light is collected through the same objective and directed to a spectrograph, for its separation into individual wavelengths. The produced lights are projected onto a Charged-Coupled Device (CCD), with their intensity being measured in the form of a spectrum. This technique has many useful applications in pharmaceutical sciences, such as API polymorphism identification [66], in vivo drug delivery investigation [67, 68], characterisation of constituent distribution in solid dosage forms [69–73] and counterfeit detection [74]. It facilitates a non-invasive analysis and limited sample preparation,

without the need of a dye, like in fluorescence spectroscopy [63]. A wide range of samples in various physical states can be supported, such as translucent, opaque, coloured, solid, semi-solid, including dosage forms like creams, suspensions, syrups and solutions and more [75]. The analysis of such components can be achieved by using glass containers, well plates or even in solubilisation in aqueous environment [76]. Despite the many advantages of Raman imaging, spatial resolution is a major limitation in optical-related microscopies. Spatial resolution in Raman microscopy is defined by the volume of the bulk sample that is irradiated by the monochromatic light. The dimensions of this volume are determined by the laser spot size (lateral resolution) and the depth of field (depth resolution) of the microscope. The lateral and axial resolutions can be calculated from Abbe's Equation 1.1 and Equation 1.2, respectively [77].

$$Abbe_{\mathrm{xy}} = \frac{\lambda}{2NA} \tag{1.1}$$

$$Abbe_{\mathrm{z}} = \frac{2\lambda}{NA^2} \tag{1.2}$$

The diffraction limited spot size is measured as the wavelength of the incident light λ, over two times the Numerical Aperture (NA) of the objective. In brief, NA is a dimensionless number which describes the size of the angle, relative to the focusing point, at which light is emitted or collected from the objective lens. The NA can be calculated from equation 1.3,

$$NA = n * \sin\theta \tag{1.3}$$

where n is the refractive index of air or immersion oil and θ is the half angle of the objective aperture. According to the first equation 1.1 for shorter, blue-shifted, wavelengths and high NA objectives, the spot size reduces and the sample spatial resolution improves. For instance, having a green 532 nm incident wavelength with an oil immersion 100× objective of 1.45 NA, the diffraction spot size is estimated to be approximately 183 nm.

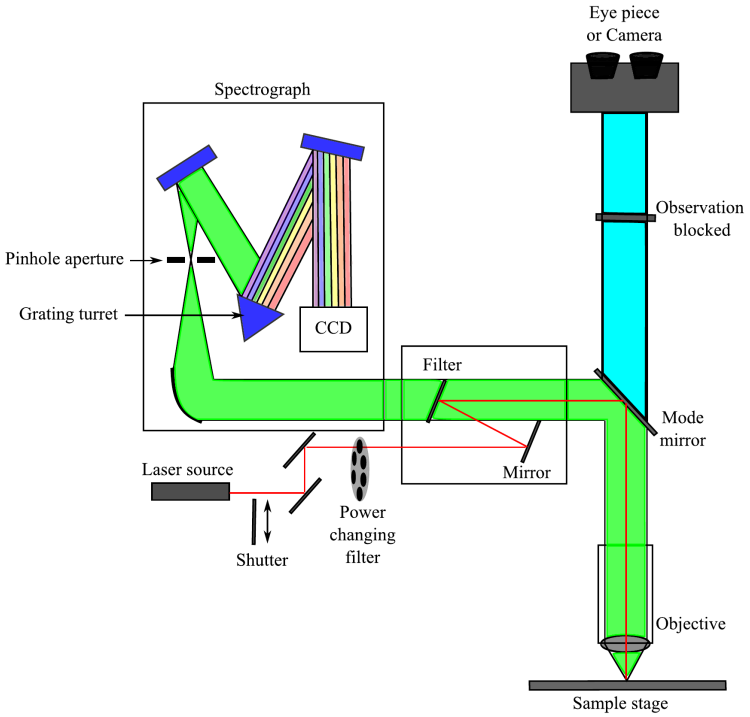

Figure 1.6: Schematic of a CCD based confocal Raman microscope [63].

1.2.2.3.1 Raman mapping Raman mapping refers to the collection of Raman spectra of an area or volume of a sample, through a virtual grid of XYZ-axial coordinate system. The collected data is also referred to as hyper-spectral data. In a Raman mapping process, there are multiple approaches to acquire spectra, due to the CCD matrix detectors, possessing pixels in a two-dimensional array. The most popular method is the point-by-point mapping, where the laser spot is being translated through the grid system sequentially

and for each point a full Raman spectrum is acquired [78–81]. There is also line-scanning, where an irradiating line gathers spectra across multiple points on a single line of the scanning grid. Another approach is the global imaging, where every pixel in the matrix detector is used to generate an image of the irradiated sample. Point-by-point mapping has several advantages over the two other approaches as it provides a better Signal-to-Noise ratio due to spectral summing or averaging in the CCD as well as provides a full spectrum per pixel for chemical analysis [82].

1.2.2.3.2 Data analysis The amount of data that can be obtained with a Raman microscopy system can be large to the scale of thousands of spectra. The analytical steps performed are divided into data pre-processing as well as data exploration and quantification.

1.2.2.3.2.1 Data Pre-processing This stage is a vital step before the interpretation, quantification and projection of the hyperspectral data. An experimentally recorded Raman spectrum is the product of various contributions [83]. A Raman spectrum can be corrupted with sharp, high intensity spikes which originate from high energy cosmic particles hitting the CCD, sample fluorescence, and CCD thermal noise. For the removal of those sharp peaks, routine processing can be performed through commercial software, or by applying an outlier detection algorithm, described in a relevant study [84]. To remove the spectral background originating from sample fluorescence or thermal fluctuations on the CCD, one can apply background correction procedures like polynomial fitting on the acquired spectrum [83]. Often-times, Raman spectra can be affected by the components of the formulation, which present different Raman scattering coefficients, generating disproportionate signal intensities. In order to eliminate these variations in the scattering efficiency, the

spectra are normalized by dividing their mean intensity [85].

1.2.2.3.2.2 Data processing The methods whereby pre-processed data can be analysed and explored are univariate, bivariate and multi-variate analyses. The univariate analytical approach focuses on measuring a Raman band signal intensity, integral or bandwidth, in order to generate images. This approach is used to project the spatial distribution of a single component [86–89]. In bivariate analysis the spatial distribution of two components is projected, by calculating the ratio of the two component band intensities or integrals [69, 70, 90]. In multivariate analysis, single component values are not utilised. Instead, the relationships between the intensities of all the data points in the hyperspectral data cube are calculated and components are generated based on their variance. Multivariate analysis was applied for generating both quantitative [91] and qualitative [85] Raman images [63].

1.2.2.4 Surface-enhanced Raman spectroscopy

While Raman spectroscopy has great popularity in pharmaceutical analysis, surface-enhanced Raman scattering acquired a lot of attention and experimentation in the Raman community over the past decades. In 1974, Fleischmann and his co-workers accidentally identified signal enhancement of the pyridine molecules over rough silver electrodes in an electrolyte cell [92]. After that event, two independent groups [93, 94] measured the enhancement in the pyridine signal by a factor of 10^5-10^6. This escalated to a series of studies to identify factors behind this event [95, 96] and applications in various field, such as electrochemistry, biology, medicine, materials science and more [97]. Especially in pharmaceutical studies, De Bleye et al [98] demonstrated the use of surface enhanced Raman chemical imaging for detecting and quantifying 4-aminophenol

impurities available in paracetamol tablets. This surface enhancement effect has been repeatedly reported for molecular analytes adsorbed of metallic clusters or roughened surfaces such as silver, gold, aluminium or copper (Figure 1.7 a)) [99–102]. This mechanism of the field enhancement comprises of two contributions, namely Electromagnetic Field Enhancement (EM) and Chemical Enhancement (CHEM).

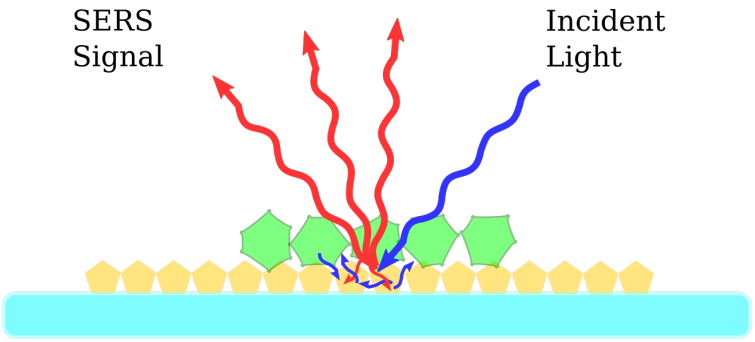

Figure 1.7: Depiction of SERS experimental setup where the incident light (blue arrow) is amplified at the rough metal substrate, due to localised surface plasmon resonance, generating and enhancement in both SERS Raman signal and that of the incident light at the laser spot vicinity.

1.2.2.4.1 Electromagnetic field enhancement This mechanism is arguably the primary cause of the enhancement as the enhancement factor can vary between 10^8-10^{11} [96, 103, 104]. The rise in EF is the result of the excitation of Localised Surface Plasmons (LSP) from the metallic nanoparticles of the SERS substrate. Specifically, plasma refers to the mobile delocalized valence electrons of metal nanoparticles, forming a dense gas of charged particles [105, 106]. Whenever an electromagnetic light or electron beam bombards the plasma, a transient change to the distribution of electrons occurs, first generating denser electron clouds followed by Coulombic electron repulsion. The resulting oscillations in electron density are called plasmons. It is important to note that the SERS nanoparticles used have a typical size of less than 100 nm, normally smaller in size than the wavelength of the excitation light. This leads to the distribution of the plasmon oscillation over the whole particle volume,

resulting in a harmonic electron oscillation driven by the energy resonant light wave. As seen in Figure 1.8 b) the electron cloud oscillates like a dipole in parallel direction to the electric field of the electromagnetic radiation, acting as a nano-antenna" [107]. With multiple metallic cluster displaying LSP resonance the local electric field at the vicinity increases, with a range of a few nanometre, amplifying the Raman signal.

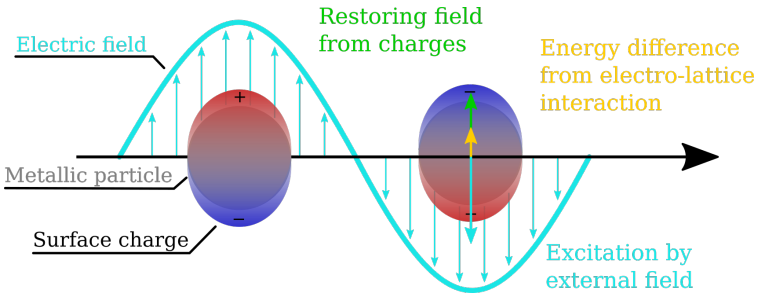

Figure 1.8: Illustration of the dynamics of a metal cluster nanoparticle during irradiation. The diagram shows a snapshot of a nanoparticle excited by an applied electric field. The incoming electric field (cyan) excites the nanoparticle, while the restoring electric field is generated by the out-of-equilibrium surface charges (green) and the ionic network causes damping (yellow), with the direction of the arrow assuming that the electrons already move downward in the diagram). If the external field oscillates at the frequency of the resonant mode of the particle, both external and restoring fields will sync, greatly enhancing the total field in and around the particle. If the external field disappears, the charge oscillation in the particle will continue until dampened by the friction-like losses [108].

1.2.2.4.2 Chemical enhancement The Chemical Enhancement (CHEM) refers to the enhancement of Raman scattering due to the transfer of electrons between the adsorbed molecules and the metallic substrate. This mechanism is based on Charge-Transfer [97, 109], either transferring charge from the conduction band of the metal to unoccupied molecular orbitals or vice-versa. According to the literature, the enhancement factor recorded is about 10^2-10^3 [110–112], although some other studies have indicated under certain conditions these values can be higher [113–116]. As both enhancement mechanisms are augmenting the Raman scattering events, unexpected chemical enhancements can lead to quantitative and qualitative misinterpretations of these results [97].

Therefore, upon data examination one must take serious consideration of certain aspects of the SERS substrate such as particulate size, shape, adsorption geometry, relative orientation as well as surface homogeneity [97], before drawing any conclusions.

1.2.2.4.3 SERS drawbacks Despite the potentially high chemical sensitivity of these technique, there are certain drawbacks that need to be addressed [117–119].

- Under a conventional microscope setup, SERS does not resolve spatial features below the diffraction limit of light, with the lowest possible limit approximating at 200 nm.
- SERS experimentations are only limited to rough metallic substrates, other than smooth which provide only CHEM to the signal.
- As aforementioned both EM and CHEM can be intertwined generating variable signal enhancement to different Raman bands. Therefore, careful consideration of the properties of the SERS substrate and studied material should be made as well as informed decision of the pre-processing technique is required before result interpretation.

1.2.3 Super-resolving microscopy techniques

1.2.3.1 Scanning probe microscopy

Scanning Probe Microscopy (SPM) is an umbrella term of a group of microscopies which are based on the interaction between a probe and the sample. Specifically, the probe is of nanometre size dimension which is used for the detection of local surface properties down to nanometre or even atomic resolution

[120]. Depending on the method of interaction applied between the probe and the sample, the type of scanning probe microscopy is determined. Two of the most popular SPM techniques to date are Scanning Tunnel Microscopy (STM) as well as Atomic Force Microscopy (AFM).

1.2.3.2 Atomic force microscopy

For the resolution of physical features down to nanometre lengths AFM has proven to be a powerful nanoscopic tool [120, 121]. The principle of this technique lies on the forces produced between the apex of a nanometre-sized probe, originating towards the edge of a flexible cantilever, and the sample surface. According to Figure 1.9a, there are two different stages of force-associated tip-sample interaction. (a) At long distances between the probe and the sample surface there is no force. (b) As the tip approaches the surface there are small negative forces of attraction. This can be due to electrostatic or van der Waals forces. After maximum negative force has been reached, thereafter with the continuous descent of the probe, a drastic increase in repulsive forces occurs.

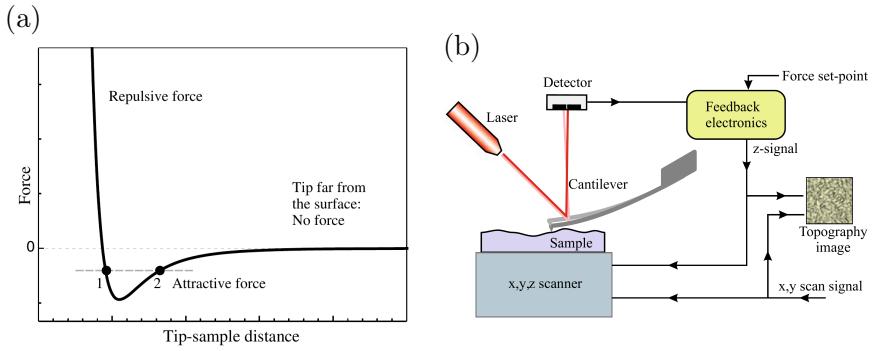

Figure 1.9: a) Force between probe and sample as a function of distance. b) Schematic of an atomic force microscope [120].

The force involved between the surface and the apex can be measured with the deflection of a laser beam across the surface of the flat spring, also known as cantilever, locating at its edge the probe. Based on the cantilever stiffness k

(spring constant), the Force in nN can be determined according to *Hookes Law* (Equation 1.4),

$$F = kz \tag{1.4}$$

where F is the spring force, and z is the displacement of the cantilever between the bent and the relaxed state. In Figure 1.9b a schematic of the operation of an AFM is displayed. Here the reflected laser from the back of the cantilever hits the surface of a photodiode. The changes in probe's movement are detected on the photodiode surface and with the help of piezo-electric transducers maintain a constant force between the tip and the sample and a raster scan of the sample's surface with free translation to all three directions.

In AFM there are mainly two modes that can be selected for a scan operation, contact and non-contact mode. The first mode refers to the constant engagement of the probe to the sample surface, causing the cantilever to deflect. While the tip scans the surface, the degree and direction of deflection is recorded to gain information of the sample topography. This approach offers high nano-scale resolution, allowing even the visualisation of electronic configuration of single atoms [122]. However, by applying strong lateral forces, this can lead to malformations and damages to the sample surface as well as apex blunting which affects the recorded image resolution [123]. The non-contact or intermittent or tapping mode overcomes to a large extent the aforementioned limitation by minimising the forces applied. In this mode, the cantilever oscillates at a certain frequency, allowing the apex to tap the surface in fractions of a second. Due to the marginal forces, this method allows the investigation of very soft samples such as cells, bio-membranes or liposomes [124–128]. It is worth mentioning that the application of AFM is not limited to morpholog-

ical identification of the sample in question. This technique can also extract mechanical information such as elasticity or adhesiveness of the sample. The frictional forces generated during contact mode as well as the energy dampening by soft materials during tapping mode in flat surfaces can be detected. These changes in force allow the analysis of different material distribution or phases within the sample, such as lipid separation [129] or drug distribution within nanoparticles [130]. AFM also finds application in multiple studies in the pharmaceutical analysis, including tablet coating [131], crystal dissolution [132], crystal growth [133] and drug polymorphism [134]. Nonetheless AFM is only constrained to extracting only the physico-mechanical properties of the sample.

1.2.3.3 AFM-IR

Another emerging nanoscopic technique for chemical characterisation of submicron sized materials is the AFM-IR or photo-thermal induced resonance IR [135]. Similarly with IR, this technique is based on the amount of IR light absorbed in the sample. First developed by Dazzi et al [136], this system comprises of an AFM system, a tunable, pulsed laser source as well as the optics to direct the light towards the apex of the AFM probe. As the IR laser irradiates the area (≈40 µm in diameter) around the tip, the sample within this space absorbs and thermally expands in a time-frame close to the laser pulse length [137, 138]. The resulting surface thermal expansion is less than 1 nm which can last between sub-nano to few micro seconds, depending on the thickness and thermal conductivity of the sample [138, 139]. With the rapid expansions in the sample surface the AFM probes are kicked into oscillation, with changes in their amplitude being proportional to the sample absorption [137, 138, 140]. The typical ΔT can range between 1 to 10K, since the thermal expansion coefficients are very small (from 10^{-6} to 10^{-4})[141, 142]. To acquire absorption

spectra the AFM tip must remain stationary on the sample surface, while sweeping across the laser wavelength. Whereas, to obtain the absorption map, the laser wavelength must remain fixed as the AFM probe performs a raster scan across the sample. For the successful execution of this technique, tip–sample contact dynamics play a critical role for resolving fine nano-particulates in a scan. Therefore, for different types of samples, the selection of experimental parameterers, such as AFM probe scan line-speed, probe force setpoint, laser power, laser frequency must be taken under careful consideration and extensive evaluation [135]. AFM-IR has found application across multiple fields, including polymer science [143–147], photovoltaics [148–151], chemistry [152, 153] or 2D materials [152, 154–157]. This technique has also been demonstrated in a series of pharmaceutical studies, such as evaluating the degree of drug-polymer miscibility in a ASD system [158] or influence of solvent properties on the phase behaviour of ASDs [159]. Regarding drug-polymer miscibility, Li and Taylor [158] investigated the miscibility of a poorly water- soluble drug telaprevir, with three different polymers, using the AFM-IR technique. From this study it was possible to resolve down to 50 nm in domain size of the phase-separated polymer regions.

1.3 Tip-Enhanced Raman Spectroscopy

1.3.1 TERS concepts

As the concept of enhanced Raman signal were first noted during the 1980s, in 1985 Wessel proposed the idea of the Tip-Enhanced Raman Scattering (TERS) [160]. This technique combines the concepts of SERS and SPM, allowing the simultaneous acquisition of physico-chemical information of the sample down to nano-scale resolution topography [118]. This recommendation cascaded in

2000 after a series of experiments [161–164] applying metal coated or full-coated SPM probes to test this concept. Upon laser illumination of the probe, LSP are generated on the apex giving a large enhancement on the electromagnetic field, resulting in boosting the Raman scattering of the compounds. Specifically, as the SPM probe approaches the sample surface, a nanolight-source is generated within the laser focal spot [117]. When approached, an enhanced Raman signal is obtained from a tiny volume of the sample by the nanolight-source of the probe apex. This Raman signal is referred as the near-field signal. At the same time Raman signal from the focal spot is also generated by the incident light. This is referred as the far-field signal. Therefore, the collected signal is the result of both far- and near-field Raman signals. One can deconvolve near-field from far-field by acquiring Raman signal with the probe retracted away from the laser spot (far-field) and subtracting it from the combined Raman signals.

TERS can provide an enhancement factor of 10^3-10^6 of the Raman signal generated under the vicinity of the probe apex, with the spatial resolution ranging between 10 to 80 nm, below the diffraction limit of light [117]. Compared to the stronger signal enhancement provided with SERS, TERS delivers very good performance at the nano-scale, reaching even single molecule detection sensitivity [165, 166]. In a TERS setup the Raman spectrometer can be coupled either with an AFM [161, 163, 164, 167] or an STM [167, 168], able to circumvent some of the issues encountered in SERS. One of these issues is the heterogeneous distribution of the metallic clusters, generating Raman scattered signals of variable enhancement factor, making quantitative analysis difficult. The second is the diffraction limited resolution of the probed molecules. In TERS, the single particle or edge feature of the probe works as an antenna to scan the sample and resolve vibrational signatures at several nanometres.

1.3.1.1 General principles

The enhancement of the electromagnetic field in the vicinity of the apex is the result of three contributions [169]:

- Lightning-rod effect: Under a plasmonically active, metal, sharp nanotip with the influence of laser irradiation, the generated surface charges are accumulating towards the apex, leading to strong optical resonances and highly confined electromagnetic field, serving as a lightning rod [170].

- Localised Surface Plasmon Resonance (SPR): Likewise in SERS, the plasmons of metallic clusters or metal surface of the probe require to resonate at the external electric field, by forming oscillating dipoles which alterate based on the frequency of that field, amplifying the incident light and the Stokes-scattered light.

- Antenna resonance effect: A single metal cluster operates as the simplest form of dipole scatterer. Due to its small size (≈10-20 nm) the wavelength of the scattered light generated from the surface plasmon is weaker compared to the incident one, making the detection of the enhanced signal in the far-field impossible [171, 172]. By manufacturing a rod or cone-shaped metallic structure, all of the individual clusters can form synergistically a bigger dipole scatterer resembling as an antenna. Like in the classical antenna theory, with the axial length of the tip being related to the integer multiple of the half wavelength of the incident light, the antenna resonates [169, 172]. This makes possible the detection of the scattered light in the far-field detector.

1.3.1.2 Optical geometries

TERS systems can be designed with different illumination and detection geometries. An illustration of all the possible combinations found in studies is displayed in Figure 1.10. A bottom illumination or transmission mode setup is one of the first configurations built in a TERS system [161, 163, 173]. This design consists of an inverted microscope coupled with either an AFM or STM and a high numerical aperture objective ($>$ 1.4 NA). The objective lens focuses the excitation monochromatic light from below through the sample onto the apex of the probe (Figure 1.10(a)). The backscattered Raman signal is collected through the same lens, further into the Raman spectrometer. High NA objective lens are often oil-immersion lenses, using coverslips as a substrate due to their small working distance. These types of objectives have the advantage of confining the laser down to $\approx$ 200 nm with less than 1 mW of laser power, reducing the background noise, generating high Signal-to-Noise spectra as well as generating strong longitudinal field at the probe, inducing strong plasmon resonance effects at the apex [173, 174]. The main drawback of this approach is the limitation in their application to thin ($<$ 1 µm) and transparent samples as the focal point of the laser has to reach the uppermost surface of the sample, inducing the signal enhancement mechanism from the probe. To circumvent this constrain, parabolic mirrors can be set on top of the sample, with a hole to allow probe movement (Figure 1.10) [175, 176] . The parabolic mirrors (NA $\approx$ 1) both irradiate and collect the Raman signal from the sample. Despite this advantage, integrating this geometry under an AFM system can be challenging [177].

Two additional types of TERS geometrical configurations are the top and side (reflection mode) illuminations. In these optical layouts long distance objectives (NA. 0.28-0.55) are focusing on the sample surface from the top and at

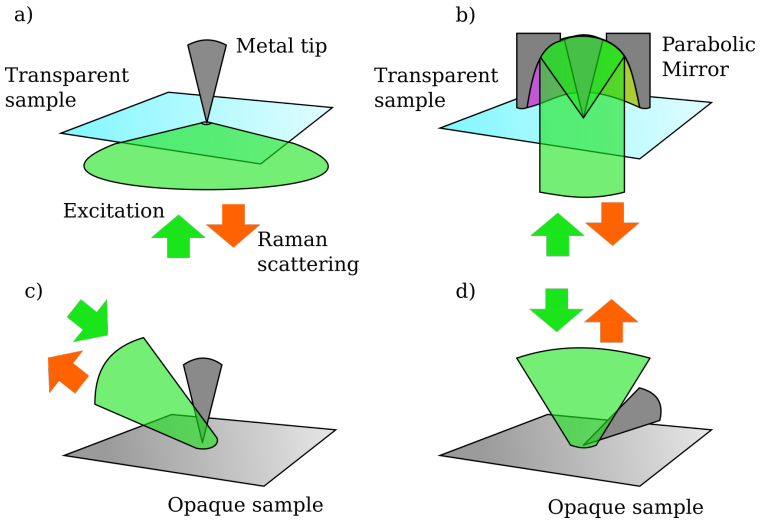

Figure 1.10: Illustration of the different TERS setup geometries. a) bottom illumination, b) side illumination with parabolic mirrors, c) side illumination, d) top illumination [177].

angles between 45°-70°, with respect to the tip (Figures 1.10 (b),(c)). In both illumination settings the same objectives are used for irradiating the sample and collecting the scattered signal. However, signal loss may occur in both top and side illuminations due to the shadowing effects of the probe as well as asymmetric confocality. Therefore, to compensate with the efficiency of signal collection, laser powers between 5-10 mW are applied. These systems have been used in a range of samples, such as lipid and protein species [178, 179]as well as opaque ones [180–182].

1.3.1.3 Polarisation effect

The selection of light's polarisation in TERS is an important aspect that can affect the signal enhancement yield, under different geometrical systems. Light polarisation refers to the way the electric field vector of the incident light propagates in space, relative to the plane of incidence. As presented in Figure 1.11, the electric fields, in the form of classical sinusoidal waves, of an s and p-polarised light are perpendicular and parallel to the plane of incidence, respectively [183]. It is important to note that the direction of the electric field

vectors mentioned are constant over the full beam profile. There is also the case where the vectors of the electric fields are oriented in the radial direction, pointing towards the centre of the beam centre axis. This effect is also known as radial polarisation (z-polarised light) [184].

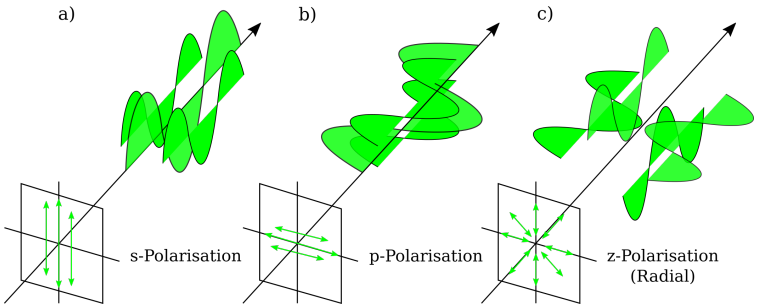

Figure 1.11: Different types of electromagnetic wave polarisation. a) s-polarisation, b) p-polarisation, c) z-polarisation (radial) [184]

Suitable laser polarisation in TERS, can provide efficient laser illumination across the axes of the tip [177, 185]. For a side-illumination setup, p-polarisation delivers high electromagnetic enhancement across the length of the probe. Whereas for a bottom-illumination a z-polarised light gives the highest enhancement, encircling the "spherical" metallic cluster.

1.3.1.4 Probe preparation

In a TERS setting, regardless of the optical setup selected, the most crucial aspect of signal enhancement, chemical-associated spatial resolution and reproducibility is the probe preparation. There are several factors which can influence the enhancement factor are well as the spatial resolution, some of them being, metal material, apex radius, angle or morphology of the probe [186]. For instance, depending of the wavelength of the excitation light, a metal should be chosen where their surface plasmon of their nanoparticles resonate with that wavelength. Ag and Au materials are selected for tip fabrication and excitation under the visible light, whereas Al is applied under the UV or deep UV spectral regions [187]. Also, the type of SPM instrument used can influence the design

of tip fabrication. For STM-TERS instruments the most common and reproducible method to produce probes is electrochemical etching of metal wires, usually Ag and Au [161]. Whereas for AFM-TERS setups, the desired metals are adsorbed on commercially available silicon or silicon nitride (Si, Si_3N_4), via vacuum evaporation or electrodeposition. The produced morphology of the deposited metal clusters or films change based on the material selected or evaporation ratio [188, 189]. Furthermore, the plasmonic enhancement of the tip is heavily influenced by the number of metal grains and their in-between distances on the probe surface [172, 190]. Also, by decreasing the refractive index of the probe substrate, i.e. from Si (n=3.48) to SiO_2 (n=1.5) of an Ag-coated tip, it allows the resonance of the localised SRP of the metallic coat with the green/blue excitation laser wavelength. This example of Silicon oxidation process can be achieved especially with thermal oxidation process [191].

Despite the method selection of tip fabrication, it is also equally important to consider the lifetime of the probe. In particular the coating of the tip i.e. thickness, purity, material as well as mechanical stress determine the stability and can further influence the duration and quality of a measurement [192]. Gold tips belong to noble metals, meaning they are inert to oxidation but mechanically soft material compared to silver. Silver coated probes on the other hand are strong, provide better signal enhancement in the visible region compared to gold [193]. However, they oxidise up to 24 hours, after fabrication or if stored properly up to 5 months under inert gas, before their use [194, 195]. Regardless of the probe used instances such as probe contamination or coat degradation may occur during the experiment, hindering the enhancement performance of the probe.

1.3.1.5 Spatial resolution

As aforementioned in a previous section, the spatial resolution in an optical microscope can be defined through the Abbe criterion Equation 1.1, which ultimately can reach down to $\approx$ 200 nm. Under a TERS system the Raman signal generated originate from the molecules in the nanocavity between the apex and the sample surface, where the electromagnetic field is stronger and confined, compared to a conventional microscope. This suggest that the spatial resolution of TERS is not limited by the diffraction of light, rather than the geometry of the tip apex [196]. Remarkably in specific cases sub-nanometer resolution Raman maps were obtained in AFM-TERS under ambient conditions in DNA sequences as well as amyloid fibrils [197, 198]. However, this cannot be always the case as biological macromolecules produce weak Raman scattering and generate low Raman signal enhancement [199–201]. There is also the case of sample degradation under room temperature, leading to generation of spurious peaks [202].

1.3.2 TERS applications

Over the past couple of decades, TERS has been applied in a series of studies across different scientific disciplines, mainly for sample examination, by obtaining nano-scale information of their physico-chemical properties. Like in Raman spectroscopy, TERS is a label-free technique and capable of retrieving information such as chemical composition, reaction mechanisms, molecular orientation, *etc* [177].

1.3.2.1 Carbon and other chemical investigations

TERS has been intensively used for the characterisation of non-biological samples. Specifically, this technique has been applied to probe 1D wire-like samples such as the investigation of nanoscale variations in diameter, defects, strain and chirality of carbon nanotube [203–205] or fraction of crystalline and amorphous content in Ge nanowires [206]. This application has been extended in 2D materials, including the characterisation of edges, defects and contamination in single-layer graphene [207–209] and many other studies on MoS_2 [210, 211], $MoSe_2$ [212], WSe_2 [213] materials. This method has also been applied for *in situ* or *ex situ* characterisation of different catalytic systems [214–220] as well as electrochemical processes [221, 222]. TERS has found application in studies focusing on multilayer polymer thin films [223], interfaces of phase-separated domains in polymer-blends [224, 225], local strain in semiconductors [226].

1.3.2.2 Biological investigations

Its application has also found use in life sciences. Unravelling the chemical composition of bacteria [227], viruses [228] and lipid membranes [229], mapping nucleic acids such as DNA [230] , RNA [231] and further investigating properties of amino acids [232], peptides [233] and proteins [234–236]. Special interest has also been seen in determining the distribution of small molecules within biological cells [237].

1.3.3 Motivation and aims of the work

As aforementioned, ASD provide many benefits to the solubility enhancement of poorly-soluble APIs. Often-times, this formulation platform may fail under certain environmental conditions or during manufacturing, affecting ultimately

the bioavailability concentration of the drugs in the systemic circulation of the human body. Many microscopy and especially vibrational spectroscopy techniques namely IR and Raman, have been implemented to address and monitor the factors which affect the solubility performance of these formulations. However, most of the conventional techniques have limited performance in resolving their physico-chemical properties at the nanometre length. For further investigation and potential optimisation of ASD, in combination with the rise of nanomedicine-based drug delivery systems, require the screening of pharmaceutical components at the sub-micrometer length. Therefore, the adoption and main-streaming of a more advanced chemo-analytical nanoscopy technique in pharmaceutical analysis is required.

To fill the gaps in knowledge, in this thesis the TERS technique has been applied on ASDs to evaluate its performance and suitability for pharmaceutical analysis. This was attempted by utilising a combined AFM-Raman system to examine the physico-chemical properties of the samples at a sub-micron scale level and further compare the information obtained with a TERS system, equipped with functionalised TERS probes. By examining two-component ASD formulations under TERS, it would make it possible to evaluate:

- the Raman spectra acquired under the TERS setup, with functionalised TERS probes. The spectra were compared when the probes were either retracted or approached (Chapter 3).
- the sensitivity of the components under different powers of laser irradiation. (Chapter 4).
- the correlation between probe-laser spot distance to the signal enhancement of the sample (Chapter 5).
- TERS maps of 2D printed ASD micron-sized dots of known dimensions

(Chapter 6).

Two APIs were employed, namely paracetamol and felodipine, a co-former nicotinamide (Vitamin B3) alongside with polymers copovidone and polyvinyl alcohol, where each component was studied either alone or in combination. For the evaluation of spatial resolution either under a Raman microscope or a TERS instrument single-wall carbon nanotubes and di-phenylalanine tubes were used, respectively, as similarly recorded in the literature [238, 239]. Regarding the APIs paracetamol belongs to class 1 of the BCS as highly aqueous soluble and intestine permeable, whereas felodipine belongs to class 2 with low solubility and high permeability. Both copovidone and polyvinyl alcohol are water-soluble polymers which improve the dissolution properties of paracetamol and felodipine. Two drug loadings were studied for paracetamol (50% w/w copovidone and 30% w/w polyvinyl alcohol) and one for felodipine (50% w/w copovidone). For the assessment of these samples, two TERS-based systems were used. Our combined AFM-Raman system was built (Chapter 2) and utilised (Chapters 2,4,6) for AFM and CRM measurements (Chapter 2). The second system was applied for TERS experiments (Chapters 3,5,6) where functionalised TERS probes were supplied for our measurement. To generate comparable data, our instrument was setup based on the protocol followed for the second instrument [195]).

Chapter 2

Instrumentation

2.1 Introduction

In order to study the physico-chemical characteristics of pharmaceutical solid dispersions and nano-particulates, a detailed description of the component assembly associated with the operation of a co-localised AFM-CRM system, tailored for TERS measurements, will follow in this chapter. In this thesis in order to compare the results, produced from the AFM-CRM and TERS systems with minimum scrutinies, we adhered closely to the design of the TERS system, which instructions has also been published as a reference instrument by Kumar et al. [195]. For this chapter we included information about the design and build of the AFM-CRM instrument, followed by software development for synchronous control of components, ending with laser-probe alignment and laser polarisation and size evaluation.

2.2 Instrument design

2.2.1 Combined AFM-CRM

For the acquisition of topographical images as well as Raman spectra, a custom-built AFM-CRM system was built in the School of Physics and Astronomy as part of this PhD. This microscope was designed based on the bottom illumination-collection configuration [195, 240]. The system is split into three main compartments, namely an AFM system (Nanowizard II, JPK) mounted on an inverted optical microscope (IX71, Olympus) and further expanded on a custom-built optical Raman system, presented in Figure 2.1. A schematic diagram is also provided in Figure 2.2. The whole system is built on an optical table offering robust support and reducing vibrations from ambient environment.

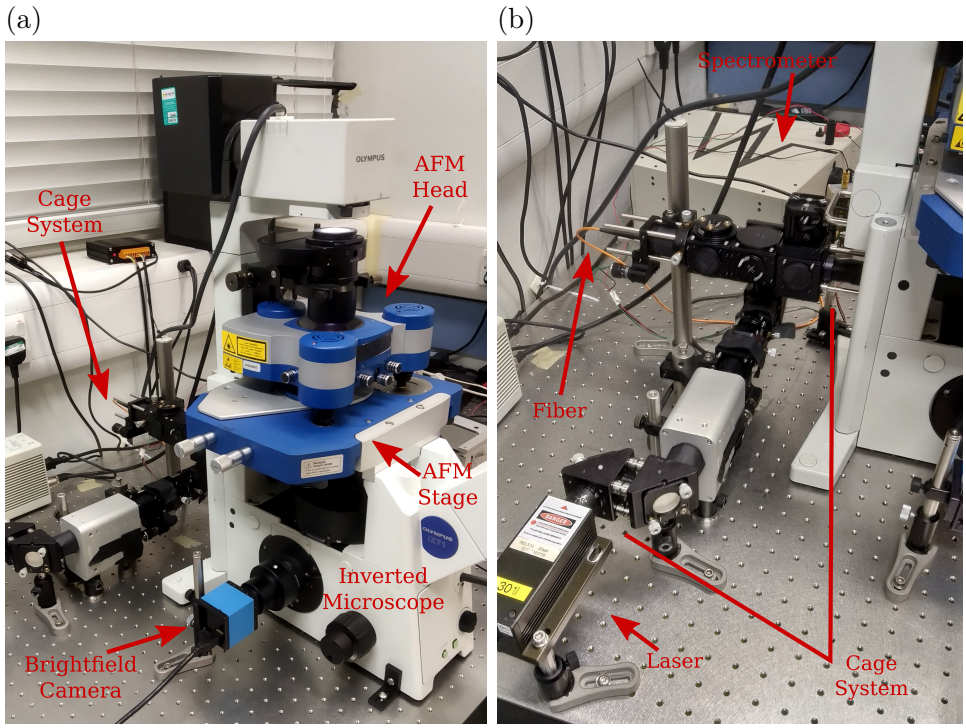

Figure 2.1: a) Side-view of the combined AFM-CRM, displaying the inverted microscope and the AFM system. b) Back-view of the microscope entailing the optical cage system, alongside with the spectrometer on the far side of the optical bench.

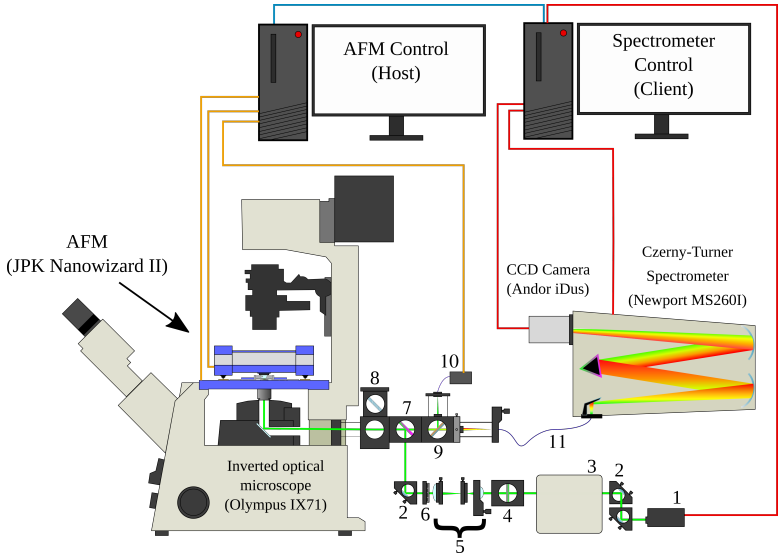

Figure 2.2: Schematic of bottom illumination-collection AFM-CRM. Legend: 1) Solid-state 532 nm Laser 20 mW, 2) kinematic mirror mount, 3) power attenuator, 4) laser line filter, 5) spatial filter, 6) rotatable radial polarisation converter, 7) dichroic mirror (532 nm reflection), 8) removable 50:50 beam splitter, 9) long pass edge filter (532 nm cancellation), 10) photodiode for backscattered light collection, 11) fibre optic linked to spectrometer.

2.2.2 Atomic Force Microscopy (AFM) setup

The AFM system is comprised of four main parts, specifically the AFM head, stage, sample holder and controller. On the AFM head a cantilever probe can be fitted, with the capacity of XYZ freedom of movement for the acquisition of physical-associated topographical images. The Tip-assisted optics™stage (JPK) setup on the optical microscope is also capable of full XYZ translation of the sample held in place (Figure 2.3). Both of these component have a translational limitation of 100 µm across the XY axis and the stage has Z-axis translational capacity of 10 µm. All samples examined, were deposited on round 24 mm coverslips (# 1.5), which were secured tightly on a coverslip-holder liquid cell (BioCell™, JPK). Last, the AFM controller is in command of the operation of all the different AFM components, which records the produced data within a Linux operating system. There all the AFM-related topographical experiments are designed and performed from the pre-installed JPK software.

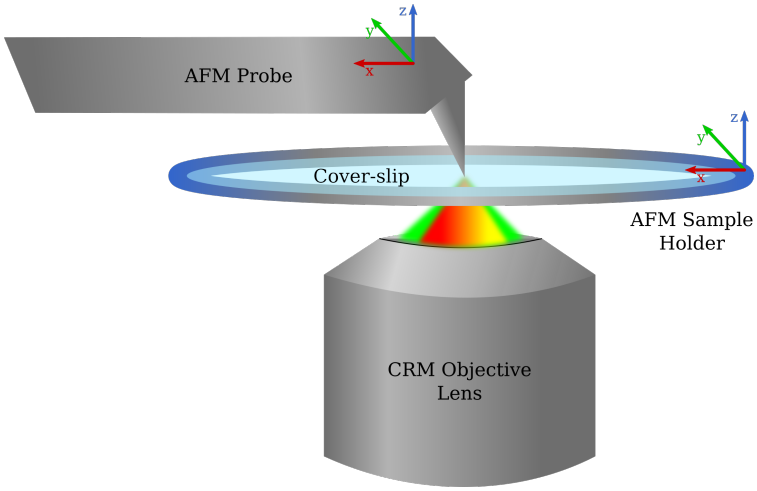

Figure 2.3: Schematic diagram of the AFM-CRM setup, in bottom-illumination mode. While the objective lens remains in static position, both the AFM probe and the sample holder stage are capable of translating across the XYZ axes.

2.2.3 Confocal Raman microscopy (CRM) setup

The Confocal Raman Microscopy (CRM) setup is designed according to the illustrated diagram Figure 2.2. Raman signal is generated with the application of a frequency doubled Neodymium-doped Yttrium Aluminium Garnet (Nd:YAG) Continuous-Wave (CW) laser (Laser2000), emitting green monochromatic laser light at 532 nm wavelength, at a power of 20 mW (Class 3B). The power level of the laser can be controlled, by directing the laser through a motorised laser attenuator (PowerXP Maxi Reflection Type, Altechna, Vilnius, Lithuania). From the attenuated laser any unwanted emission lines of different wavelength become filtered by a line filter (532 nm MaxLine©, LL01-532-12.5, Semrock). For the removal of any optical aberrations and faults with the laser, a spatial filter is set in place. It entails a light condensing aspheric lens with effective focal length of 25 mm (AL1225M-A, Thorlabs), centred at a pinhole of 5 µm in diameter (P5K, Thorlabs). Upon exit from the pinhole, the filtered laser is collimated with a second aspheric lens of 50 mm focal distance (AL2550M-A, Thorlabs). To further alter the polarisation of the laser beam from a linear to a radial orientation, the collimated laser passes through a radial polarisation converter

(RPC-0532-06, S-waveplate, Altechna, Vilnius, Lithuania). After the change in polarisation a series of mirrors mounted on optical cage-system (Thorlabs), with the dichroic mirror (RazorEdge Dichroic™, LPD02-532RU-25, Semrock) are directing the monochromatic light to the back of the microscope into a high magnification 100×, oil-immersion objective with 1.45 NA (CFI Plan Apochromat λ, Nikon, Japan). Here the collimated light becomes tightly focused on the sample surface, in order to generate the inelastic scattered light. The generated backscattered light, both 532 nm and Raman light, is collected back through the same objective into the cage-system. The dichroic mirror in place reflects an excessive amount of monochromatic 532 nm laser light and allows the transmission of the inelastic scattered light. After this point, the long-pass edge filter (532 nm RazorEdge©, LP01-532RU-25, Semrock) serves two purposes. The first being the complete filtration of the remaining 532 nm laser, allowing the desired Raman scattered light to be transmitted further towards the spectrometer. The second is the reflection of the weak scattered Rayleigh light towards a photodiode. The latter approach assists in the process of probe-laser aligment, which explanation will follow in an upcoming subsection of this chapter. The clean inelastic Raman light becomes focused towards an optic fibre of 7 µm sized diameter, and further directed into a Czerny-Turner spectrometer (Newport MS260i), where the different wavelengths of light are projected onto a Charged-Coupled device (Andor CCD iDUS 401) to record the Raman Spectra.

2.3 Software development

By closer inspection of Figure 2.2 the AFM and Raman systems are operated under separate computer units. This is due to the different manufacturer specification to software operation. In particular, the AFM JPK software works

under the GNU/Linux operating system (Linux Mint 14), whereas the CCD, spectrometer and laser can operate under the Windows 10 desktop environment. In order to communicate and synchronise those system for the needs of our experiments in a quick and easy manner, especially performing Raman map raster scan, it was vital to develop a software from the Windows desktop that would meet those requirements.

2.3.1 Software design

The development of this software has been based on Model-View-Controller (MVC) architecture [241], using Python as the programming language of choice [242], alongside Qt widget toolkit for the development of software's graphical user interface [243–245].

According to the MVC architecture, the software is composed of three separate files, each serving the roles of Model, View and Controller. A graphical abstract of the MVC is presented in Figure 2.4. Briefly the Model file, contains functions which sends commands to the CCD, AFM and Laser interlock, performing AFM stage and probe movement, switching the laser interlock on and off as well as acquiring the spectra from the CCD camera. The View file, consists of all the graphical designs and parameters, such as window size, buttons and other widgets, which are frequently updated and displayed for the end-user. Last, the Controller file is responsible for receiving the instructions given by the user and coordinate the operations of both Model and View files by sending the appropriate commands. By having the application functionalities separated between the different MVC files, this allows easy tracking of errors as well as better transition to new programming language packages and operating systems.

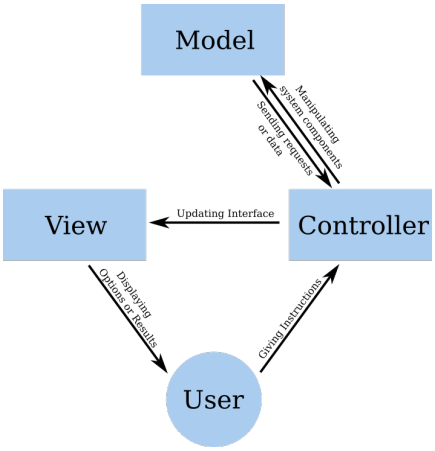

Figure 2.4: Model-View-Controller (MVC) architectural pattern in software design.

Regarding the development of the application, Python is an Open-Source, general-purpose programming language [242, 246]. The selection has been based on ease of code readability, cross-platform support, and a large variety of general and scientific packages, which provide the necessary tools for component operation, inter-system communication and data handling. Specifically, both the AFM and the CRM instruments are communicating via the TCP/IP protocol, through an Ethernet cable (Figure 2.2, blue line). Through a series of commands sent from the Windows to the Linux computer the translation of the AFM sample holder and probe across the XY axes is possible. For the control of the CCD camera, a third party package pyLabLib [247] has been imported into the software's code for acquiring Raman spectra, setting up the temperature alongside other acquisition parameters. In terms of spectra visualisation and projection of Raman images, during and after a raster scan, the package PyQtGraph [248] provides an extensive interface for quick data interpretation, which will be briefly explained in the following subsection in this chapter. Last, an arduino microcontroller (Nano v3.0, Elegoo, Shenzhen, China) connected to the Windows computer, operates as a digital power switch to the interlock controller of the laser, which is ultimately controlled by the software. All files and components necessary for the operation of this software are included in the

supplementary material for information and reference.

2.3.2 Software functionality

In Figure 2.5, a screenshot of the software's User Interface (UI) is displayed alongside with an operation schematic. From the user's point of view it is possible to:

(a)

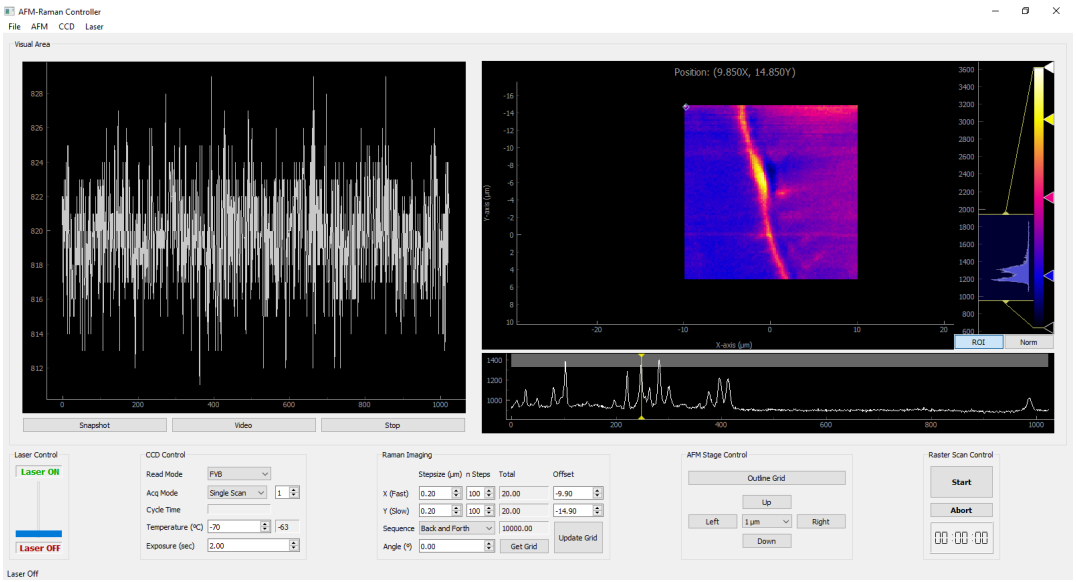

(b)

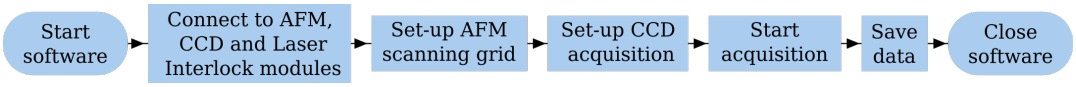

Figure 2.5: a) Screenshot of the software's User Interface and b) schematic of the software's operation

- Connect and disconnect the AFM, CCD and Laser interlock components.
- If the AFM module is connected, the grid parameters can be altered for performing Raman raster-scans, such as position, grid's point-to-point step-size, number of steps per axis, as well as the angle of the grid. In addition, the manual translation of the sample stage is also feasible, especially when observed under the optical microscope.

- When the CCD camera is connected, the temperature and exposure time can be set. The CCD temperature is also monitored, throughout the acquisition setup process. Furthermore, to ensure Raman signal can be obtained from the sample while focusing with the laser, single or continuous spectral snapshots can be recorded and displayed at the UI.

- Connecting to the laser interlock controller provides the option to switch the laser on and off, whenever this is required.

- After all experimental parameters have been set-up, the user can initiate the raster-scan as well as abort at any point of time during the measurement. A countdown clock measures the approximated finish time of the experiment. During a raster-scan experiment, all the spectra collected are plotted as a 2D image. The image viewer provides the options of selecting the desired Raman band to be plotted on the 2D plot, set the range of the minimum and maximum plots, as well as project the coordinates of a sample's location of interest, simply by dragging the mouse over that area.

- With the successful completion of a raster-scan, the acquired data in stored in an *ASCII* text file, for further analysis.

2.4 Laser polarisation and laser-probe alignment

For the operation of the AFM-CRM system it is vital to assess the dimensions and polarisation of the laser spot, in accordance to the followed protocol [195]. Also, to ensure that both the AFM probe and the CRM focal spot are at the same position, obtaining *in situ* information from the sample, we demonstrate different methods which aid and confirm their alignment [195, 249].

2.4.1 Determining the radial polarisation of the laser spot

As mentioned at the introduction of this thesis, the polarisation of the incident light is important for improving the signal enhancement generated by the metallic probe. Depending on the optical geometry of the TERS setup, different laser polarisations are set. For a bottom illumination microscope, the conversion of a linear polarised CW laser to a radial can be achieved with the use of a radial polarisation converter. The optical component used in this study has the property of converting the direction of the incident monochromatic light to either a radial or azimuthal state [250, 251]. Figure A.1 in Appendix A demonstrates this effect, according to the optics manufacturer specifications [252]. Following this procedure, similar effects can be observed in Figure 2.6, from our acquired brightfield images. In particular, after focusing on the surface of a glass cover slip without the polarisation converter in place, the focal spot (Figure 2.6(a)) presents an oval-like shape at the region where the incident laser is confined the most. After introducing the radial converter (Figure 2.6 (b)), the laser spot obtains a doughnut-like shape, indicating that all the vectors of the laser's electric fields are surrounding the centre of the beam centre axis. To further ensure whether the laser spot is radially or azimuthally polarised, we introduced a linear polariser between the radial polarisation converter and the objective lens, as per manufacturer instructions. When the laser is transmitted through a linear polariser, this polariser blocks the electric field vectors which are perpendicular to the wire-grid structure of the optic, while allowing only the parallel ones. By setting the radial polarised at a proper angle, between 0 ° (Figure 2.6 (c)) and 90° (Figure 2.6 (d)), we can observe a dumbbell shape, that is generated after the linear polarised filter. These outcome concludes the laser beam presenting a radial polarisation suitable for TERS experiments.

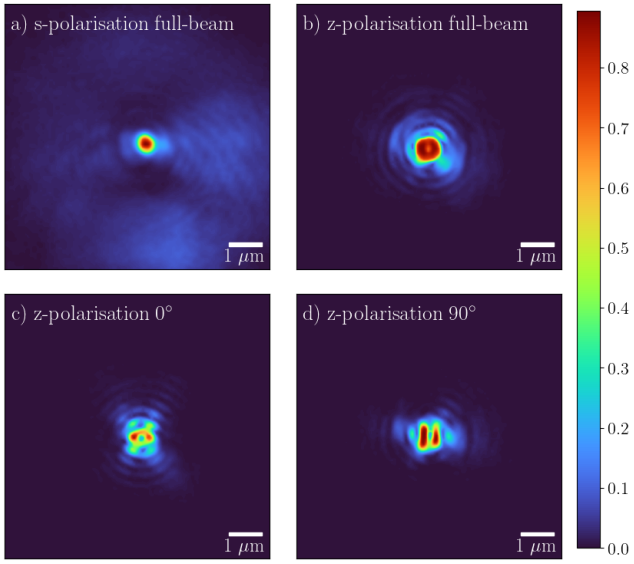

Figure 2.6: Brightfield images (pseudo-coloured) of the laser spot with different polarisations. a) Linear (s-)polarisation of the full beam of the laser spot. b) Radial (z-)polarisation of the full beam of the laser spot. c) Dumbell shape of the radially polarised beam (b) with the linear polariser being positioned at a horizontal 0 ° orientation, cutting the electric field vectors from left and right sides of the beam. d) Dumbell shape of the radially polarised beam (b) with the linear polariser being positioned at a vertical 90 ° orientation, cutting the top and bottom sides of the radial beam. Colour-bar indicates the normalised intensity of light based on the different colours used in the pseudo-coloured images, blue being the lowest up to dark red being the highest intensity obtained.

2.4.2 Laser-probe co-alignment

In order to perform TERS measurements or acquire similar topolographical images from the AFM and CRM instruments, both the apex of the probe and the laser spot must be co-localised on the same XY position, in reference to the sample's coordinates. Under the currently presented bottom-illumination microscope, the objective lens alongside with the laser focal point remain always static. By making use of the free XYZ translation movement of the probe via the AFM head, it is possible align the AFM tip with the focal spot, through three approaches.

2.4.2.1 Apex detection via brightfield video recoding

The first step of probe-laser alignment requires that the apex of the probe is at close proximity with the laser spot. A coarse alignment can be achieved with the use of the brightfield camera and by translating the probe cantilever within the camera field of view, while the laser being powered off. In Figure 2.7 we can observe the cantilever of the probe from the objective's lens point of view. Here the objective is focusing on the uppermost surface of the coverslip, with the probe being Figure 2.7 a) retracted by 1µm above the surface and Figure 2.7 b) approached on the surface. The apex location can be identified from the small dark round spot generated when the probe is in contact with the surface. At this point, as the position of the laser spot is marked and the location of the apex known, we can accurately align the probe by performing a probe raster-scan around the laser spot. The probe detection method performed either by the AFM or the CRM systems can unravel the exact coordinates of the apex's location.

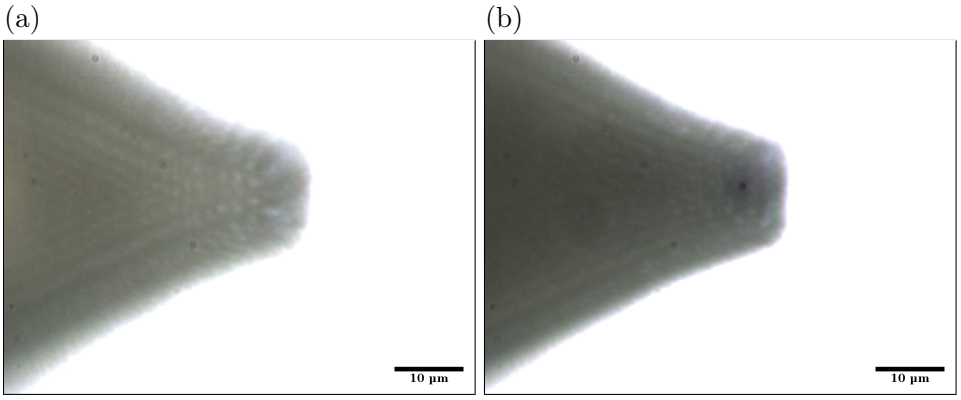

Figure 2.7: a) Tip retracted 1μm above glass coverslip surface, b) tip approached on glass coverslip surface.

2.4.2.2 Co-alignment via scattered laser light

This approach requires the laser focusing on the apex of the AFM probe, close to the cover-slip surface, while performing an XY-axial raster scan of the can-

tilever. All the reflected 532 nm light from the surface of the silicon cantilever [253, 254] can be obtained through the objective, transferred into the cage-system and focused on the photo-diode, where the light intensity is recorded in the form of electric current (mV). Through this measurement, an intensity based topographical image is recorded. (Figure 2.8). From this Figure, the reflected light forms the pyramidal shape of the cantilever, as similarly seen in the brightfield image (Figure 2.7), with the distinguishable dark spot, resembling the apex. Identifying the apex's position, from the graphical user interface provided by the AFM system the probe can be locked in position above the laser focal point.

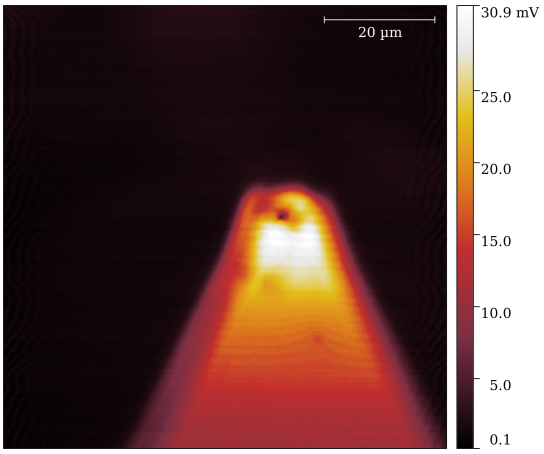

Figure 2.8: Laser back-scattered AFM raster-scan image of silicon probe in 80x80 µm area.

2.4.2.3 Co-alignment via silicon probe Raman raster-scan

Last method of detecting and fine-aligning of the probe with the focal laser spot is to perform a similar XY raster scan as aforementioned, with the only difference of acquiring Raman spectra of the silicon apex. Silicon has a single Raman band signal at 520.7 cm^{-1} [255]. Therefore, by selecting this band it is possible to identify the pixel spot with the highest intensity count at that wavelength (Figure 2.9), note the desired XY-position and fixate the probe to that location.

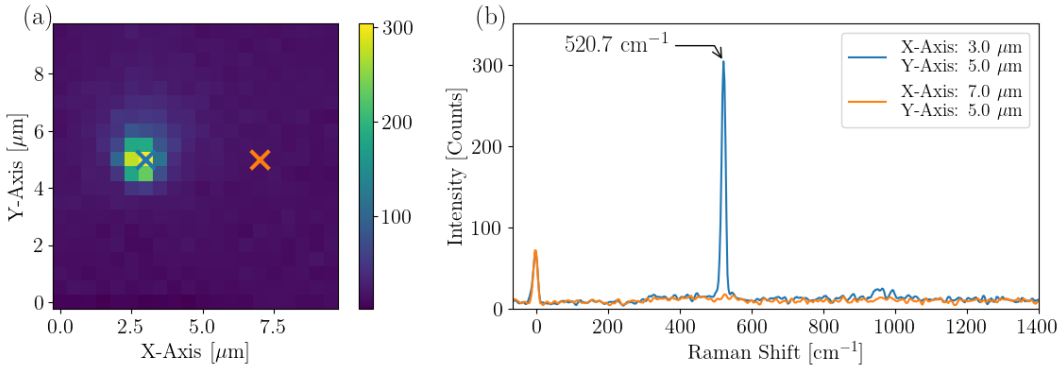

Figure 2.9: a) Raman image intensity at the 520.7 cm^1 wavelength, displaying the apex's position of the silicon probe when focused with the laser spot. b) Blue and orange spectra correspond to the annotated positions of image a) on and away from the apex location, respectively. This raster-scan has been performed under 500 µW with 1 second spectral acquisition.

2.4.3 Calculation of laser spatial resolution

After ensuring laser probe alignment, it is vital to assess the spatial resolution of the focal spot for Raman experiments. As the theoretical diffraction limit of light (Equation 1.1) rounds to 200 nm for the current setup, the actual value should range between 200-300 nm to ensure the highest achievable spatial resolution with confocal Raman and compatibility with TERS measurements [195]. To evaluate this, a sample with dimensions below the stated diffraction limit and a strong Raman scatterer is desired. For this Single-Wall Carbon Nano-Tubes (SWCNT) have been chosen, which meet both of these requirements and priorly used in the literature as a reference material [195, 239]. For the preparation of the sample similar protocol are followed with Kumar et al [195]. Briefly, salinated coverslips have been prepared and 1% w/v of probe-sonicated aqueous SWCNT solution were drop casted on the coverslip, left to dry overnight and examined

2.4.3.1 Results and Discussion

2.4.3.1.1 AFM measurements Figure 2.10 a) displays the height topography of the SWCNT sample over a 20×20 µm^2 region. The height of the presented features span up to approximately 80 nm. As SWCNT are highly hydrophobic and tend to aggregate easily [256], it is vital to scan areas which have isolated or fewer tubes for the spatial resolution assessment. Further to this map, a zoomed region has been selected, annotated with the green layout. This area corresponds to Figure 2.10b) with a 2×2 µm^2 size. Here, by applying a cross-section of the tube's profile vertically, it is possible to assess the width and height dimension of these tubes. To measure this a 1st order polynomial background line alongside with a Lorentzian curve were fitted. The data indicates that the dimension of this tube, has an approximate height of 4 nm with a width of 182 nm. This difference could be due to the degree of sharpness of the probe being able to resolve the fine details or the small amount of the collected data points that determine the height of the sample. Nonetheless, these findings indicate that the sample of interest has dimension below the diffraction limit of light, allowing the examination of the focal laser spot diameter with the CRM.

2.4.3.1.2 CRM measurements A Raman raster-scan of the same region as shown in Figure 2.10 b) was performed. From the hyperspectral data acquired, the intensity of the 1591 cm^{-1} band was selected, based on the literature [195] and plotted in Figure 2.11. Figure 2.11 a) indicates the presence of the Raman band originating from the tube, by selecting two positions on the feature (blue cross-mark) and away from it (orange cross-mark), with their corresponding spectra of the same colour shown in the below graph. After confirming the presence of a narrow SWCNT, the next step involved the measurement of the laser spot diameter. In Figure 2.11 b) a cross-section (red dashed line) of the

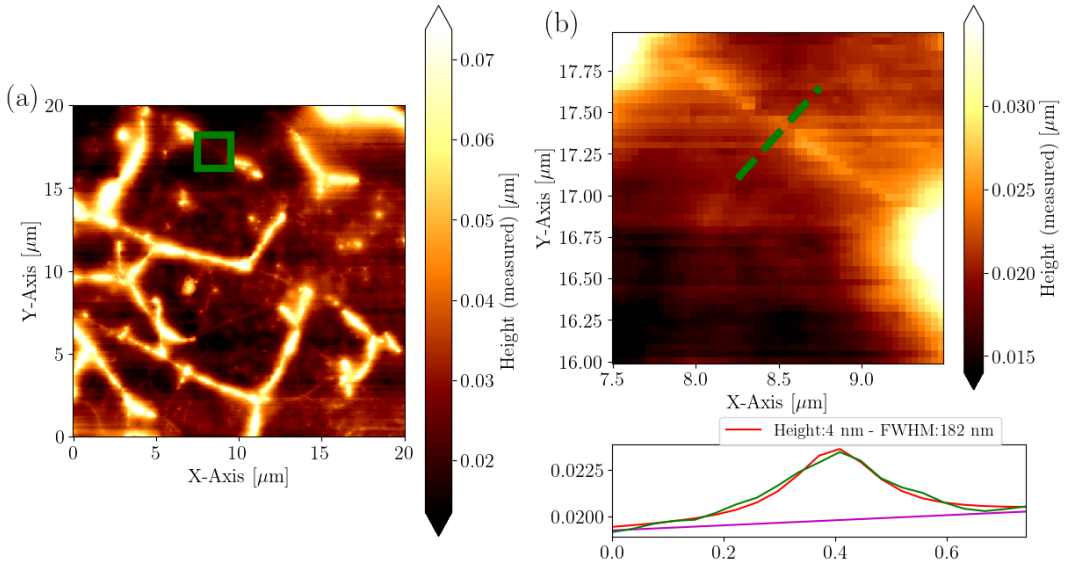

Figure 2.10: AFM topography scan of SWCNT based on their height. The scans were acquired with the probe being in contact mode. a) 20x20 µm^2 raster scan, with the highest point reaching almost 80 nm. The green rectangle contains the region of interest, further displayed in subfigure (b). b) 2x2 µm^2 raster scan displaying a narrow SWCNT, with the green line corresponding to the height profile of the sample, displayed on the graph below, alongside with a fitted 1st polynomial line representing the background (purple) and a Lorentzian curve (green), for the measurement of the tubes dimensions, such as height and width.

tube's was made perpendicularly to obtain the Raman band intensity profile. From this by fitting a Gaussian line (grey profile), it is possible to measure the Full Width Half Maximum (FWHM) of that profile, ultimately gaining the laser beam waist length. The resulting FWHM is 229 nm which is in accordance to the protocol followed, and indicates the spatial resolution of the CRM system.

2.5 Summary

To study the physico-chemical characteristics of pharmaceutical solid dispersions and nano-particulates, the development and assessment of a combined AFM-CRM system was required, which should fit the criteria of a TERS instrument based on the literature [195]. Here, the schematics of all the different components of the system were presented, namely AFM and CRM. In addition,

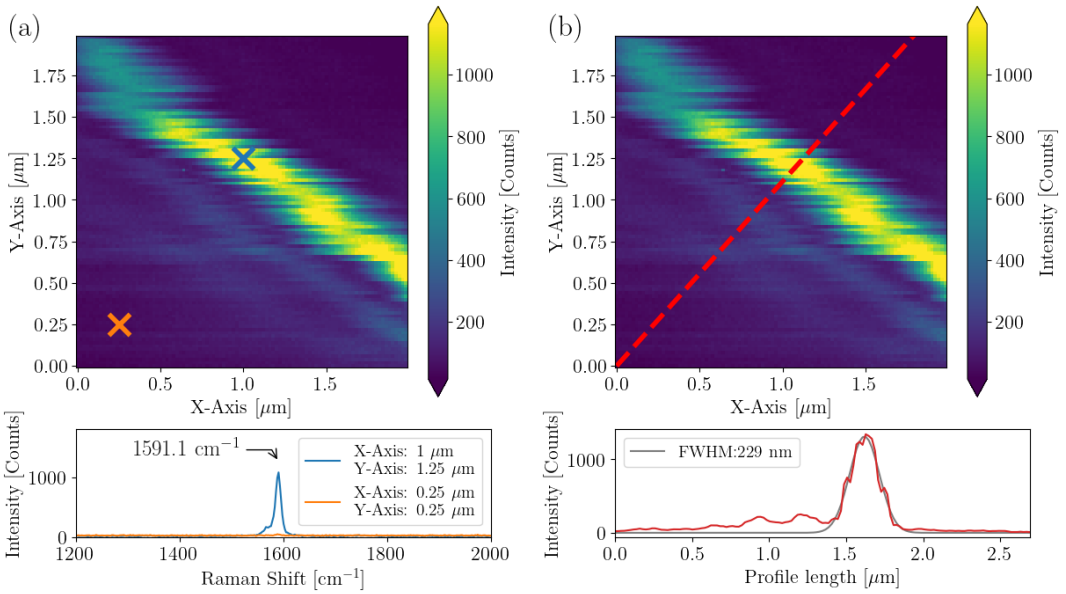

Figure 2.11: Raman raster scan of the same region (2x2 µm^2), displayed in Figure 2.10 b). The laser was set at 300 µW with the camera acquiring spectra for 1 second acquisition time. The scanning grid rises to 100x100 pixels with 20 nm step-size from pixel to pixel. a) displays a 2D image of the obtained scan based on the signal intensity originating from the SWCNT Raman band at 1591 cm^{-1}. Two annotated cross-marks with the respective colours of the spectra presented, between 1200 cm^{-1} and 2000 cm^{-1} at the bottom of the image are displayed. b) shows the same image, with the exception of a red dashed line cross-sectioning the drawn tube perpendicularly, indicating the intensity profile taken from that region and displayed at the bottom graph in red line. The grey line represent the Gaussian fit of the tube, measuring the Full-Width Half-Maximum amounting to 229 nm.

the design and operation of a custom-made software has also been shown, capable of synchronising the various parts of this system and being user-friendly in experimental parametrisation and quick data visualisation. Additional requirements of the instrument setup is the validation of laser polarisation, dimension as well as validating methods of co-aligning the probe with the laser spot. In this chapter, the focal spot under linear and radial polarisation has been displayed, including the generated dumbbell shapes after introducing a linear polariser to confirm the actual vector orientation of the incident electromagnetic field. Regarding probe-laser alignment, one coarse and two fine approaches have been demonstrated for validation. The first can be performed, by observing the brightfield camera, after the contact of the probe with the surface of a glass cover-slip. From the latter two, the raster-scan the probe over a close vicinity with the focused laser spot is required, where the only difference lies in the recording of the signal. This signal can be either from Rayleigh back-scattered light, which is detected by the photodiode of the AFM instrument or Raman back-scattered light, detecting the Silicon band of the apex at 520.7 cm^{-1}. After aligning the probe with the laser, it was then feasible to perform raster-scan of SWCNT both with AFM and CRM. This task was performed in order to measure the spatial resolution of the CRM by confirming the physical dimensions of a narrow tube with AFM and measuring the FWHM of the SWCNT profile, based on its Raman band intensity. Overall, this chapter concludes the feasibility of this instrument to generate AFM and Raman data comparable to a TERS instrument or even operate as one, being almost identical to the ones stated by the protocol [195].

Chapter 3

TERS spatial resolution and signal enhancement evaluation on L,L-Diphenylalanine tubes and ASDs

3.1 Introduction

As discussed in Chapter 1, despite the recent applications of TERS on carbon-based and biological samples, there is to-date no record of its application on pharmaceutical formulations. Obtaining chemical information at the nano-scale resolution could deem valuable in improving drug stability and therapeutic performance. In this chapter, to make these studies more relevant to pharmaceutical assessment, it is vital to take under careful consideration certain complexities of this technique. For example, these could be sample and/or tip stability to degradation, lateral resolution as well as tip-sample interaction [196, 257]. In order to allow better data interpretation and instrument evalua-

tion, sample selection has been made on single and two-component materials, of biopharmaceutical interest.

For single component analysis L,L-DiPhenylalanine (Phe-Phe) nanotubes were used. These core recognition motif of Alzheimer's β-amyloid peptide structures have proven very versatile self-assembling building blocks. Their application span from electronics [258] and sensors [259] to biomedical materials and drug-delivery systems [260–262]. In addition, Phe-Phe nanofibres are small, easy to prepare [263] and well documented in previous Raman studies [238, 264]. Given their nano-scale tubular shape, small toxicity compared to SWCNT [265] and prior characterisation from the literature, it is possible to examine the signal enhancement and spatial resolution with the TERS system provided.

For a two-component system, paracetamol or felodipine in copovidone VA64 at a 50 %w/w drug loading were investigated in the form of spin-coated films of ASDs. These API in polymer blends were formulated to aid in the solubilisation and/or dissolution rates and further improve bioavailability in the body administered. However, due to their high drug loading, these systems can be prone to phase separations, leading to formation of a drug-rich and a polymer-rich phases and further compromise any solubility and dissolution rate enhancements in the formulation [266]. To understand the change in this behaviour for API-polymer blends, it is important to investigate the intermolecular interactions, conformations as well as miscibility of these components.

The aim of this work was to examine Raman spectra of the aforementioned samples with a Ag-coated TERS probe and evaluate their signal enhancement. Assessment of the achievable nano-scale spatial resolution was specifically obtained from Phe-Phe tubes.

3.2 Material and Methods

For Phe-Phe nanofibres, similar preparation protocol was followed elsewhere [267]. Briefly a co-solvent of 70 %v/v Acetonitrile in H_2O was brought at 95 °C hotplate and Di-phenylalanine was further dissolved, constituting a total of 2 mg/ml concentration. The solution was left for 4 minutes at high heat until a transparent solution was yielded and left to cool overnight. After cooling down, the solution was used by drop-casting 50 µl droplets on microscope cover-glass # 1.5 (Scientific Laboratory Supplies, Nottingham, United Kingdom). Regarding the preparation of amorphous solid drug dispersions a similar spin-coating method was followed by Mugheirbi et al [268], where powder blends of paracetamol in copovidone (Kollidon^{TM} VA64 Fine) (50 %w/w) and felodipine in copovidone (Kollidon^{TM} VA64 Fine) (50 %w/w) (AstraZeneca, Macclesfield, United Kingdom) were dissolved in Ethanol. Afterwards, from each solution, a 50 µl droplet was applied on a microscope cover glass # 1.5 and spin-coated. The samples were spun at the first stage of the spin coating process at 500 rpm for 3 seconds and further 2000 rpm for 30 seconds at the second stage (Ossila Ltd., Sheffield, United Kingdom).

3.2.1 Instrumentation & Measurements

The bottom illumination TERS setup (National Physical Laboratory) was used in this set of experiments. The instrument consists of an AFM (AIST-NT Inc., Novato, USA) coupled with a CRM attached with an oil-immersion objective (100×, NA=1.49) [195]. The exciting laser wavelength was 532 nm (frequency doubled Nd:YAG) and the power output irradiating the sample ranged between 78-548 µW. Spectra were acquired between 400 cm^{-1} and 3600 cm^{-1}, unless otherwise stated. For this instrument, the theoretical diffraction limit of light

according to Abbe's equation of lateral resolution (Equation 1.1), approximates at 200 nm. AFM silicon probes were oxidized in a tube furnace at 1000 °C for 45 minutes, allowing afterwards to cool down at room temperature. To remove organic contaminants from the oxidised surface of the probe, UV-O_3 cleaning was performed for 60 minutes followed by an additional cool down (60 minutes) before being transferred to metal deposition thermal evaporator inside of a glovebox. A 100 nm-thick layer of silver was deposited on the surface of the apexes and left overnight before TERS experimentation [195]. For the individual probes of this study, the apex diameters were not measured. Two types of Raman spectra have been recorded in this study. The first ones involve spectra being obtained with the AFM probe retracted at ≥ 1 µm distance from the sample surface and the second with the probe approached on the surface in contact-mode at a 33 nN setpoint.

In addition to measure the performance of the Ag-coated (TERS-active) silicon probe, the Enhancement Contrast (EC) was also calculated. *EC* provides an indication of the probe's likely performance to enhance the sample Raman signal during a TERS experiment. It contrasts the intensity of a Raman band when the probe is engaged on the sample surface, inside the irradiating laser spot, and retracted away from the surface [223, 269]. By selecting the strongest Raman band for each material, the following formula in Equation 3.1 was applied:

$$EC = \frac{I_{\text{Engaged}}}{I_{\text{Retracted}}} - 1 \tag{3.1}$$

where, $I_{Engaged}$ corresponds to the intensity of Raman band at the engaged probe position at the laser spot, whereas $I_{Retracted}$ corresponds to the intensity of Raman band at retracted probe position. A contrast value ≥ 1 indicates sufficient sensitivity for TERS-based signal enhancement [195].

3.3 Results and Discussion

3.3.1 Phe-Phe measurements

3.3.1.1 AFM topography of Phe-Phe nanofibre

In order to evaluate the chemical spatial resolution at and below the diffraction limit of light, it was vital first to obtain the physical dimensions of the sample in question. Under the optical microscope, the thinnest fibre was selected and scanned under the AFM for height topography. A height map is displayed in Figure 3.1 a), where the tube approximates at 150 nm in height and 300 nm in FWHM. It is also visible from Figure 3.1 b) that the tube is not completely cylindrical, rather has steep edge from the right-hand side and a gradually declining flat surface on the left. According to the aforementioned preparation protocol [267], the width of the formed nanofibres should range between 50 and 300 nm. In addition, the formation of flat surfaces and asymmetric dimensions can be explained through the hexagonal structure created by the Phe-Phe molecules, as previously reported in AFM [264] and X-Ray diffraction studies [270, 271].

3.3.1.2 Raman Spectra of Phe-Phe tube – TERS-active probe retracted

Raman spectrum of the sample was recorded while the TERS-active probe was retracted. The spectrum is shown in Figure 3.2 a). Bands from both the Phe-Phe tube and the substrate are visible and comply with previously published studies (Appendix B - B.1) [264, 272] . The Raman bands at 997 cm^{-1}, 1026 cm^{-1} and 1600 cm^{-1} are assigned to the phenyl ring vibrations of Phe-Phe, whereas the two broad bands at 490.8 cm^{-1} and 927.3 cm^{-1} ranging between

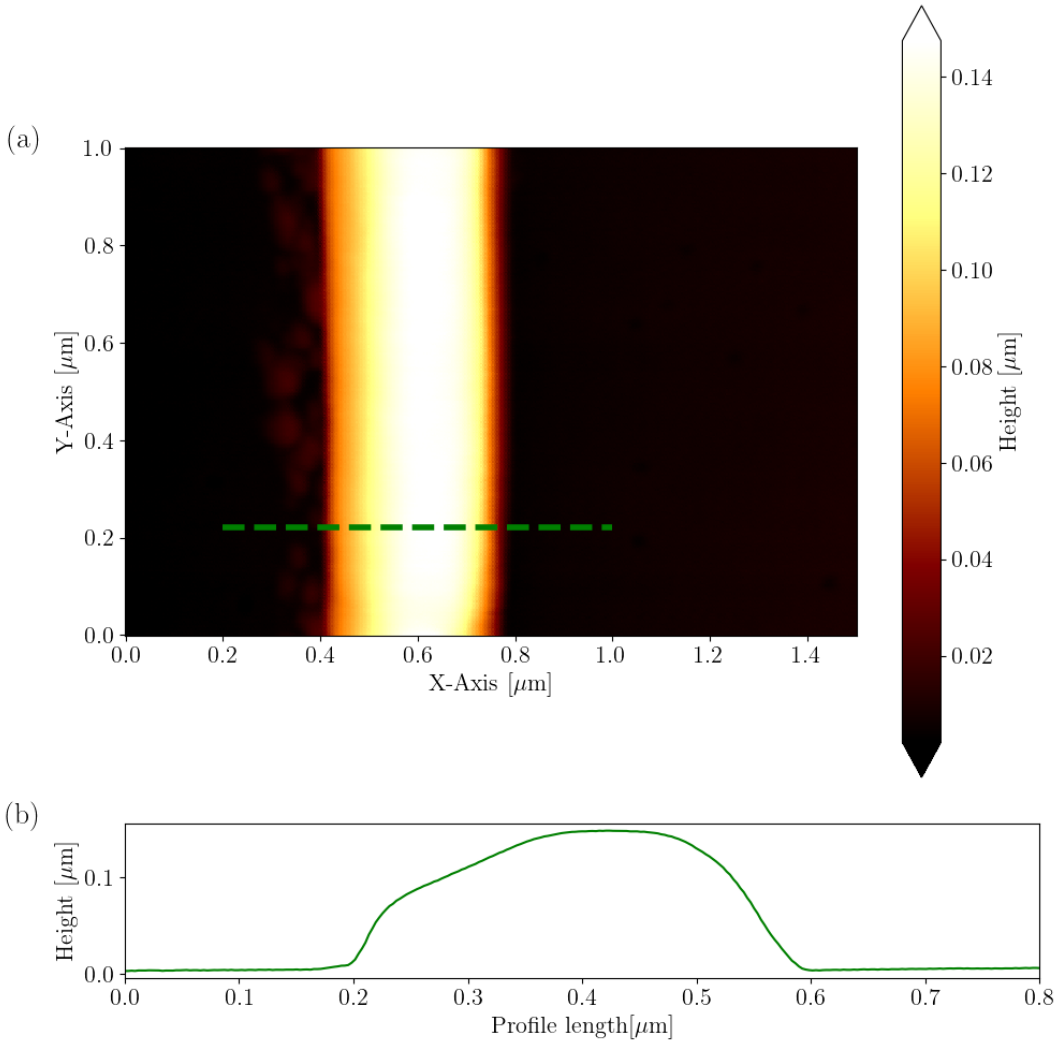

Figure 3.1: a) AFM height map of Phe-Phe tube, obtained under contact-mode. b) Height profile of Phe-Phe tube, from green line cross-section of Figure (a).

400 cm^{-1} to 1200 cm^{-1} of the lower Raman shift, originate from the cover-glass, which constitutes of borosilicate material. In the same figure, additional bands at longer wavelengths associated with −CH stretching are also present at 2931 cm^{-1} and 3046 cm^{-1}.

3.3.1.3 Raman Spectra of Phe-Phe tube – TERS-active probe approached

After approaching the TERS-active probe on the surface of Phe-Phe, the Raman spectrum acquired is presented in Figure 3.2 b). Some bands from the

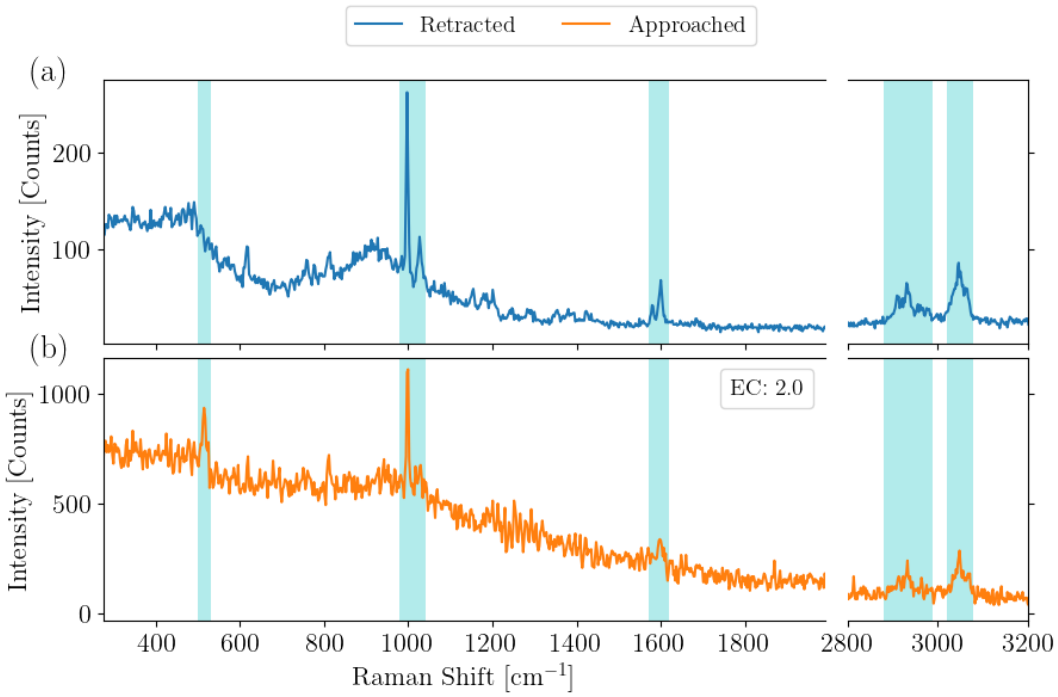

Figure 3.2: a) Tip-retracted spectrum of the Phe-Phe tube imaged in Figure 3.1. Acquisition parameters: 60s exposure time, 117 µW of laser power, cropped at fingerprint region and CH stretching region. b) Raman Spectra of Phe-Phe tube when probe is approached. Acquisition parameters, with 60 s exposure time at 117 µW of laser power, cropped at fingerprint region and CH stretching region. The enhancement contrast for the 997 cm^{-1} for both tip-retracted and approached Raman spectra is 2.

tube remained visible, specifically at the 997 cm^{-1} and 2931 cm^{-1} and 3046 cm^{-1} at the CH stretch region, while the bands at 1026 cm^{-1} and 1600 cm^{-1} were not present. The silicon peak from the probe also appeared at 514.5 cm^{-1} , instead at 520.7 cm^{-1}. This change was likely caused from the strain of probe's silicon substrate during contact with the sample [273]. It further indicated that both the laser focal point and probe were co-aligned at the same XY coordinates of the sample stage [249, 274] and in contact with the sample. The broad background noise, with gradual decline towards longer wavenumbers region occurred, likely due to the photoluminescence produced by the metallic Ag coat of the probe[275, 276]. Specifically, photoluminescence is the result of spontaneous light emission from an electronically excited material occurring after absorption of shorter-wavelength radiation (higher-energy photons) [277].

In addition, the enhancement contrast measured at 997 cm^{-1} from both tip-retracted and approached Raman spectra was 2, indicating TERS-associated signal enhancement. This is due to the near-field confinement of strong electromagnetic field generated from the laser and further causing enhanced Raman scattering under the probe apex [278, 279]. The fact that no silver sulphite (Ag_2SO_3) and silver sulfate (Ag_2SO_4) bands around 960-970 cm^{-1} [280], or carbonaceous species at 1350 cm^{-1} (D band) and 1580 cm^{-1} [168, 281] were present, we concluded that no detectable probe degradation or inactivation by these components took place.

3.3.1.4 Phe-Phe tube sensitivity to laser irradiation– TERS-active probe retracted

As the TERS probe at the near-field can increase the electromagnetic field under its apex, it was important to imitate this condition. Therefore, the endurance of the sample under high power of laser irradiation was assessed. The Phe-Phe tube was exposed under the highest laser power available (548 µW) over 10 minutes, with the probe retracted to avoid any contamination on the apex. In Figure 3.3 a), two Raman spectra are shown before (blue line) and after (red line) 10 minutes of continuous illumination. After 10 minutes of irradiation no discernible bands could be detected from the tube, with a rise in spectral noise. A brightfield image after 10 minutes of laser exposure was also recorded and presented in Figure 3.3 b). At the focal spot, where the two Raman spectra were obtained we observed a dark spot, suggesting photo-degradation of the sample at this particular location. No further test, with different laser powers were performed to identify the sample's burning threshold. These findings led to reduction of the laser power to one-fifth (117 µW) of the initial setting in order to prevent gradual sample degradation, while providing reasonable Raman spectra in both far- and near-field conditions. For comparison between

the Raman spectra after 10 min laser exposure under retracted probe and 1 min exposure with probe approached, Figure B.2 is provided, under Appendix C.

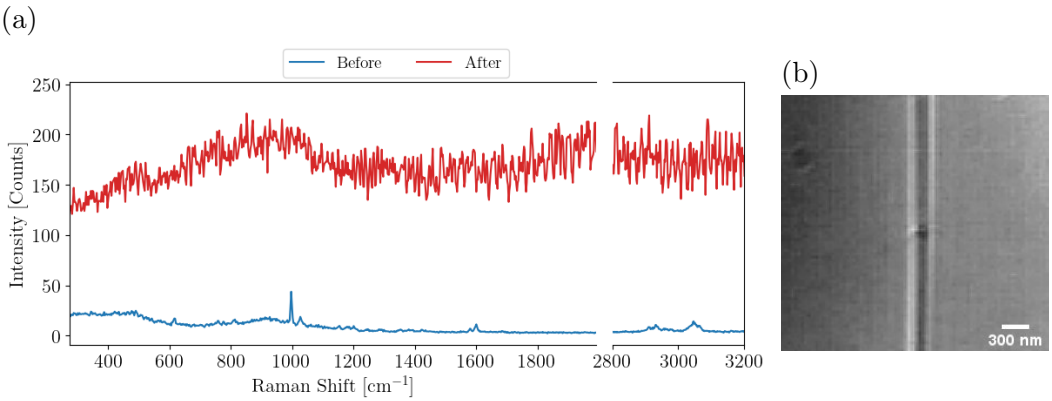

Figure 3.3: a) far-field spectrum of Phe-Phe sample before (blue line) and after 10 min (red-line) of irradiation, with 10 s exposure time at 548 µW of laser power. b) brightfield image of the interrogated Phe-Phe sample after 10 min of irradiation.

3.3.1.5 Line Intensity profiling of Phe-Phe tubes - TERS probe retracted & approached

After establishing optimal laser power (117 µW), Raman line scan measurement was performed on the same area selected from the AFM image (Figure 3.1). Figure 3.4 a) presents the Raman band 997 cm^{-1} intensity, while scanning the Phe-Phe tube through the confocal laser spot with the TERS-active probe being retracted (far-field). The Raman spectra were also subtracted from the baseline, with Asymmetric Least Squares (ALS) algorithm applied [282]. The scan included 100 steps (step size 10 nm at the X-axis) with an acquisition time of 2 s for each Raman spectrum. The raw Raman spectra at the selected positions of the X-axis are presented in Figure 3.4 b), with their respective fitted baselines. Here, the intensity of the phenyl band rises between 0.4-0.8 µm position in the X-Axis (Figure 3.4 a)), with the highest signal being located to 0.61 µm, suggesting the presence of the tube. Figure 3.4 c) displays the

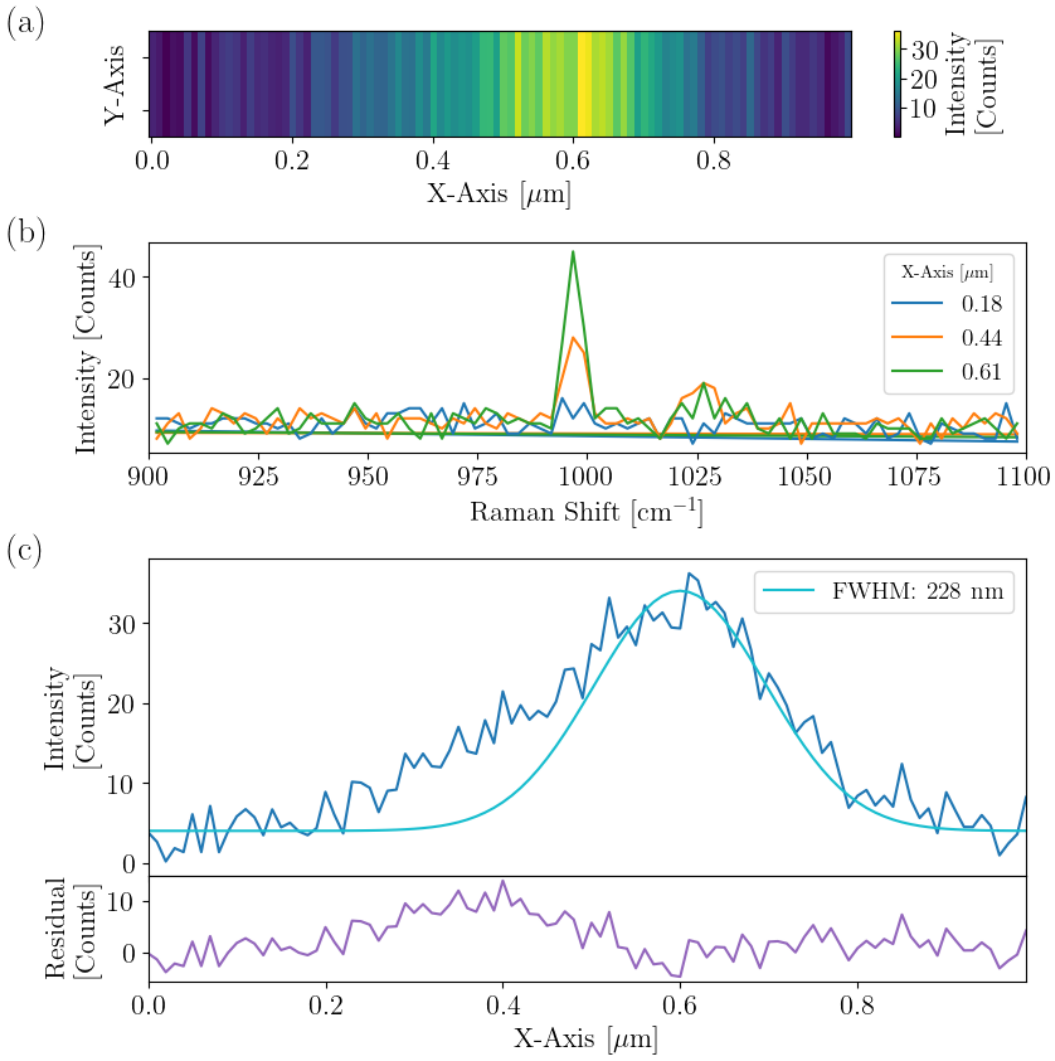

Figure 3.4: 100×1 pixels of 10 nm step size Raman map of Phe-Phe tube with tip retracted with 2 s exposure time at 117 µW laser power. a) intensity line map at the phenyl band 997 cm^{-1}, across the X axis, with ALS baseline subtracted. b) spectra at three different locations of the map at the X-axis, with their respective fitted ALS for background subtraction. c) the intensity of 997 cm^{-1} band, displayed in blue line, across the X-Axis. Cyan represents the fitted Gaussian profile of the right hand side of the tube and purple is the residuals of the blue line after subtracting it with the fitted Gaussian.

line profile, based on the intensity value of the 997 cm^{-1} Raman band, from the fitted baseline, across the Phe-Phe sample on the X-axis (blue line). As the diameter of the Phe-Phe tube (≈ 300 nm) was larger than the theoretical diffraction limit of light (≈ 200 nm), the spatial resolution was calculated by the 'step-edge' method [283]. Briefly, by fitting a Gaussian curve on the sharpest edge of the Raman intensity profile of a sample, the resulting FWHM represents

the 'waist' of the laser spot. By observing the line profile displayed in 3.4 c), the preferred edge is located at the right-hand side of the profile, which can be confirmed from the AFM height profile, shown in 3.1 b). Thus, by applying a Gaussian fit at that region, the resulting FWHM of the curve spans to 228 nm in diameter (cyan line), with no significant residuals remaining after the fit (purple line), which confirms with the theoretical value of the diffraction limit of the confocal laser spot, obtained from equation 1.1. Spatial resolution measurement could also have been simpler if Gaussian fits were applied at narrower nanofibres of less than 200 nm, as previously demonstrated in Chapter 2 with Single-Wall Carbon Nanotubes (SWCNT). The laser spot could not resolve the edges of the tube, below the diffraction limit of light, hence the width of a Raman band's intensity line profile would be similar to the spot's diameter. A higher yield of these nano-structures could be obtained if L-Diphenylalanine crystals were dissolved in $\geq$ 99% w/w acetonitrile concentration [267].

Moreover, the Raman scan across the same Phe-Phe tube was repeated, this time at the near-field with the probe engaged and position-locked within the focal laser spot. Figure 3.5 a) presents the intensity profile of the phenyl 997 cm^{-1} Raman band, from the spectra baselines (ALS applied [282]). This mapping was set at 100 steps, with 15 nm step-size on the X-axis and an acquisition time of 10 s per step. Selected positions of three spectra across the X-axis of the map are displayed in Figure 3.5 b), with their respective baselines. The phenyl band (997 cm^{-1}) was only shown at the position where the map from Figure 3.5 a) was most intense. Thus, the tube was located between 0.2 µm and 0.8 µm X-Axis µm positions. Figure 3.5 c) demonstrates the line profile of 997 cm^{-1} band intensity across the Phe-Phe sample on the X-axis (orange line). It is important to note that performing a single curve fitting as previously demonstrated (Figure 3.4 c) did not resolve the near-field laser spot diameter of several of nanometres. Considering the fact that a near-field intensity profile

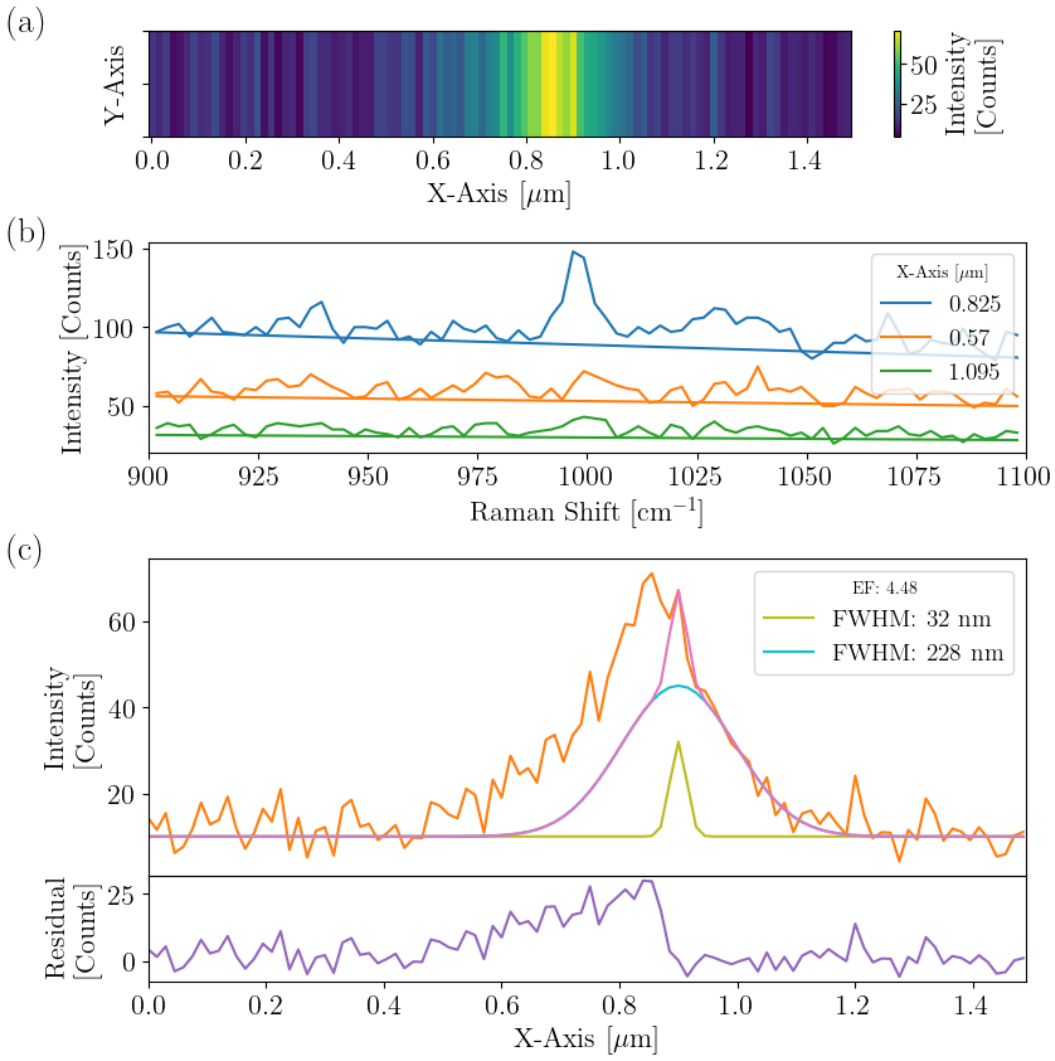

Figure 3.5: 100×1 pixels of 15 nm step size Raman map of Phe-Phe tube, while tip is approached with 10 s Exposure time at 117 µW laser power. a) shows an intensity map at the phenyl band 997 cm^{-1}, across the X axis, with ALS baseline subtracted. b) shows spectra at three different locations of the map at the X-axis, with their respective fitted ALS baselines. c) displays the area intensity profile of the 997 cm^{-1} band across the X-axis as the orange line. The cyan line is the Gaussian profile which is constrained at 228 nm FWHM, corresponding to the far-field illumination and being fitted at the right-hand side of the tube. Similarly the olive line is the second Gaussian, corresponding to the near-field illumination and fitted at the same position as the far-field. The pink line is the sum of the two Gaussians and the purple line represents the residuals from the fitted Gaussians.

of a band, is a contribution of both far-field and near-field Raman scattered light, two Gaussian fits were applied, which correspond the laser beam profiles of the near- and far-field, respectively [284], at the sharp-edge of the sample.

By keeping the FWHM of the far-field profile constant at 228 nm (3.4 c)), the FWHM of the olive coloured Gaussian line shown in Figure 3.5 c), representing the near-field laser spot, approximated at 32 nm. The Enhancement Factor (EF) contributed by the engaged probe [284] was measured by the following equation 3.2 ,where:

$$EF = \frac{I_E/W_E}{I_R/W_R} \tag{3.2}$$

where, IE , IR are the Raman intensities with the tip-engaged and retracted, respectively and WE, WR are the FWHM of the fitted Gaussian profiles, associated with tip on and away from the sample, respectively. This equation calculates the near and far-field band intensities per unit length of the sample mapped and according to our data the generated *EF* is 4.48. It should be considered, that the type of *EF* values reported in this study are different to the ones obtained from the literature, which vary from 10^3 to 10^6 [117]. Roy et al. 2009 [284] demonstrated the incomparability between studies with similar experimental setups, by producing over-estimations of their calculated *EF*, taking into account the reflection of light from the TERS probe. They further implemented the equation 3.2 in previously reported data, only on SWCNT. Their approach has shown consistent deviations in the *EF*, ranging between 4-7. Therefore, by comparing these results to ours, good enhancement factor on Phe-Phe tubes was achieved, alongside with the record of 32 nm in lateral resolution.

3.3.2 Paracetamol/copovidone 50% w/w spin-coated film

3.3.2.1 Raman Spectra of paracetamol/copovidone sample – AFM Probe retracted

Raman spectra of the individual components and the combined blend were recorded at the far-field, with the Ag-coated (TERS-active) probe retracted and displayed in Figure 3.6. Raman signal from paracetamol can be seen both in fingerprint and CH stretch regions (Figure 3.6 a)), with most intense bands being located at 854.4 cm^{-1}, 1316.3 cm^{-1}, 1614 cm^{-1}, and 2931.3 cm^{-1}, which agree with the Raman spectra of the pure material (Figure 3.6 b); green line) and the literature [285, 286](Appendix B - Figure B.4). Also, an intense 2931 cm^{-1} CH band assigned to copovidone was also evident in Figure 3.6 a) (purple line), which agree with the overlapped Raman spectra of the pure materials in Figure 3.6 b) and the study-related [73] reference Raman spectra (Appendix B - Figure B.5). By closer inspection of Figure 3.6 b) we can also notice an overlap of the CH band from the pure components.

3.3.2.2 Paracetamol/copovidone film sensitivity to laser irradiation-TERS-active probe retracted

By approaching the TERS probe on the sample surface, the electromagnetic field under its apex could rise dramatically, affecting the sample's integrity. In order to assess the lifespan of the sample under high laser power (548 µW), time series of four successive spectra at 60 s exposure were acquired. The probe was retracted in order to avoid any contamination and inactivation of the Ag coating. In Figure 3.7 a), the four spectra are displayed at different time points, namely after 60 s (olive line), 120 s (brown line), 180 s (pink line) and 240 s (grey line) of laser exposure. We notice across all four spectra a rise in photon

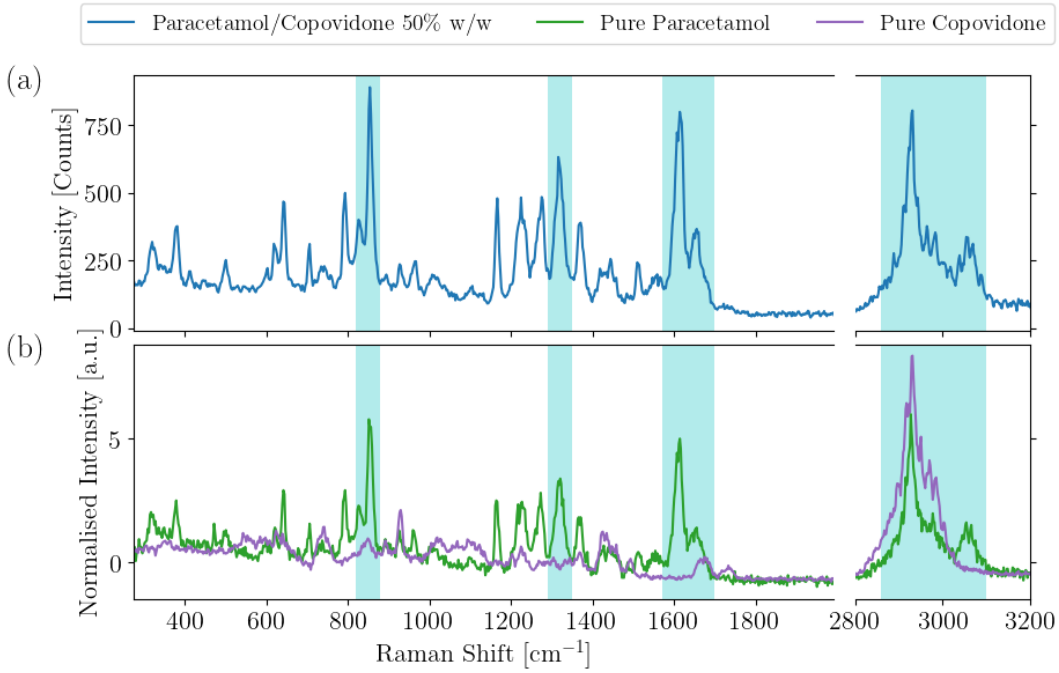

Figure 3.6: a) Spectra of 50 %w/w paracetamol/copovidone film, while probe is retracted, with 60 seconds exposure at 548 µW, of cropped fingerprint region and CH stretch region. b) Mean-centred and variance-scaled overlapped reference spectra of pure paracetamol (green line) and pure copovidone (Kollidon VA64™) (purple line) samples, displayed in cropped fingerprint and CH stretch regions.

counts and a reduction of signal-to-noise ratio as time progresses, indicating photo-degradation at the focal spot after prolonged laser exposure. Also, after 4 minutes of continuous exposure, only one paracetamol band at the 854.4 cm^{-1} remained discernible. In addition, a brightfield image after the end of the set of these measurements was also recorded and presented in Figure 3.7 b). At the focal spot, where the four Raman spectra have been obtained we observe a dark spot, indicating photo-degradation at that location after prolonged laser exposure. This outcome led to lowering the laser power to 78 µW in order to prevent gradual sample damage, while providing visible bands in the Raman spectra.

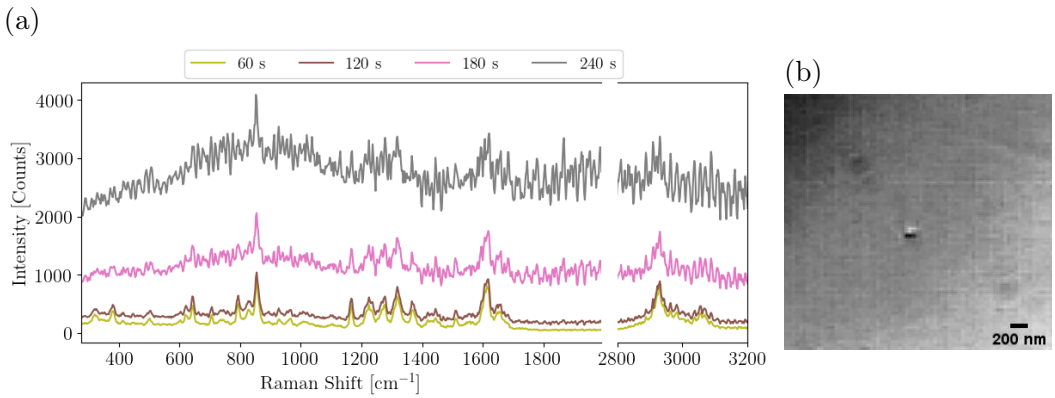

Figure 3.7: a) Four consequent far-field spectra of paracetamol/copovidone of 60 s exposure, at 548 µW of laser power, obtained after 60 s (olive line), 120 s (brown line), 180 s (pink line) and 240 s (grey line). b) brightfield image of the interrogated paracetamol/copovidone sample after the termination of laser irradiation. Spectra in (a) were obtained where dark spot is located in (b).

3.3.2.3 Raman Spectra of paracetamol/copovidone sample -AFM Probe approached

Raman spectra obtained at retracted and approached probe positions, are presented in Figure 3.8. Figure 3.8 b) shows that there is a rise at both the baseline and noise in the near-field spectra, with some Raman bands located at 854.4 cm^{-1}, 1316.3 cm^{-1}, 1614 cm^{-1} and 2931 cm^{-1} being visible in both near- and far-field spectra. From the tip-approached spectrum, the 1316.3 cm^{-1} band shows an *EC* of 1.1. This demonstrates a marginal signal enhancement at the near-field, as mentioned in the Materials and Methods section of this study. Also, the presence of the 514 cm^{-1} band in the near-field indicates the Raman scattering from the probe silicon substrate [249]. The near-field spectrum is almost comparable to the grey spectrum displayed from Figure 3.7 a), which confirms the intense laser exposure and damage of the irradiated sample. The small signal enhancement, in combination with the low signal-to-noise potentially suggested sample photo-damage at the near-field [257]. In addition, even if the sample was not impacted by degradation, the possibility to spatially resolve the distribution of the two components can be very difficult due to the

poor signal-to-noise ratio, obtained from the near-field spectra. Therefore, the experimental conditions for this sample are not suitable for TERS-based Raman mapping, as further laser power optimisations are required. No further repeats of Raman spectra, at the two probe positions, were acquired at the point of measurements.

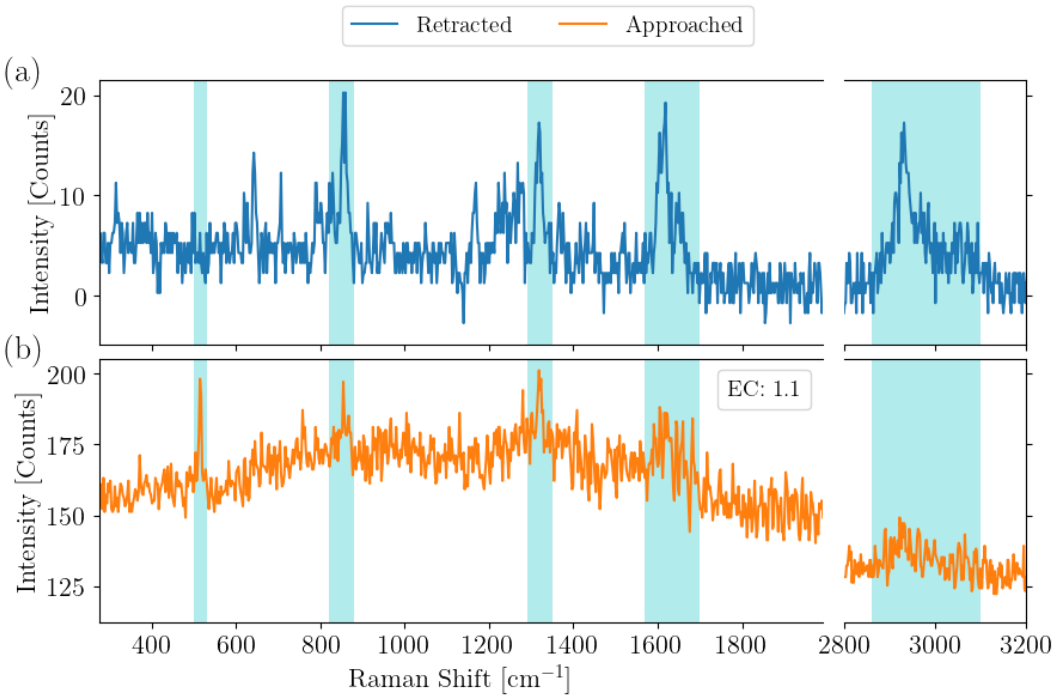

Figure 3.8: Raman spectra of 50%w/w paracetamol/copovidone film, at the a) far-field (blue) and b) near-field (orange), with 10 seconds exposure at 78 µW, at cropped fingerprint and CH stretch regions. The enhancement contrast for the 1316.3 cm^{-1} between the tip-retracted and approached Raman spectra is 1.1.

3.3.3 Felodipine/copovidone 50% w/w spin-coated film

3.3.3.1 Raman Spectra of felodipine/copovidone sample – AFM Probe retracted

Raman spectra of the sample was recorded, alongside with its individual components, while the Ag-coated (TERS-active) silicon probe was retracted (far-

field). The spectra mentioned are shown in Figure 3.9. In Figure 3.9 a), bands between 1406-1525 cm^{-1}, 1644 cm^{-1} at the fingerprint region and 2931 cm^{-1} at longer wavelengths comply with previously published study [73] (Appendix B - Figure B.3) and in Figure 3.9 b), assigned as a combination of felodipine and copovidone components. Specifically, the bands at 1479 cm^{-1} and 1644 cm^{-1} correspond to felodipine, whereas the 1425 cm^{-1} represents copovidone. In addition a combination of both components are also present at the $-CH$ stretch region (Figure 3.9), with the polymer being more intense compared to the drug.

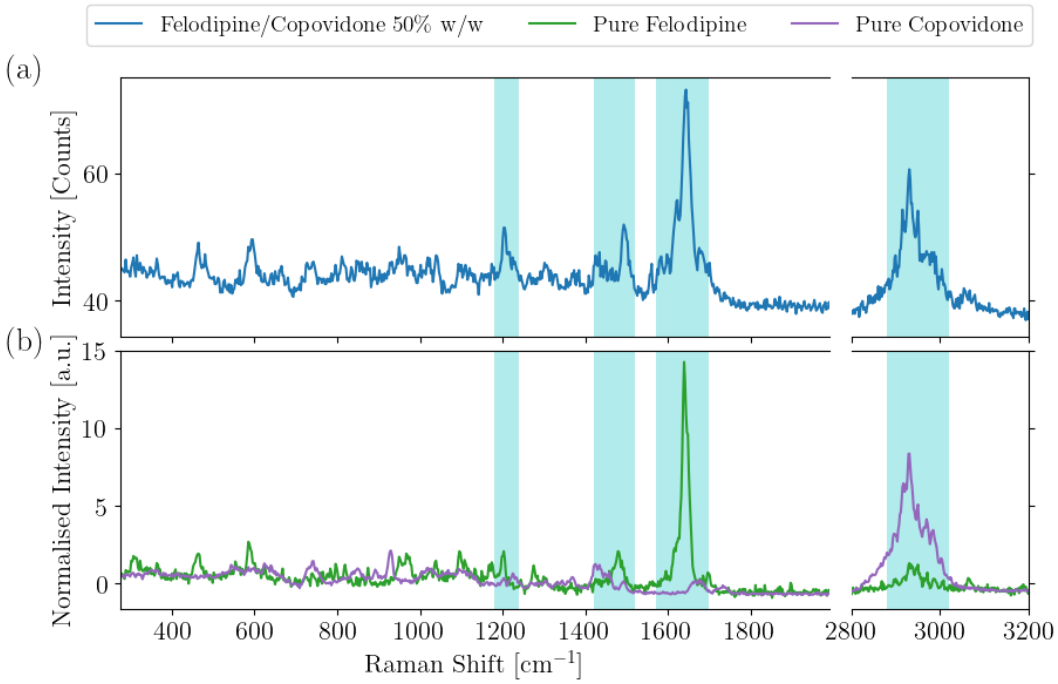

Figure 3.9: a) Spectra of 50% w/w felodipine/copovidone film while probe is retracted, with 10 seconds exposure at 78 µW of laser power, displayed at cropped fingerprint and CH stretch regions. b) Mean-centred and variance-scaled overlapped reference spectra of pure felodipine (green line) and copovidone (purple line) at the fingerprint and CH stretch region of the spectrum.

3.3.3.2 Raman Spectra of felodipine/copovidone sample – AFM Probe approached

After engaging the TERS-active probe on top of the spin-coated film (near-field), the Raman spectrum recorded is displayed in Figure 3.10. In comparison to Figure 3.9 b), only the band associated to the -CH stretch is clearly visible, at 2931 cm^{-1}. Specifically, this band shows a 5.8 *EC* indicating great signal enhancement compared to the confocal spectra. However, the baseline at the fingerprint region (Figure 3.10) is increased with prevalent noise, compared to the far-field spectrum acquired (Figure 3.9 b)). Also, a new band located at 514 cm^{-1} appears, originating from silicon strains of the probe substrate, suggesting the presence of the probe within the laser spot [249, 274]. The observed noise may be a combination of sample photo-damage and probe photoluminescence. The intensity of the laser power, the volume of the sample irradiated as well as the acquisition time are of crucial considerations, when performing these types measurements. Over the course of these experiments sample degradation was observed visually by setting different acquisition times under a minute and power levels that approximate at 78 µW, although no data was recorded. We concluded that the experimental parameters for felodipine/copovidone sample were unfit for performing TERS-based Raman mapping measurements. No further repeats of Raman spectra, at the two probe positions, were acquired at the point of measurements.

3.4 Conclusion

In this work, Phe-Phe tubes were used in order to measure the near-field spatial resolution of the TERS instrument. After obtaining the tube's physical dimensions with AFM, the acquired Raman data was evaluated and the spatial

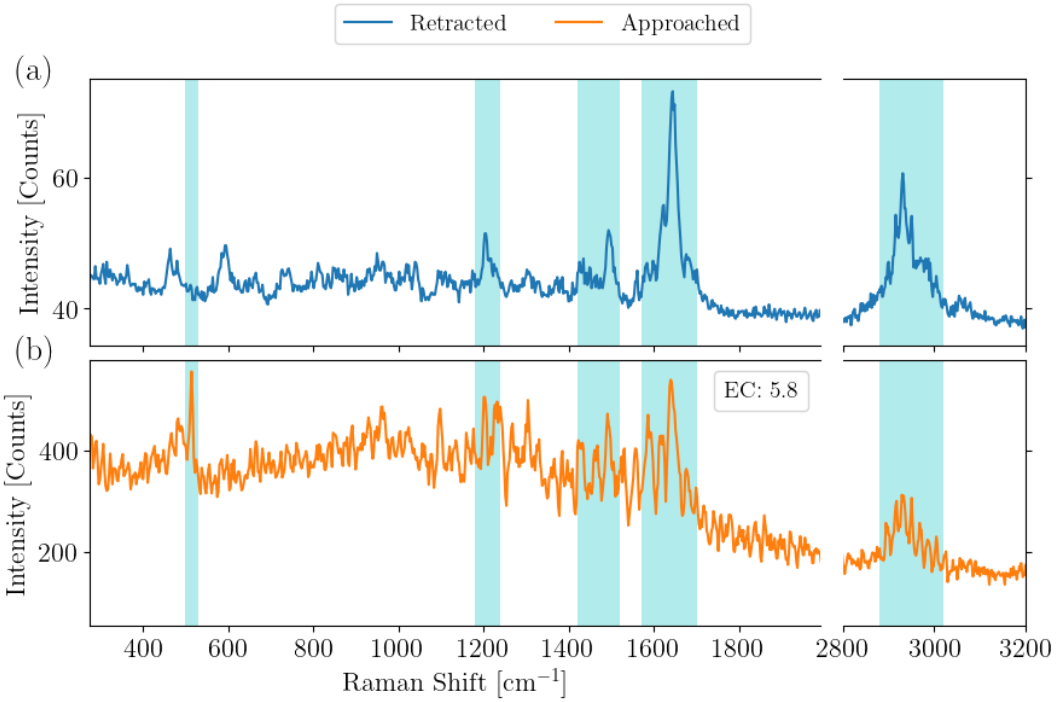

Figure 3.10: a) Spectra of 50 % w/w felodipine/copovidone film while probe is retracted (blue line), with 10 seconds exposure at 78 µW of laser power, displayed at cropped fingerprint and CH stretch regions.b) Spectra of 50 %w/w felodipine/copovidone film, while probe is approached (orange line), with 60 seconds exposure at 78 µW of laser power, displayed at the cropped fingerprint region and CH stretch region. The enhancement contrast for the 2931 cm^{-1} between the tip-retracted and approached Raman spectra is 5.8.

resolution calculated, at the two different height positions of the TERS-active probe. For the amorphous dispersions tested, paracetamol/copovidone 50% w/w and felodipine/copovidone 50% w/w, Raman spectra were obtained both in the near- and far-field and further evaluated. For the peptide structure, our findings demonstrate the presence of the probe in close proximity with the focal point, with an Enhancement Factor of 4.48 at the apex. In addition, the focal spot of the laser at the near-field was calculated at 32 nm in diameter, indicating the measurement of nanometre-scale chemical maps, below the diffraction limit of light. Although the present Phe-Phe tube sample had a diameter larger than the diffraction limit, a thinner sample would be more ideal to perform these measurements. Regarding the measurements performed on the ASD, both films were potentially prone to photo-degradation either under high

irradiation or at the probe being in contact with the sample surface, while irradiated by the monochromatic light, leading to poor signal-to-noise ratio in the Raman spectra. These finds led to discontinuing our investigation on TERS-mapping analysis on the spin-coated films. Currently there is no clear evidence on which of the components and to what extent might have been affected from both the laser and the engaged probe. Testing each component to different levels of laser power, could provide us information about their degree of sensitivity to the laser. Szczerbinski et al [287] demonstrated the impact of laser power intensity on protein structures under the plasmonic hot spot, revealing some bands which would with $>$ 78 µW laser intensity be undetected. Also, by recording their local temperature, we could evaluate if glass-transition or melting point temperatures have been reached for each material. For this case, simultaneous recording of the Stokes and Anti-Stokes spectral intensities of the probed sample near-field temperature as well as certain plasmon resonance parameters can be recorded [288]. This information could allow the optimisation of experimental conditions of the TERS measurements on pharmaceutical samples as well as optimise the laser power. In addition, TERS experimentations of pure pharmaceutical components, based on the hotspot-to-sample distances, across the XYZ-axes, could potentially provide us a clearer understanding of their sensitivity under the TERS-active probe.

Chapter 4

Laser sensitivity and Raman thermometry assessment of pharmaceutical components

4.1 Introduction

In Chapter 3, we evaluated the Raman spectra obtained from a TERS system. The samples examined were thin spin-coated solid-dispersions of felodipine/copovidone 50 % w/w and paracetamol/copovidone 50% w/w, under engaged and retracted tip positions relative to the height from the sample surface. Results indicated both samples were prone to degradation and rise in recorded photoluminescence (PL), either under continuous laser irradiation (<548 µW, with 1.49 NA objective) or probe contact with the sample. However, it is not clear whether the probe or the prolonged irradiation may had led to changes in the sample's properties and to what extent these properties alter.

To better understand this outcome, it is important to examine the contributions

of CRM and TERS towards the samples integrity. In CRM, the NA of a microscope objective lens can determine the diameter of a laser focal spot [85]. As aforementioned in the Introduction, NA is the dimensionless number which describes the size of the angle relative to the focal spot, at which light is emitted or gathered, resolving fine specimen detail at a fixed object distance. According to Abbe's Equation 1.1, the lateral dimension of the laser spot is depended on the wavelength (λ) of the incident light and the NA of the objective. This indicates that under a specific wavelength, higher NA values generate shorter focal point diameters.

The focal spot size is also connected to the irradiance on the sample surface, measured in watts per square centimetre (W/cm^2)[289]. If a constant laser power in (W) is applied on a sample, higher NA objectives generate greater amounts of irradiance. This narrowing of laser focal spot can result in an increase of the collected Raman signal. However, it may also lead to an elevated risk of igniting the sample, by absorbing a significant amount of incident laser light. In addition, there is a chance of an applied incident green laser (500-570 nm) to fluoresce the irradiated sample followed by burning. These events in return generate fluorescence background noise which can mask entirely a Raman spectrum [85].

In TERS, a plasmonically active probe under the laser irradiation, serves as a lightning rod which enhances and highly confines strong electromagnetic fields above the adsorbed sample molecules [278, 279, 281]. Due to the nanometre confinement of the near-field laser spot, it may lead to the decomposition of the interrogated sample molecules. To provide an indicative example from the literature [168], a continuous-wave laser beam of 1 mW, irradiating a spot of 1 µm radius, generates a irradiance of approximately 32 kW/cm^2. When the metallic apex of the probe of 10 nm radius is in close proximity to the target molecule, the density rises to 32 MW/cm^2. In addition, if the incident light en-

hancement is 10-100 fold higher, as often reported in studies [117, 168] the final irradiance may arise close to 3200 MW/cm^2 on several molecules. Other than decomposition, sample may also undergo plasmon-driven photocatalysis, generating reaction products under the irradiated field and making more complex the evaluation and interpretation of TERS spectra [219, 287].

Under these circumstances, one should seek balance in the laser power applied, to prevent sample transformation as well as in the parameters of Raman signal acquisition. It is understood that parameters such as the time, power as well as the size of the laser spot, are key in investigating and sustaining the integrity of the target sample during both CRM and TERS measurements. Also given the complexity of the TERS spectra, displaying events of photo-degradation or photo-catalysis [219], it is important to narrow down and examine the factors which affect the stability of the samples. By examining pure components i.e. paracetamol, felodipine and copovidone separately under the CRM, at different power levels and magnification lenses would provide more clarity to the correlation between area, powers and time-threshold to laser exposure.

In addition, obtaining the sample's temperature during irradiation could also unravel the case of sample undergoing through the glass transition, and melting point temperatures. Under these circumstances Raman thermometry can be applied, by calculating from a Stokes Raman band its shift, line-width as well as the intensity ratio with the corresponding symmetric bands at the anti-Stokes region [290–292]. The latter can be used to directly calculate the temperature based on a Boltzmann distribution of the ground and excited population of molecules [290].

Aim of this chapter was to identify the power threshold to trigger sample degradation over prolonged laser exposure, at different laser powers and NA objective lenses. In addition Raman thermometry was performed to investigate the

changes in sample temperature. Pure materials, shown in Chapter 3, were examined separately, under two Raman instrument with different laser intensities (532 nm) and magnification lenses.

4.2 Material and Methods

4.2.1 Materials & Preparation method

Crystalline felodipine, paracetamol and copovidone (Kollidon™ VA64 Fine) were provided by AstraZeneca (Macclesfield, United Kingdom). Pure films of crystalline drugs and polymer were prepared through spin-coating method, according to the method reported previously, in Chapter 3. Briefly, each component was dissolved in ethanol (1 mg/ml) and 50 µL aliquot was deposited and spun on top of coverslips. The spin-coating process was initiated at 500 rpm for 3 seconds and further increased to 2000 rpm for 30 seconds.

4.2.2 Instrumentation & Raman Measurements

For this set of experiments two CRM instruments were used. These are the AFM-CRM instrument, demonstrated in Chapter 2 and Horiba LabRAM HR (Paris, France).

4.2.2.1 AFM-CRM

For this set of measurements, the AFM-CRM setup was modified with a 532 nm centred notch filter (StopLine® - NF01-532U, Semrock, New York, USA) and 532 nm dichroic notch beam splitter (StopLine® - NFD01-532, New York, USA), in order to record Raman signal at both Stokes and Anti-Stokes regions.

4.2.2.2 Horiba LabRAM

The Horiba system was equipped with an Ultra-low frequency module to record the Stokes and Anti-stokes regions using two air-immersion objectives (Olympus LMPlanFL N, 100×, NA=0.80 & Leica HC PL FLUOTAR, 50×, NA=0.55). The power intensity of the excitation laser was controlled with neutral density filters.

4.2.2.3 Irradiance investigation

In order to examine and evaluate the sample-laser sensitivity, irradiance was calculated based on the laser power applied (kW) over the irradiated area (cm^2), as seen in Equation 4.1:

$$Irradiance = \frac{Power\ (\mathrm{kW})}{Area\ (\mathrm{cm}^2)} \tag{4.1}$$

With the power known, it is important to measure the beam area for the different objectives used. For a Gaussian beam, its waist is defined as the location where the irradiance is $1/e^2$ (13.5%) from its maximum value [293, 294]. Acquiring images of focused laser beams, for the different objectives and instruments, it was possible to measure the beam areas. For example, as shown in Figure 4.1, the red region corresponds to the laser beam, with the green and red line cross-sectioning the beam's profile and acquiring the waists. In addition the area of the beams were slightly elliptical. Therefore, the beam area was calculated from the following Equation 4.2:

$$Area = \pi \frac{BD_1 * BD_2}{4} (\mathrm{cm}^2) \tag{4.2}$$

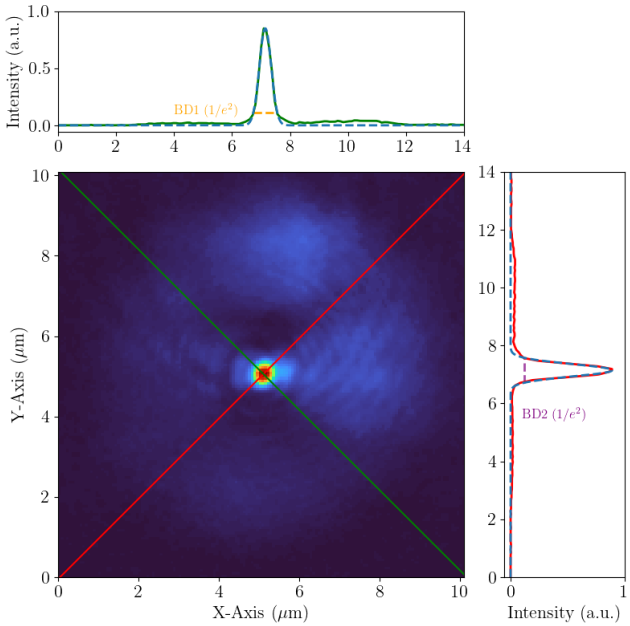

Figure 4.1: Image of Laser spot, acquired with the 100× magnification, 1.45 NA objective. The green and red plotted lines are cross sections of the laser spot, with the laser profile being displayed to the uppermost and right hand-side of the image, respectively. In each laser profile a Gaussian curve was fitted (dashed blue lines) and the effective beam waist $(1/e^2)$ was calculated.

where BD_1 and BD_2 are the beam width diameters of the perpendicular axes of the cross-section of the Gaussian beam, respectively. The laser beam waist measurement was performed by acquiring an image of the confocal laser spot under the microscope camera and further processing it with the ImageJ's plug-in, Open Beam Profiler [295, 296]. From both Raman instruments the range of laser powers applied, alongside with the corresponding objectives used, their beam area as well as irradiance are displayed in table 4.1.

In order to investigate the laser sensitivity for all the samples, each sample was brought to a focus and irradiated, across different laser powers, over 2 minutes. During that time a series of consecutive single spectra were acquired, each obtained at 2 seconds of exposure (2 seconds × 61 spectra = 122 seconds). For every consecutive run, the laser spot was relocated and focused on a different

Table 4.1: Series of Laser power intensities (mW) applied on the different samples with their corresponding beam diameters (µm × µm), areas (µm^2) and irradiance values (kW/cm^2), for the 1.45, 0.8 and 0.55 NA objective lenses used in the AFM-CRM and LabRAM CRM equipments.

Instruments	**Objectives** (NA | Power Coefficient for 532 nm)	**Beam Diameters** (µm × µm)	**Area beam** (cm^2)	**Power intensity** (mW)	**Irradiance** (kW/cm^2)
AFM-CRM	100× Nikon (1.45 | 0.88)	0.442 × 0.382	$0.13*10^{-8}$	0.03	19.91
				0.3	199.08
				0.75	497.7
				1.5	995.4
				3	1990.8
Horiba LabRAM	100× Olympus (0.8 | 0.9)	1.822 × 1.648	$2.36*10^{-8}$	2.5	95.41
				6.25	238.52
				12.5	477.04
				25	954.08
	50× Carl Zeiss (0.55 | 0.88)	3.878 × 3.802	$11.58*10^{-8}$	2.5	19.12
				6.25	47.81
				12.5	95.62
				25	191.23

XY position on the sample surface with distance >10 µm from the initial location. This was performed in order to avoid any areas where the sample might have been affected under any irradiation and prevent any discrepancies in the acquired spectra. The Raman shifts are displayed within range of -1500 cm^{-1} and 1500 cm^{-1}, unless else stated.

4.2.2.4 Thermometry investigation

Regarding the thermometry measurements, the shift, and line-width of a Raman Stokes band, alongside with the ratio of symmetric Raman bands located in the Stokes and Anti-Stokes regions, were calculated. From the time-cascade spectra obtained, a combined non-linear curve comprising of a Lorentzian curve and a 1st polynomial line were fitted across all time-spectra, on the symmetric bands of interest. Specifically, the Lorentzian curve corresponds to the shape of the produced Raman bands, whereas a 1st order polynomial line under the curve represents the baseline of that band under a selected range of wavelengths [109].

From the fitted curve models the height, centre position as well as FWHM

values, were acquired. The anti-Stokes/Stokes ratio of symmetric bands was measured after summing the height of the fitted Lorentzian curve with the height of the line. The extrapolation of temperature from the band ratio was acquired through the following equation 4.3 [297]

$$\frac{I_{AS}}{I_S} = \frac{(V_l + V_v)^3}{(V_l - V_v)^3}\, exp\left(\frac{-hv_v}{kT}\right) \tag{4.3}$$

where I_S and I_{AS} are the Stokes and Anti-Stokes Raman scattering strengths, based on the photon count signal from the CCD camera. V_l is the frequency of the laser (s^{-1}), V_v is the frequency of the vibrational mode (s^{-1}) (Raman band position), h is Planck's constant ($J * s$), k is Boltzmann's constant ($J * K^{-1}$) and T is the temperature (K), generated at the laser focal spot. All measurements undertaken were performed under ambient-air conditions (≈ 20 °C). Numerical codes for statistical analysis and figure plotting were written under the open-source Python language and relevant packages [298]. All numerical routines and raw data are included in the supplementary material for information and reference.

4.3 Results and Discussion

4.3.1 Laser sensitivity of Paracetamol

Reference Raman spectra of pure paracetamol film were obtained from the AFM-CRM and LabRAM instruments, displayed in Figure 4.2. Figure 4.2 a) shows raw paracetamol spectra obtained with the 1.45 NA (blue line), 0.8 NA (orange line) and 0.55 NA (green line) objectives, respectively. The same

spectra were also mean centred and variance scaled as presented in Figure 4.2 b). By closer inspection of Figure 4.2 a), the higher the NA objective used provided more intense Raman signal. In addition, higher NA objective produced better Signal-to-Noise (SN) ratio in the Raman spectra, as seen in Figure 4.2 B). Furthermore, according to Figure 4.2 b), several Raman bands were visible in the fingerprint region specifically at 874.4 cm^{-1}, 1168.5 cm^{-1}, the bands within the 1200-1400 cm^{-1} Raman shift , with 1323.9 cm^{-1} being the most prevalent cm^{-1} and the bands around 1628 cm^{-1}. According to the literature [299], the studied paracetamol sample resemble the crystalline form I and III,for the spectra obtained with the LabRAM and AFM-CRM, respectively. From the 0.8 NA and 0.55 NA objectives used, we observed higher intensities for the 874.4 cm^{-1} and 1648.4 cm^{-1}, compared to the 1.45 NA. The reference spectra from the literature can be viewed under Appendix E in Figure E.1.

4.3.1.1 AFM-CRM measurements for paracetamol

Time series of Raman spectra on paracetamol spin-coated film were recorded with the AFM-CRM instrument. The results are displayed in figure 4.3 obtained with the 1.45 NA objective. This figure displays the spectra in the form of heat-map versus time (1^{st} column), three spectra at different time-points (2^{nd} column) and mean intensity of spectra across time (3^{rd} column), at different irradiance kW/cm^2 per row.

On the first Figure (4.3), where the lowest irradiance was applied (19.91 kW/cm^2), both the heat-map and mean spectral intensity graphs show the intensity of every spectrum remained constant throughout the whole experiment. The SN ratio was low, with no discernible Raman bands of the paracetamol sample. The same effects on the sample were observed when the applied irradiance ranges between 199.08 and 497.7 kW/cm^2, with the only exception of improvement

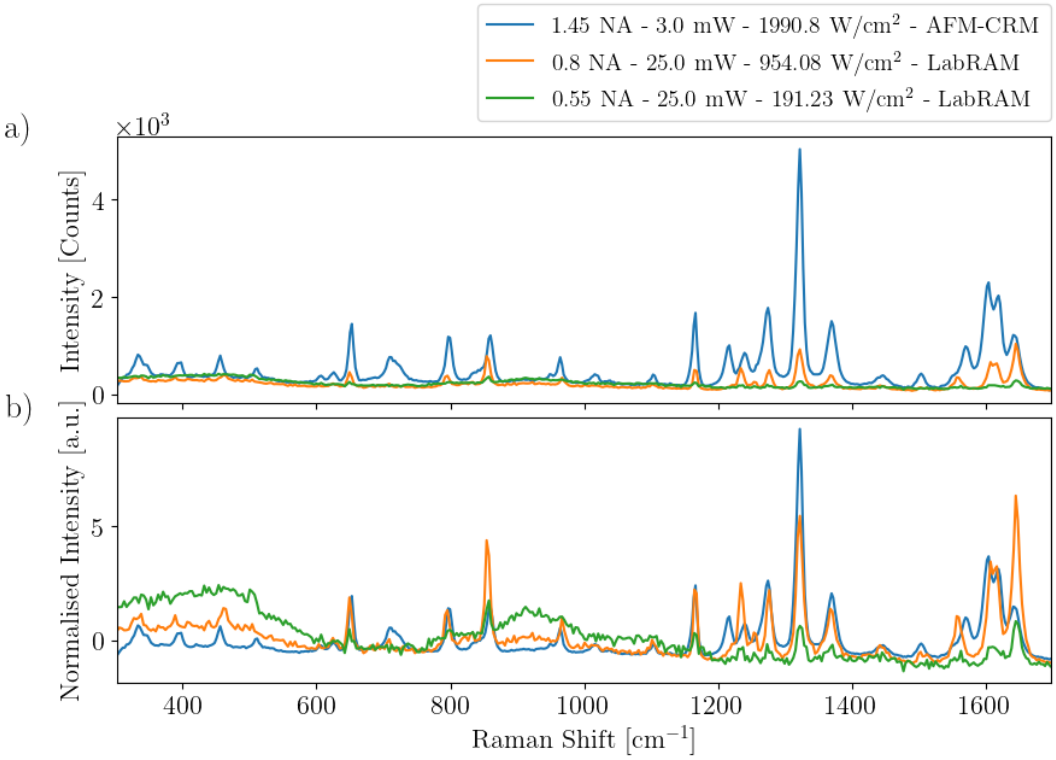

Figure 4.2: Reference Raman spectra of pure paracetamol sample. Blue line spectrum was acquired with the 1.45 NA objective under the AFM-CRM instrument, with 2 seconds of laser exposure and 3 mW of laser power. Green and orange lines spectra were acquired under the LabRAM instrument with the 0.8 NA and 0.55 NA objectives, respectively. These spectra were recorded with 2 seconds of laser exposure at 25 mW of laser power. (a) Shows raw spectra, whereas (b) presents mean centred and variance scaled spectra. The Raman shift of the spectra acquired range between 300-2000 cm^{-1} at the fingerprint region.

in SN ratio, where Raman peaks were visible. After further increase of the irradiance to 995.4 kW/cm^2, under 100 seconds of prolonged irradiation the sample remained stable. After that point, a rise in PL background became detectable, as seen at the heat-map and the mean trend line of the Figure 4.3 and the green spectra after 122 seconds of exposure. At the maximum irradiance applied (1990.8 kW/cm^2), we observe similar events as previously mentioned, only that they occur after 70 seconds of laser exposure.

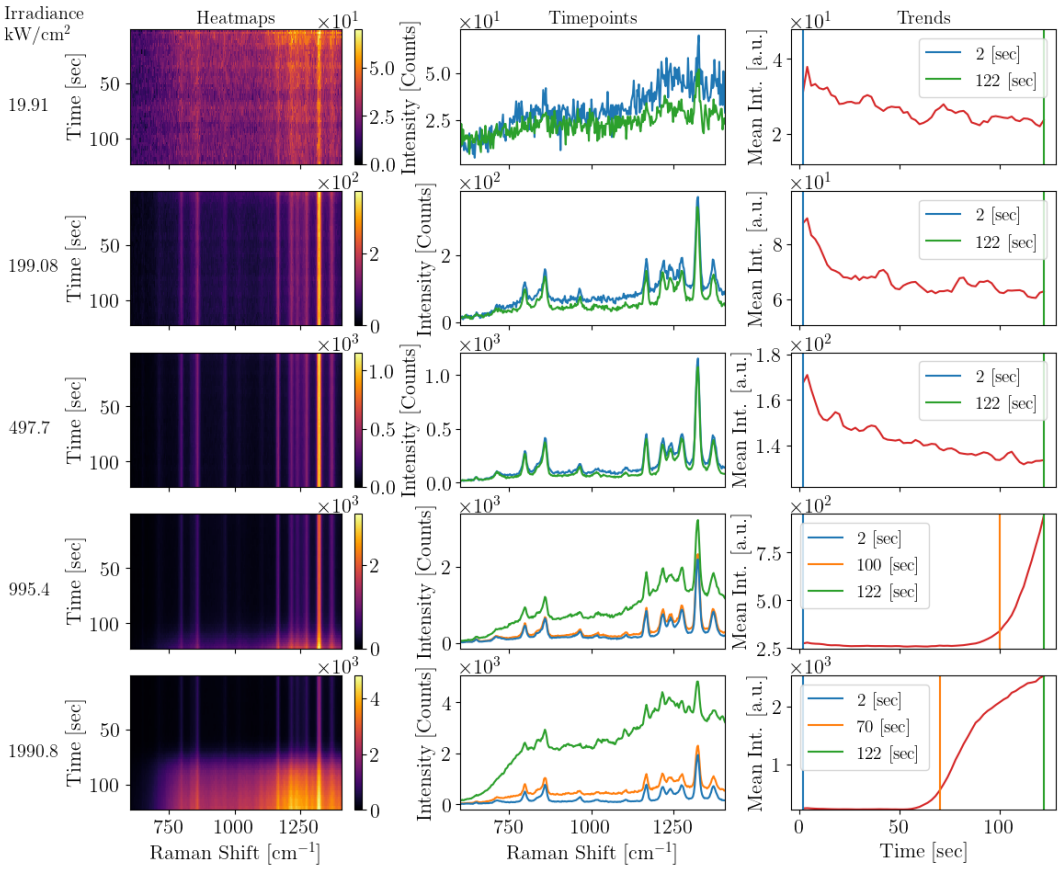

Figure 4.3: Time series of Raman spectra on Paracetamol with 2 seconds exposure, on the AFM-CRM CRM using the 1.45 NA objective. Each row displays measurements of increasing irradiance(19.91 kW/cm^2, 199.08 kW/cm^2, 497.7 kW/cm^2, 995.4 kW/cm^2, 1990.8 kW/cm^2). The left column show heat-maps of spectra for each measurement as a function of time (seconds) on the left Y-axis. The middle column presents the three time-points of single spectra, at the beginning (blue),before spectral change (orange) and at the end (green) of each measurement. The right column demonstrates the mean value of each spectra as a function of time (seconds). Each vertical colour line represent the time point of the spectra from the second column graphs.

4.3.1.2 Horiba - LabRAM measurements for paracetamol

Time series of Raman spectra on paracetamol spin-coated film were acquired from the LabRAM CRM instrument. The data acquired with the 0.8 and 0.55 NA objectives, are presented in Figures 4.4 and C.1 in the same graphical layout previously shown with the 1.45 NA objective. On Figure 4.4, laser intensities ranging between 2.5 and 25 mW have been applied on the sample, using the 0.8 NA objective. With irradiance applied up to 477.04 kW/cm^2, the sample

appeared to be stable with good signal acquisition where paracetamol bands in the Stokes region are visible and no PL was present. After applying 954.08 kW/cm^2 of laser power, an exponential increase in PL became prevalent after 100 seconds of continuous laser exposure.

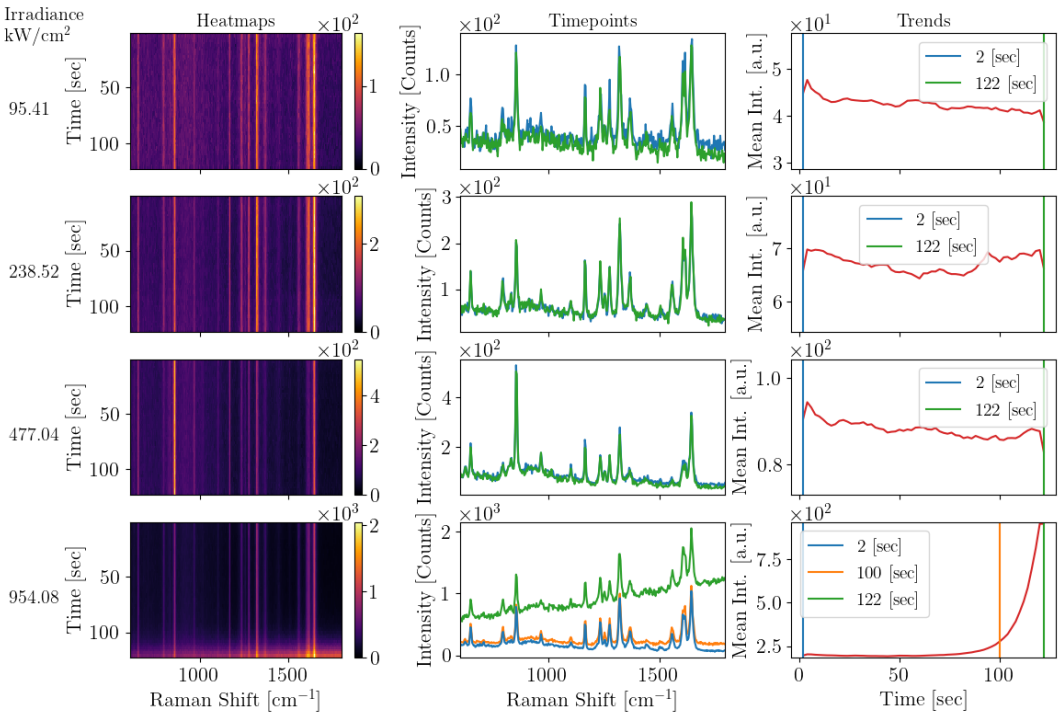

Figure 4.4: Time series of Raman spectra on Paracetamol with 2 seconds exposure, on the LabRAM CRM using the 0.8 NA objective. Each row displays measurements of increasing irradiance(95.41 kW/cm^2, 238.52 kW/cm^2, 477.04 kW/cm^2, 954.08 kW/cm^2). Each column from left to right presents heat-maps of spectra for each measurement, the time points of single spectra and the mean value of each spectra as a function of time (seconds). Each vertical colour line represent the time point of the spectra from the second column graphs.

On the last figure (C.1), provided in Appendix C, the spectra acquired with the 0.55 NA objective on paracetamol sample, showed no rise of a PL background across the different irradiance applied, between 19.12 and 47.81 kW/cm^2. The SN ratio of the Raman signal is also comparably lower to the the spectra acquired with the 0.8 NA objective, on the same system.

According to the data acquired and summarised in Table 4.2, with the rise of irradiance the occurrence of the sample starting to photoluminesce rose. By

using the 1.45 and 0.8 NA objectives an approximation of the sample sensitivity threshold can be identified. Specifically, when the irradiance applied approximates at 954 kW/cm^2, after 1 minute and 40 seconds of continuous exposure the sample exhibited PL.

Table 4.2: Series of laser power intensities (mW) and irradiance (kW/cm^2) applied on paracetamol using the 1.45, 0.8 and 0.55 NA objective lenses used on the AFM-CRM and LabRAM CRM systems. The red coloured cells indicate the time-series which present a rise in PL after prolonged laser irradiation.

Instruments	**Objectives** (NA)	**Power intensity** (mW)	**Irradiance** (kW/cm^2)
AFM-CRM	100× Nikon (1.45)	0.03	19.91
		0.3	199.08
		0.75	497.7
		1.5	995.4
		3	1990.8
Horiba - LabRAM	100× Olympus (0.8)	2.5	95.41
		6.25	238.52
		12.5	477.04
		25	954.08
	50× Carl Zeiss (0.55)	2.5	19.12
		6.25	47.81
		12.5	95.62
		25	191.23

4.3.2 Laser sensitivity of Felodipine

Reference Raman spectra of pure felodipine film were obtained from the AFM-CRM and LabRAM instrument, presented in Figure 4.5. Figure 4.5 a) shows raw felodipine spectra obtained with the 1.45 NA (blue line), 0.8 NA (orange line) and 0.55 NA (green line) objectives, respectively. The same spectra were also mean centred and variance scaled, as displayed in Figure 4.5 b). According to Figure 4.2 a), the spectra acquired by the 1.45 NA objective produced better SN ratio, compared to 0.8 NA, which in turn shows better results in relation to 0.55 NA. Also, in Figure 4.2 b) all the reference spectra presented are in

agreement with each other as well as to the literature with the most prevalent band being detected at 1644 cm^{-1} [73] (Appendix C - B.3).

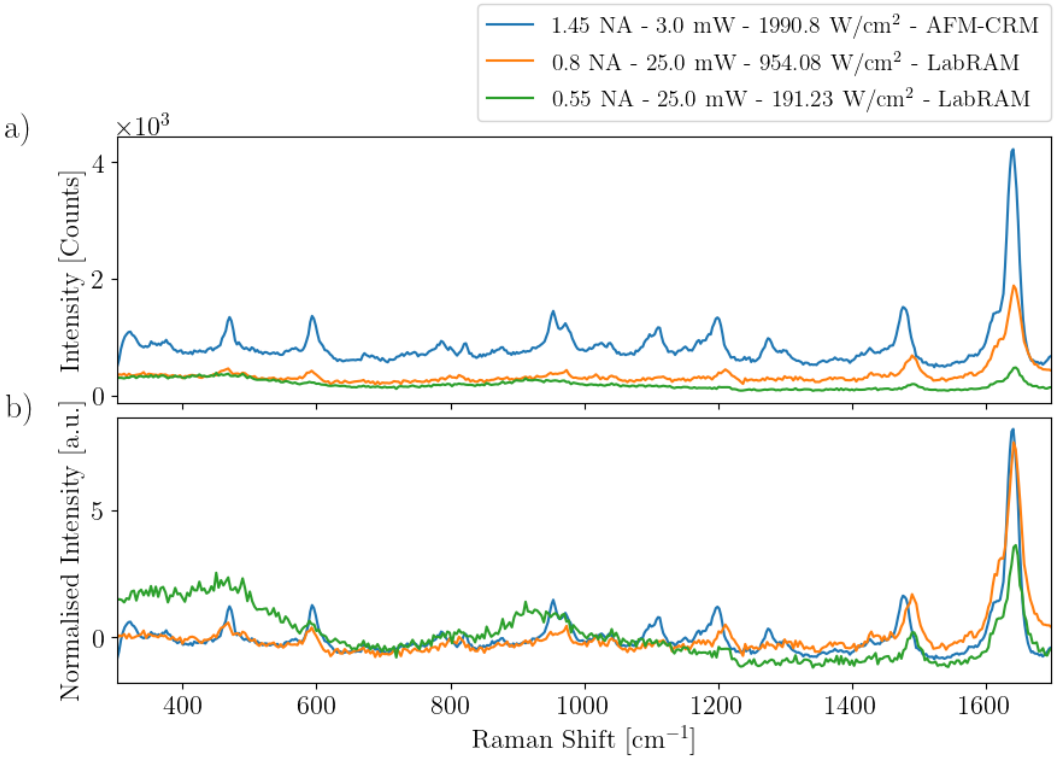

Figure 4.5: Reference Raman spectra of pure felodipine. Blue line spectrum was acquired with the 1.45 NA objective under the AFM-CRM instrument, with 2 seconds of laser exposure and 3 mW of laser power. Green and orange lines spectra were acquired under the LabRAM instrument with the 0.8 NA and 0.55 NA objectives, respectively. These spectra were recorded with 2 seconds of laser exposure at 25 mW of laser power. (a) Shows raw spectra, whereas (b) presents mean centred and variance scaled spectra. The Raman shift of the spectra acquired range between 300-2000 cm^{-1} at the fingerprint region.

4.3.2.1 AFM-CRM measurements for felodipine

Time series of Raman spectra acquired from spin-coated felodipine film were recorded with the 1.45 NA objective on the AFM-CRM instrument. The acquired results are displayed in Figure 4.6. In Figure 4.6, irradiating the sample with 19.91 kW/cm^2 using the 1.45 NA objective, a decline on the spectral mean intensity was observed at the start of the measurement. This intensity was stabilised after 44 seconds have passed, indicating sample quenching. When the

irradiance applied was 199.08 kW/cm^2 a steady fall in PL occurred after 60 seconds of prolonged exposure. At 497.7 kW/cm^2, the stability of the sample spectra endured below 12 seconds, whereafter the mean intensity of the spectra spiked and further dropped down in intensity. Under higher irradiance values; i.e. 995.4 kW/cm^2, 1990.8 kW/cm^2; the felodipine burned instantaneously showing a rapid increase in mean intensity, further followed camera saturation and termination of the experiments.

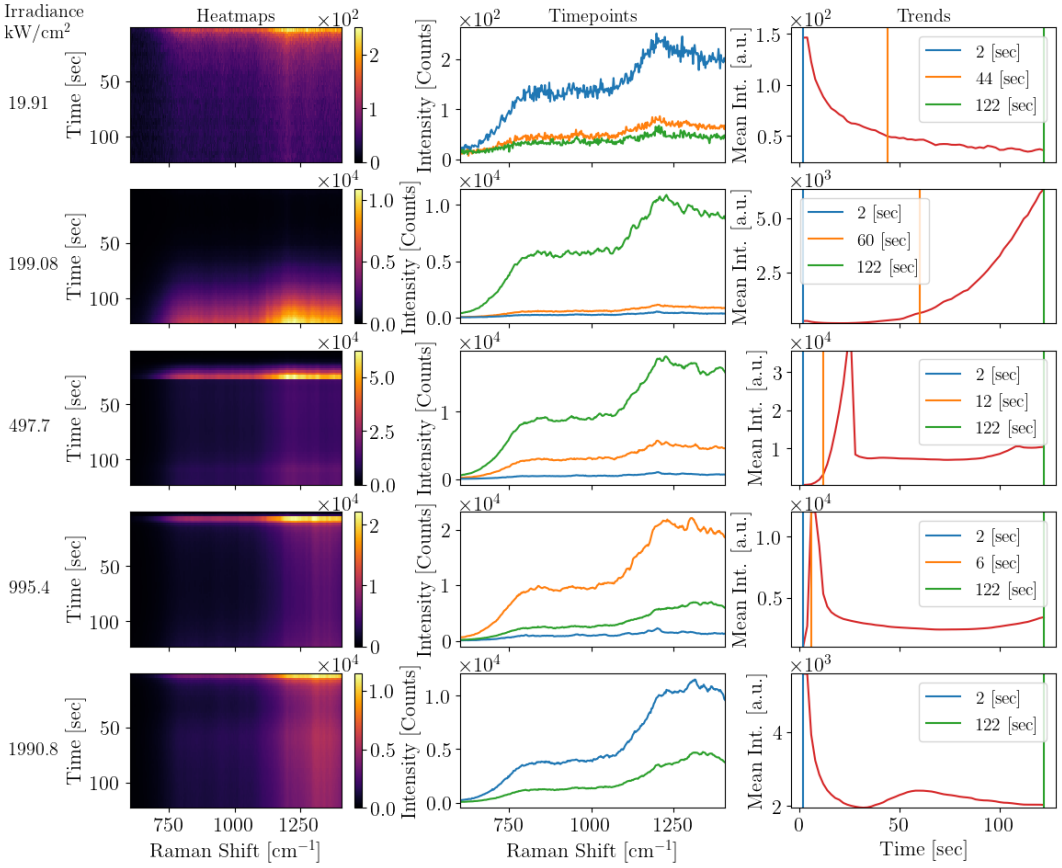

Figure 4.6: Time series of Raman spectra on felodipine with 2 seconds exposure, on the home confocal Raman microscope using the 1.45 NA objective. Each row displays measurements of increasing irradiance(19.91 kW/cm^2, 199.08 kW/cm^2, 497.7 kW/cm^2, 995.4 kW/cm^2, 1990.8 kW/cm^2). The left column show heatmaps of spectra for each measurement. The middle column presents the time points of single spectra. The right column demonstrates the mean value of each spectra as a function of time (seconds). Each vertical colour line represent the time point of the spectra from the second column graphs.

4.3.2.2 Horiba - LabRAM measurements for felodipine

Time series of Raman spectra were also obtained with the LabRAM instrument, using the 0.8 NA and 0.55 NA. The data from the Felodipine spin-coated sample are displayed in Figures 4.7 and 4.8. Under the 0.8 NA objective (Figure 4.7), at 95.41 kW/cm^2 the felodipine spectra remained stable over time, with good SN ratio across the time-length of the experiment. Raising the irradiance to 238.52 kW/cm^2 the Raman signal remained consistent until 50 seconds have passed, where afterwards a steady raise of sample PL became prevalent. By further increase of the irradiance value to 477.04 and 954.08 kW/cm^2 the PL noise appeared after 30 seconds and 6 seconds of prolonged irradiation, respectively. Intense spikes in the mean spectral intensity were also available, as seen previously with the 1.45 NA objective.

After setting the 0.55 NA objective, similar effects with the 0.8 NA were also observed with a lower SN ratio across all the different time-series spectra. Based on Figure 4.8 the PL rose when 47.81 kW/cm^2 irradiance or higher was applied. In particular, under 47.81, 95.62, 191.23 kW/cm^2, the rise of the spectral background was detected at time-points of 100, 50 and 10 seconds, respectively.

Based on the results obtained for felodipine, it is prevalent that the sample is very sensitive under continuous laser irradiation. By closer inspection of Table 4.3, regardless of the objective chosen in each experiment, at irradiance 47.81 kW/cm^2 or higher, felodipine exhibited to spectral changes upon extended laser irradiation.

4.3.3 Laser sensitivity of Copovidone

Reference Raman spectra of pure copovidone film were obtained from the AFM-CRM and LabRAM instruments, displayed in Figure 4.9. Figure 4.9 a) shows raw spectra obtained with the 1.45 NA (blue line), 0.8 NA (orange line) and 0.55 NA (green line) objectives, respectively. The same spectra were mean centred and variance scaled, which are further presented in Figure 4.9 b). According to Figure 4.9 a), the spectra acquired by the 1.45 NA objective produced better SN ratio, compared to 0.8 NA, which in turn shows better results in relation to 0.55 NA. Also, in Figure 4.9 b) all the reference spectra presented are in agreement with each other as well as to the literature with visible bands being detected at 746.6 cm^{-1}, 933 cm^{-1} and 1425 cm^{-1} [73] (Appendix C - B.3).

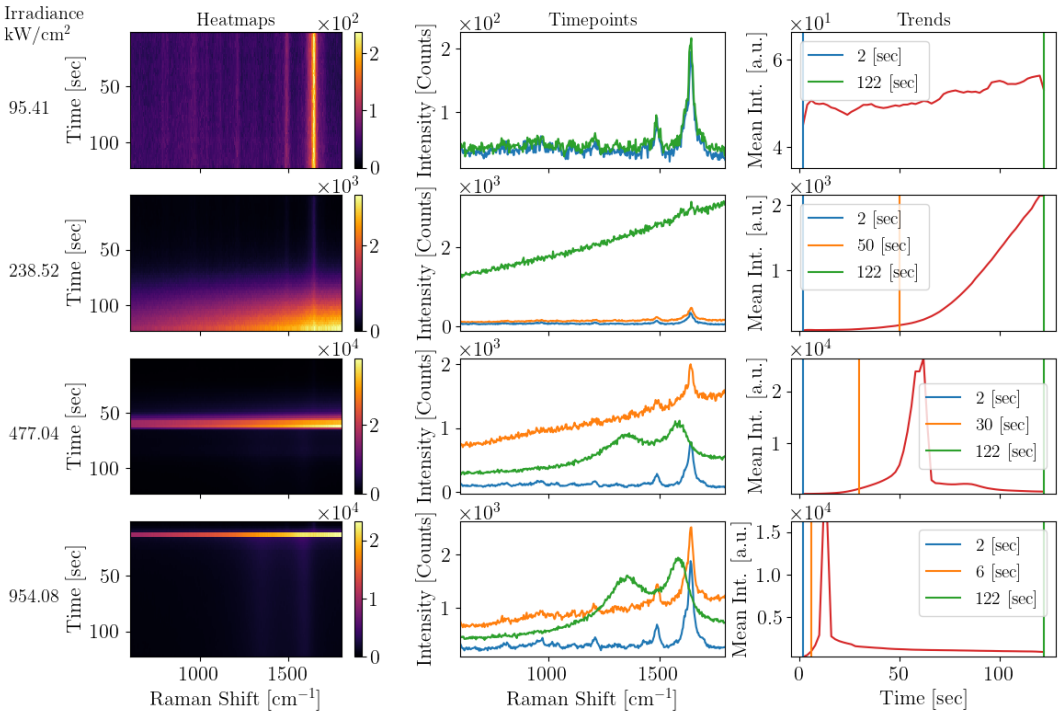

Figure 4.7: Time series of Raman spectra on Felodipine with 2 seconds exposure, on the LabRAM CRM using the 0.8 NA objective. Each row displays measurements of increasing irradiance(95.41 kW/cm^2, 238.52 kW/cm^2, 477.04 kW/cm^2, 954.08 kW/cm^2). Each column from left to right presents heat-maps of spectra for each measurement, the time points of single spectra and the mean value of each spectra as a function of time (seconds). Each vertical colour line represent the time point of the spectra from the second column graphs.

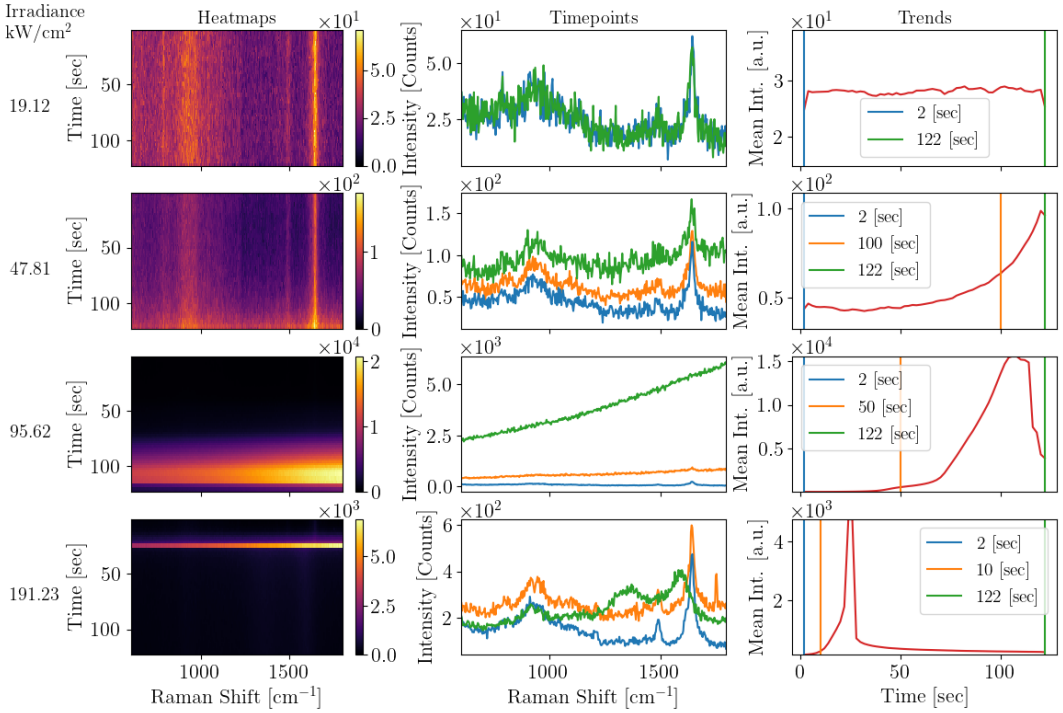

Figure 4.8: Time series of Raman spectra on felodipine with 2 seconds exposure, on the LabRAM CRM using the 0.55 NA objective. Each row displays measurements of increasing irradiance(19.12 kW/cm^2, 47.81 kW/cm^2, 95.62 kW/cm^2, 191.23 kW/cm^2). Each column from left to right shows heat-maps of spectra for each measurement, the time points of single spectra and the mean value of each spectra as a function of time (seconds). Each vertical colour line represent the time point of the spectra from the second column graphs.

4.3.3.1 AFM-CRM measurements for copovidone

Time-series of Raman spectra were acquired from copovidone spin-coated film, using the AFM-CRM system, equipped with the 1.45 NA objective. The relevant spectra are presented in Figures 4.10. According to Figure 4.10, the trends of mean spectral intensity are identical across all the different irradiance. Specifically, a negative exponential curve is presented, beginning with a rise in PL background, which gradually decreased towards the end of each measurement.

Table 4.3: Series of laser power intensities (mW) and irradiance (kW/cm^2) applied on felodipine using the 1.45, 0.8 and 0.55 NA objective lenses used on the AFM-CRM and LabRAM CRM systems. The red coloured cells indicate the time-series which present a rise in PL after prolonged laser irradiation.

Instruments	**Objectives** (NA)	**Power intensity** (mW)	**Irradiance** (kW/cm^2)
AFM-CRM	100× Nikon (1.45)	0.03	19.91
		0.3	199.08
		0.75	497.7
		1.5	995.4
		3	1990.8
Horiba - LabRAM	100× Olympus (0.8)	2.5	95.41
		6.25	238.52
		12.5	477.04
		25	954.08
	50× Carl Zeiss (0.55)	2.5	19.12
		6.25	47.81
		12.5	95.62
		25	191.23

4.3.3.2 Horiba - LabRAM measurements for copovidone

Spectra were also obtained with the LabRAM instrument using the 0.8 NA and 0.55 NA objective. Their respective data are shown in Figures 4.11 as well as C.2, in Appendix C. In Figure 4.11, we observe similar gradual decline in trend, in respect to their mean intensity. The characteristic trend is observed in all the different levels of irradiance applied. Similar outcomes is also observed with the 0.55 NA objective, across all the different irradiance (Figure C.2).

In comparison to the APIs, the polymeric material responds differently to laser exposure. At the start of every measurement, a high background PL is prevalent and over the course of time it exponentially decays until the spectra stabilise and the Raman bands of copovidone become visible. This drop is an indication of the sample being photo quenched rather than photodamaged after laser exposure prolongation (Table 4.4). This effect is present in all the different objectives and intensities applied.

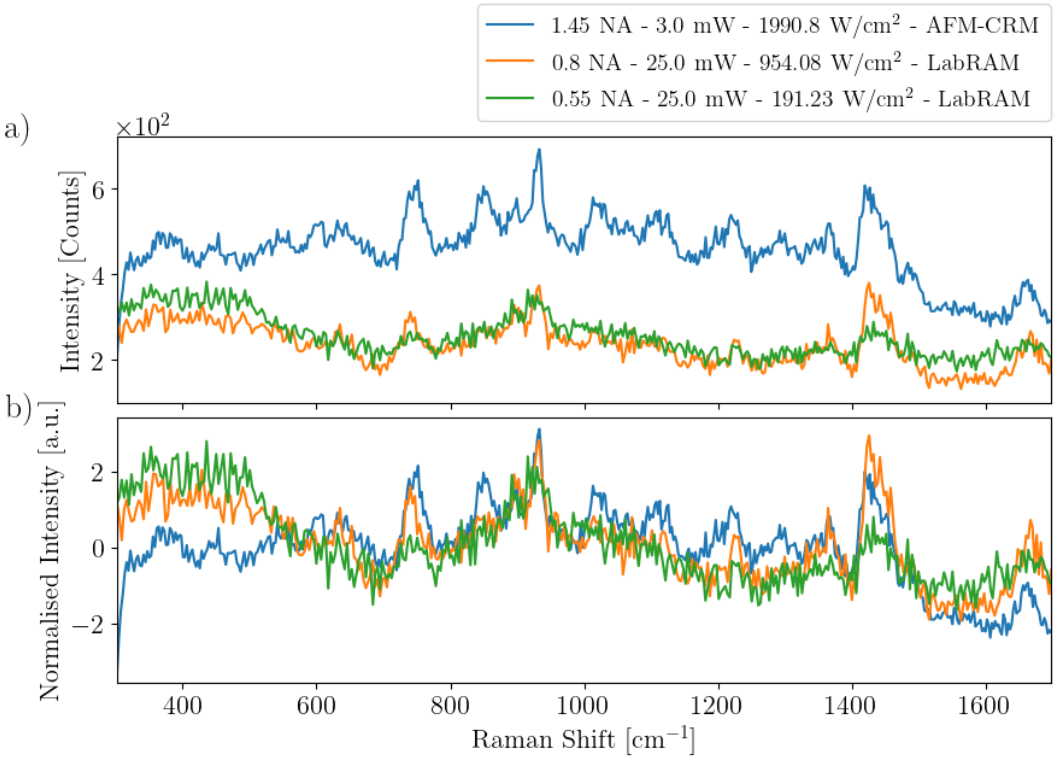

Figure 4.9: Reference Raman spectra of pure copovidone. Blue line spectrum was acquired with the 1.45 NA objective under the AFM-CRM instrument, with 2 seconds of laser exposure and 3 mW of laser power. Green and orange lines spectra were acquired under the LabRAM instrument with the 0.8 NA and 0.55 NA objectives, respectively. These spectra were recorded with 2 seconds of laser exposure at 25 mW of laser power. (a) Shows raw spectra, whereas (b) presents mean centred and variance scaled spectra. The Raman shift of the spectra acquired range between 300-2000 cm^{-1} at the fingerprint region.

In table 4.5, we concatenated all the data from tables 4.2, 4.3, 4.4, to compare their onset of PL rise as a function of irradiance applied. Between the API's studied, felodipine is more sensitive to paracetamol under prolonged laser exposure, with the sample burning after 47.81 kW/cm^2 applied compared to 995.4kW/cm^2 seen in paracetamol, which is more stable. Copovidone on the other hand, displays no sensitivity to different laser powers and objective, as it is quite robust across the tests performed.

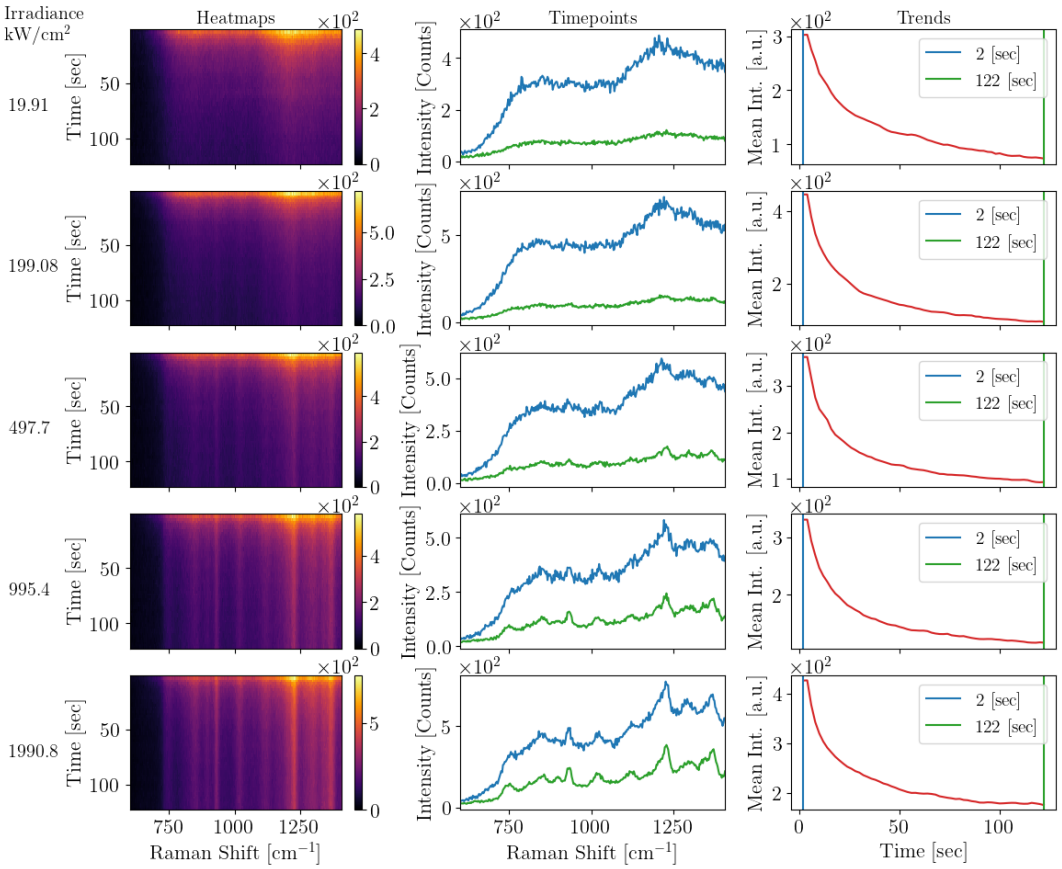

Figure 4.10: Time series of Raman spectra on Copovidone with 2 seconds exposure, on the home confocal Raman microscope using the 1.45 NA objective. Each row displays measurements of increasing irradiance(19.91 kW/cm^2, 199.08 kW/cm^2, 497.7 kW/cm^2, 995.4 kW/cm^2, 1990.8 kW/cm^2). The left column show heat-maps of spectra for each measurement. The middle column presents the time points of single spectra. The right column demonstrates the mean value of each spectra as a function of time (sec). Each vertical colour line represent the time point of the spectra from the second column graphs.

4.3.4 Sample Temperature Evaluation

To examine the sample temperature from the obtained measurements shown previously, the selection of data was based on two requirements. One being the rise in background PL during each experimental run and second being the visibility of symmetric Raman bands, both at the Stokes and anti-Stokes regions. These criteria were met with the spectra obtained from paracetamol, at 3 mW and 1.5 mW laser power, using the 1.45 NA objective as well as paracetamol at 25 mW, applying the 0.8 NA objective. These spectra are displayed

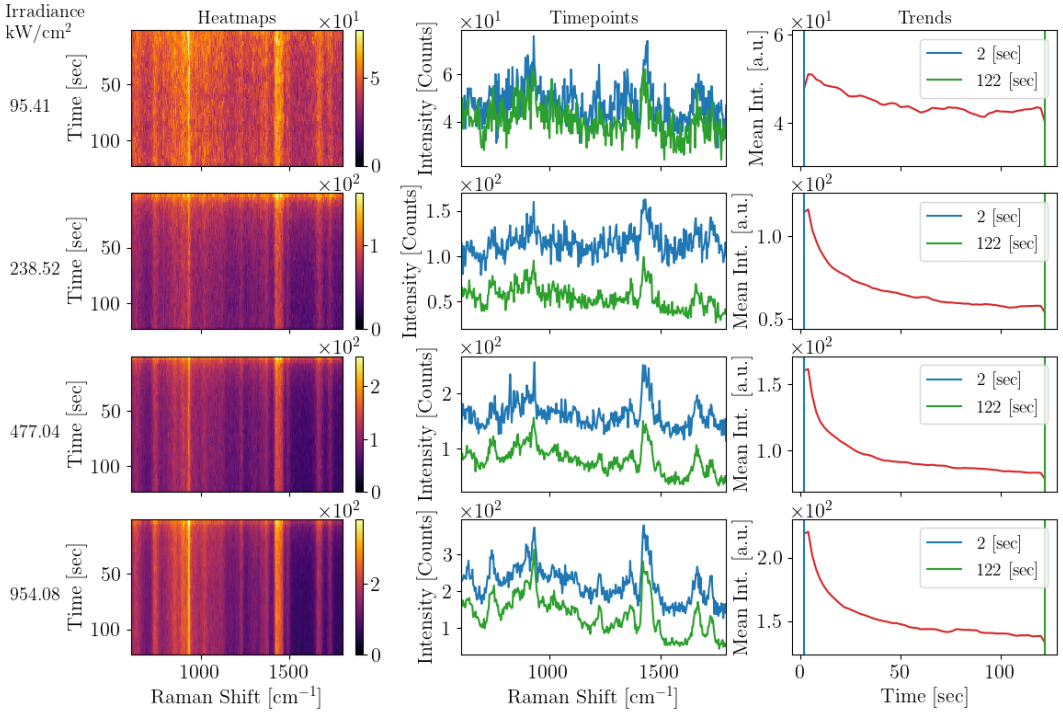

Figure 4.11: Time series of Raman spectra on Copovidone with 2 seconds exposure, on the LabRAM CRM using the 0.8 NA objective. Each row displays measurements of increasing irradiance(95.41 kW/cm^2, 238.52 kW/cm^2, 477.04 kW/cm^2, 954.08 kW/cm^2). Each column from left to right presents heat-maps of spectra for each measurement, the time points of single spectra and the mean value of each spectra as a function of time (seconds). Each vertical colour line represent the time point of the spectra from the second column graphs.

in Figure 4.12, with the annotated regions, corresponding to the Raman bands of interest. From the Figure presented, all the spectra are in agreement and almost identical intensities, specifically at the stokes fingerprint region above 750 cm^{-1}. For the spectrum recorded with the 0.8 NA objective (green), the symmetric bands at 89.4 cm^{-1} and 214.9 cm^{-1} have been analysed. Likewise, for the spectrum acquired with the 1.45 NA objective (blue and orange), the symmetric bands at 797 cm^1 and 857.9 cm^1 have been examined.

4.3.4.1 Sample Thermometry with AFM-CRM Raman instrument

From the spectra shown in Figure 4.3, thermometry measurements on paracetamol data were performed, with 3 mW laser exposure (1990.8 kW/cm^2) on

Table 4.4: Series of laser power intensities (mW) and irradiance (kW/cm^2) applied on copovidone using the 1.45, 0.8 and 0.55 NA objective lenses used on the AFM-CRM and LabRAM CRM systems.

Instruments	**Objectives** (NA)	**Power intensity** (mW)	**Irradiance** (kW/cm^2)
AFM-CRM	100× Nikon (1.45)	0.03	19.91
		0.3	199.08
		0.75	497.7
		1.5	995.4
		3	1990.8
Horiba - LabRAM	100× Olympus (0.8)	2.5	95.41
		6.25	238.52
		12.5	477.04
		25	954.08
	50× Carl Zeiss (0.55)	2.5	19.12
		6.25	47.81
		12.5	95.62
		25	191.23

Table 4.5: Series of laser power intensities (mW) and irradiance (kW/cm^2) applied on copovidone using the 1.45, 0.8 and 0.55 NA objective lenses used on the AFM-CRM and LabRAM CRM systems.

Sample	**Paracetamol**			**Felodipine**			**Copovidone**		
Numerical Aperture	1.45	0.8	0.55	1.45	0.8	0.55	1.45	0.8	0.55
Irradiance (kW/cm^2)	19.91	-	-	19.91	-	-	19.91	-	-
	199.08	95.41	19.12	199.08	95.41	19.12	199.08	95.41	19.12
	497.7	238.52	47.81	497.7	238.52	47.81	497.7	238.52	47.81
	995.4	477.04	95.62	995.4	477.04	95.62	995.4	477.04	95.62
	1990.8	954.08	191.23	1990.8	954.08	191.23	1990.8	954.08	191.23

the 797 cm^{-1} bands in both Stokes and Anti-Stokes regions. The results are shown in Figure 4.13. Figure 4.13 a) displays the two Raman shift regions, where combined Lorentzian and 1st order polynomial curves were fitted upon the bands at time points 2 seconds, 100 seconds and 122 seconds. For each time point the temperature (°C) was calculated based on Equation 4.3 and plotted as cyan coloured dots as presented in Figure 4.13 b). Figure 4.13 c) demonstrates the changes of the band waist, at the Stokes region, across the different time points of the spectra acquired (purple points). Figure 4.13 d) presents the shift

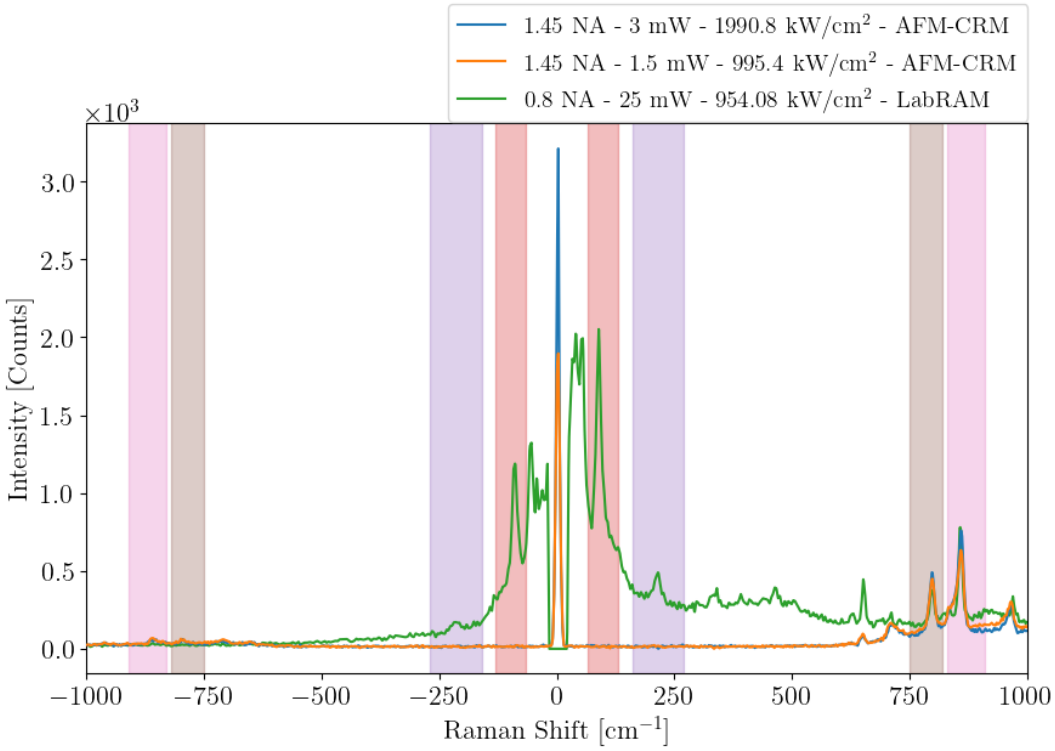

Figure 4.12: Reference Raman spectra of paracetamol sample obtained with the 1.45 NA (blue and orange line) and 0.8 NA (green line) objectives. All spectra were recorded after 2 seconds of exposure. The blue Raman spectrum was acquired under 3 mW of laser power, the orange under 1.5 mW of and the orange under 25 mW of laser power. The Raman shift displayed, covers both Stokes and Anti-Stokes regions between -1000 to 1000 cm^{-1}. The highlighted coloured areas, cover pairs of symmetric bands used to perform thermometric analysis. These are the 89.4 cm^{-1} (red) and 214.9 cm^{-1} (purple), 797 cm^{1} brown and 857.9 cm^{1} pink.

in band position of the Stokes region, as a function of time (brown dots). In Figures (b-d), the red line indicates the mean spectral intensity as a function of time, whereas the coloured vertical lines (blue, yellow, green) demonstrate the different time-points, where the spectra in Figure 4.13 a) are shown.

According to figure 4.13 b) both mean intensity and temperature display similar trends across time. At the early seconds of the measurement both graphs remained stable across time, until PL in the spectra occurred (right hand side of orange line). In addition, the average measured temperature over the first 40 seconds of laser irradiation was 24 ± 152.8 °C. With the rise in PL there was

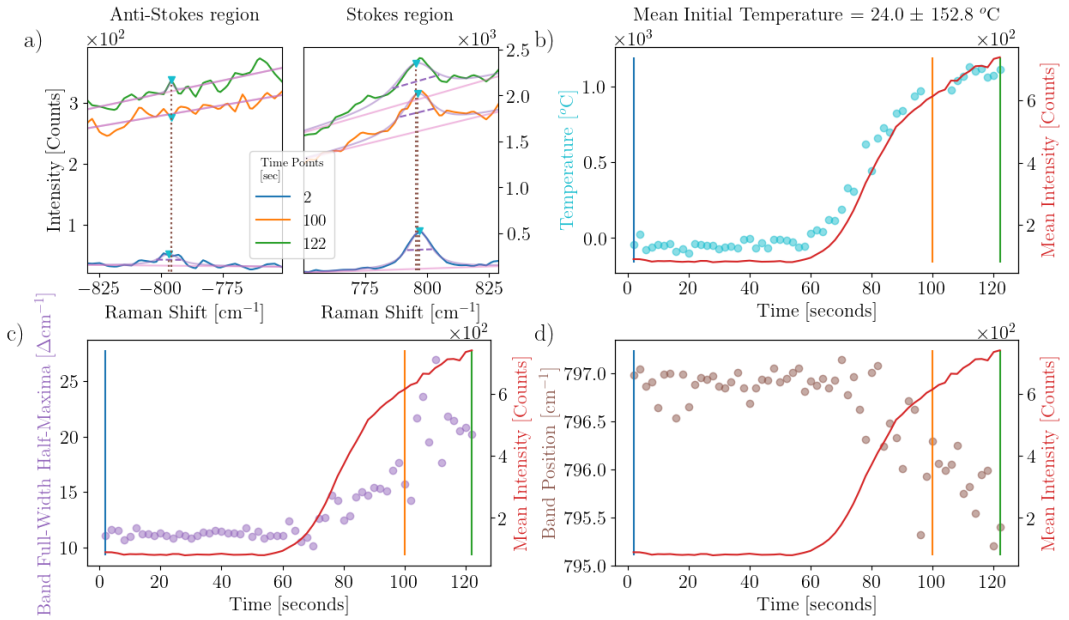

Figure 4.13: Thermometry of paracetamol, with time-series spectra acquired on the custom-made CRM instrument using the 1.45 NA objective (as shown in Figure 4.3), irradiated with 3 mW laser power (1990.8 kW/cm^2). Symmetric bands at 797 cm^{-1}, in both Stokes and anti-Stokes region were selected (a) and analysed. b), c) and d) display the mean value of spectra (red line) alongside the calculated temperature (cyan dots) from the I_{AS}/I_S, the change in FWHM (purple dots) as well as the shift of the Raman bands (brown dots), respectively, as a function of time. Orange vertical line indicates the time threshold, where PL background is first observed.

an rise in both temperature and mean spectral intensity, as the temperature increased beyond 1000 °C. Moreover in Figure 4.13 c), the line-width of the band remained constant prior to sample PL, whereafter, there was an inconsistent distorted rise in the values ($12 < \Delta\text{cm}^{-1}$). Similar effects were demonstrated in the literature [300], where increasing temperature showed an increase in band line-width. In Figure 4.13 d), the position of the band remained constant, until PL occurred where the Raman band shifts to lower wavelengths ($\approx$ 1-1.5 Δcm^{-1}). This event was proven in literature [300] to be an indication of temperature increase. Overall, these outcomes demonstrated temperature increase on the paracetamol sample after prolonged irradiation. Although, the mean initial temperature indicated room temperature recording, which agreed with the experimental conditions available at the time of measurements, the stan-

dard deviation errors were large. This could potentially be due to the small acquisition times of the spectra recorded [291]. Same procedure was repeated for the band 857.9 cm^{-1} at the same laser power, as shown in Figure C.4 in Appendix C, demonstrating similar outcomes to Figure 4.13. For both symmetric bands 797 cm^{-1} and 857.9 cm^{-1}, their fitted intensity, estimated standard deviation (ESD) errors, R^2 and root mean square errors are displayed in Figures C.3 and C.5, respectively, under Appendix C.

From the acquired spectra displayed in Figure 4.3, thermometry measurements on paracetamol data were performed, with 1.5 mW laser exposure (995.4 kW/cm^2) on the 797 cm^{-1} bands in both Stokes and Anti-Stokes regions. The results are shown in Figure 4.14. Figure 4.14 a) displays the two Raman shift regions, where combined Lorentzian and 1^{st} order polynomial curves were fitted on the Raman bands recorded at 2, 62 and 122 seconds. For each time point the temperature (°C) was calculated based on Equation 4.3 and plotted as cyan coloured dots as presented in Figure 4.14 b). Figure 4.14 c) demonstrates the changes of the band waist, at the Stokes region, across the different time points of the spectra acquired (purple points). Figure 4.14 d) presents the shift in band position of the Stokes region, as a function of time (brown dots). In Figures (b-d), the red line indicates the mean spectral intensity as a function of time, whereas the coloured vertical lines (blue, yellow, green) demonstrate the different time-points, where the spectra in Figure 4.14 a) are shown.

Based on Figure 4.14 b) both mean intensity and temperature display similar trends across time, as similarly shown in previous Figure 4.14. At the early seconds of the measurement both graphs remained stable across time, until PL in the spectra occurred (right hand side of orange line). In addition, the average measured temperature over the first 40 seconds of laser irradiation was 16.8 ± 27.8 °C. The mean initial temperature indicated room temperature recording, which agreed with the experimental conditions available at the time

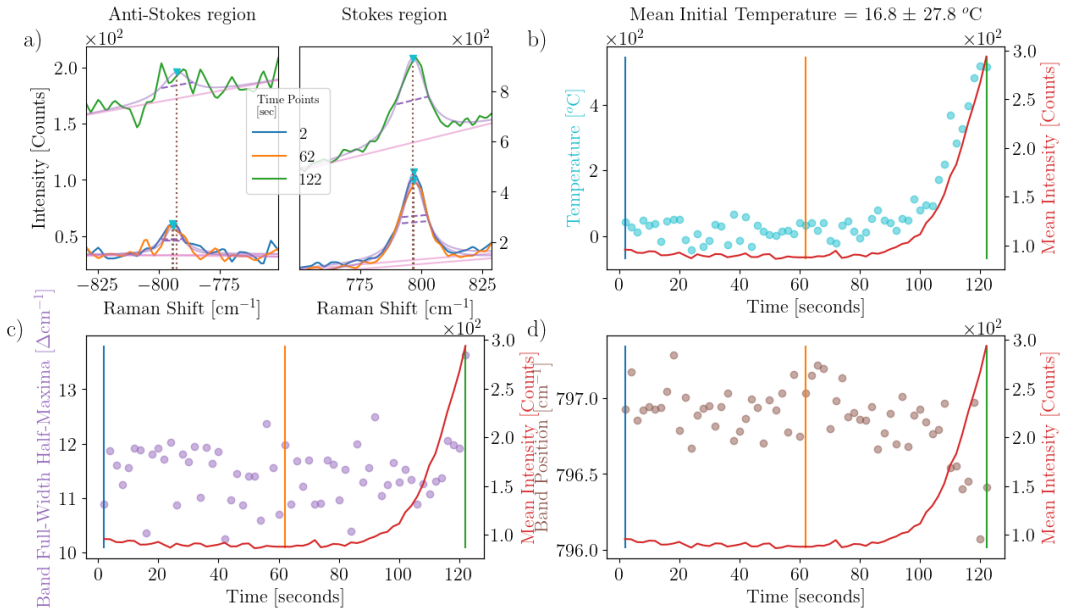

Figure 4.14: Thermometry of paracetamol, with time-series spectra acquired on the custom-made CRM instrument using the 1.45 NA objective (as shown in Figure 4.3), irradiated with 1.5 mW laser power (995.4 kW/cm^2). Symmetric bands at 797 cm^{-1}, in both Stokes and anti-Stokes region were selected (a) and analysed. b), c) and d) display the mean value of spectra (red line) alongside the calculated temperature (cyan dots) from the I_{AS}/I_S, the change in FWHM (purple dots) as well as the shift of the Raman bands (brown dots), respectively, as a function of time. Orange vertical line indicates the time threshold, where PL background is first observed.

of measurements. With the rise in PL there was an increase in both temperature and mean spectral intensity 4.14, as the temperature reached beyond 400 °C. Moreover in Figure 4.14 c), the line-width of the band remained distorted prior to sample PL, with a slight trend upwards (11 $<$ Δcm^{-1}). In Figure 4.14 d), the band position remained constant, until PL occurs where the Raman band shifts to lower wavelengths ($\approx$ 1 Δcm^{-1}). Same procedure was repeated for the band 857.9 cm^{-1} at the same laser power, as shown in Figure C.7 in Appendix C, demonstrating similar outcomes to Figure 4.14. For both symmetric bands 797 cm^{-1} and 857.9 cm^{-1}, their fitted intensity, estimated standard deviation (ESD) errors, R^2 and root mean square errors are displayed in Figures C.6 and C.8, respectively, under Appendix C.

4.3.4.2 Sample Thermometry with LabRAM Raman instrument

From the acquired spectra displayed in Figure 4.4, thermometry measurements on paracetamol data were performed, with 25 mW laser irradiation (954.08 kW/cm^2) on the 214.9 cm^{-1} bands in both Stokes and Anti-Stokes regions. The results are shown in Figure 4.15. Figure 4.15 a) displays the two Raman shift regions, where combined Lorentzian and 1st order polynomial curves were fitted on the Raman bands recorded at 2, 104 and 122 seconds. For each time point the temperature (°C) was calculated based on Equation 4.3 and plotted as cyan coloured dots as presented in Figure 4.15 b). Figure 4.15 c) demonstrates the changes of the band waist, at the Stokes region, across the different time points of the spectra acquired (purple points). Figure 4.15 d) presents the shift in band position of the Stokes region, as a function of time (brown dots). In Figures (b-d), the red line indicates the mean spectral intensity as a function of time, whereas the coloured vertical lines (blue, yellow, green) demonstrate the different time-points, where the spectra in Figure 4.15 a) are shown.

Based on Figure 4.15 b) both mean intensity and temperature display similar trends across time. At the early seconds of the measurement both graphs remained stable across time, until PL in the spectra occurred (right hand side of orange line). In addition, the average measured temperature over the first 40 seconds of laser irradiation was 195.5 ± 52.2°C. This result does not resemble the ambient conditions where the experiments were undertaken. With the rise in PL there was an increase in both temperature and mean spectral intensity 4.15, as the temperature reached up to 800 °C. Moreover, Figures 4.15 (c-d) presenting the line-width and position of the band display no changes as a function of time, other than fluctuations. Same procedure were repeated for the band 89.4 cm^{-1} at the same laser power, as shown in Figure C.10 in Appendix C, demonstrating similar outcomes to Figure 4.14. For both symmetric bands

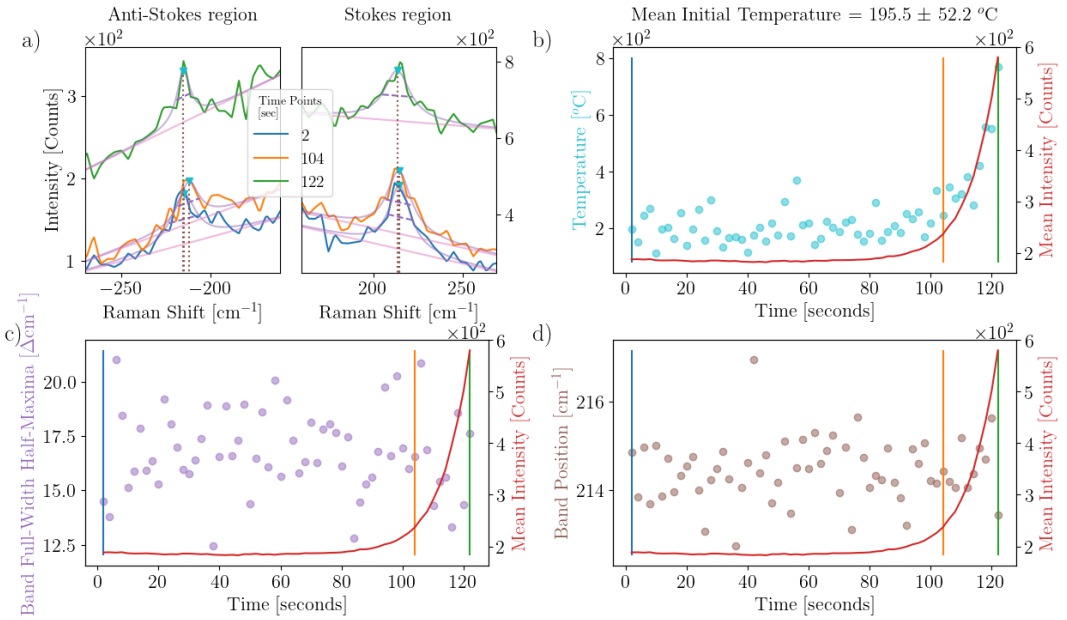

Figure 4.15: Thermometry of paracetamol, with time-series spectra acquired on the LabRAM CRM instrument using the 0.8 NA objective (as shown in Figure 4.4), irradiated with 25 mW laser power (954.08 kW/cm^2). Symmetric bands at 214.9 cm^{-1}, in both Stokes and anti-Stokes region were selected (a) and analysed. b), c) and d) display the mean value of spectra (red line) alongside the calculated temperature (cyan dots) from the I_{AS}/I_S, the change in FWHM (purple dots) as well as the shift of the Raman bands (brown), respectively, as a function of time. Orange vertical line indicates the time threshold, where PL background is first observed.

214.9 cm^{-1} and 89.4 cm^{-1}, their fitted intensity, estimated standard deviation (ESD) errors, R^2 and root mean square errors are displayed in Figures C.9 and C.11, respectively, under Appendix C.

4.4 Conclusion

In this set of experiments, we obtained spectra from crystalline spin-coated paracetamol, felodipine and polymeric copovidone samples, wherein we evaluated the sensitivity of each sample over prolonged laser exposures, by using different laser irradiances and objective lenses. Both felodipine and paracetamol, were prone to alteration in their spectra, with raise in PL over the course

of time, under the two Raman systems. In the data presented in this chapter we showed that the irradiance threshold for paracetamol photodegradation is approximately 954 kW/cm^2, whereas for felodipine it is 47.81 kW/cm^2, under different points in time. In contrast to crystalline drugs, copovidone shown an opposite response to laser exposure. At the highest laser power output and across all objectives, the sample did not show any sign of spectral change towards the finish of every measurement. Instead, most of the PL produced was prevalent at the start of each set, with an intensity decay later on.

Alongside the spectral evaluations, temperature measurements have also been performed on spin-coated paracetamol sample, where PL in the background spectra occurred. Thermometry calculations have been based on the obtained I_{AS}/I_S ratio, as well as the Stokes line-width and shift. Across most measurements at the point of PL, there was an increase of the sample temperature. By comparing the I_{AS}/I_S ratio or the band dimensions with the mean spectral trend across time, the ratio displays better correlation compared to the FWHM and shift values. This confirms, with the rise in PL, rise in sample temperature also takes place. It is also worth mentioning that the melting point of paracetamol lies between 169-170°C [301]. By closer inspection of Figures 4.13 b), 4.14 b) and 4.15 b), the recorded temperatures surpassed the stated melting point. For future studies, it is important to acquire spectra with higher acquisition times, in order to obtain more stable temperature measurements but also keeping a note of the sample onset of photodegradation.

Nevertheless, understanding the sensitivity of the pharmaceutical materials and evaluating their laser sensitivity threshold, is a valuable asset to examine and rectify the quality of the spectra acquired under TERS experimental conditions, in current and future studies. This information may also prove useful under a CRM setup, using 100× magnification objectives.

Chapter 5

Sample integrity and signal enhancement evaluation based on focal point-to-probe distance

5.1 Introduction

In Chapter 3 , we identified spectral changes of spin-coated ASDs under approached TERS probe and prolonged laser exposure, with the probe retracted. Further in Chapter 4, we tested two different CRM systems to detect any changes in the spectra, associated to the sample integrity. Based on the results obtained, a gradual rise in background Photoluminescence (PL) becomes prevalent for the pure API samples. Depending on the sample, the rise in background occurs at specific irradiance levels and certain time points of continuous exposure to the irradiation. The opposite is observed for the polymeric copovidone, by remaining stable across all experiments over time. Thermometry measurements were also performed on paracetamol, with rise in temperature being associated with time of prolonged laser irradiation.

By recognising sample degradation under a CRM instrument, it is possible to further discern spectral changed occurring under a TERS system. In particular, a distinguishable broadband PL background can be generated from an irradiated metallic substrate, not related to sample burning. Enhanced plasmon-dependent PL noise can rise from the rough metal surface [302, 303], as similarly shown in Figure D.4 under Appendix D. Regarding, sample-derived fluorescence it is expected to quench through the electronic coupling of the metal probe, therefore not considered in the observed broad background signal [304].

Another aspect that requires careful consideration, when obtaining TERS-based spectra is the degree of the signal enhancement recorded. In these types of experiments, the enhancement factor in the spectra could be subject to instabilities in the tip-to-sample distance [281]. One plausible cause of enhancement drop is the lateral thermal drift across the XY-axis of a acquired TERS map. Under ambient conditions, the probe of an AFM equipment can drift in the range of 0.1-0.01 nm/second, which may ultimately rise between 36-360 nm in total, during an hour-long experiment [269]. A second cause to the tip-sample separation can occur on the axial direction (Z-axis). According to the literature, when the tip-sample distance rise above 20 nm, no near-field TERS contribution can be observed. Whereas shortening this distance, the Raman signal could rise exponentially [305, 306].

Therefore, studying spectra across the lateral and axial directions, from the approached TERS probe position, deemed valuable to detect any inconsistencies in probe-to-sample distance. This investigation would allow the identification of any potential enhancement in the Raman signal at any probe-to-focal spot position, onset of sample photodegradation as well as spurious Raman spectra that could occur during a TERS measurement [168, 281]. This approach was achieved by raster-scanning the surface of a pharmaceutical material through

small steps-sizes, as the functionalised tip came in closer proximity with the focal laser spot. Aim of this chapter was to examine any spectral changes, such as signal enhancement and/or sample degradation, on pure pharmaceutical materials, as a function to apex-to-focal spot distances across the XYZ directions. In Chapter 4 pure samples were tested in order to assess their integrity. Adding to the prior knowledge, pure pharmaceutical components were also used in this study, under engaged TERS probe. Each sample was examined separately, in the form of thin molten-quenched films. These types of films were produced to avoid any potential entrapment of solvents with the spin-casting method, executed in Chapters 3,4.

5.2 Material and Methods

Paracetamol, nicotinamide, Polyvinyl Alcohol (PVA) were purchased from Sigma Aldrich, (St. Louis, MO). Felodipine was kindly contributed by AstraZeneca (Macclesfield UK).

For the preparation of thin sample films, each material in powder form was weighted at 100 µg and pressed between two round 24 mm diameter microscope coverslips (# 1.5). These samples were transferred into a hot-stage (THMS600; Linkam; Tadworth; UK) and heated to 10 °C above their respective melting point. Afterwards, the molten films were cooled to room temperature at a nominal rate of 30 °C per minute. To ensure the samples were completely molten, brightfield images were acquired, as displayed in Figures D.1, D.2 and D.3 under Appendix D (PVA images not presented in this study). Before initiating a TERS measurement for each sample, the sandwiched cover-slips were separated and the exposed clean films from the deposited face of each glass were tested under the instrument, facing upwards towards the apex.

The same TERS instrument discussed in Chapter 3 (National Physical Laboratory) was used. The exciting laser power ranged between 0.097 and 0.782 mW. Spectra were acquired between 400 cm^{-1} and 3600 cm^{-1}, unless otherwise stated.

5.2.1 XY-Coordinate experimental setup

For evaluating the acquired spectra on the basis of focal point-probe distance evaluation, probe-laser co-alignments were performed. These entail lateral (XY) raster-scans of the TERS probe, by translating the laser focal point. With the probe in static position approached on the sample surface, the objective lens moved across the XY-Axes, to detect the probe hotspot location. This experimental procedure is demonstrated in Figure 5.1. The acquisition times ranged between 3 to 5 seconds with applied laser power of 0.246 mW. The size of these raster-scans acquired were 1 x 1 µm, unless otherwise stated. Each run was performed at a different location on the sample surface.

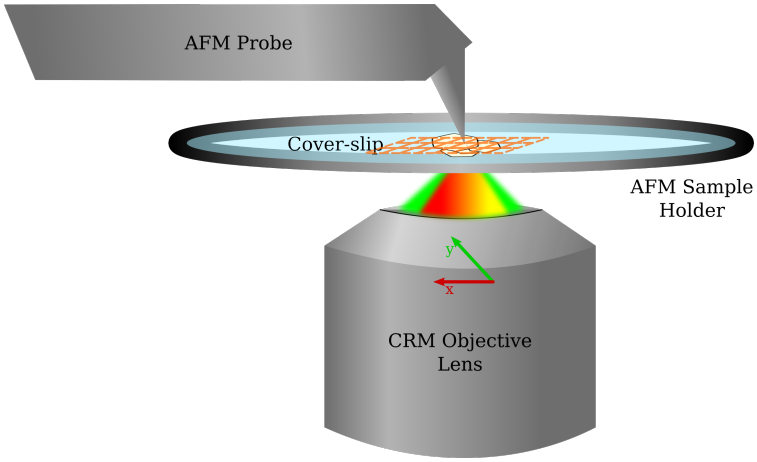

Figure 5.1: Schematic diagram of the TERS setup, in bottom-illumination mode. While the probe and the sample remain in static position, the objective lens performs a raster-scan across the XY-axes.

From these measurements the signal Enhancement Contrast (EC) was also calculated. EC provides an indication of the probe's likely performance to enhance

the Raman signal during a TERS experiment, by comparing the intensity of a Raman band at the hotspot and away from it [223]. By selecting the strongest Raman band for each material, the following formula in Equation 5.1 was applied:

$$EC = \frac{I_{\text{Hotspot}}}{I_{\text{Confocal}}} - 1 \tag{5.1}$$

where, $I_{Hotspot}$ corresponds to the intensity of Raman band at the hotspot region, where the probe is within the laser spot and $I_{Confocal}$, which intensity is acquired away from the hotspot. A contrast value ≥ 1 indicates sufficient sensitivity for TERS-based signal enhancement [195].

5.2.2 Z-Coordinate experimental setup

The acquisition of multiple spectra along the Z-axis with nano-scaled step-sizes were also obtained. To perform this task under the AFM-TERS instrument, either the probe or objective required to translate the Z-axis, with the sample stage being held in fixed position throughout the whole measurement. Choosing the first scenario, where the microscope objective stays in focus with the sample surface and the probe approaches it incrementally, there was concern of inconsistency to the probe translation. Specifically, as the distance between the probe and focal point shortens, van der Waals or electrostatic forces from the sample surface could be generated by attracting or repulsing the Ag nanoparticles of the probe's apex. This further causes the probe to vibrate, producing fluctuations and uncertainties to the recorded distance on the AFM instrument [120]. Alternatively, by approaching and stabilizing the probe on the sample, it was feasible to perform a objective lens raster-scan across the XZ axis with the current instrument. This is due to the objective being fitted on a XYZ

translational piezo stage (AIST-NT, Novato, USA).

Another aspect which requires careful consideration is the size of the laser spot along the Z-axis, also known as axial or depth resolution. Having an estimation of the spot dimension, this allowed the determination of the spatial limits of these measurements capturing both confocal and tip-enhanced Raman spectra. An estimation of the axial resolution was determined from *Abbe's* following equation (1.2) [77], Based on the known parameters of the instrumental setup used in our experiments, according to equation 1.2 the resulting depth resolution amounted to ≈ 500 nm. To cover the whole range of spectra acquired across the sample height, Z-axis raster-scans were limited to 1 µm. This experimental procedure is demonstrated in Figure 5.2. After co-aligning the probe with the

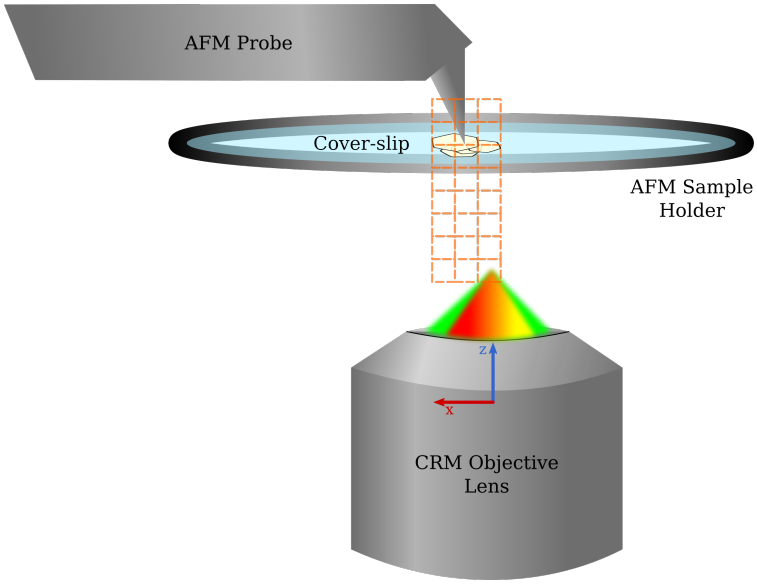

Figure 5.2: Schematic diagram of the TERS setup, in bottom-illumination mode. While the probe and the sample remain in static position, the objective lens performs a raster-scan across the XZ-axes.

laser on the XY-Axis, the probe was first approached and held static on the sample surface. Afterwards, the microscope lens was shifted approximately 0.7 µm focusing below the surface and apex Z-Axis position. This was performed to obtain all the spectra below, on and above the probe apex. The XZ raster-scans were performed at 0.246 mW laser with 5 seconds spectral acquisition.

The step-sizes selected were 10 and 20 nm at both directions. The regions of the spectra displayed were cropped at the fingerprint region (252-1750 cm^{-1}) and the $-CH$ stretch region (2800-3200 cm^{-1}). In order to ensure scanning region was not affected by photodegradation, the sample was shifted to a different location prior recording. EC values from the Raman bands of interest were also recorded. From the aforementioned equation 5.1, the intensity of the confocal Raman band ($I_{Confocal}$), was selected as the lower-most position of the Z-Axis scan. This is where the objective lens is out of focus with the apex of the TERS probe. For every other position the intensity of the Raman band of interest was picked as the $I_{Hotspot}$ and the EC was measured for each of the recorded positions. Reason behind this approach is to evaluate the change in EC value as a function of distance across the Z-Axis direction. All numerical data analysis routines and raw data are included in the supplementary material for information and reference.

5.3 Results and Discussion

5.3.1 Paracetamol measurements

Reference Raman spectrum from pure paracetamol film was obtained, with the probe retracted from the film surface. The result is displayed in Figure 5.3. According to the Figure four Raman bands are prevalent in the fingerprint region, namely at 864 cm^{-1}, 1168.5 cm^{-1}, 1323.9 cm^{-1} and 1628 cm^{-1}. From the intensity of these bands, the pure paracetamol studied was in crystalline form III, according to the literature [299] as shown in Figure E.1 under Appendix E.

Hotspot and Z-scan Raman maps were obtained from pure paracetamol film, while the TERS probe was approached on the sample surface and the objec-

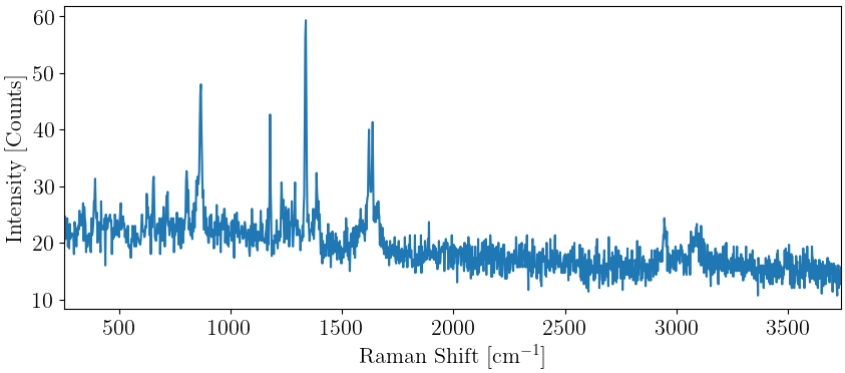

Figure 5.3: Reference Raman spectrum of pure paracetamol sample. Spectrum was acquired under 5 seconds of laser exposure, with 0.246 mW of laser power.

tive was raster-scanning across the XY and Z, respectively. These results are displayed in Figures 5.4 and 5.5.

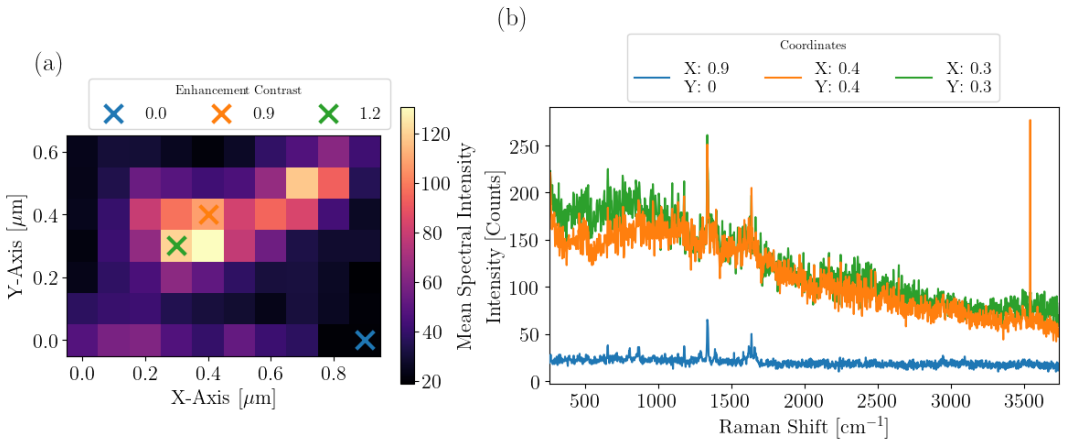

Figure 5.4: a) Hotspot Raman map of paracetamol film, acquired at 0.246 mW of laser power at 5 seconds acquisition time, with dimensions 0.9 x 0.6 µm and 100 nm pixel-size. b) Respective spectra (blue, orange, green) of the annotated pixels on the hotspot map (a).

In Figure 5.4 a), each pixel on the hotspot map indicates the mean intensity of the spectrum used to generate the hotspot Raman map. The coloured annotated crosses on this map correspond to the spectra of similar colour shown in Figure 5.4 b). Within the region of 0.9 x 0.6 µm^2 a rise in the mean spectral intensity was detected at the centre of this image (Figure 5.4 a)). By comparing the spectra within and away from the hotspot (Figure 5.4 b)), we observed a rise in the PL background around the central region of this map. The gen-

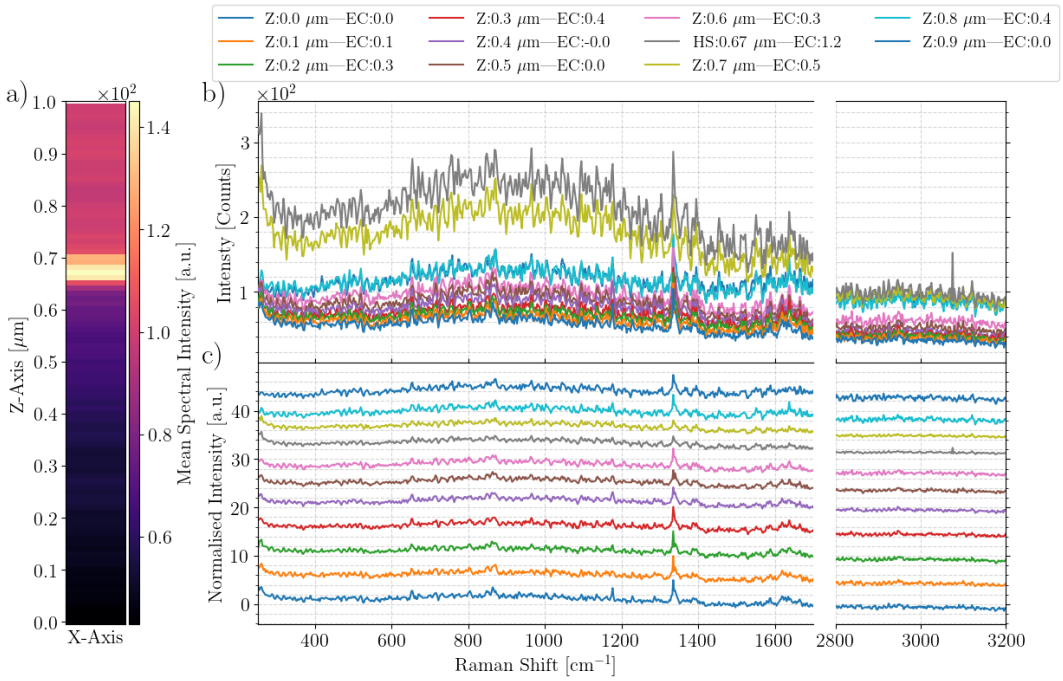

Figure 5.5: Z-scan measurement of paracetamol film was obtained at 10 nm step-sizes. From the raw data acquired, with dimensions 1 x 0.03 µm across the ZX axes, the spectra across the X-axis were averaged. a) displays a heatmap of these spectra across the Z-axis. b) and c) project overlapped and cascaded spectra across the Z-axis, respectively, at 100 nm intervals including the position at which the Hotspot becomes detected. Each spectrum shown in c) was mean centred and variance scaled. For each spectrum the *EC* from the band of interest (1323.9 cm^{-1}) was also measured against the the spectrum at Z=0.

erated luminescent background is characteristic of the PL obtained from the Ag-coated probes [269]. Specifically, a gradually declining slope in the PL signal was observed as the wavelength increases. Furthermore, the paracetamol band at 1323.9 cm^{-1} remains clearly visible across all spectra displayed. Throughout the entire acquisition process, no sample degradation was observed, due to visibility of the paracetamol Raman bands across all pixels. To assess the performance of the TERS probe we evaluated the *EC*, based on equation 5.1. The *EC* values were measured from the Raman band 1323.9 cm^{-1} for the spectra at X:0.4 - Y:0.4 (orange line) and X:0.3 - Y:0.3 (green line) coordinates within the hotspot region, against the spectrum at X:0.9 - Y:0, which is away from it. At the hotspot the *EC* rose up to 1.2, indicating good TERS performance generated from the probe.

After acquiring the hotspot image, a Z-Axis raster-scan was performed and displayed in Figure 5.5. On Figure 5.5 a), the spectra were averaged across the X-Axis and further plotted as a heatmap towards the Z direction in a 1-Dimensional line. The length of this map across the Z-Axis reached up to 1 µm. In the second subplot of this Figure (5.5 b)) the overlapped spectra from subplot a) are presented. On Figure 5.5 c), the same spectra were normalised and set in cascaded order from 0 to 0.9 µm from the lowest to the uppermost spectrum. The accompanied labels indicate the position of each spectrum acquired on the Z-scan, alongside with the calculated *EC* for Z $>$ 0.1 µm against Z = 0.

According to Figure 5.5 a), as the objective comes in focus with the probe and the sample surface, a sharp intensity rise is observed at 0.67 µm, originating from the hotspot of the probe. At this position we observe in Figure 5.5 b) a rise at the PL background signal. The Raman band of 1323.9 cm^{-1} band remains also visible across the different locations in the map. The *EC* calculated at the hotspot location reached to 1.2 (Z: 0.67 µm, grey line), which is in agreement with the hotspot map presented in Figure 5.4.

Based on the results observed in Figures 5.4 and 5.5, paracetamol film remained stable throughout both processes, at 0.246 mW of laser exposure. This finding confirms the sample stability tested under prolonged laser exposure seen Chapter 4, Table 4.2. The *EC* acquired was also above 1.2 in both measurement, indicating strong plasmonic enhancement was generated from the TERS probe apex.

5.3.2 Felodipine measurements

Reference Raman spectrum from pure felodipine film was obtained, with the probe retracted from the film surface. The spectrum is displayed in Figure 5.6.

Based on the Figure shown, the most prevalent Raman band was located at 1644 cm^{-1} of the fingerprint region of the Raman shift. This band was picked to investigate the signal band enhancement in the TERS measurements. This spectrum also confirms with the literature as seen in Figure B.3 under Appendix B.

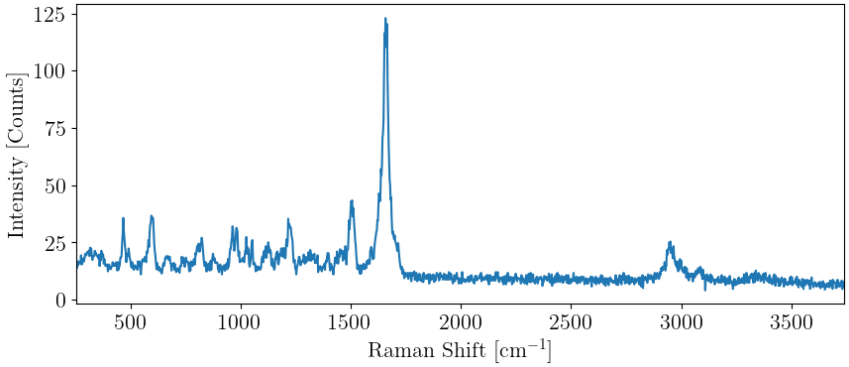

Figure 5.6: Reference Raman spectrum of pure felodipine sample. Spectrum was acquired under 5 seconds of laser exposure, with 0.246 mW of laser power.

Hotspot and Z-scan Raman maps were obtained from pure felodipine film, with the TERS probe being in engaged position on the sample surface while the objective was performing raster-scan translations across the XY and Z coordinates. These results are displayed in Figures 5.7 and 5.8, respectively.

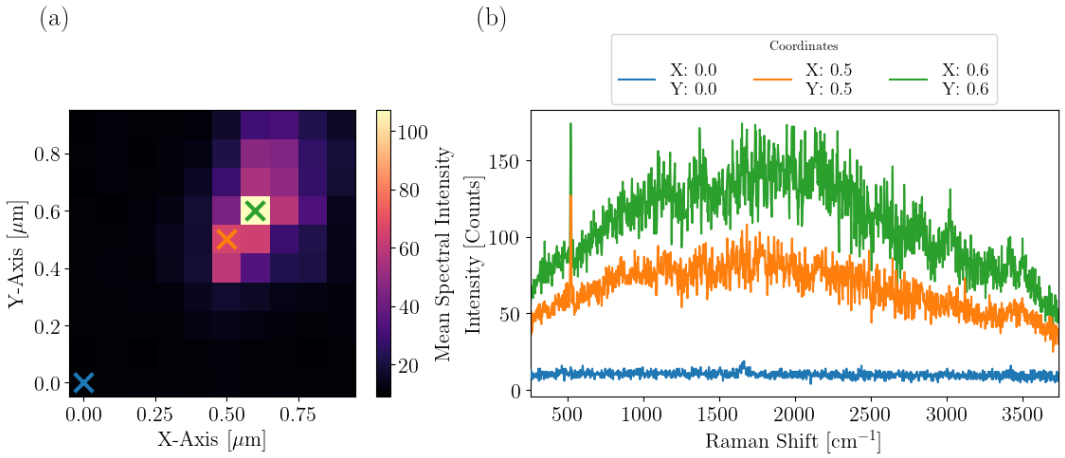

Figure 5.7: a) Hotspot Raman map of felodipine film, acquired at 0.095 mW of laser power at 3s acquisition time, with dimensions 1 x 1 µm and 100 nm pixel-size. b) Coloured spectra (blue, orange, green) representing the annotated pixels marked on the hotspot map (a).

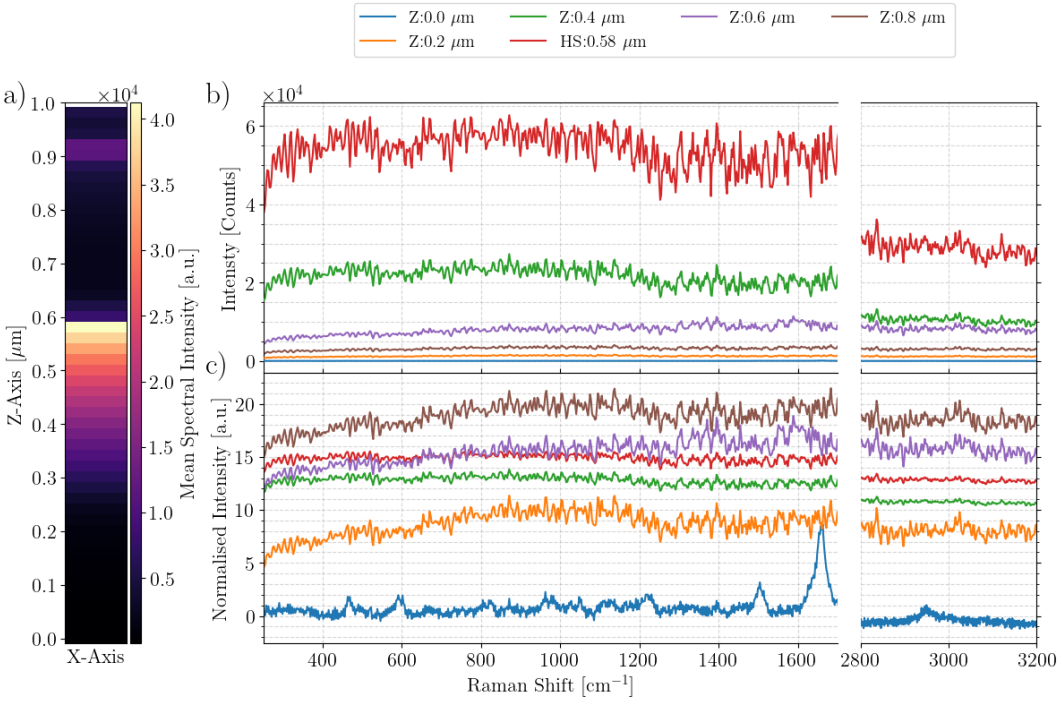

Figure 5.8: Z-scan measurement of felodipine film obtained with 0.246 mW laser power at 5 seconds exposure time and 20 nm step-size. From the raw data acquired, with dimensions 1 x 0.06 µm across the ZX axes, the spectra across the X-axis were averaged. a) displays a heatmap of these spectra across the Z-axis. b) and c) project overlapped and cascaded spectra across the Z-axis, respectively, at 200 nm intervals including the position at which the Hotspot becomes detected. Each spectrum shown in c) was mean centred and variance scaled.

In Figure 5.7 a), each pixel on the hotspot map shows the mean intensity of the spectrum used to display the hotspot Raman map. The coloured crosshairs correspond to similarly coloured spectra in Figure 5.8 b). In Figure 5.7 a), within the region of 1 x 1 µm^2, a rise in the mean spectral intensity is detected close to the centre of this image. By comparing the spectra within and away from the hotspot (Figure 5.7 b)), we observe an intense rise in the PL background around the central region of this map, alongside with an increase of silicon band of the probe located at 520.7 cm^{-1}. In comparison to Figure 5.4 of paracetamol hotspot, the PL is not gradually declining in intensity at longer wavelengths. Instead, according to the spectra obtained at the hotspot region (Figure 5.7 b) orange and green) the highest points of the PL is observed around 1500 to 2000

cm^{-1}. This has been similarly been observed in chapter 3,4, where felodipine had been rapidly undergoing photodegradation. Brightfield images of the irradiated spot are also displayed in Appendix D, Figure D.5. Due to sample degradation, the *EC* was not calculated.

After performing probe-laser co-alignment at the XY-Axis, a Z-Axis raster-scan was executed at a different location on the sample surface and displayed in Figure 5.8. On the first subplot (5.8 a)), the spectra were averaged across the X-Axis and plotted as a line image towards the Z direction, within the range of 1 µm. In the second subplot of this Figure (5.8 b)) the spectra from subplot a) were shown overlapped. On the third subplot (5.8 c)), the spectra were normalised and set in cascaded order from 0 to 0.9 µm, from the lowest to the uppermost spectrum. The labels indicate the position of each spectrum acquired on the Z-scan.

In accordance with Figure 5.8 a), as the focal point of the lens came at closer proximity to the apex location, we observed a rapid photodegradation of felodipine while the objective was still defocused from the sample. First spectra to observe this effect can be seen on Figure 5.8 c) (Z = 0.2µm), where all felodipine bands disappear and wide PL background is prevalent. This suggest that the sample was already damaged, while the objective was below and out-of-focus from the sample.

5.3.3 Nicotinamide measurements

Reference Raman spectrum of pure nicotinamide film was obtained, with the probe retracted from the film surface. The result is displayed in Figure 5.9. From the Figure presented, one strong Raman band is visible at 1047.7 cm^{-1} of the fingerprint region. This band was selected to evaluate the signal enhance-

ment in the TERS measurements. In addition this spectrum complies with published data shown in Figure D.6 under Appendix D.

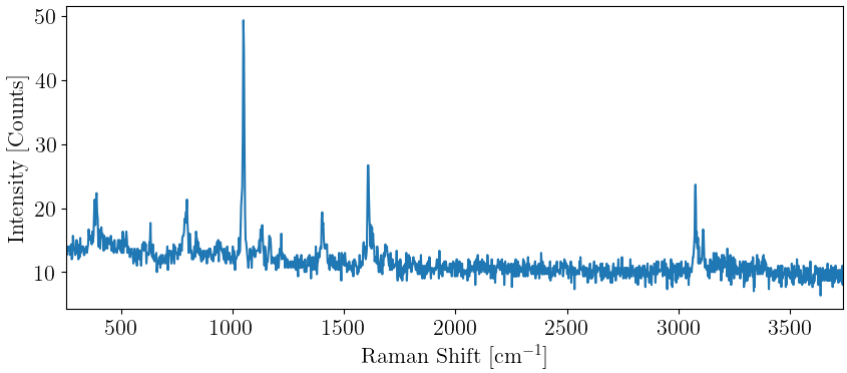

Figure 5.9: Reference Raman spectrum of pure nicotinamide sample. Spectrum was acquired under 5 seconds of laser exposure, with 0.246 mW of laser power.

Hotspot and Z-scan Raman maps were recorded from pure nicotinamide film. These results were displayed in Figures 5.10 and 5.11. Based on Figure 5.10

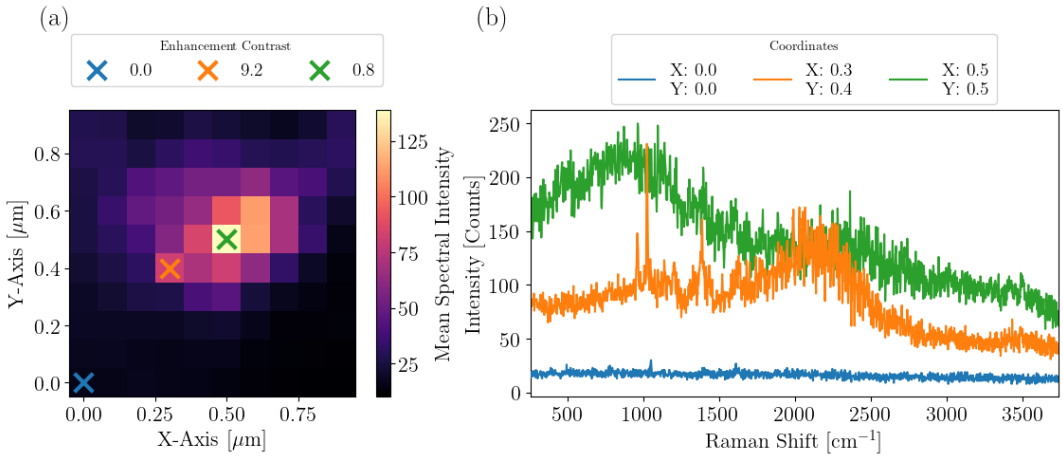

Figure 5.10: a) Hotspot Raman map of nicotinamide film, acquired at 0.246 mW of laser power at 5 seconds acquisition time, with dimensions 1 x 1 µm and 100 nm pixel-size. b) Coloured spectra (blue, orange, green) correspond to the annotated pixels marked on the hotspot map (a).

a), the hotspot Raman map displays the mean spectral intensity per pixel. The annotated crosshairs correspond to the spectra shown in Figure 5.11 b). Within the region of 1 x 1 µm^2 of Figure 5.10 a) a rise in the mean spectral intensity was detected at the centre of this image. Through comparison of the spectra at and away of the hotspot region (Figure 5.10 b)), we observed an intense rise in

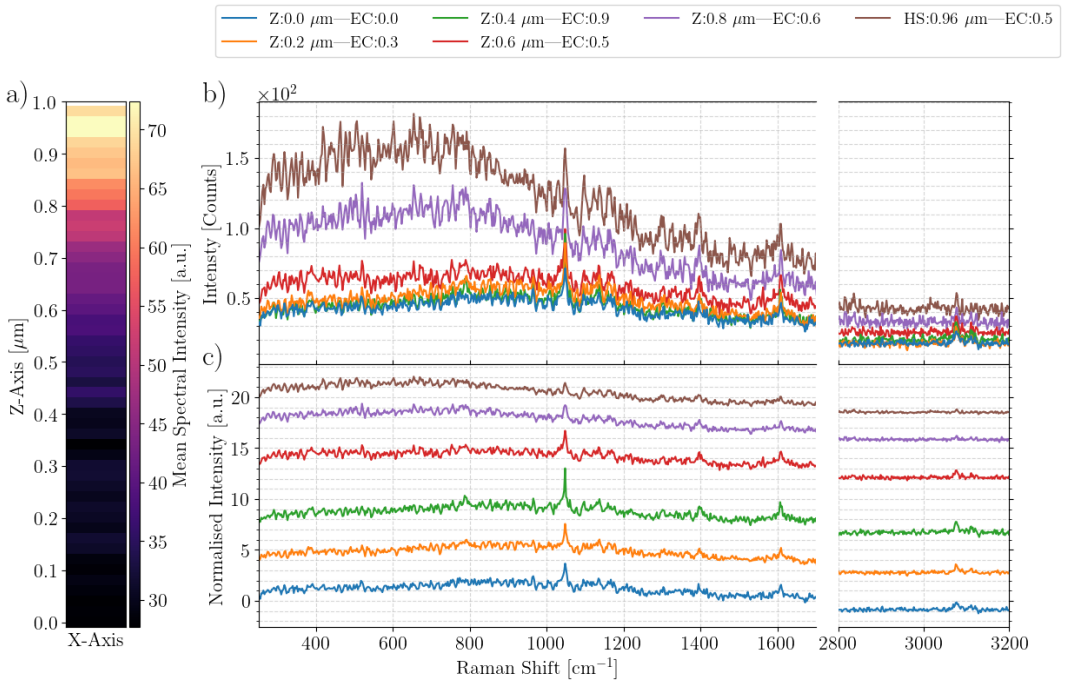

Figure 5.11: Z-scan measurement of nicotinamide film was obtained at 20 nm step-size. From the raw data acquired, with dimensions 1 x 0.06 µm across the ZX axis, the spectra across the X-axis were averaged. a) displays a heatmap of these spectra across the Z-axis. b) and c) project overlapped and cascaded spectra across the Z-axis, respectively, at 200 nm intervals including the position at which the Hotspot becomes detected. Each spectrum shown in c) was mean centered and variance scaled. For each spectrum the *EC* from the band of interest (1047.7 cm^{-1}) was also measured against the the spectrum at Z=0.

the PL background around the central region of this map (green line). Added to that, an intense signal of the nicotinamide Raman bands was detected at the coordinates X: 0.3 µm - Y: 0.4 µm. To further confirm this enhancement the *EC* was calculated, for band 1047.7 cm^{-1}. For the same position the *EC* value reached up to 9.2, indicating intense signal enhancement. This was not the same for the position X: 0.5 µm - Y: 0.5 µm, where the *EC* reached up to 0.8 which is below the indicated value [195]. In order to ensure the maximum signal was acquired at this region, an additional hotspot map of 0.1 x 0.1 $µm^2$ was performed to locate this signal enhancement (Appendix D - Figure D.7). The produced map showed no spectra originating from Nicotinamide at any position, indicating that the signal enhancement was lost.

Figure 5.11 displays a Z-Axis Raman map alongside with its respective spectra. On the first subplot (5.11 a)), the spectra were averaged across the X-Axis and plotted as a 1-Dimensional line map across the Z-Axis, within the range of 1 µm distance. In the second subplot of this Figure (5.11 b)) the spectra from subplot a) are shown overlapped. On the third subplot (5.11 c)), the normalised spectra of Figure 5.11 b) are projected in cascaded order from 0 to 0.9 µm, from the bottom to the uppermost spectrum. The labels indicate the position of each spectrum acquired from the Z-Axis raster scan. *EC* values were also acquired with positions at Z $>$ 0.1 µm being measured against Z = 0, based on the equation 5.1, for the nicotinamide band 1047.7 cm^{-1}.

Based on Figure 5.11 a) as the focal point comes at close proximity to the apex location, the spectral intensity gradually rises until maximised at 0.96 µm in height. At this level we observe in Figure 5.11 b) a rise at the PL background signal. The *EC* acquired across the different positions reached up to 0.9, at the Z: 0.4 µm position, which is just below the required value.

Through inspection of Figures 5.10 and 5.11, nicotinamide remained stable throughout both Hotspot and Z-scan raster scans, at 0.246 mW of laser exposure, with consistent *EC* values of 0.8-0.9. Also instabilities in TERS Raman spectra can be recorded around the hotspot, as seen in Figure 5.10.

5.3.4 PVA measurements

Reference Raman spectrum from pure PVA film was obtained, with the probe retracted from the film surface. The result is displayed in Figure 5.12. According to the Figure, one strong Raman band is visible at 2928 cm^{-1}, at the $-CH$ stretch region. This band was selected to evaluate the signal enhancement in the TERS measurements. In addition this spectrum complies with published

data shown in Figure D.8 under Appendix D.

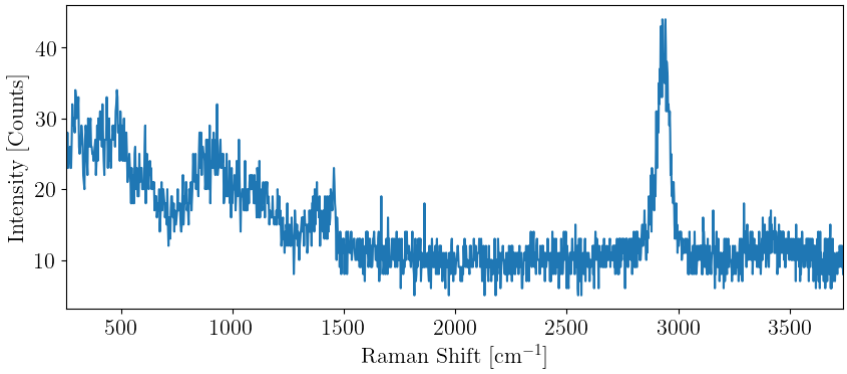

Figure 5.12: Reference Raman spectrum of pure PVA sample. Spectrum was acquired under 30 seconds of laser exposure, with 0.167 mW of laser power.

Last, hotspot and Z-scan Raman maps were collected from pure PVA film. These results are shown in Figures 5.13 and 5.14.

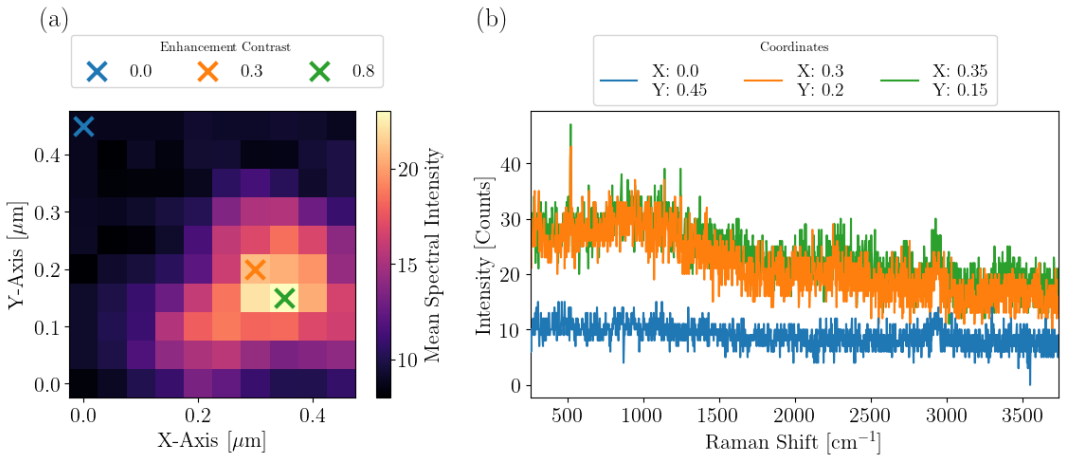

Figure 5.13: a) Hotspot Raman map of PVA film, acquired at 0.246 mW of laser power at 5s acquisition time, with dimensions 0.5 x 0.5 µm and 100 nm pixel-size. b) Coloured spectra (blue, orange, green) correspond to the annotated pixels marked on the hotspot map (a).

In Figure 5.13 a), each pixel on the image shows the mean spectral intensity acquired to project the hotspot Raman map. The annotated crosses correspond to similarly coloured spectra shown in Figure 5.13 b). Within the region of 0.5 x 0.5 µm^2 a rise in the mean spectral intensity is observed on the right bottom side of this image (Figure 5.13 a)). By comparing the spectra within and away from the hotspot region (Figure 5.13 b)), a rise in the PL background, originated

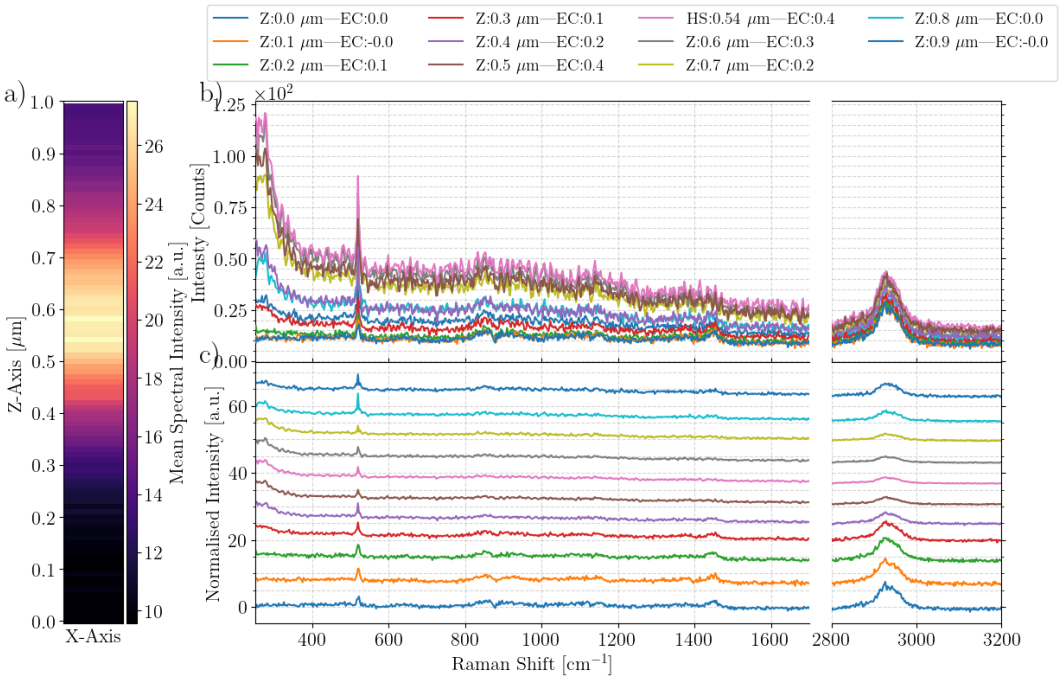

Figure 5.14: Z-scan measurement of PVA film was obtained at 10 nm step-size. From the raw data acquired, with dimensions 1 x 0.05 µm across the ZX axis, the spectra across the X-axis were averaged. a) displays a heatmap of these spectra across the Z-axis. b) and c) project overlapped and cascaded spectra across the Z-axis, respectively, at 100 nm intervals including the position at which the Hotspot becomes detected. Each spectrum shown in c) was mean centered and variance scaled. For each spectrum the *EC* from the band of interest (2928 cm^{-1}) was also measured against the the spectrum at Z=0.

from the TERS probe, becomes prevalent (orange and green lines). Also, the Raman band at 520.7 cm^{-1} can be observed from the silicon substrate of the probe. To evaluate the probe's performance the *EC* was calculated, where the PL values were assessed on and away from the hotspot location. The maximum *EC* measured was 0.8 at X: 0.35 µm - Y: 0.15 µm. This indicates weak signal enhancement was acquired.

After the XY-Axis probe-laser co-alignment, a Z-Axis raster-scan was obtained and displayed in Figure 5.14. On the first subplot (5.14 a)), the spectra were averaged across the X-Axis and plotted as 1-Dimensional heatmap towards the Z direction, within the range of 1 µm. In the second subplot (Figure 5.14 b)) the spectra from subplot a) are presented as overlapped. On the third subplot

(Figure 5.14 c)), the spectra were normalised and set in cascaded order from 0 to 0.9 µm, from the bottom to the uppermost spectrum. The labels indicate the position of each spectrum acquired on the Z-scan, alongside with their recorded EC values for band 2928 cm^{-1}.

Based on Figure 5.14 a) as the focal point comes at close proximity to the apex location, the spectral intensity gradually rises until maximised at 0.54 µm in height. At this level we observe in Figure 5.14 b) a small rise at the PL background signal, originating from the Ag-coating. The silicon band of the probe is also visible at 520.7 cm^{-1}. EC also reached up to 0.4, indicating weak signal enhancement acquired from the band of interest.

After the inspection of Figures 5.14 and 5.14, PVA showed no instabilities throughout the hotspot and Z-scan measurements, with the laser being set at 0.246 mW. Furthermore, the signal enhancement acquired in both Figures was $EC < 1$, indicating weak enhancement.

5.4 Conclusion

In this chapter, we obtained spectra as a function to apex-to-focal spot distances across the XY and Z axes, using with pure pharmaceutical materials and keeping the exposure time and laser power constant. These materials were molten-quenched paracetamol, felodipine, nicotinamide and PVA films. From the hotspot and Z-scan maps acquired, a rise in PL signal was observed as the laser spot was approaching the apex of the probe. This was due to the plasmon-dependent photoluminescence noise rising from the rough metal Ag surface. Regarding the Enhancement Contrast of the samples measured, paracetamol demonstrated $EC > 1$ at the 1323.9 cm^{-1}, whereas nicotinamide and PVA were < 1, for the 1047.7 cm^{-1} and 2928 cm^{-1}, respectively, indicated weaker signal

enhancement. This was not the case for felodipine as early photodegradation was detected at longer distances from the apex hotspot site. The produced PL was a combination of both plasmon-driven and photodegradation of the sample, therefore no EC could be evaluated.

With these findings we understand how these samples perform under a functionalised TERS probe and what information we can obtain for further tests. With the exception of felodipine, the rest of the samples remained stable throughout these experiments. However, for every intact material our analysis is limited to single characteristic band with small signal enhancement. Due to the poor signal-to-noise ratio of the TERS spectra presented in this study, investigating the TERS maps of amorphous solid dispersions for nano-scale inhomogeneities requires careful analysis and evaluation of the outcomes. Therefore for paracetamol material with $EC > 1$, qualitative evaluation of the chemical-associated spatial information was performed under the TERS setup.

Chapter 6

AFM-CRM-TERS measurement on 2D-printed microdot ASD

6.1 Introduction

Following chapters 3,4,5 and 6, we acquired a better understanding of the performance of pharmaceutical components under intense laser irradiation or during a TERS experimentation. For each material there is a certain laser power threshold which each material can withstand. In addition, the photoluminescence background noise generated can be discriminated either from sample degradation or TERS probe plasmon effect. From the stable materials investigated i.e paracetamol under TERS, a small signal enhancement has been identified (EC $>$ 1). In addition, due to the low SN ratio one to two characteristic Raman bands could be discernible from the spectra acquired, allowing further analysis and interpretation of the results.

Under the current TERS instrument, pharmaceutical materials do not display strong signal enhancement under an Ag-coated TERS probe. Interestingly,

biological macromolecules such as single-strand DNA sequences [197] as well as insulin amyloid fibrils [198], have been studied under similar AFM-TERS setups, despite their classification as weak Raman scatterers [199].

Herein, we will evaluate the feasibility of obtaining nanometre-scaled spatially resolved chemical information of ASDs. The first step will involve the physico-chemical characterisation of ASD in the form of 2D inject printed micron-sized micro-arrays, also known as microdots [307]. Each microdot size and drug-polymer composition can be tunable, compared to spin-coated or molten-quenched samples, allowing efficient formulation screening in drug stability assessment of the produced ASDs. To assess the properties, selected microdot was interrogated under the AFM and CRM instruments, in order to detect inhomogeneities on its surface. Specifically the regions of interest would either be boundaries between an API and a polymer, or a location of physically-associated topographical interest were a certain component may have been accumulated over the other. Afterwards, these same regions will be investigated to extract nano-scale spatio-chemical information.

6.2 Material and Methods

Paracetamol, polyvinyl alcohol (PVA) and triethoxy(octyl)silane were purchased from Sigma Aldrich, (St. Louis, MO, USA). Toluene was purchased from Fisher Scientific (Loughborough, UK).

6.2.1 Coverslip and sample preparation

For the preparation of microdots, salinised coverslips were prepared. For this, plasma surface treatment machine (Zepto, Diener electronic, Germany) was

applied. The coverslips were treated with both Oxygen and Nitrogen gases under 0.06 mbar for 5 minutes, at 1 kW of power. Afterwards, the plasma-cleaned coverslips were stored in a glass vessel, filled with 500 ml of toluene and 10 ml of triethoxy(octly)silane and further heated to 50°C on a hot-plate (ADS-HP-NT, Asynt, UK). To remove the excess of liquids, coverslips were blown with Argon and further left to dry for 22 hours. After this step, any settled dirt was removed with acetone. Last, coverslips were dried inside a vacuum oven before use (Heraeus, Thermo Scientific).

Paracetamol was weighed out (Metler Toledo balance) into a scintillation vial, dissolved in DMSO (10 mg/ml) and further agitated until homogenous as a clear solution. Solutions were prepared on the same day of 2D-printing microdot formulation.

6.2.2 2D inject printing

A piezo electric 2D inkjet printer (Scienion AG Sciflexarrayer S5) was used for microdot assay preparation, using a piezo dispensing capillary (PDC 70 - type 2 coating). 30-40 µL of the drug solutions were pipetted in each well of a well plate (Costar 96). The filled well plate was further inserted into a designated station. Afterwards, the functionalised borosilicate cover slips were set on top of a microscope slide at the slide-holder section of the printer. The array layout as well as droplet volume were designed through the Scienion Software™. After printing, the microdot arrays were left for 48 hours to dry-out and allow the ASD to collapse.

6.2.3 AFM-Raman measurements

To extract the physico-chemical information of the sample in question at the micrometre length scale, the AFM-CRM instrument was applied (Chapter 2). The Raman shift of the spectra acquired range between 600-3000 cm^{-1}, unless otherwise stated.

For the recording of topographical AFM maps, non-conductive silicon nitride probes (DNP-S10, Bruker, MA, USA), were used. For the acquisition of height and friction maps, these probes were raster-scanning each sample surface in contact mode, with $\approx$ 2.3 nN force applied at 0.1 Hz scan rate. Friction maps are associated with the torsion of the probe cantilever arising from the lateral forces generated on the sample surface during a scan. Adhesion map was also generated from force scan mapping, with 0.4 µm length of engaged cantilever deflection, at a setpoint of 1.5 nN and over the duration of 0.2 seconds. This map represents the forces of attraction generated after the probe is retracted from the surface, followed by approach. Both friction and adhesion maps allowed the investigation of sample inhomogeneities based on the materials' mechanical properties.

6.2.4 TERS measurements

The same TERS instrument discussed in Chapters 3 and 5 was used to extract the nanometre spatio-chemical information of the sample of interest. The exciting laser power ranged between 0.097 and 0.782 mW. Spectra were acquired between 400 cm^{-1} and 3600 cm^{-1}, unless otherwise stated.

6.2.5 Computational preprocessing and analysis of data

In order to interpret the data acquired from AFM, CRM and TERS instruments a series of computational processes and techniques were applied. For the AFM data, routine pre-processing tasks were performed (i.e. plane levelling), by using the open-source Gwyddion ™. For the Raman and TERS data obtained, all spectra obtained were normalised through mean centring and variance scaling of the data points. This was performed to reduce any drifts from the baseline of the spectra due to scattering or fluorescence events, occurring during the experimental analysis [308].

For measuring the intensity of Raman bands, a combination of linear and Lorentzian curves were fitted on the bands of interest. The Lorentzian curve corresponds to the shape of a produced signal, whereas a 1^{st} order polynomial line under the curve represents the baseline of the spectra [109], under a selected range of wavelengths. After fitting the combined curve onto every band on the dataset, the height of the Lorentzian curves were extracted, alongside with their Estimated Standard Deviations (ESDs). During fitting procedure, some outlying intensities and ESD values were generated, which did not correspond to the expected band intensity. Therefore, for ESD values ranging below 0 and more than 1, their respective intensities were classified as Not a Number (NaN). Furthermore, to ensure that the curves were fitted on the bands of interest, the centre position of the curve remained constrained at 4 Δcm^{-1}. All numerical routines and raw data are included in the supplementary material for information and reference.

6.3 Results and Discussion

6.3.1 AFM-CRM Instrument

6.3.1.1 AFM measurements

For the acquisition of AFM topographical images, the edge of a round 2D-printed microdot was selected, consisting of 30 % w/w Paracetamol and PVA materials, as observed in Figure 6.1. The rationale behind this selection was based on the resemblance of this concentration with marketed solid dispersion formulations [40]. Also, compared to lower ASD drug concentration, there is a high probability of phase separation between the two components to occur [40]. This would allow the formation as well as detection of rich and poor API or polymer domains, to study their inhomogeneity down the nanoscale lengths.

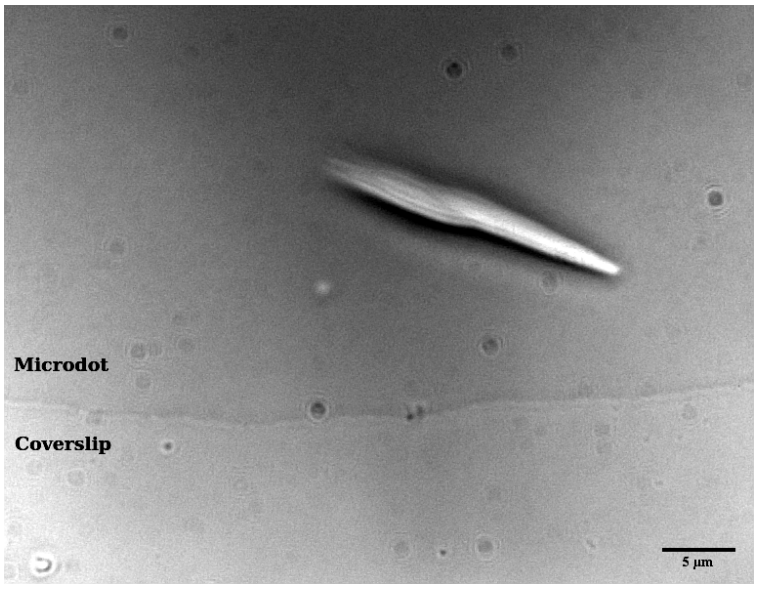

Figure 6.1: Brightfield image of Paracetamol PVA 30 % w/w in the form of a 2D-printed microdot. Scale bar: 5 µm

AFM topography maps were acquired by raster-scanning a region of 80 × 80 µm on the edge of the sample. These maps are shown in Figure 6.2 and 6.3. Figure 6.2 a) displays the height topography, whereas Figure 6.2 b) shows the

frictional topography of the region of interest. Through closer inspection of Figure 6.2 a), the sample height reaches up to 4 µm, from the coverslip surface. In addition, the sample shows a smooth surface, with a root mean square surface roughness of 0.3 ± 0.07 µm. At the same image two small elevated areas are also prevalent, located at the centre and the lower left of the map, indicating deformities on the micro-dot surface.

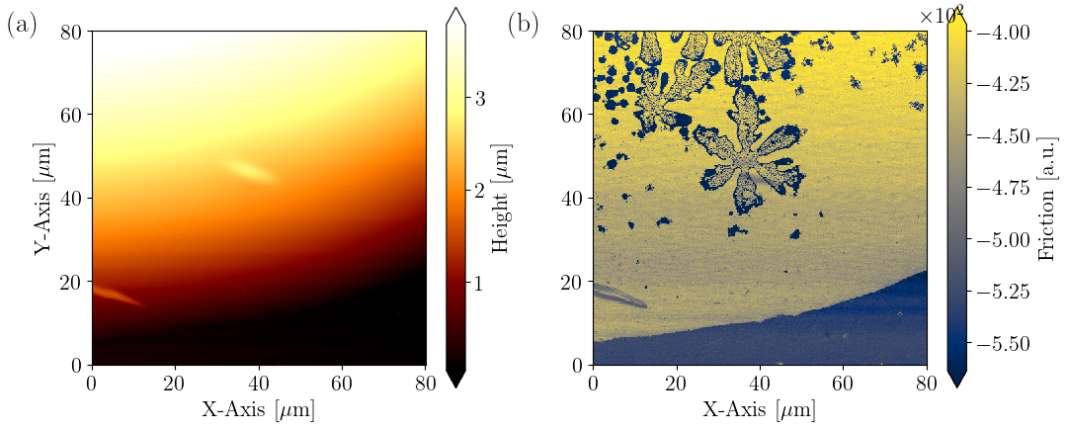

Figure 6.2: AFM (a) Height and (b) Friction maps. The size of the map is 80x80 µm, acquired through contact mode.

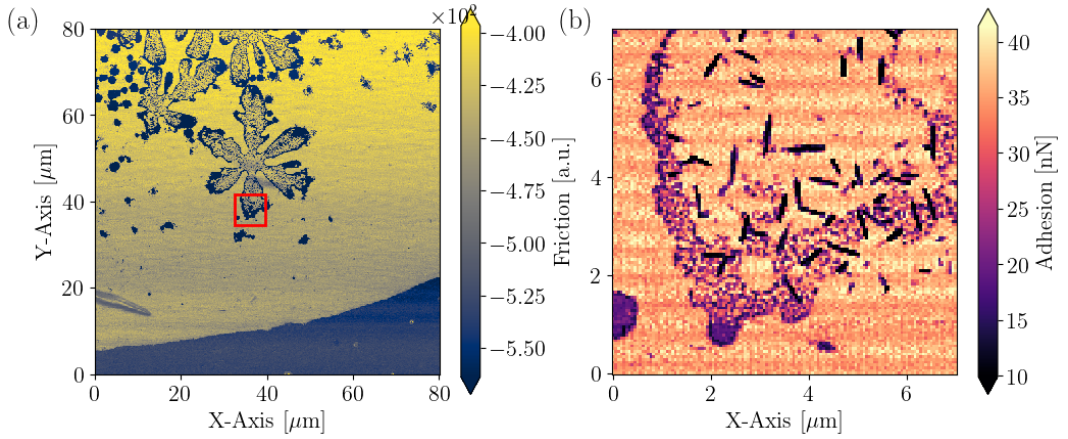

Figure 6.3: (a) AFM friction map shown in Figure 6.2 (b), with highlighted region (red rectangle) where adhesion map (b) was obtained. The adhesion map was acquired by force-mapping mode, over a region of 7x7 µm.

Moving to the frictional topography image of the same region (Figure 6.2 b)), the inner-most part of the microdot indicate some dark spots, including flower-like features. This image indicates that the dark areas presented less frictional

force against the probe, compared to the bright ones.

To further, obtain a better understanding of the sample surface physical properties, Figure 6.3 a) highlights a narrowed region (red rectangle), where adhesion measurements were acquired, as shown in Figure 6.3 b). Specifically, each pixel in this map represent the forces of attraction, whenever a probe is retracted from the surface, after being approached. The darker regions on this sample show less attraction to the apex of the probe, in comparison to the brighter areas. The same area is also in agreement with the zoomed region, in Figure 6.3 a), demonstrating, areas with lower frictional forces also display low forces of attraction. Based on a similar study, associated with the discrimination between crystalline and amorphous lactose based on AFM adhesion measurements [309], crystalline lactose demonstrated less probe pull-off force (6.34 $\pm$ 0.35 nN), in comparison to amorphous lactose (10.01 $\pm$ 0.80 nN). This finding, in combination with the aforementioned result, suggest the dark regions correspond to crystalline matter, potentially originating from paracetamol, PVA or both. However, from the physical information acquired it is unfeasible to discern the components in question. Therefore, confocal Raman spectroscopy was performed.

6.3.1.2 Raman measurements

Single confocal Raman spectra of pure paracetamol, pure PVA materials as well as their combination, from the 30 % w/w Paracetamol/PVA microdot were acquired. The resulting spectra are displayed in Figure 6.4. Figures 6.4 (a-b) shows the pure components, with their actual and normalised intensities, respectively, to allow their assessment. The pure paracetamol material investigated exhibits as a Form III polymorph [299] (Appendix E - Figure E.1), having two prominent bands located at 1323.9 cm^{-1} and 1628 cm^{-1}, at the fingerprint

region of the spectrum. Pure PVA shows one strong band at 2939 cm^{-1} at the −CH stretch region of the spectrum. In Figure 6.4 c), the reference spectrum of 30 % w/w Paracetamol/PVA is shown. At the fingerprint region, all of the paracetamol bands indicate the sample was amorphous [299] (Appendix E - Figure E.1). Furthermore, the most prevalent bands shown in this spectrum are the paracetamol band located in 1628 cm^{-1} as well as the PVA band at 2939 cm^{-1}. The increased intensity of these two bands allowed univariate as well as bivariate analysis of the sample under investigation.

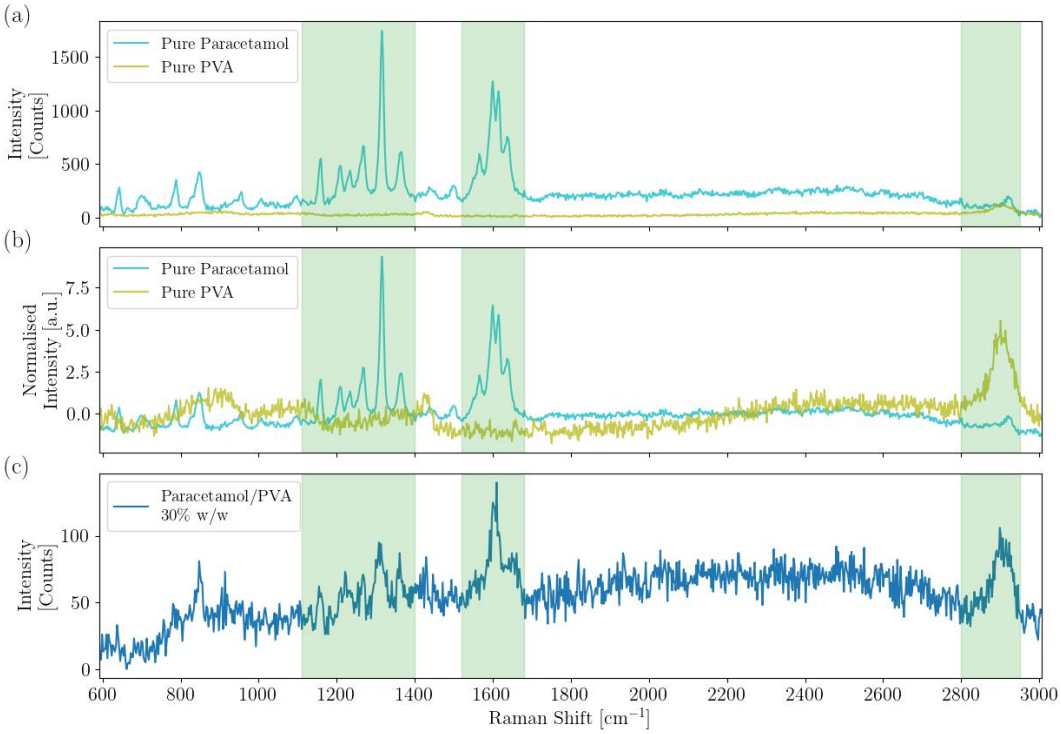

Figure 6.4: Reference Raman spectra of pure paracetamol (cyan coloured) and PVA (olive coloured) samples, with spectra displayed as (a) raw and (b) mean centered and variance scaled. The raw data was acquired after 2 seconds of laser exposure, irradiated under 0.8 mW of power, using the AFM-CRM instrument. (c) Raman spectrum acquired from Paracetamol/PVA 30 % w/w microdot sample (blue coloured). This data was acquired after 2 seconds of laser exposure, under 1 mW of power, using the AFM-CRM instrument.

From the same coordinates of the AFM map presented in Figure 6.2, multiple Raman spectra were obtained. This measurement was obtained with 1 second camera acquisition under 300 µW of laser power. It is important to note here,

that compared to the reference spectra (6.4 c)), the down scaled acquisition parameters applied for this measurement led to reduction in the spectral signal intensity (Appendix E - Figure E.2). However, they were sufficient to keep the bands of interest visible (i.e. 1628 cm^{-1} and 2939 cm^{-1}). This is to prevent any prolonged sample degradation and allow further sample investigation under the TERS instrument. In order to measure the intensities of the bands in question and calculate the ratio between the two, Lorentzian curve fittings were applied and their intensities used. Goodness of fit values such as average R^2, average Root Mean Square Errors (RMSE), as well as intensity Estimated Standard Deviations (ESDs) were calculated for all the spectra's bands of interest. The results can be found under Appendix E.

The produced Raman measurement is displayed in Figure 6.5. Figure 6.5 a) demonstrates the intensity map of the Lorentzian curve fitted at 1628 cm^{-1}. Figure 6.5 b) shows the intensity map of the Lorentzian curve fitted at 2939 cm^{-1}. Figure 6.5 c) displays the intensity ratio of band 1628 cm^{-1} over 2939 cm^{-1}. Figure 6.5 d) contains the average spectra, under the area represented by the annotated boxes of same colour in the ratio map (Figure 6.5 c)). The spectra are presented under the fingerprint region (600 - 1800 cm^{-1}) as well as $-CH$ stretch region (2700 - 3100 cm^{-1}) . The number of spectra averaged under this region are 256 pixels (16×16). The Goodness of fit as well as the intensity ESDs values for this measurement are provided in Figure E.3, under Appendix E.

From first observation across Figures 6.5 (a-b), we observe similar topographical features, seen from the AFM image in Figure 6.2 a). In particular, both 1628 cm^{-1} and 2939 cm^{-1} bands, which correspond to paracetamol and PVA respectively, are detected and evenly dispersed throughout the microdot. In addition, two dark regions in the centre and lower left position of these maps are also visible. Under the same locations the elevated areas from the AFM im-

age of Figure 6.2 a) are positioned. This potentially indicates internal cavities formed within the microdot, occurred during solvent evaporation, due to drop in signal intensity, hence reduction in material concentration. In Figure 6.5

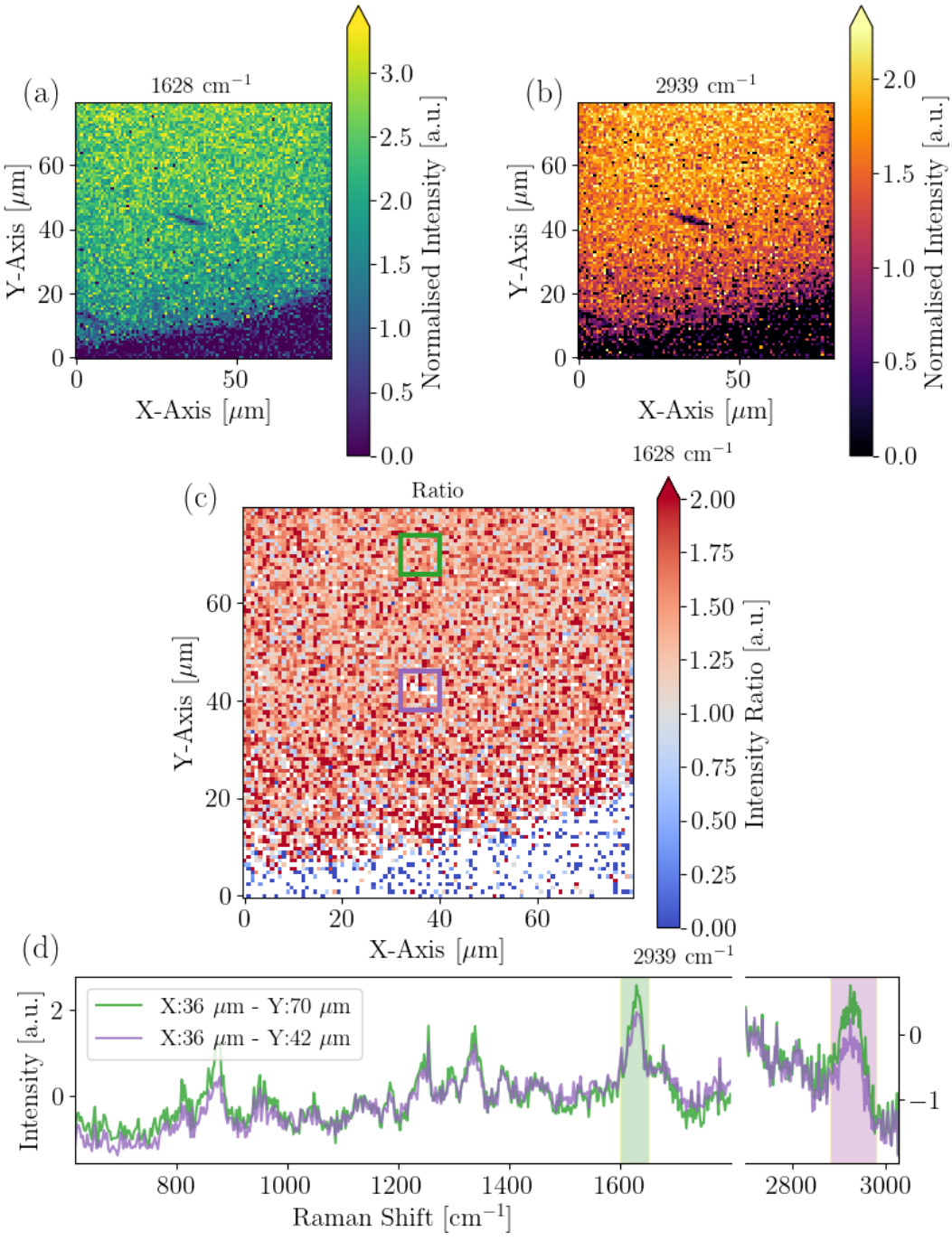

Figure 6.5: Normalised Raman intensity maps, acquired with the CRM instrument. The intensities are presented from fitted Lorentzian curves of bands located at (a) 1628 cm^{-1}, (b) 2939 cm^{-1} and their respective ratio intensity (c).The area covered under the coloured rectangular regions (5x5 pixel area) correspond to the averaged spectra displayed in (d).

c), where the ratio between the 1628 cm^{-1} and 2939 cm^{-1} bands is displayed, both components show great homogeneity within the microdot. Through comparison of the two spectra in Figure 6.5 d), both spectra are similar across the two XY coordinate positions (X:36 µm Y:70 µm - X:36 µm Y:42 µm). Due to the 1628 cm^{-1} increased band's intensity over 2939 cm^{-1}, paracetamol displays prevalence within the map. Also, there are no defined component segregation over the other, showing any resemblance with the crystalline regions seen on the AFM friction and adhesion maps in figure 6.3. As there might be spatial resolution limitations with the CRM, TERS measurements have been performed in a narrowed region of the map.

6.3.2 TERS Instrument

6.3.2.1 AFM measurements

After analysing the sample at the micron length scale, it was further transferred over the TERS instrument. To confirm similar topologies across the two instruments, the sample was examined under the AFM equipment of the TERS system. Figure 6.6 a), is the exact friction image shown under Figure 6.2 obtained with the AFM-CRM instrument, which highlights the region (red rectangle) where an additional friction topography was further recorded by the TERS instrument. This is displayed in Figure 6.6 b). Both the highlighted region in Figure 6.6 a) as well as the whole image in Figure 6.6 b) appear to be in good agreement. In Figure 6.6 b), Confocal Raman and TERS measurements have been acquired under the purple-coloured highlighted area, located over the top right hand-side of this image. The round feature, presented in the annotated rectangle shape, correlates to the dark region seen in Figure 6.6 a). Investigating this location, would allow the evaluation of the Confocal Raman and TERS spatial resolution and unravel the chemical identity of this feature.

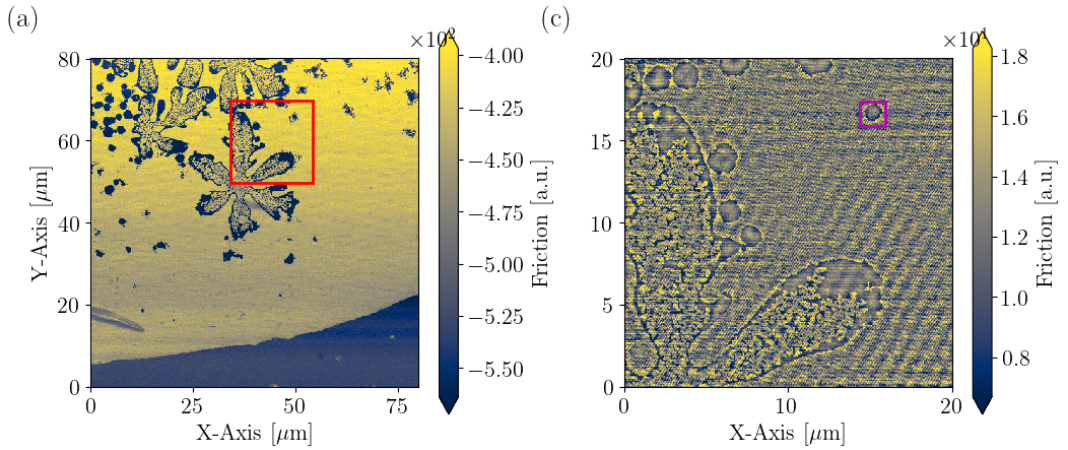

Figure 6.6: (a-b) are extracted from Figure 6.2 b), with b focusing on a 20x20 µm region from a. (c) is the friction AFM image acquired with the TERS instrument. The size of this map extents to 20 × 20 µm. 2D Fast Fourier Transform was applied for remove any generated sinusoidal artefacts. The original image is provided under Figure E.4 in Appendix E.

6.3.2.2 Raman measurements

Single confocal Raman spectra were recorded from pure PVA and paracetamol as well as both materials combined, in the form of 30 % w/w Paracetamol/PVA microdot. These results are displayed in Figure 6.7. Figure 6.7 (a-b) presents the spectra of pure components, with their intensities raw and normalised to allow their assessment. Pure paracetamol material exhibits as a Form III crystalline polymorph [299] (Appendix E - Figure E.1), having three prominent bands located at 864, 1323.9 cm^{-1} and 1628 cm^{-1}, at the fingerprint region of the spectrum. Pure PVA shows one strong band at 2939 cm^{-1} at the $-CH$ stretch region of the spectrum. In Figure 6.7 b), the reference spectrum of 30 % w/w Paracetamol/PVA is shown. At the fingerprint region, all of the paracetamol bands indicate that the sample exists in an amorphous state [299] (Appendix E - Figure E.1). Furthermore, two most prevalent bands shown in this spectrum from paracetamol are located in 864 and 1628 cm^{-1} as well as the PVA band at 2939 cm^{-1}. These results confirm that all the materials studied across the two instruments, remained in the same state, either crystalline for

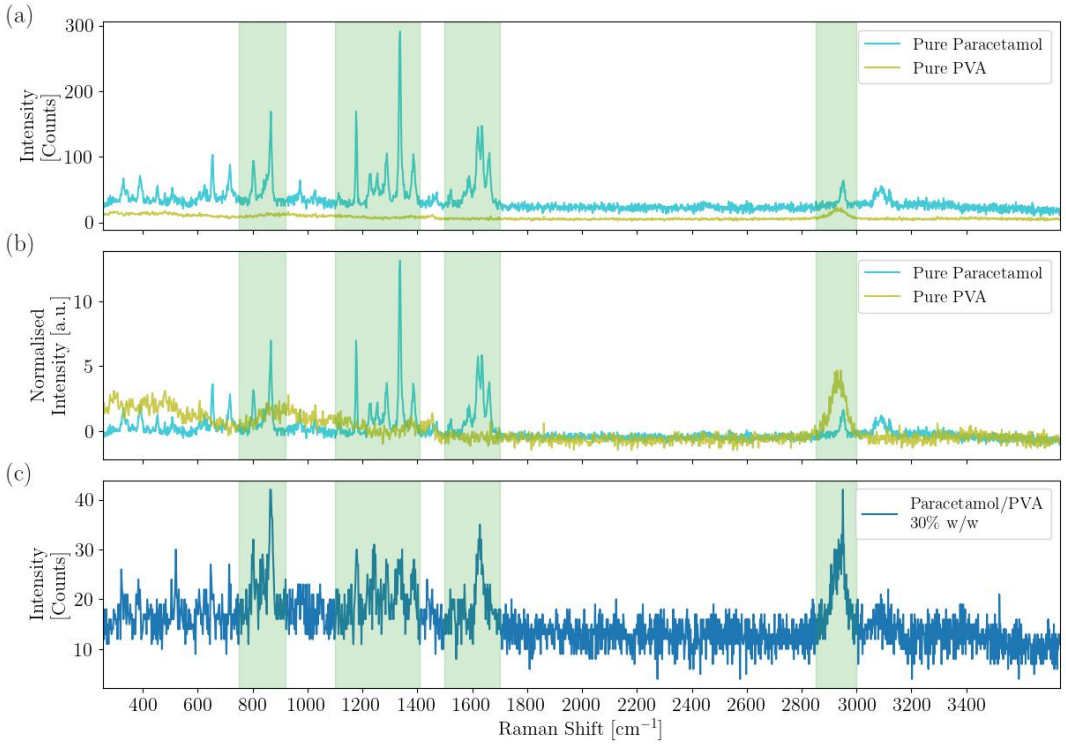

Figure 6.7: Reference Raman spectra of pure PVA (olive coloured) and paracetamol (cyan coloured) sample in Form III, with spectra displayed as (a) raw and (b) mean centered and variance scaled. The raw data was acquired after 30 seconds of laser exposure, irradiated under 95 µW of power, using the TERS instrument. (c) Raman spectrum acquired from Paracetamol/PVA 30 % w/w microdot sample (blue coloured), exhibiting in an amorphous state. The data was obtained after 10 seconds of laser exposure, under 0.167 mW of power, using the TERS instrument.

pure paracetamol or amorphous for 30 % w/w Paracetamol/PVA.

Confocal Raman map from the annotated region of interest (purple rectangle, Figure 6.6 b)) was acquired, while the TERS probe was retracted, as displayed in Figure 6.8. Figure 6.8 a) presents the intensity map of the fitted Lorentzian curve at 1628 cm^{-1}. Figure 6.8 b) shows the intensity map of the Lorentzian curve fitted at 2939 cm^{-1}. Figure 6.8 c) demonstrates the intensity ratio of the fitted 1628 cm^{-1} band over 2939 cm^{-1}. Figure 6.8 d) contains the average spectra, under the area represented from the annotated boxes of same colour shown the ratio map (Figure 6.8 c)). The spectra are presented under the fingerprint region (600 - 1800 cm^{-1}) and –CH stretch region (2700 - 3100

cm^{-1}). The number of spectra averaged under this region are 49 pixels (7 × 7). The Goodness of fit as well as the intensity ESDs values for this measurement are provided in Figure E.5, under Appendix E. In addition, Figure E.6 under Appendix E is also provided. It is similar to Figure 6.8, with the exception of displaying individual spectra with their respective fittings at the allocated coordinates.

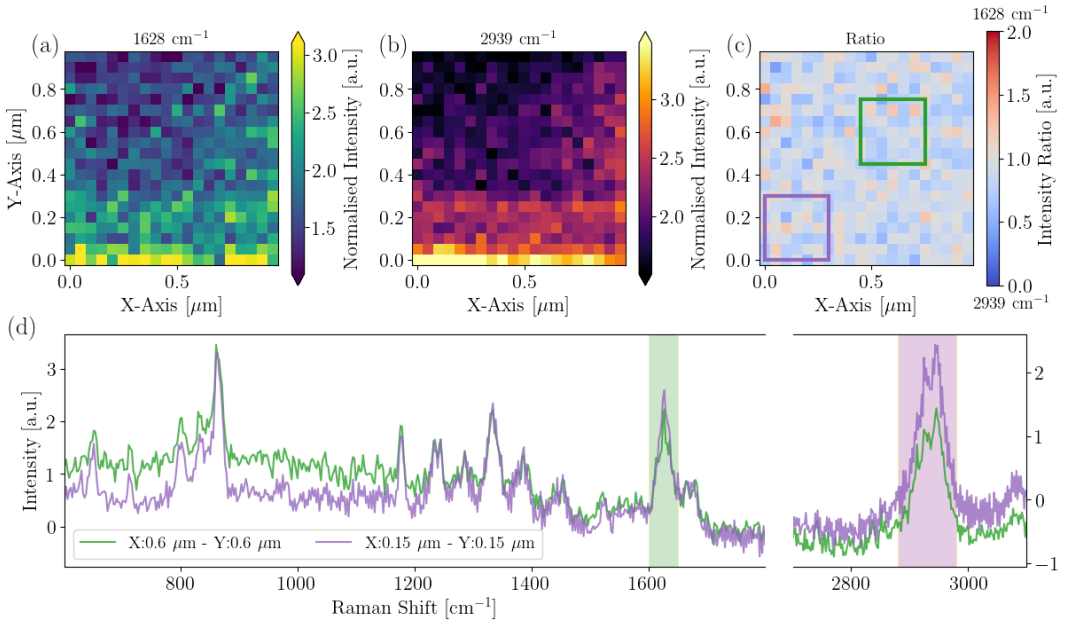

Figure 6.8: 1x1 µm normalised intensity maps acquired on the TERS instrument, while the probe was retracted from the sample surface. The intensities are displayed based on the fitted Lorentzian curves of the bands located at (a) 1628 cm^{-1}, (b) 2939 cm^{-1}, and their respective ratio intensity (c).The area covered under the coloured rectangular regions (5 × 5 pixel area) correspond to the averaged spectra shown in (d).

According to Figures 6.8 (a-b), both 1628 and 2939 cm^{-1} intensity maps show similarities in their topographies. Both images show high intensity values at the lowest part of the map (Y-Axis = 0 µm), with a decline as the Y-Axis coordinate rises. Moving to the ratiometric figure of the two bands (Figure 6.8 c)), the image displays great homogeneity for the two materials, with no indication of phase separation between the two components occurring. This finding is also in agreement with the ratiometric map acquired with the AFM-CRM instrument (Figure 6.5 c)). Furthermore, from the annotated regions seen

in Figure 6.8 c), the corresponding spectra are almost similar, with the purple spectrum showing higher intensities both at the 1628 and 2939 cm^{-1} bands.

A TERS map at the same coordinates as the confocal Raman map was recorded, with the probe approached on the sample surface. The results are displayed in Figure 6.9. Figure 6.9 a) shows the intensity map of the fitted Lorentzian curve at 1628 cm^{-1}. Figure 6.9 b) presents the intensity map of the Lorentzian curve fitted at 2939 cm^{-1}. Figure 6.9 c) demonstrates the intensity ratio of band 1628 cm^{-1} over 2939 cm^{-1}. Figure 6.9 d) contains the average spectra, under the area represented from the annotated boxes of same colour shown the ratio map (Figure 6.9 c)). The spectra are presented under the fingerprint region (600 - 1800 cm^{-1}) as well as $-CH$ stretch region (2700 - 3100 cm^{-1}) . The number of spectra averaged under this region are 49 pixels (7×7). The Goodness of fit as well as the intensity ESDs values for this measurement are provided in Figure E.7, under Appendix E. Under the same Appendix, Figure E.8 is also provided. This Figure is similar to 6.8, with the exception of displaying individual spectra with their respective fittings at the allocated coordinates.

Based on Figures 6.9 (a-b), both 1628 and 2939 cm^{-1} intensity maps display similarities in their topographical features. High intensity values are observed at the lowest regions of the two maps (Y-Axis $\rightarrow$ 0-0.05 µm), indicating high concentration of both components. Towards higher Y-Axis coordinates, this intensity further declines for the two materials. This finding was similarly observed previously in Figures 6.8 (a-b). After measuring the ratio between the two bands, a ratiometric map was generated and displayed in Figure 6.9 c). From first observation, an accumulation of the 1628 cm^{-1} band is located at the centre and upper region of this image. Specifically, this corresponds to paracetamol indicating up to 4-fold increased concentration, compared to 2939 cm^{-1} band from PVA. In Figure 6.9 d) the green annotated spectra, shows a slight drop in intensity (0.5 [Δa.u.]) at the 2939 cm^{-1} band, from the spectrum

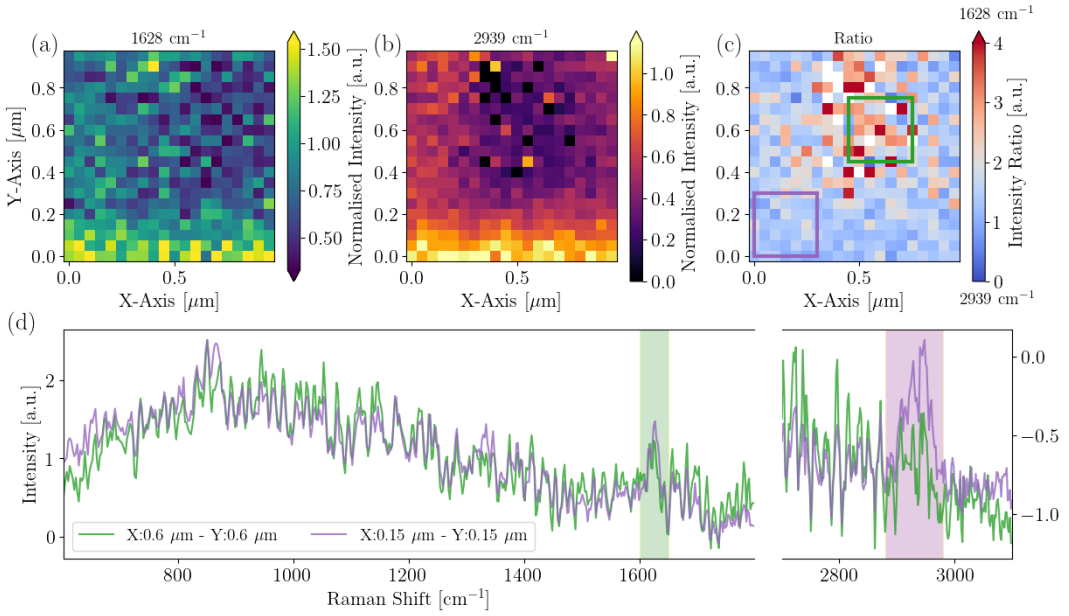

Figure 6.9: 1x1 µm normalised intensity maps obtained on the TERS instrument, while the probe was approached on the sample surface. The intensities are demonstrated based on the fitted Lorentzian curves of bands located at (a) 1628 cm^{-1}, (b) 2939 cm^{-1} and their respective ratio intensity (c).The area covered under the coloured rectangular regions (5 × 5 pixel area) correspond to the averaged spectra displayed in (d).

baseline, in relation to the purple line. In regards to the 1628 cm^{-1} band, a slight reduction in intensity is observed between the green over the purple line is detected (0.1 [Δa.u.]). Also, from the individual spectra shown in Figure E.8 under Appendix E, lower Lorentzian curve intensity was demonstrated at the 2939 cm^{-1} compared to the 1628 cm^{-1} bands at the centre of the same ratiometric map. These findings suggest the 4-fold increase in paracetamol band due to the drop in the 2939 cm^{-1} band, associated with PVA.

In an ideal scenario, further assessment of TERS spatial resolution performance would be performed. This would entail the measurement of near-field spatial resolution generated by the TERS probe. However, due to the low SN ratio obtained as well as the uncertain spatio-chemical characteristics of the sample beneath the AFM-interrogated surface, by using the calculated Lorentzian fittings would lead to a series of uncertainties and discrepancies in these measurements.

6.4 Conclusion

In this chapter, we acquired physical and chemical information about the surface morphology of a 30% w/w Paracetamol/PVA 2D printed microdot. The data was recorded from two instruments, namely one combined AFM-CRM for micron-length AFM and Raman measurements and a TERS instrument for nanoscale Raman assessment. From the AFM-CRM instrument, flower-like features were identified on the surface of the microdot from friction-based AFM images (Figure 6.2). Adhesion map was also recorded upon these areas, suggesting these regions are crystalline (Figure 6.3). Chemical inspection of the sample has also been performed through Raman spectroscopy. The printed microdot was exhibiting an amorphous state and was completely homogeneous from its two excipients (Figure 6.5). Moreover, the same sample was transferred over the TERS instrument. To ensure consistency in the measurements across the two microscopes, the flower-like features were identified over the AFM equipment of the TERS system (Figure 6.6). To examine sample inhomogeneities between confocal Raman and TERS, a round feature was detected and raster-scans were performed around that vicinity. Under the confocal Raman measurement, the sample has shown complete homogeneity from the two pharmaceutical ingredients (Figure 6.8). Whereas after the TERS measurement, an elevated concentration of paracetamol was identified, where the round dot is located (Figure 6.9). This suggests that the crystalline flower-like structures may potentially originate from paracetamol re-crystallisation.

Based on these findings we were able to identify nanoscale inhomogeneity at the surface of the pharmaceutical formulation, both with the AFM and TERS instruments. However, due to poor TERS signal obtained and lack of multiple visible Raman bands, it was unfeasible obtain a clearer image of the region investigated. Furthermore, no additional information could be extracted, such

as TERS probe derived spatial resolution, API polymorphism or PVA crystallinity. In this study, applying bottom-illumination TERS on the surface of a transparent pharmaceutical formulations could deem very useful for extracting nanometre-length spatio-chemical information. However, careful consideration must be given to sample stability and surface topology, in order to optimise the acquisition parameters and obtain meaningful results.

Chapter 7

Conclusions and Future Work

The aim of the work in this thesis was to apply and evaluate the TERS technique on ASDs based on its performance and suitability. Gaps in the current knowledge of pharmaceutical analysis is that most conventional analytical techniques have limited performance in resolving both physical and chemical properties of ASDs at the nanometre length. Unravelling such information would allow a more in-depth understanding of the complex mechanisms involved in the ASD dissolution process and further improve the performance.

In these series of studies, two bottom-illumination AFM-CRM and TERS systems, both equipped with 532 nm wavelength laser were used. The AFM-CRM instrument was developed, demonstrating compatibility of becoming a TERS system (Chapter 2). AFM-CRM has also been used, in evaluating pharmaceutical material stability under prolonged laser irradiation (Chapter 4) as well as recording at the micrometer level the physical and chemical topographies of a 2D-printed ASD microdot (Chapter 6). The TERS instrument was applied to obtain and assess single or multiple Raman spectra in tip retracted and approached positions on single or binary pharmaceutical components (Chapters 3 and 5). Finally, in combination with the AFM-CRM instrument, TERS was

used to discern the chemical inhomogeneities of the 2D-printed microdot at the nanometre length scales (Chapter 6).

In (Chapter 2), a combined AFM-CRM system was developed and assessed. The instrument schematics, software development, laser polarisation assessment as well as the laser spot-to-probe co-aligment have been presented. In particular, the desired orientation of the incident electromagnetic field from linear to radial has been achieved. Also, the laser-probe co-alignment was demonstrated, either through Rayleigh light back-scattering of the apex to the AFM photodiode or Raman signal, based on the probe silicon band at 520.7 cm^{-1}. Furthermore, to confirm the Raman instrument's laser spot dimension, the Raman band intensity of SWCNT cross-section was obtained, allowing the calculation of the FWHM, with an estimate of 229 nm laser focal point diameter.

In (Chapter 3), the TERS instrument was tested on bio-pharmaceutical components of interest. First, for single-component material analysis, Phe-Phe tubes were used to assess the Raman spectra obtained with TERS probe being retracted or approached on the sample surface as well as to examine the spatial resolution obtained at the near-field, while the probe is in contact with the sample. The results indicated TERS-based signal-enhancement from the probe, providing an Enhancement Factor of 4.48 and resolving spatial features at 32 nm. Regarding, two component-material analysis, ASDs were tested namely 50 % w/w spin-coated paracetamol/copovidone and 50 % w/w spin-coated felodipine/copovidone. While the TERS probe was retracted, the Raman bands were visible across the acquired spectra. However, with the probe being engaged on the sample surface, change in the spectra were noted, including rise in photo luminescent background, lowering of signal-to-noise ratio as well as loss of multiple bands. In combination with brightfield images acquired, the detected dark spots to the ASD film indicated sample photodegradation.

In (Chapter 4), pure spin-coated paracetamol, felodipine and copovidone films were tested, to evaluate the degree of photodegradation, as well as record any change in temperature. These experiments were performed under prolonged laser exposures of different power outputs (mW) and different objective lenses (0.55 NA, 0.8 NA, 1.45 NA). Raman spectra in the form of time series were acquired with the AFM-CRM and the Horiba ™, recording the Stokes and Anti-Stokes regions. The outcomes of this study showed that felodipine exhibited early photodegradation at a threshold of 49 kW/cm^2, whereas paracetamol degradation threshold reached up to 954 kW/cm^2. In comparison to the crystalline drugs, copovidone displayed no sign of photodegradation, throughout the measurement. In regards to Raman thermometry, from paracetamol sample the the I_{AS}/I_S ratio of symmetric bands as well as the line-width and shift of Stokes bands has been used, to measure the temperature. According to the results, with the rise in photoluminescence, the rise in sample temperature also takes place, with the photoluminescence effect occuring beyond 170 °C, which is the melting point threshold for paracetamol.

In (Chapter 5), Raman spectra were acquired from the TERS system, across the XYZ coordinates. Pure molten-quenched paracetamol, felodipine, nicotinamide and PVA films were tested for this set of experiments. Paracetamol, nicotinamide and PVA remained stable throughout the measurements, with photoluminescence background signal being generated from the Ag-coating of the probe. This was not the case for felodipine as plasmon-driven photodegradation occurred. In addition for paracetamol the highest and stable *EC* value was obtained up to 1.2.

In (Chapter 6), the edge of a 2D printed microdot with 30% w/w paracetamol/PVA was interrogated under the AFM-CRM and TERS instruments. First, from the AFM-CRM system, AFM height, friction as well as adhesion maps were acquired, with the latter two unveiling crystalline features on the

microdot surface. From the CRM system, the microdot displayed great homogeneity between amorphous paracetamol and PVA components. The same sample was transferred over the TERS system and the location of interest found through AFM friction measurement. Afterwards, two Raman maps were recorded, over a 1 × 1 µm region entailing a crystalline feature. These two measurements were performed with the probe being retracted and approached on the sample surface, respectively. When the probe was retracted, no inhomogeneities or phase separations of the sample surface was detected. After the probe was approached on the surface, the crystalline feature corresponded to an accumulation of paracetamol. This suggests that the crystalline features recorded from the AFM, correspond to nano-scale length paracetamol molecules which re-crystallised.

In summary, TERS technique in complement with AFM and CRM was studied extensively on ASDs and pharmaceutical materials. Due to high laser irradiation generated under the vicinity of a plasmon-resonating probe or after prolonged exposure by a high NA objective, crystalline API or ASDs can be sensitive to photodegradation. By keeping a balance in power output and Raman spectra acquisition, from the studied TERS configuration, samples display weak signal enhancement, with losses of multiple Raman bands under the photoluminescence background noise. With the information obtained, limited qualitative analysis can be performed about the ASD sample inhomogeneity.

For the continuation of this work, one potential amendment would be the introduction of metal substrate underneath the sample surface, also known as gap-mode configuration. In order to provide additional enhancement to the localised Raman signal, the sample of interest is deposited onto a thin gold or silver-based substrate layer. When the sample becomes sandwiched between the probe and the substrate, both metallic surfaces create a strong and confined electromagnetic coupling leading to an enhancement factor of 2 to 3 orders of

magnitude [310, 311], compared to the non-gap mode in these studies. However, additional parameters are required to be taken under consideration, such as type of metal, particle size, shape, as well as the gap size [312, 313]. Depending on the sample's thickness, gap-mode enhancements can be observed only if the gap between tip and substrate is less than 30 nm distance [179, 313]. For thin biological samples, or samples with weak Raman scattering, such as these circumstances, the gap-mode configuration has proven to generate fair SN ratio [192].

A second potential future work would be the changes in TERS system's optical settings. Specifically, changing the incident laser's wavelength from 532 nm to 633 nm would reduce the risk of sample burning, as demonstrated in similar studies with proteins and amyloid fibres [177, 287, 314]. Changing the optical configuration from a bottom to a side illumination setup, could also provide better control in laser power output, by using long-working distance objectives (NA 0.28-0.55) and preventing rapid changes in sample's integrity [315]. Especially, in case of opaque samples, using a side or top-illumination objective setup, in combination with a metallic substrate, can be efficient in recording TERS spectra at the surface of pharmaceutical formulations.

Bibliography

[1] Aulton's Pharmaceutics: The Design and Manufacture of Medicines. page 933.

[2] Srikonda Venkateswara Sastry, Janaki Ram Nyshadham, and Joseph A. Fix. Recent technological advances in oral drug delivery – a review. 3(4):138–145.

[3] Franz Gabor, Christian Fillafer, Lukas Neutsch, Gerda Ratzinger, and Michael Wirth. Improving Oral Delivery. In Monika Schäfer-Korting, editor, *Drug Delivery*, Handbook of Experimental Pharmacology, pages 345–398. Springer.

[4] Robert O. Williams III, Alan B. Watts, and Dave A. Miller, editors. *Formulating Poorly Water Soluble Drugs*, volume 22 of *AAPS Advances in the Pharmaceutical Sciences Series*. Springer International Publishing.

[5] Ruth R. Levine. Factors affecting gastrointestinal absorption of drugs. 15(2):171–188.

[6] Marilyn N. Martinez and Gordon L. Amidon. A Mechanistic Approach to Understanding the Factors Affecting Drug Absorption: A Review of Fundamentals. 42(6):620–643.

[7] Vinod P. Shah and Gordon L. Amidon. G.L. Amidon, H. Lennernas, V.P. Shah, and J.R. Crison. A Theoretical Basis for a Biopharmaceutic Drug

Classification: The Correlation of In Vitro Drug Product Dissolution and In Vivo Bioavailability, Pharm Res 12, 413–420, 1995—Backstory of BCS. 16(5):894–898.

[8] Leslie Z Benet, Chi-Yuan Wu, and Joseph M Custodio. Predicting drug absorption and the effects of food on oral bioavailability. 99:9–16.

[9] James M. Butler and Jennifer B. Dressman. The Developability Classification System: Application of Biopharmaceutics Concepts to Formulation Development. 99(12):4940–4954.

[10] Alexander T Florence and David Attwood. *Physicochemical Principles of Pharmacy: In Manufacture, Formulation and Clinical Use*. Pharmaceutical press.

[11] Teófilo Vasconcelos, Bruno Sarmento, and Paulo Costa. Solid dispersions as strategy to improve oral bioavailability of poor water soluble drugs. 12(23-24):1068–1075.

[12] Jae Hong Seo, Jung Bae Park, Woong-Kee Choi, Sunhwa Park, Yun Jin Sung, Euichaul Oh, and Soo Kyung Bae. Improved oral absorption of cilostazol via sulfonate salt formation with mesylate and besylate. 9:3961–3968.

[13] K. Seefeldt, J. Miller, F. Alvarez-Núñez, and N. Rodríguez-Hornedo. Crystallization Pathways and Kinetics of Carbamazepine–Nicotinamide Cocrystals from the Amorphous State by In Situ Thermomicroscopy, Spectroscopy, and Calorimetry Studies. 96(5):1147–1158.

[14] Meimei Zhang, Houli Li, Bo Lang, Kevin O'Donnell, Haohao Zhang, Zhouhua Wang, Yixuan Dong, Chuanbin Wu, and Robert O. Williams. Formulation and delivery of improved amorphous fenofibrate solid dispersions prepared by thin film freezing. 82(3):534–544.

[15] Kodukula Sai Gouthami, Dinesh Kumar, Rajesh Thipparaboina, Rahul B. Chavan, and Nalini R. Shastri. Can crystal engineering be as beneficial as micronisation and overcome its pitfalls?: A case study with cilostazol. 491(1):26–34.

[16] Dolores R. Serrano, Kieran H. Gallagher, and Anne Marie Healy. Emerging Nanonisation Technologies: Tailoring Crystalline Versus Amorphous Nanomaterials. 15(22):2327–2340.

[17] Colin W. Pouton. Formulation of poorly water-soluble drugs for oral administration: Physicochemical and physiological issues and the lipid formulation classification system. 29(3):278–287.

[18] Jinglu Zhang, Run Han, Weijie Chen, Weixiang Zhang, Ying Li, Yuanhui Ji, Lijiang Chen, Hao Pan, Xinggang Yang, Weisan Pan, and Defang Ouyang. Analysis of the Literature and Patents on Solid Dispersions from 1980 to 2015. 23(7):1697.

[19] Pablo G. Debenedetti and Frank H. Stillinger. Supercooled liquids and the glass transition. 410(6825):259–267.

[20] Bruno C Hancock and Sheri L Shamblin. Molecular mobility of amorphous pharmaceuticals determined using differential scanning calorimetry. 380(2):95–107.

[21] S. L Raghavan, A Trividic, A. F Davis, and J Hadgraft. Crystallization of hydrocortisone acetate: Influence of polymers. 212(2):213–221.

[22] Ping Gao, Anna Akrami, Francisco Alvarez, Jack Hu, Lan Li, Chandra Ma, and Sekhar Surapaneni. Characterization and optimization of AMG 517 supersaturatable self-emulsifying drug delivery system (S-SEDDS) for improved oral absorption. 98(2):516–528.

[23] Dave A. Miller, James C. DiNunzio, Wei Yang, James W. McGinity, and Robert O. Williams. Enhanced In Vivo Absorption of Itraconazole via Stabilization of Supersaturation Following Acidic-to-Neutral pH Transition. 34(8):890–902.

[24] Grace A. Ilevbare, Haoyu Liu, Kevin J. Edgar, and Lynne S. Taylor. Maintaining Supersaturation in Aqueous Drug Solutions: Impact of Different Polymers on Induction Times. 13(2):740–751.

[25] Fang Tian, Dorothy J. Saville, Keith C. Gordon, Clare J. Strachan, J. Axel Zeitler, Niklas Sandler, and Thomas Rades. The influence of various excipients on the conversion kinetics of carbamazepine polymorphs in aqueous suspension. 59(2):193–201.

[26] Wei-Guo Dai, Liang C. Dong, Shu Li, and Zhengyu Deng. Combination of Pluronic/Vitamin E TPGS as a potential inhibitor of drug precipitation. 355(1):31–37.

[27] Christian Leuner and Jennifer Dressman. Improving drug solubility for oral delivery using solid dispersions. 50(1):47–60.

[28] Scott V. Jermain, Chris Brough, and Robert O. Williams. Amorphous solid dispersions and nanocrystal technologies for poorly water-soluble drug delivery – An update. 535(1):379–392.

[29] Michael A Repka, Sejal Shah, Jiannan Lu, Sindhuri Maddineni, Joe Morott, Ketaki Patwardhan, and Noorullah Naqvi Mohammed. Melt extrusion: Process to product. 9(1):105–125.

[30] Hemlata Patil, Roshan V. Tiwari, and Michael A. Repka. Hot-Melt Extrusion: From Theory to Application in Pharmaceutical Formulation. 17(1):20–42.

[31] Pia Thybo, Lars Hovgaard, Jesper Sæderup Lindeløv, Anders Brask, and Sune Klint Andersen. Scaling Up the Spray Drying Process from Pilot to Production Scale Using an Atomized Droplet Size Criterion. 25(7):1610–1620.

[32] Dan E. Dobry, Dana M. Settell, John M. Baumann, Rod J. Ray, Lisa J. Graham, and Ron A. Beyerinck. A Model-Based Methodology for Spray-Drying Process Development. 4(3):133–142.

[33] Lulu Wang, Yingying Ma, Yu Gu, Yangyang Liu, Juan Zhao, Beibei Yan, and Yancai Wang. Cryoprotectant choice and analyses of freeze-drying drug suspension of nanoparticles with functional stabilisers. 35(3):241–248.

[34] Shrawan Baghel, Helen Cathcart, and Niall J. O'Reilly. Polymeric Amorphous Solid Dispersions: A Review of Amorphization, Crystallization, Stabilization, Solid-State Characterization, and Aqueous Solubilization of Biopharmaceutical Classification System Class II Drugs. 105(9):2527–2544.

[35] Ashish L. Sarode, Harpreet Sandhu, Navnit Shah, Waseem Malick, and Hossein Zia. Hot Melt Extrusion for Amorphous Solid Dispersions: Temperature and Moisture Activated Drug–Polymer Interactions for Enhanced Stability. 10(10):3665–3675.

[36] Michael Lee Branham, Thomas Moyo, and Thirumala Govender. Preparation and solid-state characterization of ball milled saquinavir mesylate for solubility enhancement. 80(1):194–202.

[37] Sujinda Keratichewanun, Yasuo Yoshihashi, Narueporn Sutanthavibul, Katsuhide Terada, and Jittima Chatchawalsaisin. An Investigation of Nifedipine Miscibility in Solid Dispersions Using Raman Spectroscopy. 32(7):2458–2473.

[38] Jung Hyun Joe, Won Mo Lee, Young-Joon Park, Kwan Hyung Joe, Dong Hoon Oh, Youn Gee Seo, Jong Soo Woo, Chul Soon Yong, and Han-Gon Choi. Effect of the solid-dispersion method on the solubility and crystalline property of tacrolimus. 395(1):161–166.

[39] Alireza Homayouni, Fatemeh Sadeghi, Ali Nokhodchi, Jaleh Varshosaz, and Hadi Afrasiabi Garekani. Preparation and Characterization of Celecoxib Dispersions in Soluplus®: Comparison of Spray Drying and Conventional Methods. 14(1):35–50.

[40] Yanbin Huang and Wei-Guo Dai. Fundamental aspects of solid dispersion technology for poorly soluble drugs. 4(1):18–25.

[41] Xu Liu, Xin Feng, Robert O. Williams, and Feng Zhang. Characterization of amorphous solid dispersions. 48(1):19–41.

[42] David G. Watson. *Pharmaceutical Analysis: A Textbook for Pharmacy Students and Pharmaceutical Chemists*. Churchill Livingstone Elsevier, 3rd ed edition.

[43] Gary Nichols. Light Microscopy. In *Polymorphism*, pages 167–209. John Wiley & Sons, Ltd.

[44] Jonathan G. Moffat, Sheng Qi, and Duncan Q. M. Craig. Spatial Characterization of Hot Melt Extruded Dispersion Systems Using Thermal Atomic Force Microscopy Methods: The Effects of Processing Parameters on Phase Separation. 31(7):1744–1752.

[45] Xingyou Ye, Hemlata Patil, Xin Feng, Roshan V. Tiwari, Jiannan Lu, Andreas Gryczke, Karl Kolter, Nigel Langley, Soumyajit Majumdar, Dipesh Neupane, Sanjay R. Mishra, and Michael A. Repka. Conjugation of Hot-Melt Extrusion with High-Pressure Homogenization: A Novel Method of Continuously Preparing Nanocrystal Solid Dispersions. 17(1):78–88.

[46] Patrick J. Marsac, Alfred C. F. Rumondor, David E. Nivens, Umesh S. Kestur, Lia Stanciu, and Lynne S. Taylor. Effect of temperature and moisture on the miscibility of amorphous dispersions of felodipine and poly(vinyl pyrrolidone). 99(1):169–185.

[47] Jared A. Baird and Lynne S. Taylor. Evaluation of amorphous solid dispersion properties using thermal analysis techniques. 64(5):396–421.

[48] Bin Tian, Xing Tang, and Lynne S. Taylor. Investigating the Correlation between Miscibility and Physical Stability of Amorphous Solid Dispersions Using Fluorescence-Based Techniques. 13(11):3988–4000.

[49] Frederick G. Vogt. Solid-State Characterization of Amorphous Dispersions. In *Pharmaceutical Sciences Encyclopedia*, pages 1–62. American Cancer Society.

[50] Amrit Paudel, Marco Geppi, and Guy Van den Mooter. Structural and Dynamic Properties of Amorphous Solid Dispersions: The Role of Solid-State Nuclear Magnetic Resonance Spectroscopy and Relaxometry. 103(9):2635–2662.

[51] Peter Larkin. IR and Raman Spectroscopy: Principles and spectra interpretation. In *Infrared and Raman Spectroscopy*, pages 1–5. Elsevier.

[52] Anette Müllertz, Yvonne Perrie, and Thomas Rades, editors. *Analytical Techniques in the Pharmaceutical Sciences*. Advances in Delivery Science and Technology. Springer New York.

[53] M. Blanco and A. Villar. Development and validation of a method for the polymorphic analysis of pharmaceutical preparations using near infrared spectroscopy. 92(4):823–830.

[54] Marcelo Blanco, Dámarih Valdés, Isidro Llorente, and Miguel Bayod. Ap-

plication of NIR spectroscopy in polymorphic analysis: Study of pseudo-polymorphs stability. 94(6):1336–1342.

[55] Ziyaur Rahman, Ahmed S. Zidan, and Mansoor A. Khan. Formulation and Evaluation of a Protein-loaded Solid Dispersions by Non-destructive Methods. 12(2):158–170.

[56] Ziyaur Rahman, Ahmed S. Zidan, and Mansoor A. Khan. Risperidone solid dispersion for orally disintegrating tablet: Its formulation design and non-destructive methods of evaluation. 400(1-2):49–58.

[57] Ahmed S. Zidan, Ziyaur Rahman, Vilayat Sayeed, Andre Raw, Lawrence Yu, and Mansoor A. Khan. Crystallinity evaluation of tacrolimus solid dispersions by chemometric analysis. 423(2):341–350.

[58] J. Mantanus, E. Ziémons, P. Lebrun, E. Rozet, R. Klinkenberg, B. Streel, B. Evrard, and Ph. Hubert. Moisture content determination of pharmaceutical pellets by near infrared spectroscopy: Method development and validation. 642(1):186–192.

[59] Claudia C. Corredor, Dongsheng Bu, and Douglas Both. Comparison of near infrared and microwave resonance sensors for at-line moisture determination in powders and tablets. 696(1-2):84–93.

[60] C. V. Raman. A Change of Wave-length in Light Scattering. 121(3051):619–619.

[61] C. V. Raman and K. S. Krishnan. A New Type of Secondary Radiation. 121(3048):501–502.

[62] Richard L. McCreery. *Raman Spectroscopy for Chemical Analysis*. John Wiley & Sons.

[63] Geoffrey P.S. Smith, Cushla M. McGoverin, Sara J. Fraser, and Keith C. Gordon. Raman imaging of drug delivery systems. 89:21–41.

[64] B Schrader and DS Moore. Laser-based molecular spectroscopy for chemical analysis-Raman scattering processes. 69:1451–1468.

[65] Wayne Sinclair, Michael Leane, Graham Clarke, Andrew Dennis, Mike Tobyn, and Peter Timmins. Physical stability and recrystallization kinetics of amorphous ibipinabant drug product by fourier transform raman spectroscopy. 100(11):4687–4699.

[66] Cushla M. McGoverin, Michael D. Hargreaves, Pavel Matousek, and Keith C. Gordon. Pharmaceutical polymorphs quantified with transmission Raman spectroscopy. 43(2):280–285.

[67] Samir F. El-Mashtoly, Dennis Petersen, Hesham K. Yosef, Axel Mosig, Anke Reinacher-Schick, Carsten Kötting, and Klaus Gerwert. Label-free imaging of drug distribution and metabolism in colon cancer cells by Raman microscopy. 139(5):1155–1161.

[68] Mickaël Mélot, Paul D. A. Pudney, Ann-Marie Williamson, Peter J. Caspers, Andre Van Der Pol, and Gerwin J. Puppels. Studying the effectiveness of penetration enhancers to deliver retinol through the stratum cornum by in vivo confocal Raman spectroscopy. 138(1):32–39.

[69] Evangelos Karavas, Manolis Georgarakis, Aristides Docoslis, and Dimitrios Bikiaris. Combining SEM, TEM, and micro-Raman techniques to differentiate between the amorphous molecular level dispersions and nanodispersions of a poorly water-soluble drug within a polymer matrix. 340(1):76–83.

[70] Jörg Breitenbach, Wolfgang Schrof, and Jörg Neumann. Confocal Raman-Spectroscopy: Analytical Approach to Solid Dispersions and Mapping of Drugs. 16(7):1109–1113.

[71] Attila Balogh, Gábor Drávavölgyi, Kornél Faragó, Attila Farkas, Tamás

Vigh, Péter Lajos Sóti, István Wagner, János Madarász, Hajnalka Pataki, György Marosi, and Zsombor Kristóf Nagy. Plasticized Drug-Loaded Melt Electrospun Polymer Mats: Characterization, Thermal Degradation, and Release Kinetics. 103(4):1278–1287.

[72] Zsombor K. Nagy, Attila Balogh, Balázs Vajna, Attila Farkas, Gergo Patyi, Aron Kramarics, and György Marosi. Comparison of electrospun and extruded Soluplus®-based solid dosage forms of improved dissolution. 101(1):322–332.

[73] Francesco Tres, Kevin Treacher, Jonathan Booth, Les P. Hughes, Stephen A.C. Wren, Jonathan W. Aylott, and Jonathan C. Burley. Real time Raman imaging to understand dissolution performance of amorphous solid dispersions. 188:53–60.

[74] Saleh Trefi, Corinne Routaboul, Saleh Hamieh, Véronique Gilard, Myriam Malet-Martino, and Robert Martino. Analysis of illegally manufactured formulations of tadalafil (Cialis) by 1H NMR, 2D DOSY 1H NMR and Raman spectroscopy. 47(1):103–113.

[75] Amrit Paudel, Dhara Raijada, and Jukka Rantanen. Raman spectroscopy in pharmaceutical product design. 89:3–20.

[76] Xiaoqin Zhu, Tao Xu, Qingyu Lin, and Yixiang Duan. Technical Development of Raman Spectroscopy: From Instrumental to Advanced Combined Technologies. 49(1):64–82.

[77] E. Abbe. Beiträge zur theorie des mikroskops und der mikroskopischen wahrnehmung. 9(1):413–468.

[78] Pavel Matousek and Michael Morris, editors. *Emerging Raman Applications and Techniques in Biomedical and Pharmaceutical Fields*. Biological and Medical Physics, Biomedical Engineering. Springer-Verlag.

[79] Arnaud Zoubir, editor. *Raman Imaging: Techniques and Applications.* Springer Series in Optical Sciences. Springer-Verlag.

[80] José Manuel Amigo. Practical issues of hyperspectral imaging analysis of solid dosage forms. 398(1):93–109.

[81] Rudolf W. Kessler. Perspectives in process analysis. 27(11):369–378.

[82] Sebastian Schlücker, Michael D. Schaeberle, Scott W. Huffman, and Ira W. Levin. Raman Microspectroscopy: A Comparison of Point, Line, and Wide-Field Imaging Methodologies. 75(16):4312–4318.

[83] Thomas Bocklitz, Angela Walter, Katharina Hartmann, Petra Rösch, and Jürgen Popp. How to pre-process Raman spectra for reliable and stable models? 704(1-2):47–56.

[84] Darren A. Whitaker and Kevin Hayes. A simple algorithm for despiking Raman spectra. 179:82–84.

[85] Sean Ekins. *Pharmaceutical Applications of Raman Spectroscopy.* John Wiley & Sons.

[86] K. M. Balss, G. Llanos, G. Papandreou, and C. A. Maryanoff. Quantitative spatial distribution of sirolimus and polymers in drug-eluting stents using confocal Raman microscopy. 85(1):258–270.

[87] Lutz Franzen and Maike Windbergs. Accessing Raman spectral variability in human stratum corneum for quantitative in vitro depth profiling. 45(1):82–88.

[88] Aart A. van Apeldoorn, Henk-Jan van Manen, Jeroen M. Bezemer, Joost D. de Bruijn, Clemens A. van Blitterswijk, and Cees Otto. Raman Imaging of PLGA Microsphere Degradation Inside Macrophages. 126(41):13226–13227.

[89] Khalida Rizi, Rebecca J Green, Olga Khutoryanskaya, Michael Donaldson, and Adrian C Williams. Mechanisms of burst release from pH-responsive polymeric microparticles. 63(9):1141–1155.

[90] Guojin Zhang, Carol R. Flach, and Richard Mendelsohn. Tracking the dephosphorylation of resveratrol triphosphate in skin by confocal Raman microscopy. 123(2):141–147.

[91] Agnese Miro, Ivana d' Angelo, Antonella Nappi, Pietro La Manna, Marco Biondi, Laura Mayol, Pellegrino Musto, Roberto Russo, Maria Immacolata La Rotonda, Francesca Ungaro, and Fabiana Quaglia. Engineering poly(ethylene oxide) buccal films with cyclodextrin: A novel role for an old excipient? 452(1):283–291.

[92] M. Fleischmann, P. J. Hendra, and A. J. McQuillan. Raman spectra of pyridine adsorbed at a silver electrode. 26(2):163–166.

[93] David L. Jeanmaire and Richard P. Van Duyne. Surface raman spectroelectrochemistry: Part I. Heterocyclic, aromatic, and aliphatic amines adsorbed on the anodized silver electrode. 84(1):1–20.

[94] M. Grant Albrecht and J. Alan Creighton. Anomalously intense Raman spectra of pyridine at a silver electrode. 99(15):5215–5217.

[95] Michael R. Philpott. Effect of surface plasmons on transitions in molecules. 62(5):1812–1817.

[96] M. Moskovits. Surface roughness and the enhanced intensity of Raman scattering by molecules adsorbed on metals. 69(9):4159–4161.

[97] Judith Langer, Dorleta Jimenez de Aberasturi, Javier Aizpurua, Ramon A. Alvarez-Puebla, Baptiste Auguié, Jeremy J. Baumberg, Guillermo C. Bazan, Steven E. J. Bell, Anja Boisen, Alexandre G. Brolo, Jaebum Choo, Dana Cialla-May, Volker Deckert, Laura Fabris,

Karen Faulds, F. Javier García de Abajo, Royston Goodacre, Duncan Graham, Amanda J. Haes, Christy L. Haynes, Christian Huck, Tamitake Itoh, Mikael Käll, Janina Kneipp, Nicholas A. Kotov, Hua Kuang, Eric C. Le Ru, Hiang Kwee Lee, Jian-Feng Li, Xing Yi Ling, Stefan A. Maier, Thomas Mayerhöfer, Martin Moskovits, Kei Murakoshi, Jwa-Min Nam, Shuming Nie, Yukihiro Ozaki, Isabel Pastoriza-Santos, Jorge Perez-Juste, Juergen Popp, Annemarie Pucci, Stephanie Reich, Bin Ren, George C. Schatz, Timur Shegai, Sebastian Schlücker, Li-Lin Tay, K. George Thomas, Zhong-Qun Tian, Richard P. Van Duyne, Tuan Vo-Dinh, Yue Wang, Katherine A. Willets, Chuanlai Xu, Hongxing Xu, Yikai Xu, Yuko S. Yamamoto, Bing Zhao, and Luis M. Liz-Marzán. Present and Future of Surface-Enhanced Raman Scattering. 14(1):28–117.

[98] C. De Bleye, P. Y. Sacré, E. Dumont, L. Netchacovitch, P. F. Chavez, G. Piel, P. Lebrun, Ph. Hubert, and E. Ziemons. Development of a quantitative approach using surface-enhanced Raman chemical imaging: First step for the determination of an impurity in a pharmaceutical model. 90:111–118.

[99] R. Griffith Freeman, Katherine C. Grabar, Keith J. Allison, Robin M. Bright, Jennifer A. Davis, Andrea P. Guthrie, Michael B. Hommer, Michael A. Jackson, Patrick C. Smith, Daniel G. Walter, and Michael J. Natan. Self-Assembled Metal Colloid Monolayers: An Approach to SERS Substrates. 267(5204):1629–1632.

[100] Constantine Douketis, Zhouhang Wang, Tom L. Haslett, and Martin Moskovits. Fractal character of cold-deposited silver films determined by low-temperature scanning tunneling microscopy. 51(16):11022–11031.

[101] Xiaoge Hu, Tie Wang, Liang Wang, and Shaojun Dong. Surface-Enhanced Raman Scattering of 4-Aminothiophenol Self-Assembled

Monolayers in Sandwich Structure with Nanoparticle Shape Dependence: Off-Surface Plasmon Resonance Condition. 111(19):6962–6969.

[102] J. B. Jackson and N. J. Halas. Surface-enhanced Raman scattering on tunable plasmonic nanoparticle substrates. 101(52):17930–17935.

[103] H Metiu and P Das. The Electromagnetic Theory of Surface Enhanced Spectroscopy. 35(1):507–536.

[104] Hongxing Xu, Erik J. Bjerneld, Mikael Käll, and Lars Börjesson. Spectroscopy of Single Hemoglobin Molecules by Surface Enhanced Raman Scattering. 83(21):4357–4360.

[105] Vincenzo Amendola, Roberto Pilot, Marco Frasconi, Onofrio M Maragò, and Maria Antonia Iatì. Surface plasmon resonance in gold nanoparticles: A review. 29(20):203002.

[106] P. W. Atkins and Julio De Paula. *Physical Chemistry: Thermodynamics, Structure, and Change*. W.H. Freeman, tenth edition edition.

[107] Paolo Biagioni, Jer-Shing Huang, and Bert Hecht. Nanoantennas for visible and infrared radiation. 75(2):024402.

[108] Alexandra Gellé, Tony Jin, Luis de la Garza, Gareth D. Price, Lucas V. Besteiro, and Audrey Moores. Applications of Plasmon-Enhanced Nanocatalysis to Organic Transformations. 120(2):986–1041.

[109] Jan Toporski, Thomas Dieing, and Olaf Hollricher, editors. *Confocal Raman Microscopy*, volume 66 of *Springer Series in Surface Sciences*. Springer International Publishing.

[110] Masatoshi Osawa, Naoki Matsuda, Katsumasa Yoshii, and Isamu Uchida. Charge transfer resonance Raman process in surface-enhanced Raman scattering from p-aminothiophenol adsorbed on silver: Herzberg-Teller contribution. 98(48):12702–12707.

[111] A. Otto, I. Mrozek, H. Grabhorn, and W. Akemann. Surface-enhanced Raman scattering. 4(5):1143–1212.

[112] Lixin Xia, Maodu Chen, Xiuming Zhao, Zhenglong Zhang, Jiarui Xia, Hongxing Xu, and Mengtao Sun. Visualized method of chemical enhancement mechanism on SERS and TERS. 45(7):533–540.

[113] Lin Lin Zhao, Lasse Jensen, and George C. Schatz. Surface-Enhanced Raman Scattering of Pyrazine at the Junction between Two Ag20 Nanoclusters. 6(6):1229–1234.

[114] Babak Nikoobakht, Jianping Wang, and Mostafa A. El-Sayed. Surface-enhanced Raman scattering of molecules adsorbed on gold nanorods: Off-surface plasmon resonance condition. 366(1):17–23.

[115] Encai Hao and George C. Schatz. Electromagnetic fields around silver nanoparticles and dimers. 120(1):357–366.

[116] David P. Fromm, Arvind Sundaramurthy, P. James Schuck, Gordon Kino, and W. E. Moerner. Gap-Dependent Optical Coupling of Single "Bowtie" Nanoantennas Resonant in the Visible. 4(5):957–961.

[117] Prabhat Verma. Tip-Enhanced Raman Spectroscopy: Technique and Recent Advances. 117(9):6447–6466.

[118] Bruno Pettinger, Philip Schambach, Carlos J. Villagómez, and Nicola Scott. Tip-Enhanced Raman Spectroscopy: Near-Fields Acting on a Few Molecules. 63(1):379–399.

[119] Eric Le Ru and Pablo Etchegoin. *Principles of Surface-Enhanced Raman Spectroscopy: And Related Plasmonic Effects*. Elsevier.

[120] Bert Voigtländer. *Atomic Force Microscopy*. NanoScience and Technology. Springer International Publishing.

[121] Daniel J Müller, Michael Krieg, David Alsteens, and Yves F Dufrêne. New frontiers in atomic force microscopy: Analyzing interactions from single-molecules to cells. 20(1):4–13.

[122] Franz J. Giessibl, S. Hembacher, H. Bielefeldt, and J. Mannhart. Subatomic Features on the Silicon (111)-(7×7) Surface Observed by Atomic Force Microscopy. 289(5478):422–425.

[123] Johannes Sitterberg, Aybike Özcetin, Carsten Ehrhardt, and Udo Bakowsky. Utilising atomic force microscopy for the characterisation of nanoscale drug delivery systems. 74(1):2–13.

[124] Ricardo de Souza Pereira. Detection of the absorption of glucose molecules by living cells using atomic force microscopy. 475(1):43–46.

[125] Guanglu Ge, Dong Han, Danying Lin, Weiguo Chu, Yunxu Sun, Lei Jiang, Wanyun Ma, and Chen Wang. MAC mode atomic force microscopy studies of living samples, ranging from cells to fresh tissue. 107(4):299–307.

[126] Katrin Christ, Imke Wiedemann, Udo Bakowsky, Hans-Georg Sahl, and Gerd Bendas. The role of lipid II in membrane binding of and pore formation by nisin analyzed by two combined biosensor techniques. 1768(3):694–704.

[127] Xuemei Liang, Guangzhao Mao, and K. Y. Simon Ng. Effect of chain lengths of PEO–PPO–PEO on small unilamellar liposome morphology and stability: An AFM investigation. 285(1):360–372.

[128] Anna Tarasova, Hans J. Griesser, and Laurence Meagher. AFM Study of the Stability of a Dense Affinity-Bound Liposome Layer. 24(14):7371–7377.

[129] Wan-Chen Lin, Craig D. Blanchette, Timothy V. Ratto, and Marjorie L. Longo. Lipid Asymmetry in DLPC/DSPC-Supported Lipid Bilayers: A Combined AFM and Fluorescence Microscopy Study. 90(1):228–237.

[130] M. Simon, M. Wittmar, U. Bakowsky, and T. Kissel. Self-Assembling Nanocomplexes from Insulin and Water-Soluble Branched Polyesters, Poly[(vinyl-3-(diethylamino)- propylcarbamate-co-(vinyl acetate)-co-(vinyl alcohol)]-graft- poly(l-lactic acid): A Novel Carrier for Transmucosal Delivery of Peptides. 15(4):841–849.

[131] Paulus Seitavuopio, Jyrki Heinämäki, Jukka Rantanen, and Jouko Yliruusi. Monitoring tablet surface roughness during the film coating process. 7(2):E1–E6.

[132] Ardeshir Danesh, Simon D. Connell, Martyn C. Davies, Clive J. Roberts, Saul J. B. Tendler, Phillip M. Williams, and M. J. Wilkins. An In Situ Dissolution Study of Aspirin Crystal Planes (100) and (001) by Atomic Force Microscopy. 18(3):299–303.

[133] Tamaki Miyazaki, Yukio Aso, and Toru Kawanishi. Feasibility of atomic force microscopy for determining crystal growth rates of nifedipine at the surface of amorphous solids with and without polymers. 100(10):4413–4420.

[134] C.M. Yip and M.D. Ward. Atomic force microscopy of insulin single crystals: Direct visualization of molecules and crystal growth. 71(2):1071–1078.

[135] Dmitry Kurouski, Alexandre Dazzi, Renato Zenobi, and Andrea Centrone. Infrared and Raman chemical imaging and spectroscopy at the nanoscale.

[136] A. Dazzi, R. Prazeres, F. Glotin, and J. M. Ortega. Local infrared microspectroscopy with subwavelength spatial resolution with an atomic force microscope tip used as a photothermal sensor. 30(18):2388–2390.

[137] A. Dazzi, F. Glotin, and R. Carminati. Theory of infrared nanospectroscopy by photothermal induced resonance. 107(12):124519.

[138] Jungseok Chae, Sangmin An, Georg Ramer, Vitalie Stavila, Glenn Holland, Yohan Yoon, A. Alec Talin, Mark Allendorf, Vladimir A. Aksyuk, and Andrea Centrone. Nanophotonic Atomic Force Microscope Transducers Enable Chemical Composition and Thermal Conductivity Measurements at the Nanoscale. 17(9):5587–5594.

[139] Sebastian Volz. *Thermal Nanosystems and Nanomaterials*. Springer Science & Business Media.

[140] Georg Ramer, Vladimir A. Aksyuk, and Andrea Centrone. Quantitative Chemical Analysis at the Nanoscale Using the Photothermal Induced Resonance Technique. 89(24):13524–13531.

[141] Le Wang, Haomin Wang, Martin Wagner, Yong Yan, Devon S. Jakob, and Xiaoji G. Xu. Nanoscale simultaneous chemical and mechanical imaging via peak force infrared microscopy. 3(6):e1700255.

[142] Aaron M. Katzenmeyer, Glenn Holland, Kevin Kjoller, and Andrea Centrone. Absorption Spectroscopy and Imaging from the Visible through Mid-Infrared with 20 nm Resolution. 87(6):3154–3159.

[143] Fuguang Tang, Peite Bao, and Zhaohui Su. Analysis of Nanodomain Composition in High-Impact Polypropylene by Atomic Force Microscopy-Infrared. 88(9):4926–4930.

[144] Rolando Rebois, Delphine Onidas, Curtis Marcott, Isao Noda, and

Alexandre Dazzi. Chloroform induces outstanding crystallization of poly(hydroxybutyrate) (PHB) vesicles within bacteria. 409(9):2353–2361.

[145] Liang Gong, D. Bruce Chase, Isao Noda, Curtis A. Marcott, Jinglin Liu, David C. Martin, Chaoying Ni, and John F. Rabolt. Polymorphic Distribution in Individual Electrospun Poly[(R)-3-hydroxybutyrate-co-(R)-3-hydroxyhexanoate] (PHBHx) Nanofibers. 50(14):5510–5517.

[146] Mark A. Rickard, Gregory F. Meyers, Brian M. Habersberger, Carl W. Reinhardt, and Jamie J. Stanley. Nanoscale chemical imaging of a deuterium-labeled polyolefin copolymer in a polyolefin blend by atomic force microscopy-infrared spectroscopy. 129:247–251.

[147] Suzanne Morsch, Yanwen Liu, Stuart B. Lyon, and Simon R. Gibbon. Insights into Epoxy Network Nanostructural Heterogeneity Using AFM-IR. 8(1):959–966.

[148] Jungseok Chae, Qingfeng Dong, Jinsong Huang, and Andrea Centrone. Chloride Incorporation Process in CH3NH3PbI3–xClx Perovskites via Nanoscale Bandgap Maps. 15(12):8114–8121.

[149] Yohan Yoon, Jungseok Chae, Aaron M. Katzenmeyer, Heayoung P. Yoon, Joshua Schumacher, Sangmin An, Andrea Centrone, and Nikolai Zhitenev. Nanoscale imaging and spectroscopy of band gap and defects in polycrystalline photovoltaic devices. 9(23):7771–7780.

[150] Evgheni Strelcov, Qingfeng Dong, Tao Li, Jungseok Chae, Yuchuan Shao, Yehao Deng, Alexei Gruverman, Jinsong Huang, and Andrea Centrone. CH3NH3PbI3 perovskites: Ferroelasticity revealed. 3(4):e1602165.

[151] Yongbo Yuan, Jungseok Chae, Yuchuan Shao, Qi Wang, Zhengguo Xiao, Andrea Centrone, and Jinsong Huang. Photovoltaic Switching Mechanism in Lateral Structure Hybrid Perovskite Solar Cells. 5(15):1500615.

[152] Aaron M. Katzenmeyer, Jerome Canivet, Glenn Holland, David Farrusseng, and Andrea Centrone. Assessing Chemical Heterogeneity at the Nanoscale in Mixed-Ligand Metal–Organic Frameworks with the PTIR Technique. 53(11):2852–2856.

[153] Guusje Delen, Zoran Ristanović, Laurens D. B. Mandemaker, and Bert M. Weckhuysen. Mechanistic Insights into Growth of Surface-Mounted Metal-Organic Framework Films Resolved by Infrared (Nano-) Spectroscopy. 24(1):187–195.

[154] Zilong Liu, Kasper Nørgaard, Marc H. Overgaard, Marcel Ceccato, David M. A. Mackenzie, Nicolas Stenger, Susan L. S. Stipp, and Tue Hassenkam. Direct observation of oxygen configuration on individual graphene oxide sheets. 127:141–148.

[155] Lisa V. Brown, Marcelo Davanco, Zhiyuan Sun, Andrey Kretinin, Yiguo Chen, Joseph R. Matson, Igor Vurgaftman, Nicholas Sharac, Alexander J. Giles, Michael M. Fogler, Takashi Taniguchi, Kenji Watanabe, Kostya S. Novoselov, Stefan A. Maier, Andrea Centrone, and Joshua D. Caldwell. Nanoscale Mapping and Spectroscopy of Nonradiative Hyperbolic Modes in Hexagonal Boron Nitride Nanostructures. 18(3):1628–1636.

[156] C. Ciano, V. Giliberti, M. Ortolani, and L. Baldassarre. Observation of phonon-polaritons in thin flakes of hexagonal boron nitride on gold. 112(15):153101.

[157] Cian Bartlam, Suzanne Morsch, Kane W. J. Heard, Peter Quayle, Stephen G. Yeates, and Aravind Vijayaraghavan. Nanoscale infrared identification and mapping of chemical functional groups on graphene. 139:317–324.

[158] Na Li and Lynne S. Taylor. Nanoscale Infrared, Thermal, and Mechanical

Characterization of Telaprevir–Polymer Miscibility in Amorphous Solid Dispersions Prepared by Solvent Evaporation. 13(3):1123–1136.

[159] Naila A. Mugheirbi, Laura I. Mosquera-Giraldo, Carlos H. Borca, Lyudmila V. Slipchenko, and Lynne S. Taylor. Phase Behavior of Drug-Hydroxypropyl Methylcellulose Amorphous Solid Dispersions Produced from Various Solvent Systems: Mechanistic Understanding of the Role of Polymer using Experimental and Theoretical Methods. 15(8):3236–3251.

[160] John Wessel. Surface-enhanced optical microscopy. 2(9):1538–1541.

[161] Raoul M. Stöckle, Yung Doug Suh, Volker Deckert, and Renato Zenobi. Nanoscale chemical analysis by tip-enhanced Raman spectroscopy. 318(1):131–136.

[162] Bruno Pettinger, Gennaro Picardi, Rolf Schuster, and Gerhard Ertl. Surface Enhanced Raman Spectroscopy: Towards Single Molecule Spectroscopy. 68(12):942–949.

[163] Norihiko Hayazawa, Yasushi Inouye, Zouheir Sekkat, and Satoshi Kawata. Metallized tip amplification of near-field Raman scattering. 183(1-4):333–336.

[164] Mark S. Anderson. Locally enhanced Raman spectroscopy with an atomic force microscope. 76(21):3130–3132.

[165] Weihua Zhang, Boon Siang Yeo, Thomas Schmid, and Renato Zenobi. Single Molecule Tip-Enhanced Raman Spectroscopy with Silver Tips. 111(4):1733–1738.

[166] Jens Steidtner and Bruno Pettinger. Tip-Enhanced Raman Spectroscopy and Microscopy on Single Dye Molecules with 15 nm Resolution. 100(23):236101.

[167] Bruno Pettinger, Gennaro Picardi, Rolf Schuster, and Gerhard Ertl. Surface-enhanced and STM-tip-enhanced Raman Spectroscopy at Metal Surfaces. 3(5-6):285–294.

[168] Katrin F. Domke, Dai Zhang, and Bruno Pettinger. Enhanced Raman Spectroscopy: Single Molecules or Carbon? 111(24):8611–8616.

[169] Xian Shi, Nicolás Coca-López, Julia Janik, and Achim Hartschuh. Advances in Tip-Enhanced Near-Field Raman Microscopy Using Nanoantennas. 117(7):4945–4960.

[170] John T. Krug, Erik J. Sánchez, and X. Sunney Xie. Design of near-field optical probes with optimal field enhancement by finite difference time domain electromagnetic simulation. 116(24):10895–10901.

[171] Igor I. Smolyaninov, Christopher C. Davis, Jill Elliott, and Anatoly V. Zayats. Resolution enhancement of a surface immersion microscope near the plasmon resonance. 30(4):382–384.

[172] Atsushi Taguchi. Plasmonic tip for nano Raman microcopy: Structures, materials, and enhancement. 24(3):462–469.

[173] Norihiko Hayazawa, Yuika Saito, and Satoshi Kawata. Detection and characterization of longitudinal field for tip-enhanced Raman spectroscopy. 85(25):6239–6241.

[174] A. Bouhelier, M. Beversluis, A. Hartschuh, and L. Novotny. Near-Field Second-Harmonic Generation Induced by Local Field Enhancement. 90(1):013903.

[175] C. Stanciu, M. Sackrow, and A.j. Meixner. High NA particle- and tip-enhanced nanoscale Raman spectroscopy with a parabolic-mirror microscope. 229(2):247–253.

[176] Dai Zhang, Xiao Wang, Kai Braun, Hans-Joachim Egelhaaf, Monika Fleischer, Laura Hennemann, Holger Hintz, Catrinel Stanciu, Christoph J. Brabec, Dieter P. Kern, and Alfred J. Meixner. Parabolic mirror-assisted tip-enhanced spectroscopic imaging for non-transparent materials. 40(10):1371–1376.

[177] Tanja Deckert-Gaudig, Atsushi Taguchi, Satoshi Kawata, and Volker Deckert. Tip-enhanced Raman spectroscopy – from early developments to recent advances. 46(13):4077–4110.

[178] Denys Naumenko, Valentinas Snitka, Elena Serviene, Ingrida Bruzaite, and Boris Snopok. In vivo characterization of protein uptake by yeast cell envelope: Single cell AFM imaging and μ-tip-enhanced Raman scattering study. 138(18):5371–5383.

[179] Manola Moretti, Remo Proietti Zaccaria, Emiliano Descrovi, Gobind Das, Marco Leoncini, Carlo Liberale, Francesco De Angelis, and Enzo Di Fabrizio. Reflection-mode TERS on Insulin Amyloid Fibrils with Top-Visual AFM Probes. 8(1):25–33.

[180] D. Mehtani, N. Lee, R. D. Hartschuh, A. Kisliuk, M. D. Foster, A. P. Sokolov, and J. F. Maguire. Nano-Raman spectroscopy with side-illumination optics. 36(11):1068–1075.

[181] J. Stadler, T. Schmid, and R. Zenobi. Nanoscale Chemical Imaging Using Top-Illumination Tip-Enhanced Raman Spectroscopy. 10(11):4514–4520.

[182] N. Lee, R. D. Hartschuh, D. Mehtani, A. Kisliuk, J. F. Maguire, M. Green, M. D. Foster, and A. P. Sokolov. High contrast scanning nano-Raman spectroscopy of silicon. 38(6):789–796.

[183] Jeanne L. McHale. *Molecular Spectroscopy*. CRC Press, Taylor & Francis Group, second edition edition.

[184] Dr Rüdiger Paschotta. Polarization of Light.

[185] Matthew D. Sonntag, Jordan M. Klingsporn, Luis K. Garibay, John M. Roberts, Jon A. Dieringer, Tamar Seideman, Karl A. Scheidt, Lasse Jensen, George C. Schatz, and Richard P. Van Duyne. Single-Molecule Tip-Enhanced Raman Spectroscopy. 116(1):478–483.

[186] Teng-Xiang Huang, Sheng-Chao Huang, Mao-Hua Li, Zhi-Cong Zeng, Xiang Wang, and Bin Ren. Tip-enhanced Raman spectroscopy: Tip-related issues. 407(27):8177–8195.

[187] Zhilin Yang, Qianhong Li, Yurui Fang, and Mengtao Sun. Deep ultraviolet tip-enhanced Raman scattering. 47(32):9131–9133.

[188] Vicki L. Schlegel and Therese M. Cotton. Silver-island films as substrates for enhanced Raman scattering: Effect of deposition rate on intensity. 63(3):241–247.

[189] Teng-Xiang Huang, Cha-Wei Li, Li-Kun Yang, Jin-Feng Zhu, Xu Yao, Chuan Liu, Kai-Qiang Lin, Zhi-Cong Zeng, Si-Si Wu, Xiang Wang, Fang-Zu Yang, and Bin Ren. Rational fabrication of silver-coated AFM TERS tips with a high enhancement and long lifetime. 10(9):4398–4405.

[190] Atsushi Taguchi, Jun Yu, Prabhat Verma, and Satoshi Kawata. Optical antennas with multiple plasmonic nanoparticles for tip-enhanced Raman microscopy. 7(41):17424–17433.

[191] Norihiko Hayazawa, Taka-aki Yano, and Satoshi Kawata. Highly reproducible tip-enhanced Raman scattering using an oxidized and metallized silicon cantilever tip as a tool for everyone: Tip-enhanced Raman scattering using an oxidized and metallized silicon cantilever tip. 43(9):1177–1182.

[192] Gaurav Sharma, Tanja Deckert-Gaudig, and Volker Deckert. Tip-enhanced Raman scattering—Targeting structure-specific surface characterization for biomedical samples. 89:42–56.

[193] P. B. Johnson and R. W. Christy. Optical Constants of the Noble Metals. 6(12):4370–4379.

[194] Naresh Kumar, Steve J. Spencer, Dario Imbraguglio, Andrea M. Rossi, Andrew J. Wain, Bert M. Weckhuysen, and Debdulal Roy. Extending the plasmonic lifetime of tip-enhanced Raman spectroscopy probes. 18(19):13710–13716.

[195] Naresh Kumar, Bert M. Weckhuysen, Andrew J. Wain, and Andrew J. Pollard. Nanoscale chemical imaging using tip-enhanced Raman spectroscopy. 14(4):1169–1193.

[196] Marie Richard-Lacroix, Yao Zhang, Zhenchao Dong, and Volker Deckert. Mastering high resolution tip-enhanced Raman spectroscopy: Towards a shift of perception. 46(13):3922–3944.

[197] Xiu-Mei Lin, Tanja Deckert-Gaudig, Prabha Singh, Michael Siegmann, Stephan Kupfer, Zhenglong Zhang, Stefanie Gräfe, and Volker Deckert. Direct Base-to-Base Transitions in ssDNA Revealed by Tip-Enhanced Raman Scattering.

[198] Tanja Deckert-Gaudig, Dmitry Kurouski, Martin A. B. Hedegaard, Pushkar Singh, Igor K. Lednev, and Volker Deckert. Spatially resolved spectroscopic differentiation of hydrophilic and hydrophobic domains on individual insulin amyloid fibrils. 6(1):33575.

[199] N. Uzunbajakava, A. Lenferink, Y. Kraan, E. Volokhina, G. Vrensen, J. Greve, and C. Otto. Nonresonant Confocal Raman Imaging of DNA and Protein Distribution in Apoptotic Cells. 84(6):3968–3981.

[200] Sébastien Bonhommeau and Sophie Lecomte. Tip-Enhanced Raman Spectroscopy: A Tool for Nanoscale Chemical and Structural Characterization of Biomolecules. 19(1):8–18.

[201] Nastaran Kazemi-Zanjani, Sylvain Vedraine, and François Lagugné-Labarthet. Localized enhancement of electric field in tip-enhanced Raman spectroscopy using radially and linearly polarized light. 21(21):25271–25276.

[202] Jordan M. Klingsporn, Nan Jiang, Eric A. Pozzi, Matthew D. Sonntag, Dhabih Chulhai, Tamar Seideman, Lasse Jensen, Mark C. Hersam, and Richard P. Van Duyne. Intramolecular Insight into Adsorbate–Substrate Interactions via Low-Temperature, Ultrahigh-Vacuum Tip-Enhanced Raman Spectroscopy. 136(10):3881–3887.

[203] Yoshito Okuno, Yuika Saito, Satoshi Kawata, and Prabhat Verma. Tip-Enhanced Raman Investigation of Extremely Localized Semiconductor-to-Metal Transition of a Carbon Nanotube. 111(21):216101.

[204] Taka-aki Yano, Taro Ichimura, Shota Kuwahara, Fekhra H'Dhili, Kazumasa Uetsuki, Yoshito Okuno, Prabhat Verma, and Satoshi Kawata. Tip-enhanced nano-Raman analytical imaging of locally induced strain distribution in carbon nanotubes. 4(1):2592.

[205] Taka-aki Yano, Prabhat Verma, Yuika Saito, Taro Ichimura, and Satoshi Kawata. Pressure-assisted tip-enhanced Raman imaging at a resolution of a few nanometres. 3(8):473–477.

[206] Y. Ogawa, Y. Yuasa, F. Minami, and S. Oda. Tip-enhanced Raman mapping of a single Ge nanowire. 99(5):053112.

[207] Sandro Mignuzzi, Naresh Kumar, Barry Brennan, Ian S. Gilmore, David

Richards, Andrew J. Pollard, and Debdulal Roy. Probing individual point defects in graphene via near-field Raman scattering. 7(46):19413–19418.

[208] Weitao Su, Naresh Kumar, Ning Dai, and Debdulal Roy. Nanoscale mapping of intrinsic defects in single-layer graphene using tip-enhanced Raman spectroscopy. 52(53):8227–8230.

[209] Andrew J. Pollard, Naresh Kumar, Alisdair Rae, Sandro Mignuzzi, Weitao Su, and Debdulal Roy. Nanoscale Optical Spectroscopy: An Emerging Tool for the Characterisation of 2 D Materials. 1(1):39–49.

[210] Weitao Su, Naresh Kumar, Steve J. Spencer, Ning Dai, and Debdulal Roy. Transforming bilayer MoS2 into single-layer with strong photoluminescence using UV-ozone oxidation. 8(12):3878–3886.

[211] Weitao Su, Naresh Kumar, Sandro Mignuzzi, Jason Crain, and Debdulal Roy. Nanoscale mapping of excitonic processes in single-layer MoS2 using tip-enhanced photoluminescence microscopy. 8(20):10564–10569.

[212] Kirby K. H. Smithe, Andrey V. Krayev, Connor S. Bailey, Hye Ryoung Lee, Eilam Yalon, Özgür Burak Aslan, Miguel Muñoz Rojo, Sergiy Krylyuk, Payam Taheri, Albert V. Davydov, Tony F. Heinz, and Eric Pop. Nanoscale Heterogeneities in Monolayer MoSe2 Revealed by Correlated Scanning Probe Microscopy and Tip-Enhanced Raman Spectroscopy. 1(2):572–579.

[213] Kyoung-Duck Park, Omar Khatib, Vasily Kravtsov, Genevieve Clark, Xiaodong Xu, and Markus B. Raschke. Hybrid Tip-Enhanced Nanospectroscopy and Nanoimaging of Monolayer WSe2 with Local Strain Control. 16(4):2621–2627.

[214] Evelien M. van Schrojenstein Lantman, Tanja Deckert-Gaudig, Arjan J. G. Mank, Volker Deckert, and Bert M. Weckhuysen. Catalytic pro-

cesses monitored at the nanoscale with tip-enhanced Raman spectroscopy. 7(9):583–586.

[215] N. Kumar, B. Stephanidis, R. Zenobi, A. J. Wain, and D. Roy. Nanoscale mapping of catalytic activity using tip-enhanced Raman spectroscopy. 7(16):7133–7137.

[216] Katrin F. Domke and Bruno Pettinger. In Situ Discrimination between Axially Complexed and Ligand-Free Co Porphyrin on Au(111) with Tip-Enhanced Raman Spectroscopy. 10(11):1794–1798.

[217] Jin-Hui Zhong, Xi Jin, Lingyan Meng, Xiang Wang, Hai-Sheng Su, Zhi-Lin Yang, Christopher T. Williams, and Bin Ren. Probing the electronic and catalytic properties of a bimetallic surface with 3 nm resolution. 12(2):132–136.

[218] Thomas Hartman, Caterina S. Wondergem, Naresh Kumar, Albert van den Berg, and Bert M. Weckhuysen. Surface- and Tip-Enhanced Raman Spectroscopy in Catalysis. 7(8):1570–1584.

[219] Jacek Szczerbiński, Luzia Gyr, Jérôme Kaeslin, and Renato Zenobi. Plasmon-Driven Photocatalysis Leads to Products Known from E-beam and X-ray-Induced Surface Chemistry. 18(11):6740–6749.

[220] Hacksung Kim, Kathryn M. Kosuda, Richard P. Van Duyne, and Peter C. Stair. Resonance Raman and surface- and tip-enhanced Raman spectroscopy methods to study solid catalysts and heterogeneous catalytic reactions. 39(12):4820–4844.

[221] Zhi-Cong Zeng, Sheng-Chao Huang, De-Yin Wu, Ling-Yan Meng, Mao-Hua Li, Teng-Xiang Huang, Jin-Hui Zhong, Xiang Wang, Zhi-Lin Yang, and Bin Ren. Electrochemical Tip-Enhanced Raman Spectroscopy. 137(37):11928–11931.

[222] Michael Mattei, Gyeongwon Kang, Guillaume Goubert, Dhabih V. Chulhai, George C. Schatz, Lasse Jensen, and Richard P. Van Duyne. Tip-Enhanced Raman Voltammetry: Coverage Dependence and Quantitative Modeling. 17(1):590–596.

[223] Naresh Kumar, Alasdair Rae, and Debdulal Roy. Accurate measurement of enhancement factor in tip-enhanced Raman spectroscopy through elimination of far-field artefacts. 104(12):123106.

[224] Boon-Siang Yeo, Esther Amstad, Thomas Schmid, Johannes Stadler, and Renato Zenobi. Nanoscale Probing of a Polymer-Blend Thin Film with Tip-Enhanced Raman Spectroscopy. 5(8):952–960.

[225] L. Xue, W. Li, G. G. Hoffmann, J. G. P. Goossens, J. Loos, and G. de With. High Resolution Tip Enhanced Raman Mapping on Polymer Thin Films. 305(1):73–80.

[226] Y. Saito, M. Motohashi, N. Hayazawa, M. Iyoki, and S. Kawata. Nanoscale characterization of strained silicon by tip-enhanced Raman spectroscope in reflection mode. 88(14):143109.

[227] Ute Neugebauer, Petra Rösch, Michael Schmitt, Jürgen Popp, Carine Julien, Akiko Rasmussen, Christian Budich, and Volker Deckert. On the Way to Nanometer-Sized Information of the Bacterial Surface by Tip-Enhanced Raman Spectroscopy. 7(7):1428–1430.

[228] Dana Cialla, Tanja Deckert-Gaudig, Christian Budich, Michael Laue, Robert Möller, Dieter Naumann, Volker Deckert, and Jürgen Popp. Raman to the limit: Tip-enhanced Raman spectroscopic investigations of a single tobacco mosaic virus. 40(3):240–243.

[229] R. Böhme, M. Richter, D. Cialla, P. Rösch, V. Deckert, and J. Popp. Towards a specific characterisation of components on a

cell surface—combined TERS-investigations of lipids and human cells. 40(10):1452–1457.

[230] Samar Najjar, David Talaga, Léonard Schué, Yannick Coffinier, Sabine Szunerits, Rabah Boukherroub, Laurent Servant, Vincent Rodriguez, and Sébastien Bonhommeau. Tip-Enhanced Raman Spectroscopy of Combed Double-Stranded DNA Bundles. 118(2):1174–1181.

[231] Elena Bailo and Volker Deckert. Tip-Enhanced Raman Spectroscopy of Single RNA Strands: Towards a Novel Direct-Sequencing Method. 47(9):1658–1661.

[232] Tanja Deckert-Gaudig and Volker Deckert. Tip-enhanced Raman scattering studies of histidine on novel silver substrates. 40(10):1446–1451.

[233] Carolin Blum, Thomas Schmid, Lothar Opilik, Simon Weidmann, Stephan R. Fagerer, and Renato Zenobi. Understanding tip-enhanced Raman spectra of biological molecules: A combined Raman, SERS and TERS study. 43(12):1895–1904.

[234] Boon-Siang Yeo, Stefanie Mädler, Thomas Schmid, Weihua Zhang, and Renato Zenobi. Tip-Enhanced Raman Spectroscopy Can See More: The Case of Cytochrome c. 112(13):4867–4873.

[235] Heather S. Davies, Prabha Singh, Tanja Deckert-Gaudig, Volker Deckert, Karine Rousseau, Caroline E. Ridley, Sarah E. Dowd, Andrew J. Doig, Paul D. A. Pudney, David J. Thornton, and Ewan W. Blanch. Secondary Structure and Glycosylation of Mucus Glycoproteins by Raman Spectroscopies. 88(23):11609–11615.

[236] Ewelina Lipiec, David Perez-Guaita, Janina Kaderli, Bayden R. Wood, and Renato Zenobi. Direct Nanospectroscopic Verification of the Amyloid Aggregation Pathway. 130(28):8655–8660.

[237] Naresh Kumar, Marek M. Drozdz, Haibo Jiang, Daniela M. Santos, and David J. Vaux. Nanoscale mapping of newly-synthesised phospholipid molecules in a biological cell using tip-enhanced Raman spectroscopy. 53(16):2451–2454.

[238] Faris Sinjab, Georgi Bondakov, and Ioan Notingher. Co-localised Raman and force spectroscopy reveal the roles of hydrogen bonds and π-π interactions in defining the mechanical properties of diphenylalanine nano- and micro-tubes. 104(25):251905.

[239] Youngbum Kim, Eun Ji Lee, Shrawan Roy, Anir S. Sharbirin, Lars-Gunnar Ranz, Thomas Dieing, and Jeongyong Kim. Measurement of lateral and axial resolution of confocal Raman microscope using dispersed carbon nanotubes and suspended graphene. 20(1):71–77.

[240] Lucas Langelüddecke, Prabha Singh, and Volker Deckert. Exploring the Nanoscale: Fifteen Years of Tip-Enhanced Raman Spectroscopy. 69(12):1357–1371.

[241] John Deacon. Model-view-controller (mvc) architecture.

[242] Welcome to Python.org.

[243] Qt | Cross-platform software development for embedded & desktop.

[244] B. M. Harwani. *Qt5 Python GUI Programming Cookbook: Building Responsive and Powerful Cross-Platform Applications with PyQt*. Packt.

[245] M. Fitzpatrick. *Create GUI Applications with Python & Qt5 (PyQt5 Edition): The Hands-on Guide to Making Apps with Python*. Martin Fitzpatrick.

[246] Dave Kuhlman. A Python Book: Beginning Python.

[247] Alexey Shkarin. AlexShkarin/pyLabLib.

[248] PyQtGraph - Scientific Graphics and GUI Library for Python.

[249] Robert Meyer, Xiaobin Yao, and Volker Deckert. Latest instrumental developments and bioanalytical applications in tip-enhanced Raman spectroscopy. 102:250–258.

[250] R. Drevinskas, M. Beresna, M. Gecevičius, A. Kazanskii, O. Konkov, Y. Svirko, and P. Kazansky. Radially polarized optical vortex microconverters imprinted by femtosecond laser nanostructuring in amorphous silicon.

[251] Yasuhiko Shimotsuma, Peter G. Kazansky, Jiarong Qiu, and Kazuoki Hirao. Self-Organized Nanogratings in Glass Irradiated by Ultrashort Light Pulses. 91(24):247405.

[252] S-waveplates (Radial Polarization Converters) | Altechna.

[253] Atte Haapalinna, Petri Kärhä, and Erkki Ikonen. Spectral reflectance of silicon photodiodes. 37(4):729.

[254] Martin A. Green and Mark J. Keevers. Optical properties of intrinsic silicon at 300 K. 3(3):189–192.

[255] David Tuschel. Raman Imaging of Silicon Structures. 28:9.

[256] Byumseok Koh and Wei Cheng. Mechanisms of Carbon Nanotube Aggregation and the Reversion of Carbon Nanotube Aggregates in Aqueous Medium. 30(36):10899–10909.

[257] Xiang Wang, Sheng-Chao Huang, Teng-Xiang Huang, Hai-Sheng Su, Jin-Hui Zhong, Zhi-Cong Zeng, Mao-Hua Li, and Bin Ren. Tip-enhanced Raman spectroscopy for surfaces and interfaces. 46(13):4020–4041.

[258] Brahim Akdim, Ruth Pachter, and Rajesh R. Naik. Self-assembled peptide nanotubes as electronic materials: An evaluation from first-principles calculations. 106(18):183707.

[259] Roberto de la Rica, Ernest Mendoza, Laura M. Lechuga, and Hiroshi Matsui. Label-free pathogen detection with sensor chips assembled from Peptide nanotubes. 47(50):9752–9755.

[260] Simon L. Porter, Sophie M. Coulter, Sreekanth Pentlavalli, and Garry Laverty. Pharmaceutical Formulation and Characterization of Dipeptide Nanotubes for Drug Delivery Applications. n/a(n/a):2000115.

[261] Qiuju Li, Min Chen, Daoyong Chen, and Limin Wu. One-Pot Synthesis of Diphenylalanine-Based Hybrid Nanospheres for Controllable pH- and GSH-Responsive Delivery of Drugs. 28(18):6584–6590.

[262] Meiwen Cao, Sha Lu, Ningning Wang, Hai Xu, Henry Cox, Ruiheng Li, Thomas Waigh, Yuchun Han, Yilin Wang, and Jian R. Lu. Enzyme-Triggered Morphological Transition of Peptide Nanostructures for Tumor-Targeted Drug Delivery and Enhanced Cancer Therapy. 11(18):16357–16366.

[263] Silvia Marchesan, Attilio V. Vargiu, and Katie E. Styan. The Phe-Phe Motif for Peptide Self-Assembly in Nanomedicine. 20(11):19775–19788.

[264] Banyat Lekprasert, Vladimir Korolkov, Alexandra Falamas, Vasile Chis, Clive J. Roberts, Saul J. B. Tendler, and Ioan Notingher. Investigations of the Supramolecular Structure of Individual Diphenylalanine Nano- and Microtubes by Polarized Raman Microspectroscopy. 13(7):2181–2187.

[265] Reem Alshehri, Asad Muhammad Ilyas, Anwarul Hasan, Adnan Arnaout, Farid Ahmed, and Adnan Memic. Carbon Nanotubes in Biomedical Ap-

plications: Factors, Mechanisms, and Remedies of Toxicity. 59(18):8149–8167.

[266] Jianxin Zhang, Matthew Bunker, Andrew Parker, Claire E. Madden-Smith, Nikin Patel, and Clive J. Roberts. The stability of solid dispersions of felodipine in polyvinylpyrrolidone characterized by nanothermal analysis. 414(1):210–217.

[267] Renliang Huang, Wei Qi, Rongxin Su, Jun Zhao, and Zhimin He. Solvent and surface controlled self-assembly of diphenylalanine peptide: From microtubes to nanofibers. 7(14):6418.

[268] Naila A. Mugheirbi, Patrick J. Marsac, and Lynne S. Taylor. Insights into Water-Induced Phase Separation in Itraconazole–Hydroxypropylmethyl Cellulose Spin Coated and Spray Dried Dispersions. 14(12):4387–4402.

[269] Thomas Schmid, Lothar Opilik, Carolin Blum, and Renato Zenobi. Nanoscale chemical imaging using tip-enhanced Raman spectroscopy: A critical review. 52(23):5940–5954.

[270] Carl Henrik Görbitz. Nanotube Formation by Hydrophobic Dipeptides. 7(23):5153–5159.

[271] Carl Henrik Görbitz. The structure of nanotubes formed by diphenylalanine, the core recognition motif of Alzheimer's β-amyloid polypeptide. (22):2332–2334.

[272] Guodong Zhang, Razvan Stoian, Wei Zhao, and Guanghua Cheng. Femtosecond laser Bessel beam welding of transparent to non-transparent materials with large focal-position tolerant zone. 26(2):917–926.

[273] Hiroaki Hanafusa, Nobumitsu Hirose, Akifumi Kasamatsu, Takashi Mimura, Toshiaki Matsui, Harold M. H. Chong, Hiroshi Mizuta, and

Yoshiyuki Suda. Strain Distribution Analysis of Sputter-Formed Strained Si by Tip-Enhanced Raman Spectroscopy. 4(2):025701.

[274] Taro Ichimura, Hiroyuki Watanabe, Yasuhiro Morita, Prabhat Verma, Satoshi Kawata, and Yasushi Inouye. Temporal Fluctuation of Tip-Enhanced Raman Spectra of Adenine Molecules. 111(26):9460–9464.

[275] Kai-Qiang Lin, Jun Yi, Jin-Hui Zhong, Shu Hu, Bi-Ju Liu, Jun-Yang Liu, Cheng Zong, Zhi-Chao Lei, Xiang Wang, Javier Aizpurua, Rubén Esteban, and Bin Ren. Plasmonic photoluminescence for recovering native chemical information from surface-enhanced Raman scattering. 8(1):14891.

[276] Maggie L. Weber, Jonathan P. Litz, David J. Masiello, and Katherine A. Willets. Super-Resolution Imaging Reveals a Difference between SERS and Luminescence Centroids. 6(2):1839–1848.

[277] The Surface Science Society of Japa, editor. *Compendium of Surface and Interface Analysis*. Springer Singapore.

[278] Mehdi Asghari-Khiavi, Bayden R. Wood, Pejman Hojati-Talemi, Andrew Downes, Don McNaughton, and Adam Mechler. Exploring the origin of tip-enhanced Raman scattering; preparation of efficient TERS probes with high yield. 43(2):173–180.

[279] Weihua Zhang, Xudong Cui, and Olivier J. F. Martin. Local field enhancement of an infinite conical metal tip illuminated by a focused beam. 40(10):1338–1342.

[280] I. Martina, R. Wiesinger, and M. Schreiner. Micro-Raman investigations of early stage silver corrosion products occurring in sulfur containing atmospheres. 44(5):770–775.

[281] Feng Shao and Renato Zenobi. Tip-enhanced Raman spectroscopy: Principles, practice, and applications to nanospectroscopic imaging of 2D materials. 411(1):37–61.

[282] Hans F. M. Boelens, Paul H. C. Eilers, and Thomas Hankemeier. Sign Constraints Improve the Detection of Differences between Complex Spectral Data Sets: LC-IR As an Example. 77(24):7998–8007.

[283] Marc Offroy, Yves Roggo, Peyman Milanfar, and Ludovic Duponchel. Infrared chemical imaging: Spatial resolution evaluation and super-resolution concept. 674(2):220–226.

[284] Debdulal Roy, Jian Wang, and Craig Williams. Novel methodology for estimating the enhancement factor for tip-enhanced Raman spectroscopy. 105(1):013530.

[285] Acetaminophen - Raman Spectrum - SpectraBase.

[286] Jagadeesh Babu Nanubolu and Jonathan C. Burley. Investigating the Recrystallization Behavior of Amorphous Paracetamol by Variable Temperature Raman Studies and Surface Raman Mapping. 9(6):1544–1558.

[287] Jacek Szczerbiński, Jonas B. Metternich, Guillaume Goubert, and Renato Zenobi. How Peptides Dissociate in Plasmonic Hot Spots. 16(4):1905197.

[288] Marie Richard-Lacroix and Volker Deckert. Direct molecular-level near-field plasmon and temperature assessment in a single plasmonic hotspot. 9(1):35.

[289] Sarhan M. Musa and Anchal Srivastava. *Optics: An Introduction*. Mercury Learning and Information, reprinted and revised edition.

[290] David Tuschel. Raman Thermometry.

[291] Marta Quintanilla and Luis M. Liz-Marzán. Guiding Rules for Selecting a Nanothermometer. 19:126–145.

[292] Myeongsub Mike Kim, Alexandre Giry, Mohammad Mastiani, Gustavo O. Rodrigues, Alessandro Reis, and Philippe Mandin. Microscale thermometry: A review. 148:129–142.

[293] Andri M. Gretarsson. *A First Course in Laboratory Optics*. Cambridge University Press, 1 edition.

[294] John C. Fisher. The power density of a surgical laser beam: Its meaning and measurement. 2(4):301–315.

[295] Tony J Collins. ImageJ for microscopy. 43(S1):S25–S30.

[296] Wenjamin Rosenfeld. Open Beam Profiler.

[297] David Tuschel. Raman Thermometry: Understanding the Mathematics to Better Design Raman Measurements.

[298] Jake VanderPlas. *Python Data Science Handbook: Essential Tools for Working with Data*. O'Reilly Media, Inc., 1st edition.

[299] Sarah Al-Dulaimi, Adeyinka Aina, and Jonathan Burley. Rapid polymorph screening on milligram quantities of pharmaceutical material using phonon-mode Raman spectroscopy. 12(4):1038–1040.

[300] H. Wayne Nesbitt, G. Michael Bancroft, and Grant S. Henderson. Temperature dependence of Raman shifts and line widths for Q0 and Q2 crystals of silicates, phosphates, and sulfates. 103(6):966–976.

[301] PubChem. Acetaminophen.

[302] Sumeet Mahajan, Robin M. Cole, Jonathon D. Speed, Suzanne H. Pelfrey, Andrea E. Russell, Philip N. Bartlett, Stephen M. Barnett, and Jeremy J.

Baumberg. Understanding the Surface-Enhanced Raman Spectroscopy "Background". 114(16):7242–7250.

[303] Tamitake Itoh, Vasudevanpillai Biju, Mitsuru Ishikawa, Yasuo Kikkawa, Kazuhiro Hashimoto, Akifumi Ikehata, and Yukihiro Ozaki. Surface-enhanced resonance Raman scattering and background light emission coupled with plasmon of single Ag nanoaggregates. 124(13):134708.

[304] Catalin C. Neacsu, Samuel Berweger, and Markus B. Raschke. Tip-Enhanced Raman Imaging and Nanospectroscopy: Sensitivity, Symmetry, and Selection Rules. 3(3):172–196.

[305] Miriam Böhmler and Achim Hartschuh. Tip-Enhanced Near-Field Optical Microscopy of Quasi-1 D Nanostructures. 13(4):927–929.

[306] L. G. Cançado, A. Jorio, A. Ismach, E. Joselevich, A. Hartschuh, and L. Novotny. Mechanism of Near-Field Raman Enhancement in One-Dimensional Systems. 103(18):186101.

[307] Vincenzo Taresco, Iria Louzao, David Scurr, Jonathan Booth, Kevin Treacher, James McCabe, Eleanor Turpin, Charles A. Laughton, Cameron Alexander, Jonathan C. Burley, and Martin C. Garnett. Rapid Nanogram Scale Screening Method of Microarrays to Evaluate Drug–Polymer Blends Using High-Throughput Printing Technology. 14(6):2079–2087.

[308] P. Y. Sacré, C. De Bleye, P. F. Chavez, L. Netchacovitch, Ph. Hubert, and E. Ziemons. Data processing of vibrational chemical imaging for pharmaceutical applications. 101:123–140.

[309] Jianxin Zhang, Stephen Ebbens, Xinyong Chen, Zheng Jin, Shen Luk, Claire Madden, Nikin Patel, and Clive J. Roberts. Determination of the

Surface Free Energy of Crystalline and Amorphous Lactose by Atomic Force Microscopy Adhesion Measurement. 23(2):401–407.

[310] Johannes Stadler, Benedikt Oswald, Thomas Schmid, and Renato Zenobi. Characterizing unusual metal substrates for gap-mode tip-enhanced Raman spectroscopy. 44(2):227–233.

[311] M. Futamata, Y. Maruyama, and M. Ishikawa. Local electric field and scattering cross section of Ag nanoparticles under surface plasmon resonance by finite difference time domain method. 107(31):7607–7617.

[312] Eric A. Pozzi, Guillaume Goubert, Naihao Chiang, Nan Jiang, Craig T. Chapman, Michael O. McAnally, Anne-Isabelle Henry, Tamar Seideman, George C. Schatz, Mark C. Hersam, and Richard P. Van Duyne. Ultrahigh-Vacuum Tip-Enhanced Raman Spectroscopy. 117(7):4961–4982.

[313] Prabhat Verma, Kohei Yamada, Hiroyuki Watanabe, Yasushi Inouye, and Satoshi Kawata. Near-field Raman scattering investigation of tip effects on ${\mathrm{C}}_{60}$ molecules. 73(4):045416.

[314] Sébastien Bonhommeau, David Talaga, Julien Hunel, Christophe Cullin, and Sophie Lecomte. Tip-Enhanced Raman Spectroscopy to Distinguish Toxic Oligomers from Aβ1–42 Fibrils at the Nanometer Scale. 56(7):1771–1774.

[315] Bojan Zikic, Andrew Bremner, David Talaga, Sophie Lecomte, and Sébastien Bonhommeau. Tip-enhanced Raman spectroscopy of Aβ(1-42) fibrils. 768:138400.

[316] Sheila Hernandez, Juan V. Perales-Rondon, Alvaro Arnaiz, Martin Perez-Estebanez, Elvira Gomez, Alvaro Colina, and Aranzazu Heras. Determi-

nation of nicotinamide in a multivitamin complex by electrochemical-surface enhanced Raman spectroscopy. 879:114743.

[317] Raman spectrum of Polyvinyl alcohol | PublicSpectra.

Appendices

Appendix A

Supplementary information part-I

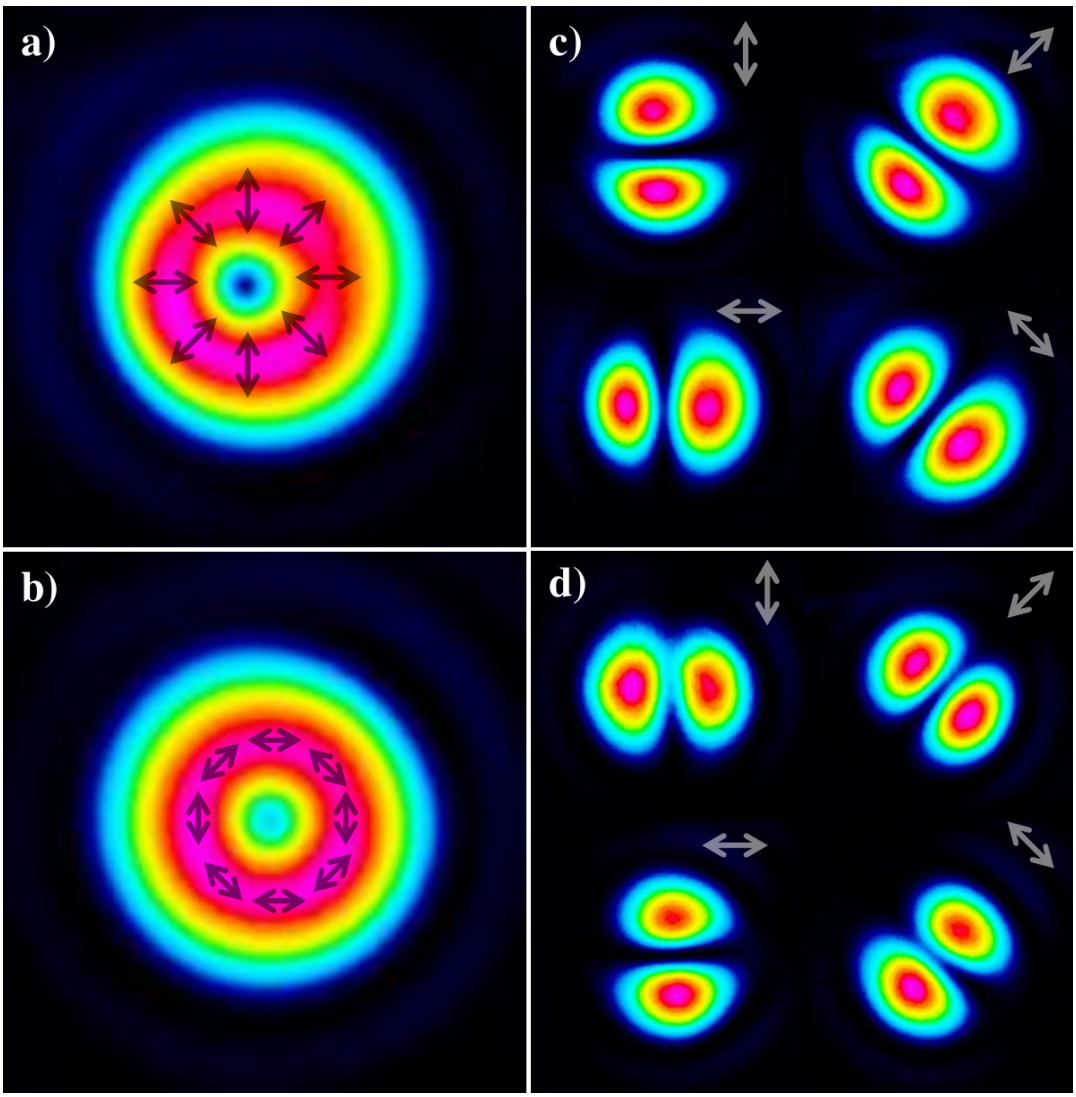

Figure A.1: HeNe laser a) radial and b) azimuth polarization intensity distributions measured with CCD camera. Measured intensity distributions c) radial and d) azimuth - linear polarizer (at different angles) was placed after converter. White arrow indicates polarizer orientation [252].

Appendix B

Supplementary information part-II

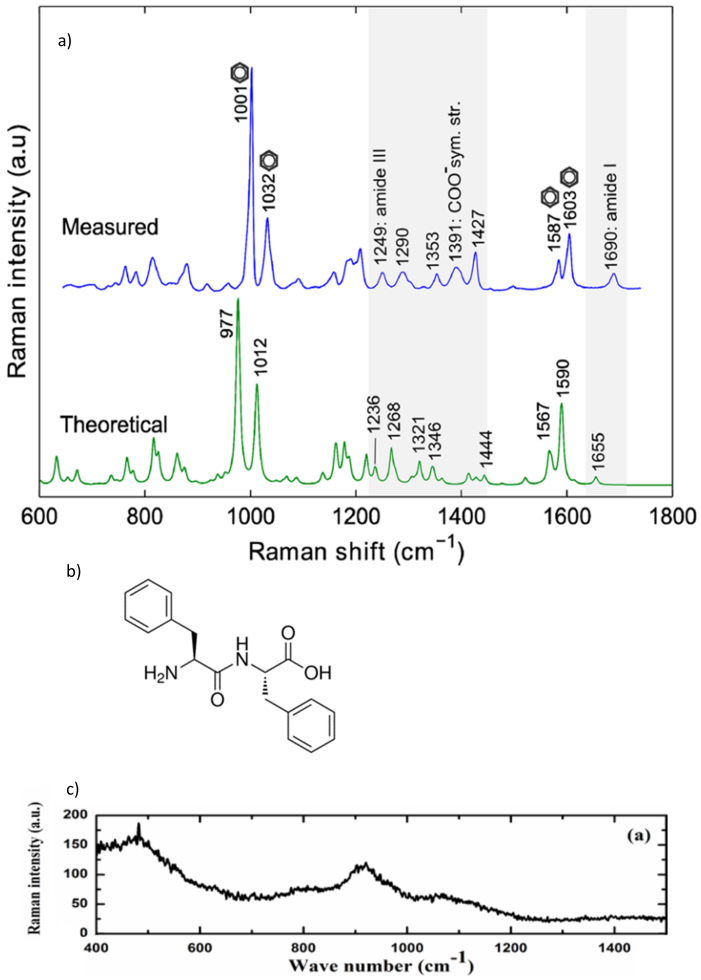

Figure B.1: Reference Raman spectra of a) L-Diphenylalanine tube [264], accompanied with the b) chemical structure of a LL-Diphenylalanine molecule and c) spectra of borosilicate glass [272].

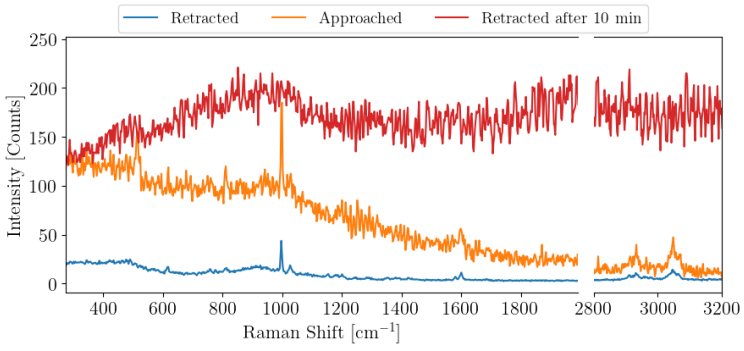

Figure B.2: Far-field spectrum of Phe-Phe sample before (blue) and after 10 min (red) of irradiation, with 10 s exposure time at 548 µW of laser power. Near-field spectrum of Phe-Phe sample under engaged probe (orange), with 10 s exposure at 117 µW of laser power.

(a)

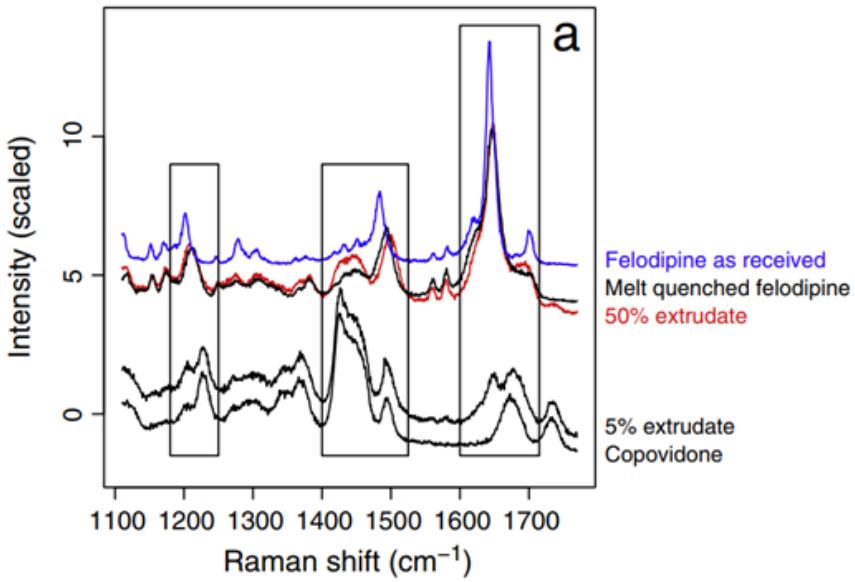

(b)

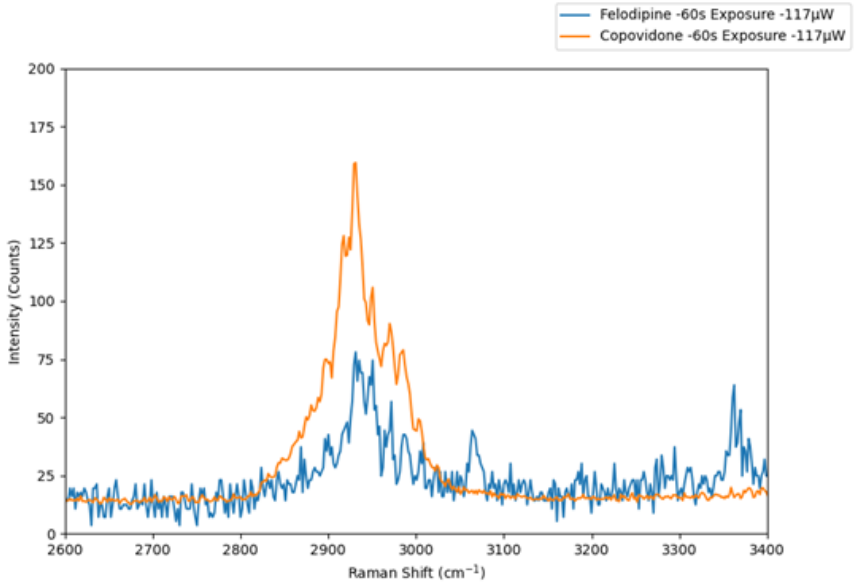

Figure B.3: a) Reference spectra of pure Felodipine, pure Copovidone and their 5% and 50% extrudates mixture, obtained from literature [73]. b) Reference spectra of pure Felodipine and Copovidone at the -CH stretch region of the spectrum, with 60 s exposure at 117 μW laser power.

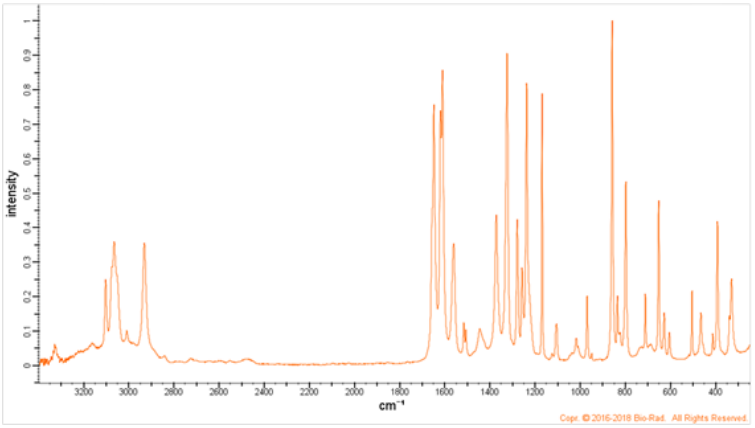

Figure B.4: Raman spectra of Pure Paracetamol sample acquired from SpectraBase™ database [285].

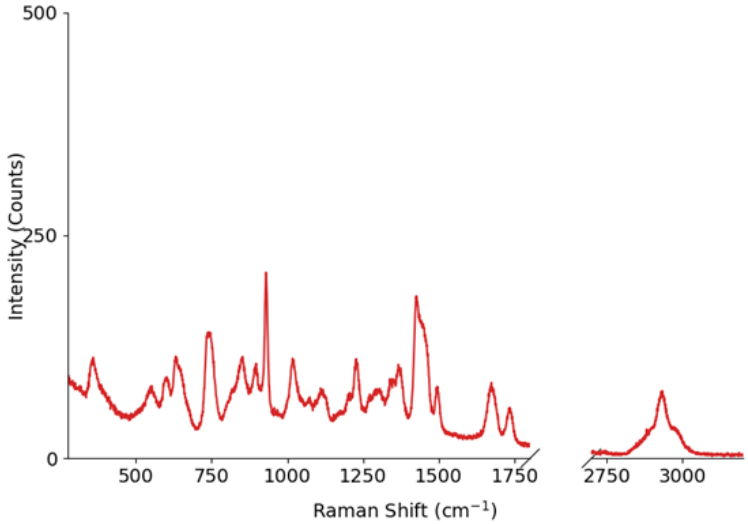

Figure B.5: Raman spectra of Pure Copovidone sample (Kollidon VA64™) obtained from published literature [73].

Appendix C

Supplementary information part-III

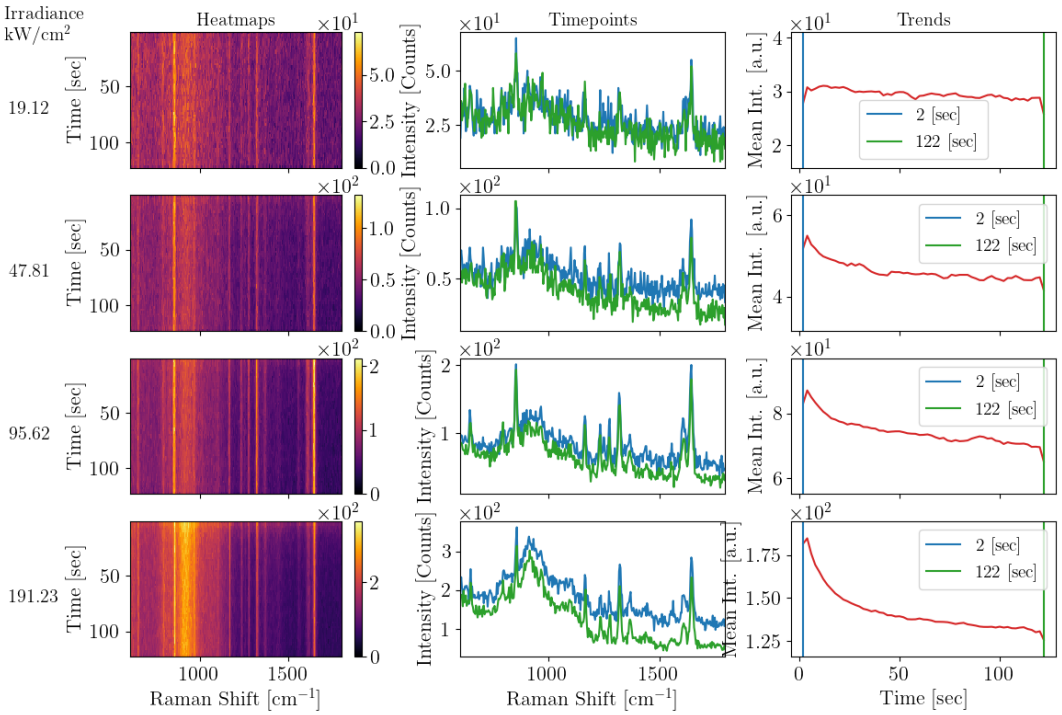

Figure C.1: Time series of Raman spectra on Paracetamol with 2 seconds exposure, on the LabRAM CRM using the 0.55 NA objective. Each row displays measurements of increasing area power density (4.78 kW/cm^2, 11.95 kW/cm^2, 23.9 kW/cm^2, 47.81 kW/cm^2). Each column from left to right shows heat-maps of spectra for each measurement, the time points of single spectra and the mean value of each spectra as a function of time (seconds). Each vertical colour line represent the time point of the spectra from the second column graphs.

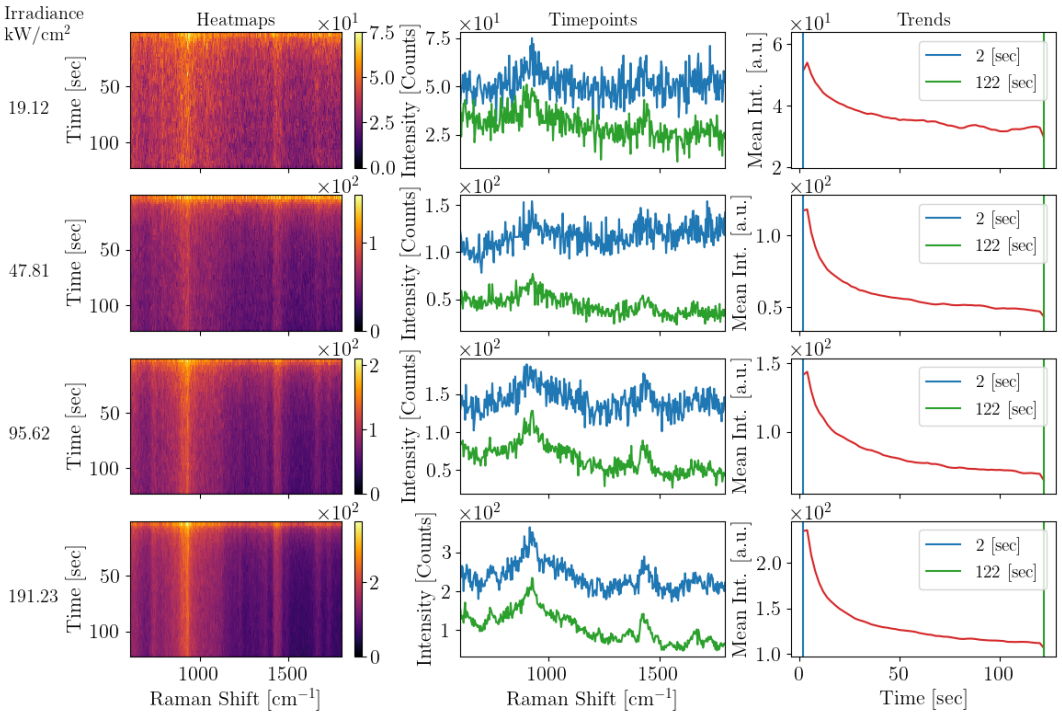

Figure C.2: Time series of Raman spectra on Copovidone with 2 seconds exposure, on the LabRAM CRM using the 0.55 NA objective. Each row displays measurements of increasing area power density (4.78 kW/cm^2, 11.95 kW/cm^2, 23.9 kW/cm^2, 47.81 kW/cm^2). Each column from left to right shows heat-maps of spectra for each measurement, the time points of single spectra and the mean value of each spectra as a function of time (seconds). Each vertical colour line represent the time point of the spectra from the second column graphs.

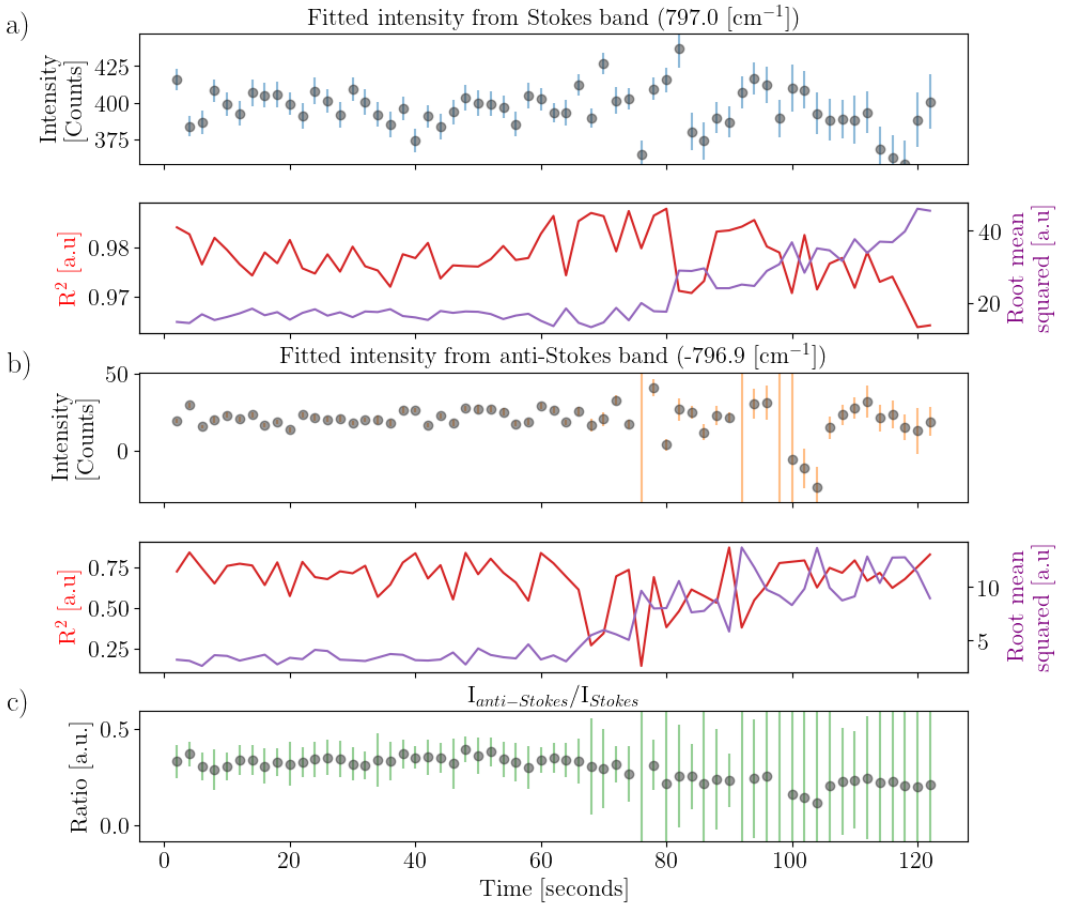

Figure C.3: Fitted intensity of paracetamol data, across all time-points acquired on the AFM-CRM instrument using the 1.45 NA objective, irradiated with 3 mW of laser power (1990.8 kW/cm^2) of the 797 cm^{-1} band. a) shows the fitted intensity of the Stokes band in each point alongside with their ESD errors (blue lines). Beneath it, the calculated R^2 and the RMS error are plotted against the time points acquired. b) shows the fitted intensity of the anti-Stokes band in each point alongside with their ESD errors (orange lines). Beneath it, the calculated R^2 and the RMS error are plotted against the time points acquired. c) displays the ratio of the $I_{anti\text{-}Stokes}/I_{Stokes}$, alongside with their ESD errors (green lines).

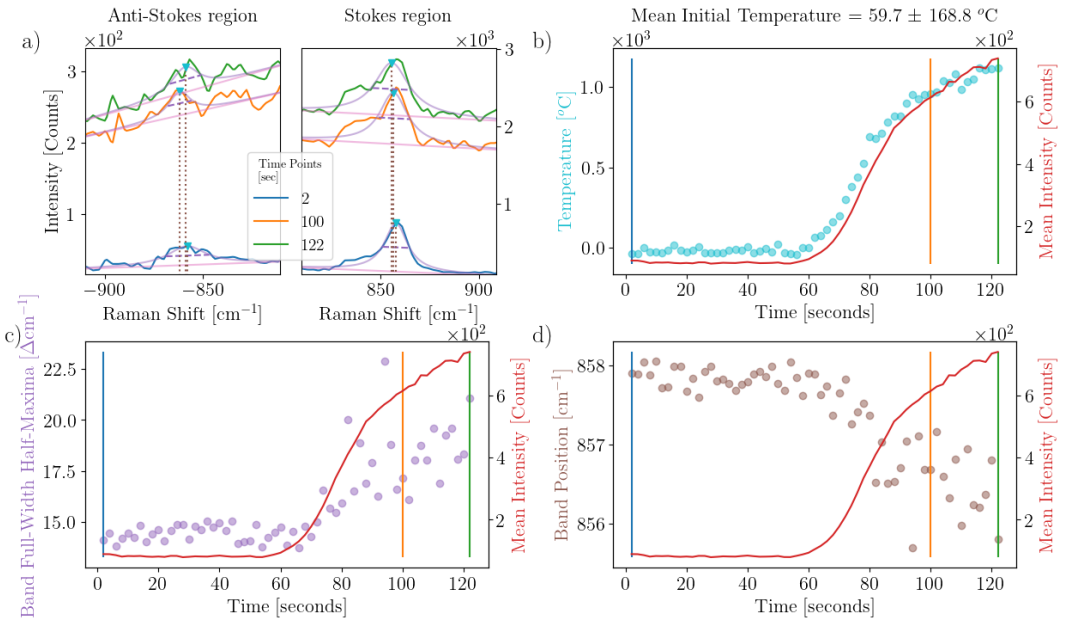

Figure C.4: Thermometry of paracetamol, with time-series spectra acquired on the AFM-CRM instrument using the 1.45 NA objective (as shown in Figure 4.3), irradiated with 1.5 mW laser power (1990.8 kW/cm^2). Symmetric bands at 857.9 cm^1, in both Stokes and anti-Stokes region were selected (a) and analysed. b), c) and d) display the mean value of spectra (red line) alongside the calculated temperature (cyan dots) from the I_{AS}/I_S, the change in FWHM (purple dots) as well as the shift (brown dots) of the Raman bands, respectively, as a function of time. Grey vertical line indicates the time threshold, where photoluminescence background is first observed.

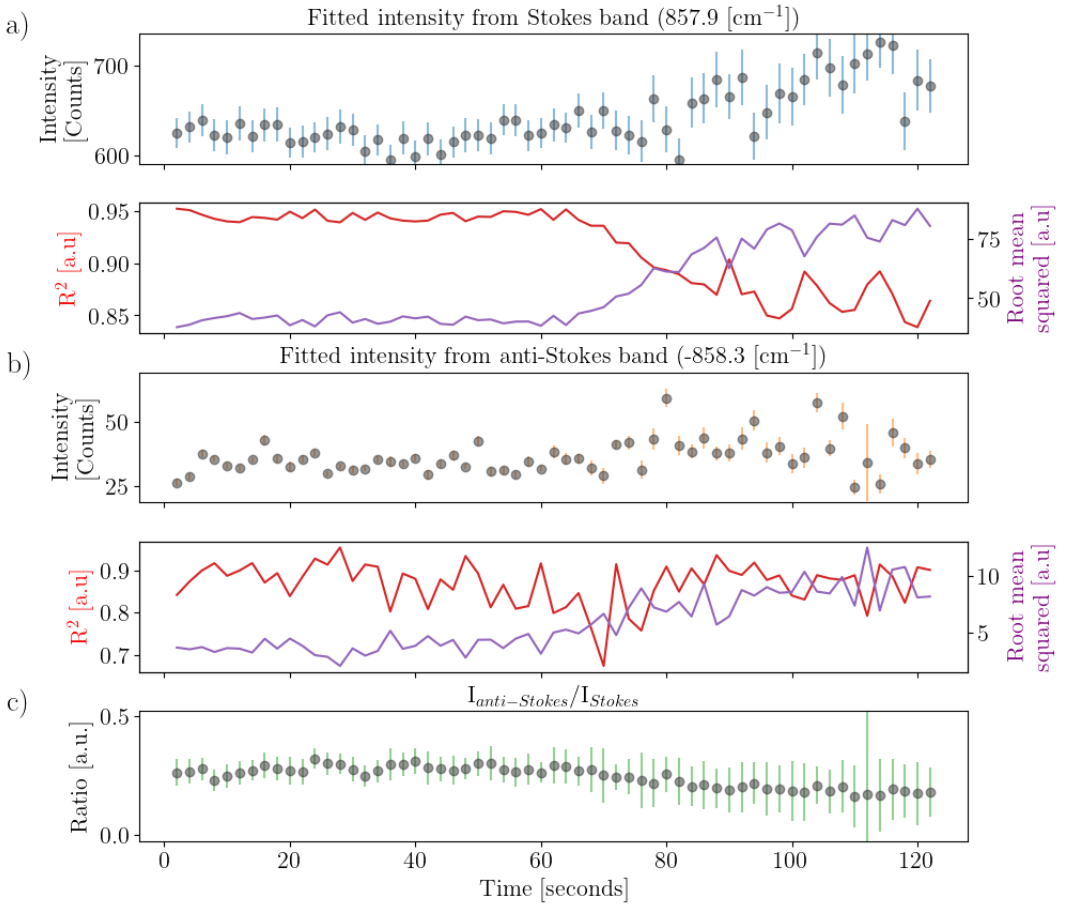

Figure C.5: Fitted intensity of paracetamol data, across all time-points acquired on the AFM-CRM instrument using the 1.45 NA objective, irradiated with 3 mW of laser power (1990.8 kW/cm^2) of the 857.9 cm^1 band. a) shows the fitted intensity of the Stokes band in each point alongside with their ESD errors (blue lines). Beneath it, the calculated R^2 and the RMS error are plotted against the time points acquired. b) shows the fitted intensity of the anti-Stokes band in each point alongside with their ESD errors (orange lines). Beneath it, the calculated R^2 and the RMS error are plotted against the time points acquired. c) displays the ratio of the $I_{anti\text{-}Stokes}/I_{Stokes}$, alongside with their ESD errors (green lines).

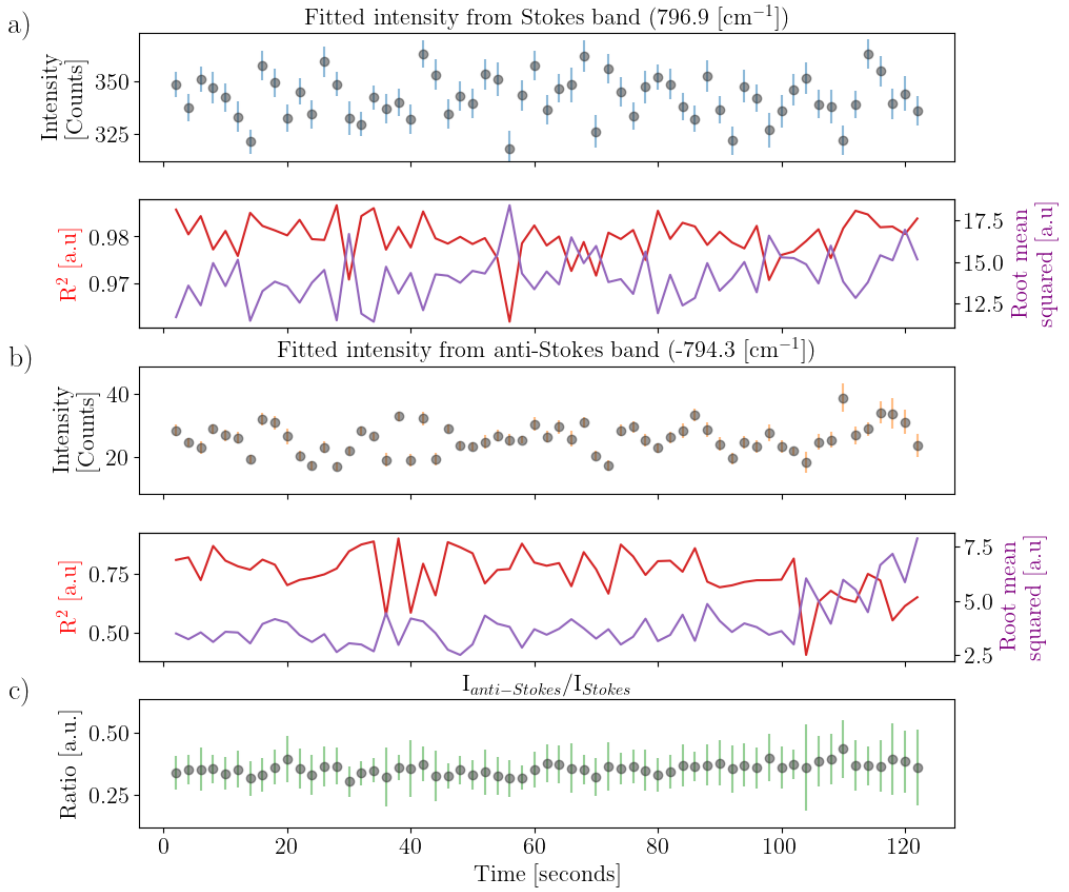

Figure C.6: Fitted intensity of paracetamol data, across all time-points acquired on the AFM-CRM instrument using the 1.45 NA objective, irradiated with 1.5 mW of laser power (1990.8 kW/cm^2) of the 797 cm^{-1} band. a) shows the fitted intensity of the Stokes band in each point alongside with their ESD errors (blue lines). Beneath it, the calculated R^2 and the RMS error are plotted against the time points acquired. b) shows the fitted intensity of the anti-Stokes band in each point alongside with their ESD errors (orange lines). Beneath it, the calculated R^2 and the RMS error are plotted against the time points acquired. c) displays the ratio of the $I_{anti\text{-}Stokes}/I_{Stokes}$, alongside with their ESD errors (green lines).

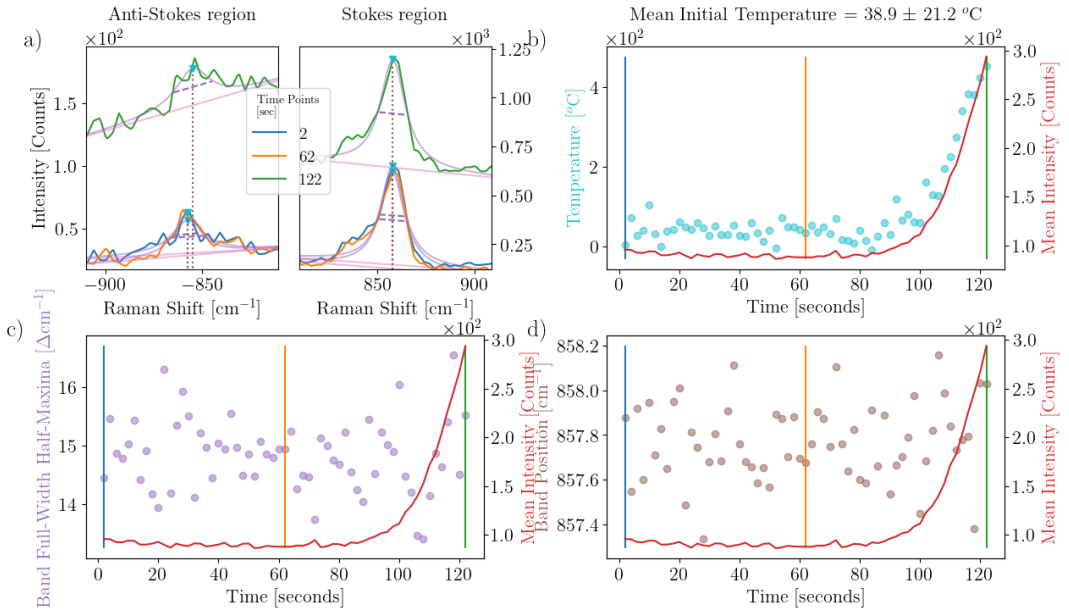

Figure C.7: Thermometry of paracetamol, with time-series spectra acquired on the AFM-CRM instrument using the 1.45 NA objective (as shown in Figure 4.3), irradiated with 1.5 mW laser power (995.4 kW/cm^2). Symmetric bands at 857.9 cm^1, in both Stokes and anti-Stokes region were selected (a) and analysed. b), c) and d) display the mean value of spectra (red line) alongside the calculated temperature (cyan dots) from the I_{AS}/I_S, the change in FWHM (purple dots) as well as the shift (brown dots) of the Raman bands, respectively, as a function of time. Grey vertical line indicates the time threshold, where photoluminescence background is first observed.

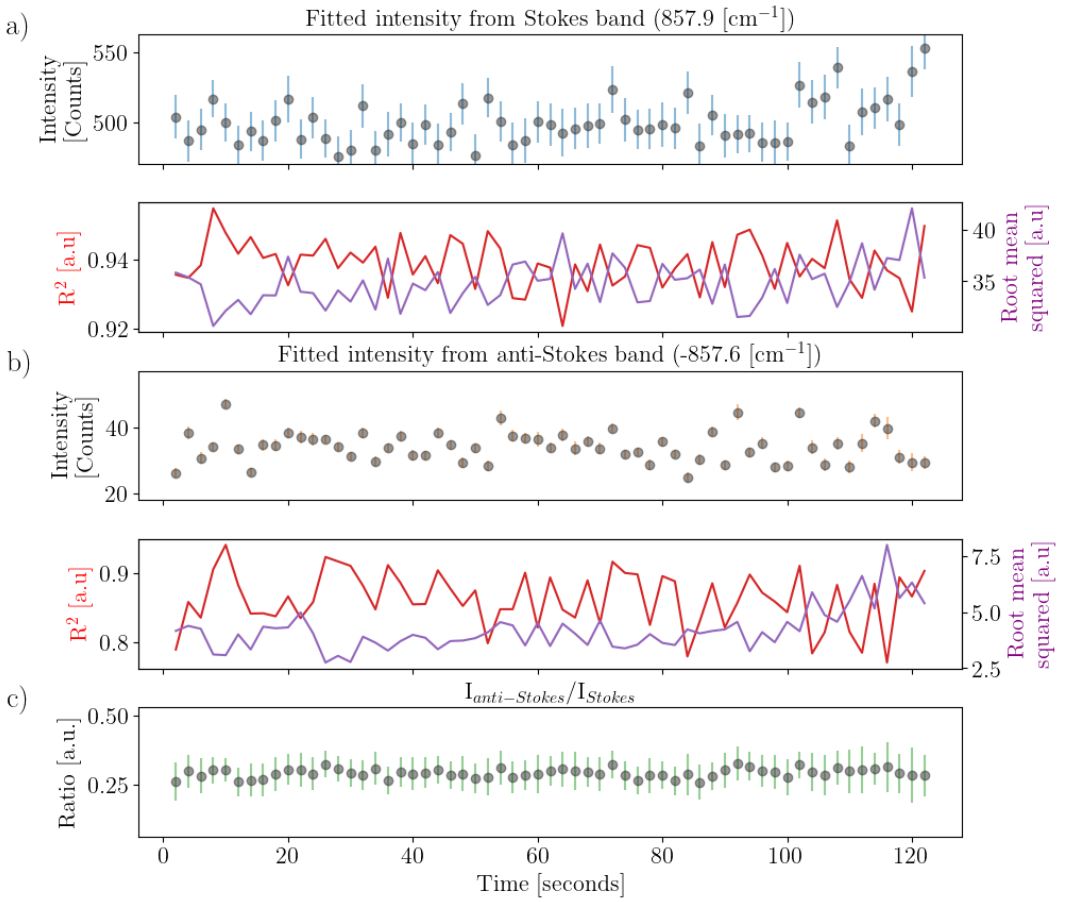

Figure C.8: Fitted intensity of paracetamol data, across all time-points acquired on the AFM-CRM instrument using the 1.45 NA objective, irradiated with 1.5 mW of laser power (995.4 kW/cm^2) of the 857.9 cm^{-1} band. a) shows the fitted intensity of the Stokes band in each point alongside with their ESD errors (blue lines). Beneath it, the calculated R^2 and the RMS error are plotted against the time points acquired. b) shows the fitted intensity of the anti-Stokes band in each point alongside with their ESD errors (orange lines). Beneath it, the calculated R^2 and the RMS error are plotted against the time points acquired. c) displays the ratio of the $I_{anti\text{-}Stokes}/I_{Stokes}$, alongside with their ESD errors (green lines).

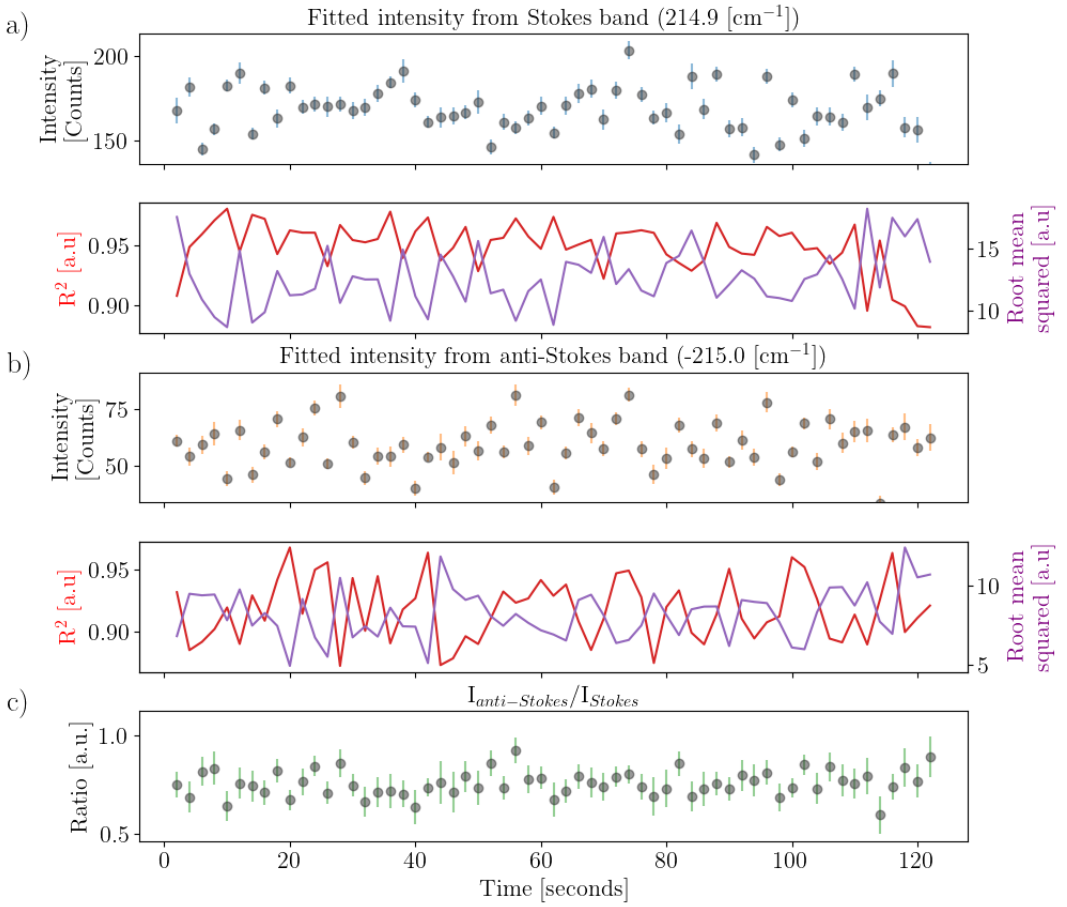

Figure C.9: Fitted intensity of paracetamol data, across all time-points acquired on the AFM-CRM instrument using the 0.8 NA objective, irradiated with 25 mW of laser power (954.08 kW/cm^2) of the 214.9 cm^{-1} band. a) shows the fitted intensity of the Stokes band in each point alongside with their ESD errors (blue lines). Beneath it, the calculated R^2 and the RMS error are plotted against the time points acquired. b) shows the fitted intensity of the anti-Stokes band in each point alongside with their ESD errors (orange lines). Beneath it, the calculated R^2 and the RMS error are plotted against the time points acquired. c) displays the ratio of the $I_{\text{anti-Stokes}}/I_{\text{Stokes}}$, alongside with their ESD errors (green lines).

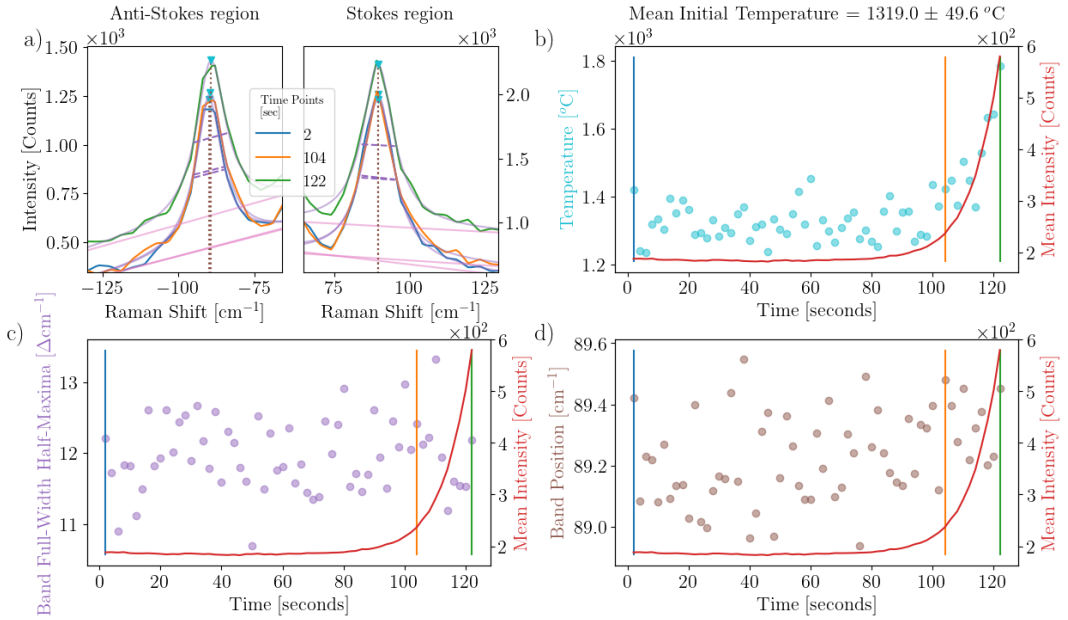

Figure C.10: Thermometry of paracetamol, with time-series spectra acquired on the LabRAM CRM instrument using the 0.8 NA objective (as shown in Figure 4.4), irradiated with 25 mW laser power (954.08 kW/cm^2). Symmetric bands at 89.4 cm^1, in both Stokes and anti-Stokes region were selected (a) and analysed. b), c) and d) display the mean value of spectra (red line) alongside the calculated temperature (cyan dots) from the I_{AS}/I_S, the change in FWHM (purple dots) as well as the shift (brown dots) of the Raman bands, respectively, as a function of time. Grey vertical line indicates the time threshold, where photoluminescence background is first observed.

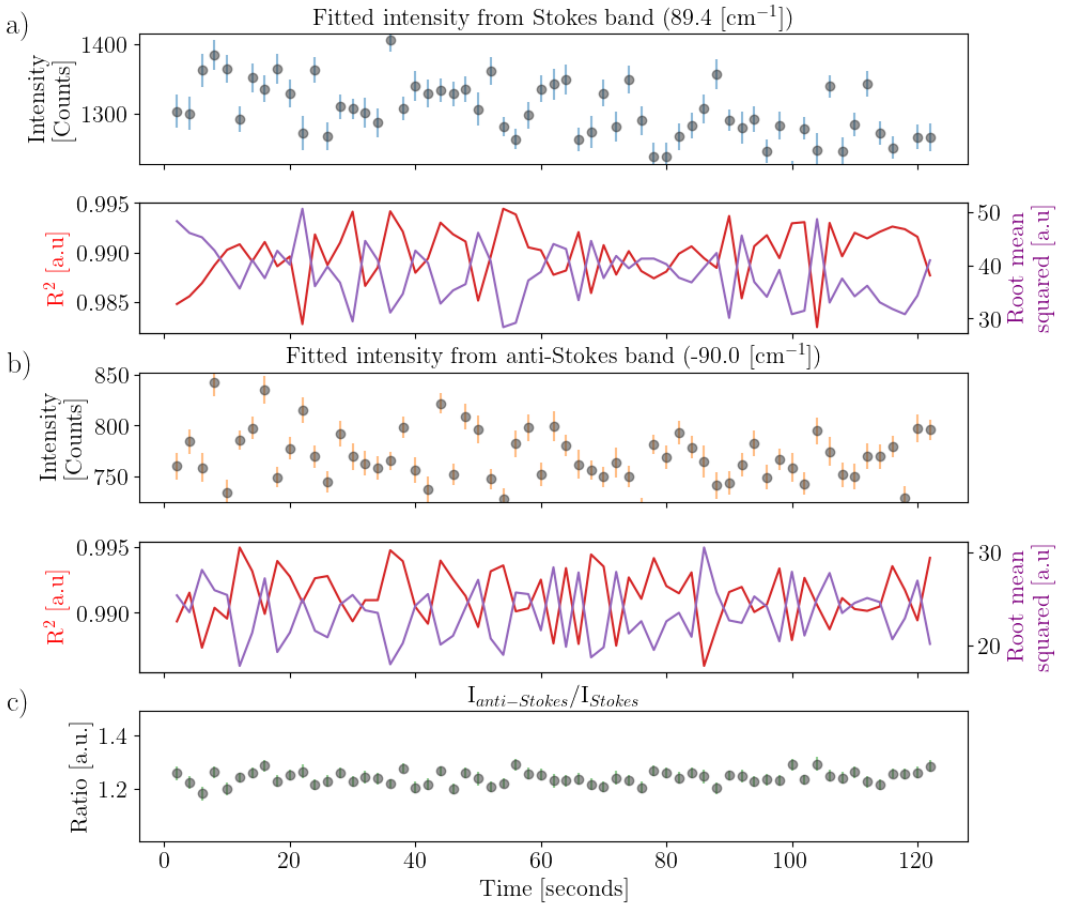

Figure C.11: Fitted intensity of paracetamol data, across all time-points acquired on the AFM-CRM instrument using the 0.8 NA objective, irradiated with 25 mW of laser power (954.08 kW/cm^2) of the 89.4 cm^{-1} band. a) shows the fitted intensity of the Stokes band in each point alongside with their ESD errors (blue lines). Beneath it, the calculated R^2 and the RMS error are plotted against the time points acquired. b) shows the fitted intensity of the anti-Stokes band in each point alongside with their ESD errors (orange lines). Beneath it, the calculated R^2 and the RMS error are plotted against the time points acquired. c) displays the ratio of the $I_{\text{anti-Stokes}}/I_{\text{Stokes}}$, alongside with their ESD errors (green lines).

Appendix D

Supplementary information part-IV

(a)

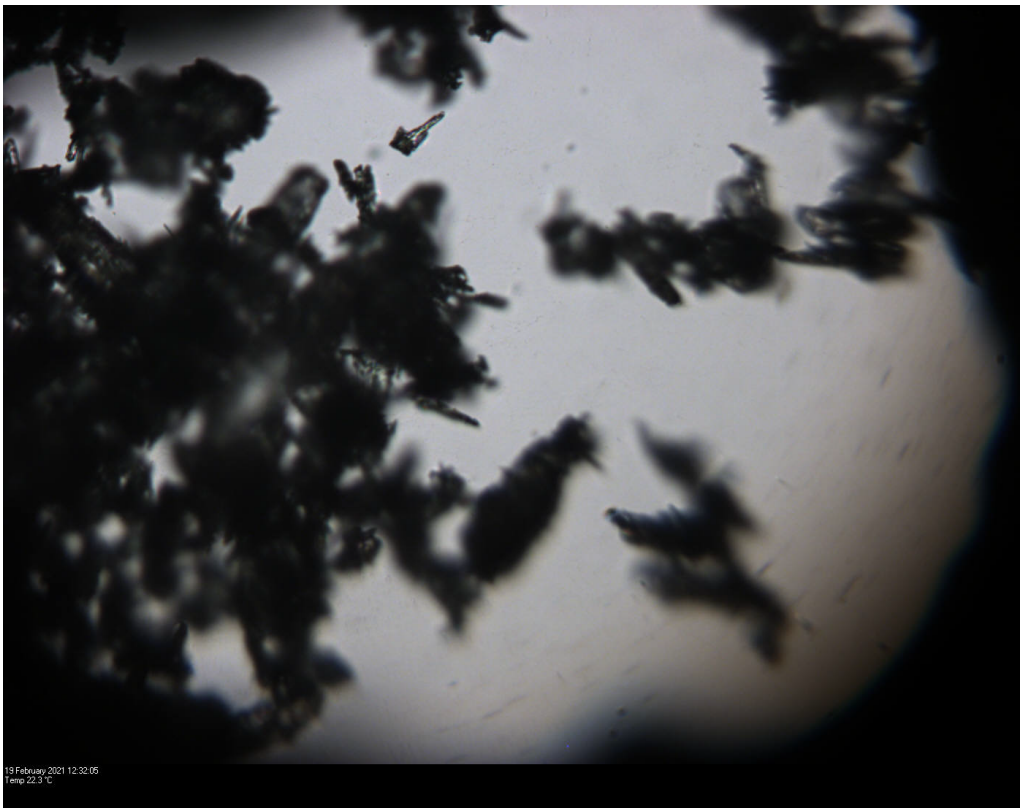

(b)

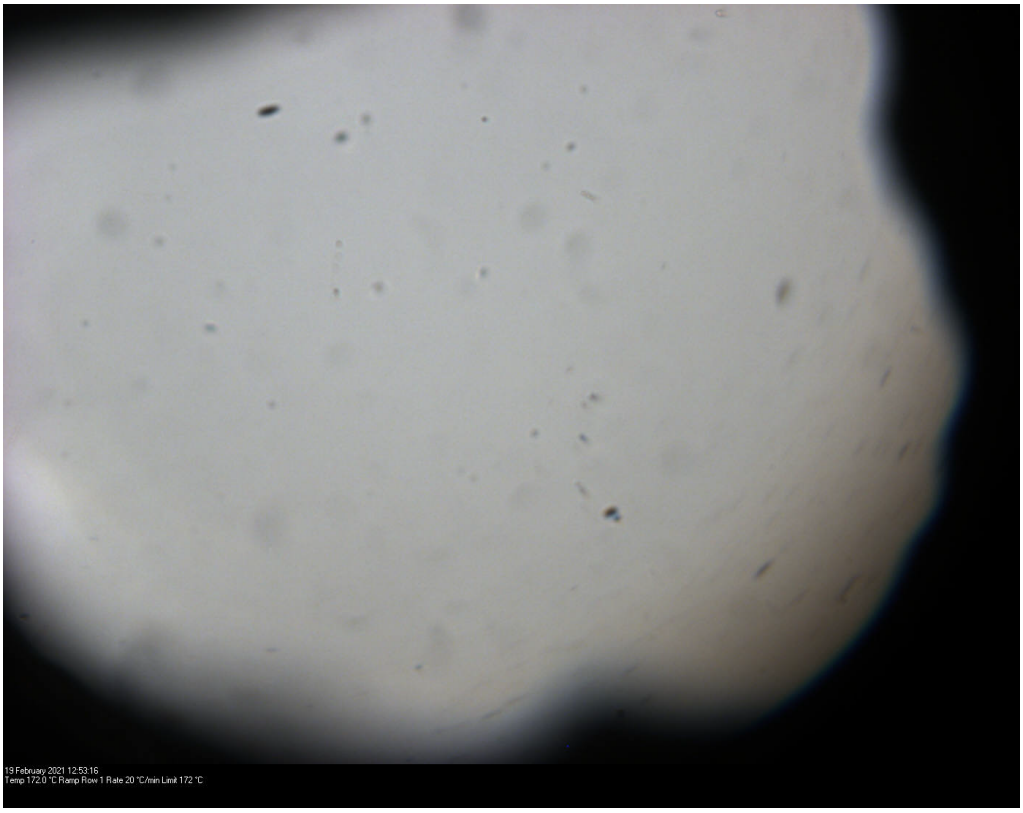

Figure D.1: Brightfield images of a) crystalline and b) molten paracetamol.

(a)

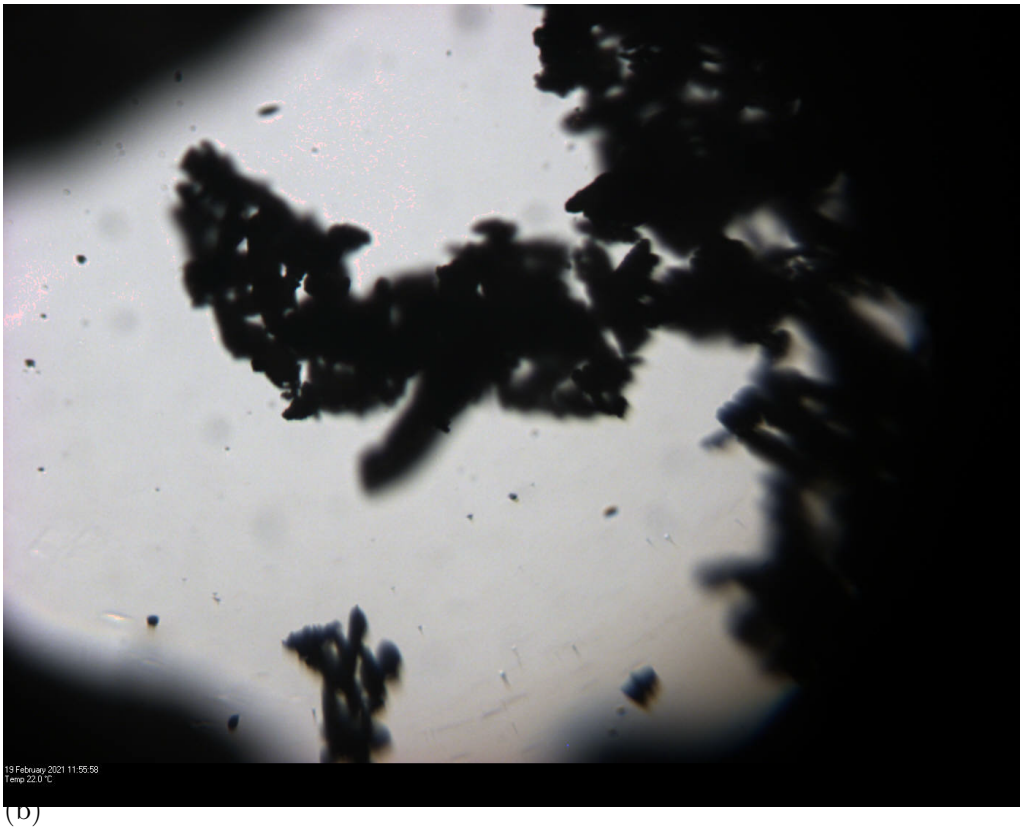

(b)

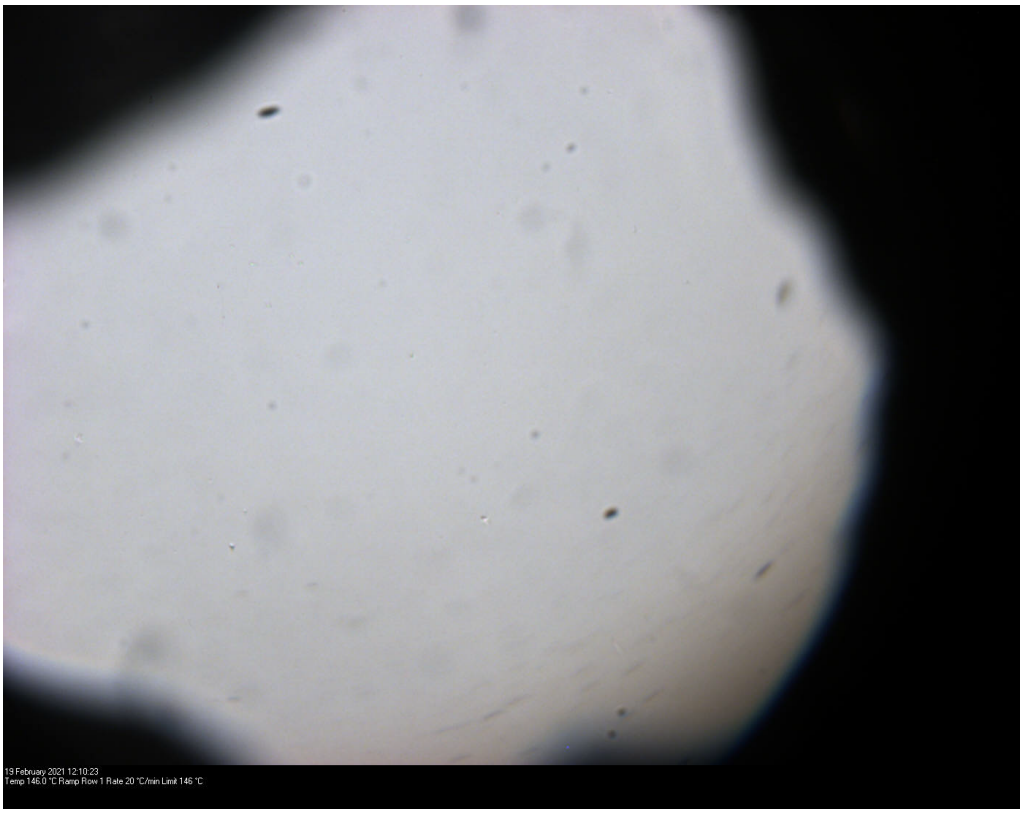

Figure D.2: Brightfield images of a) crystalline and b) molten felodipine.

(a)

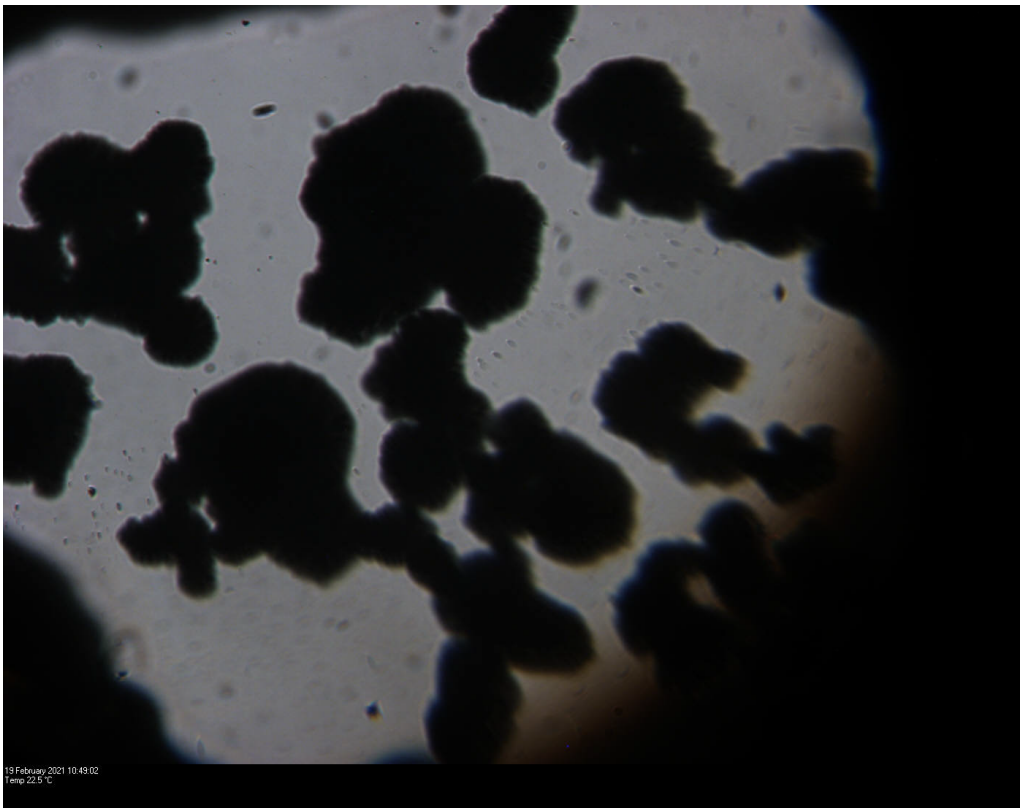

(b)

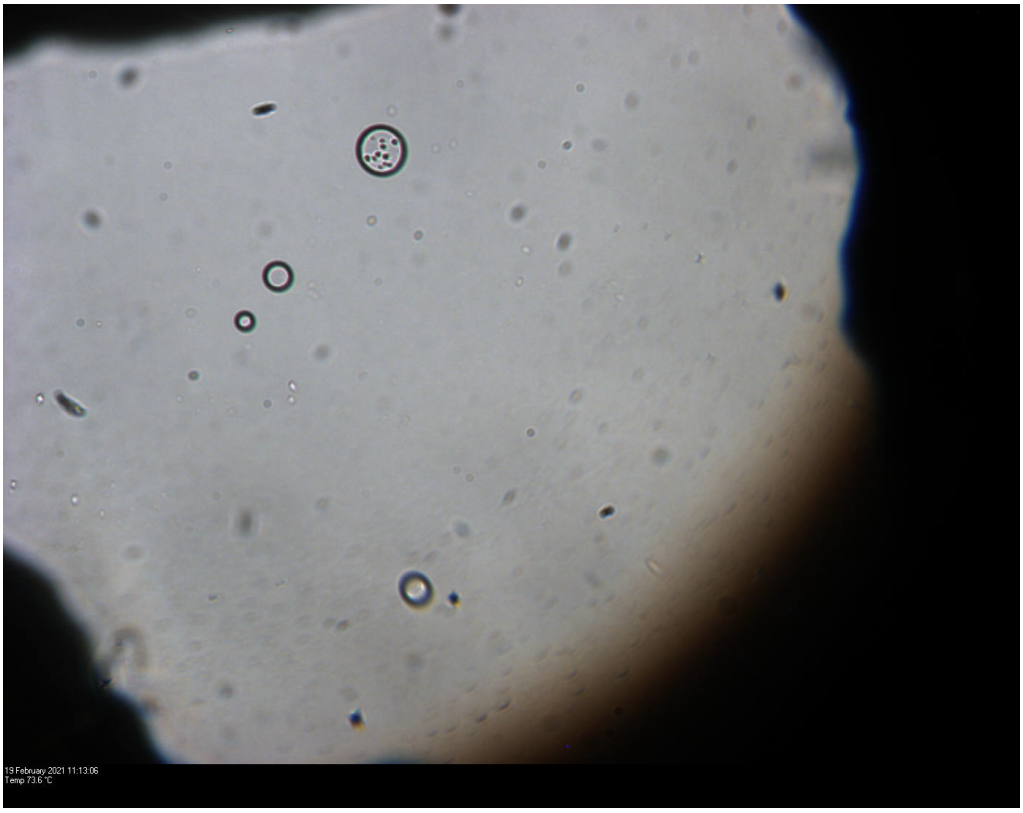

Figure D.3: Brightfield images of a) crystalline and b) molten nicotinamide.

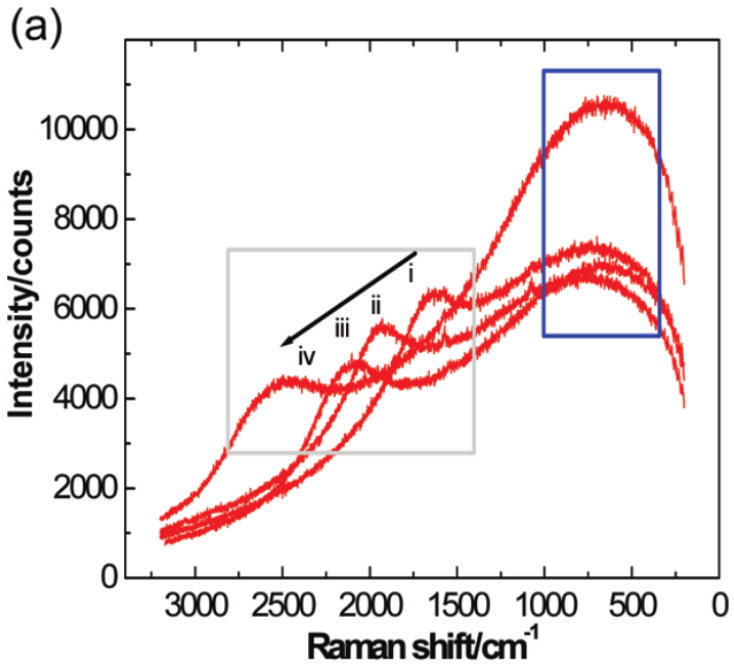

Figure D.4: Features in the background shown for a series of spectra recorded at increasing film heights (i-iv: $\bar{t}$=0.4-0.5) on a 600 nm sphere templated gold substrate. The broad maximum discussed in the text is indicated by the blue box and the smaller film height dependent feature by the gray box [302].

(a)

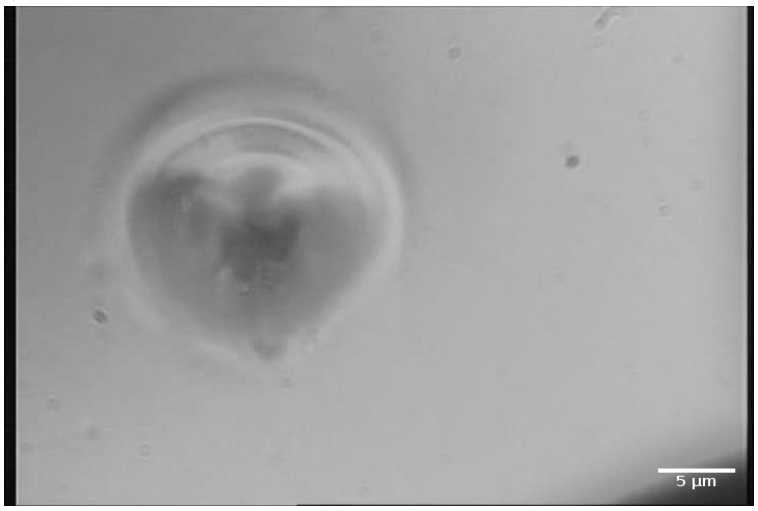

(b)

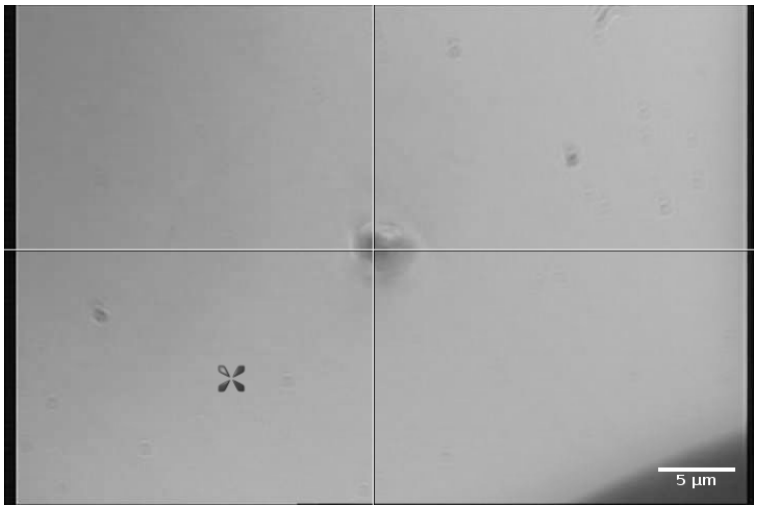

Figure D.5: Brightfield images of felodipine, with dark spots indicating sample photodegradation after a) hotspot and b) Z-scan acquisitions.

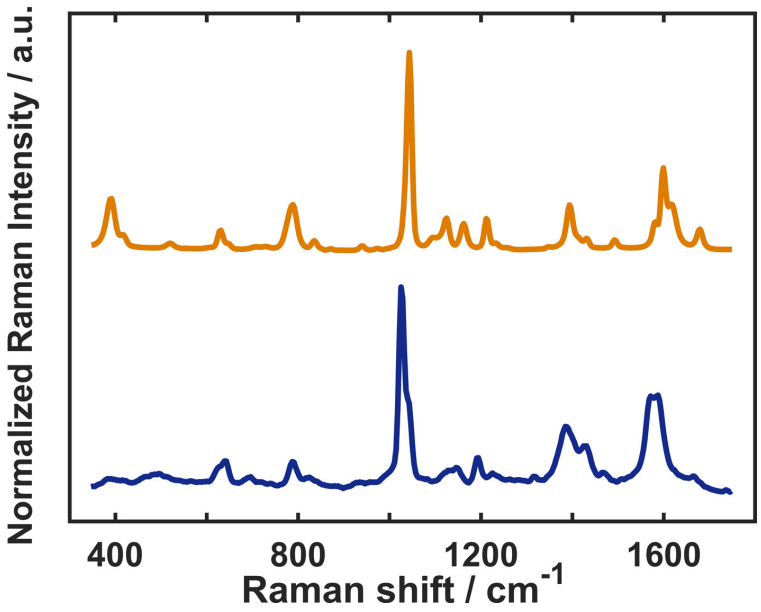

Figure D.6: Normalized Raman spectrum of solid nicotinamide (yellow line) compare with normalized EC-SERS spectrum of 20 μM nicotinamide in 0.1 M KCl medium (blue line) [316].

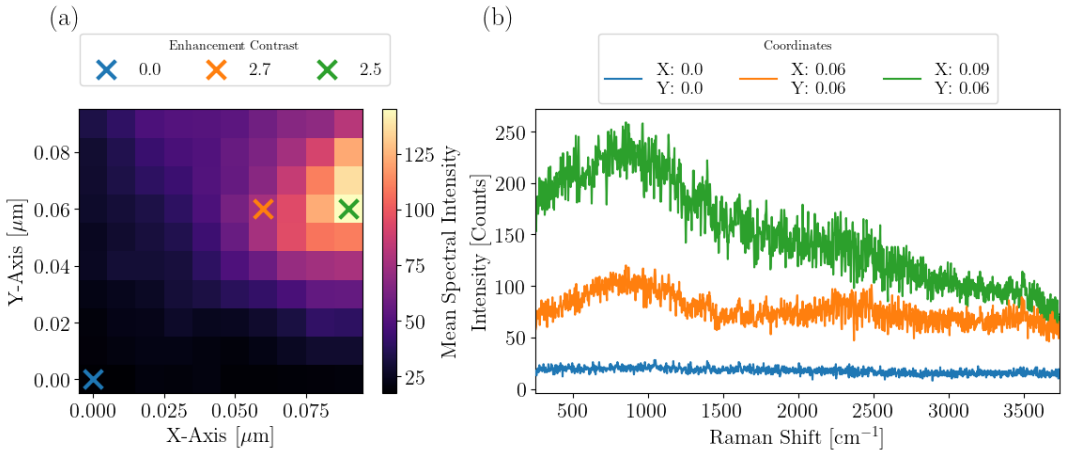

Figure D.7: a) Hotspot Raman map of nicotinamide film, acquired at 0.246 mW of laser power at 5s acquisition time, with dimensions 0.1 x 0.1 µm and 10 nm pixel-size. b) Coloured spectra (blue, orange, green) correspond to the annotated pixels marked on the hotspot map (a).

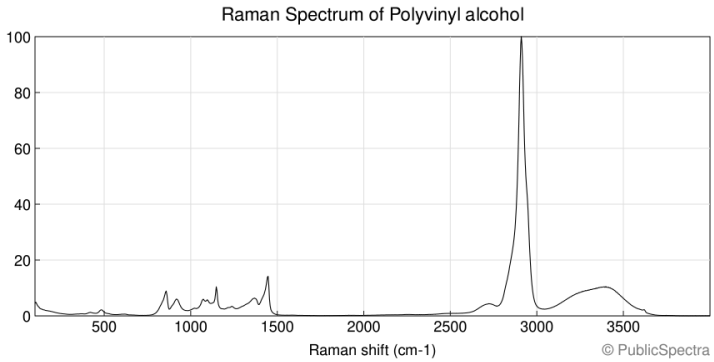

Figure D.8: Raman spectrum of Polyvinyl Alcohol [317].

Appendix E

Supplementary information part-V

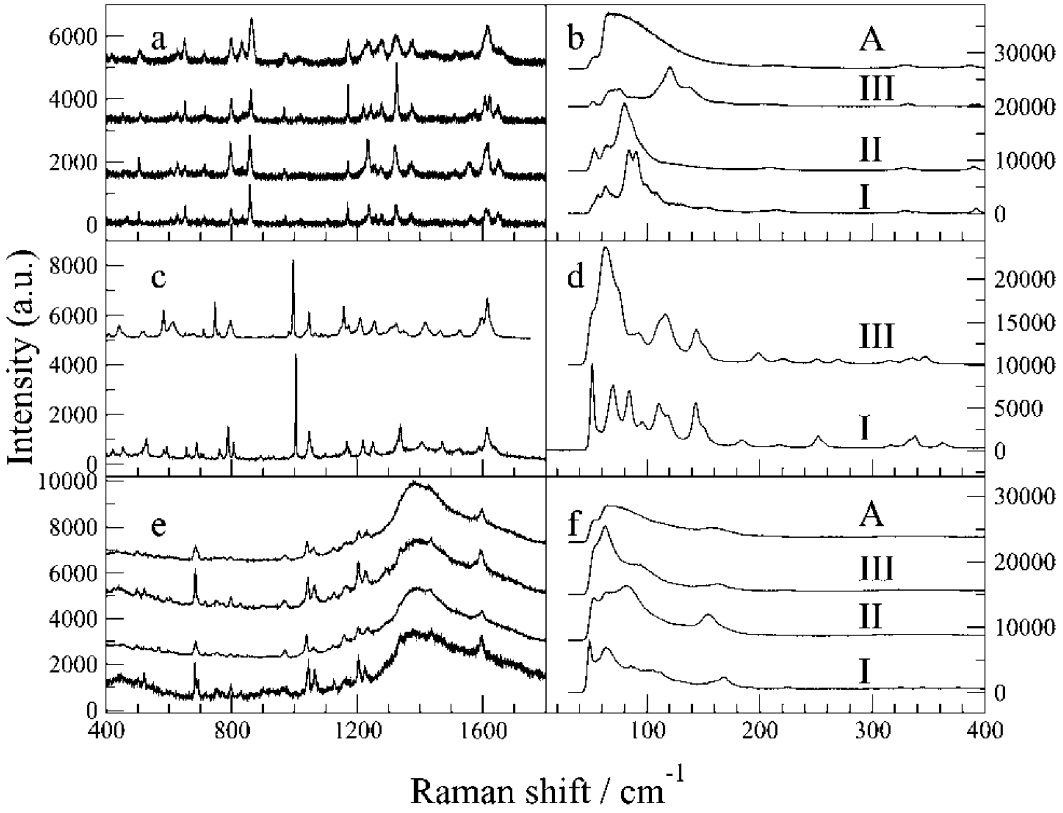

Figure E.1: Raman spectra of the solid forms of: paracetamol (a, b); FFA (c, d); imipramine hydrochloride (e, f). A 1/4 amorphous [299].

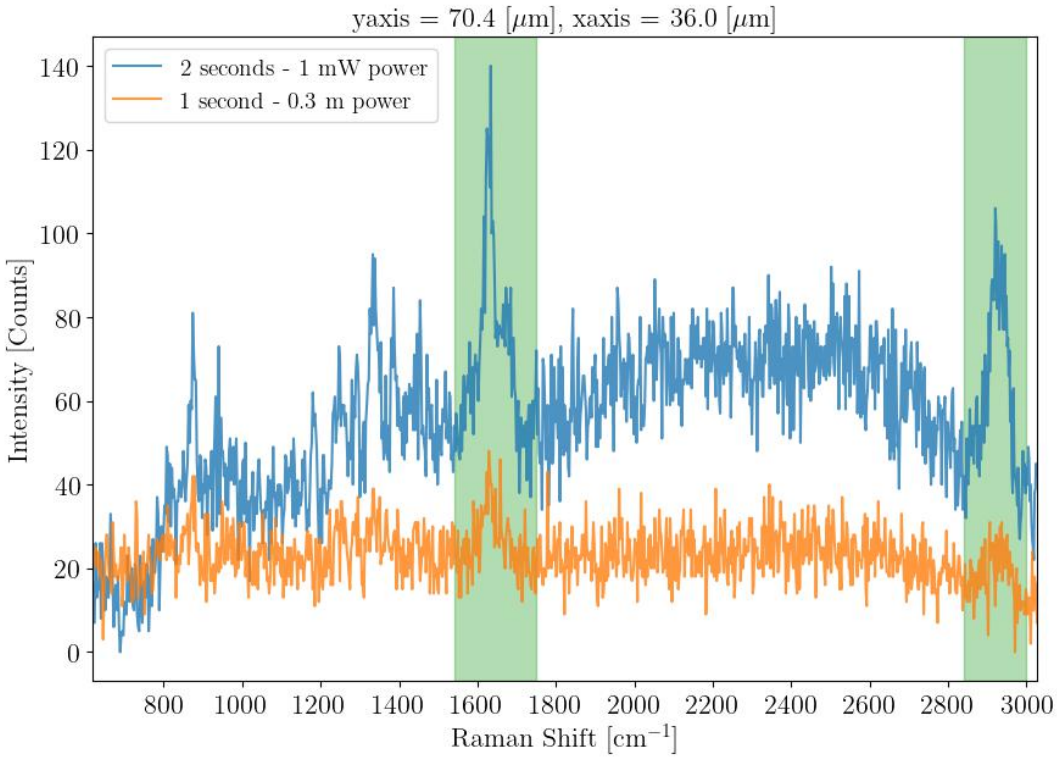

Figure E.2: Paracetamol/PVA 30% w/w single Raman spectra, obtained at 2 seconds of laser exposure at 1 mW of power (blue line) and 1 second of laser exposure at 0.3 nW of power (orange line)

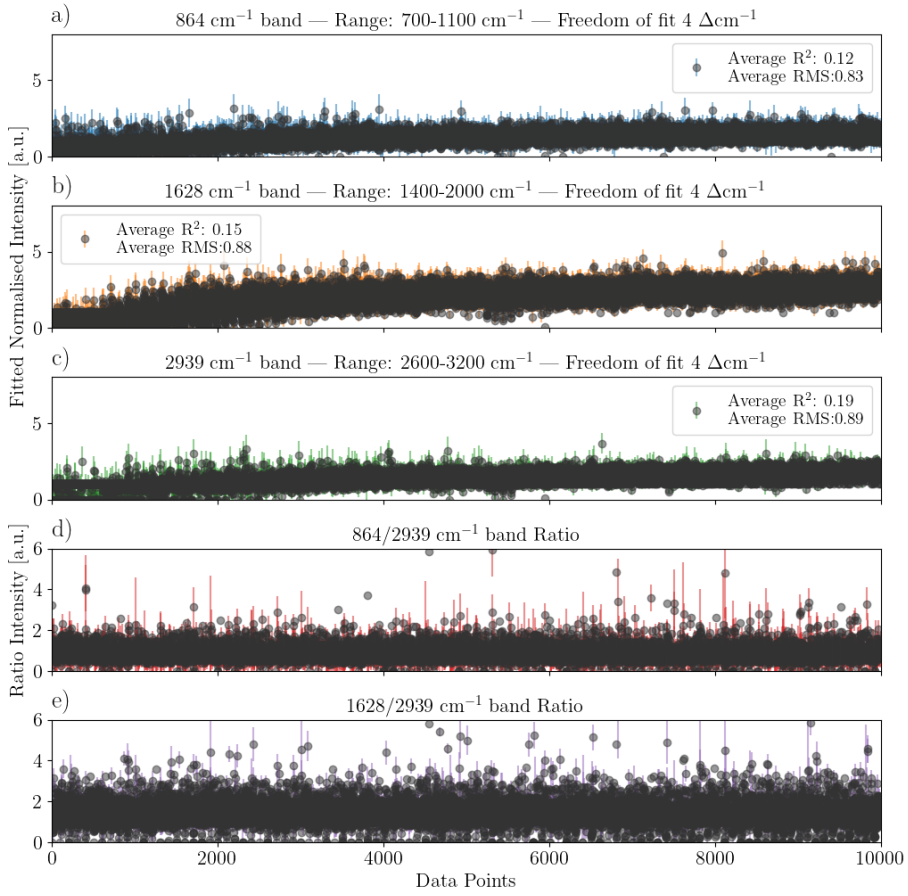

Figure E.3: Intensities of non-linear Lorentzian fitting for bands (a) 864 cm^{-1}, (b) 1628 cm^{-1}, (c) 2939 cm^{-1} and ratios (d) 864/2939 cm^{-1} (e) 1628/2939 cm^{-1} are provided. In each subfigure, each data point (black dot), corresponds to its calculated amplitude (a-c) or ratio intensity (d-e), with the respective estimated standard deviations as the coloured vertical lines. Furthermore, the average calculated R^2 and Root Mean Squared (RMS) errors are calculated and displayed in the subfigure legends. The range of fit for the fitted Lorentzian models as well as the constraints across the Raman Shift (Δcm^{-1}) are also provided in each subfigure title.

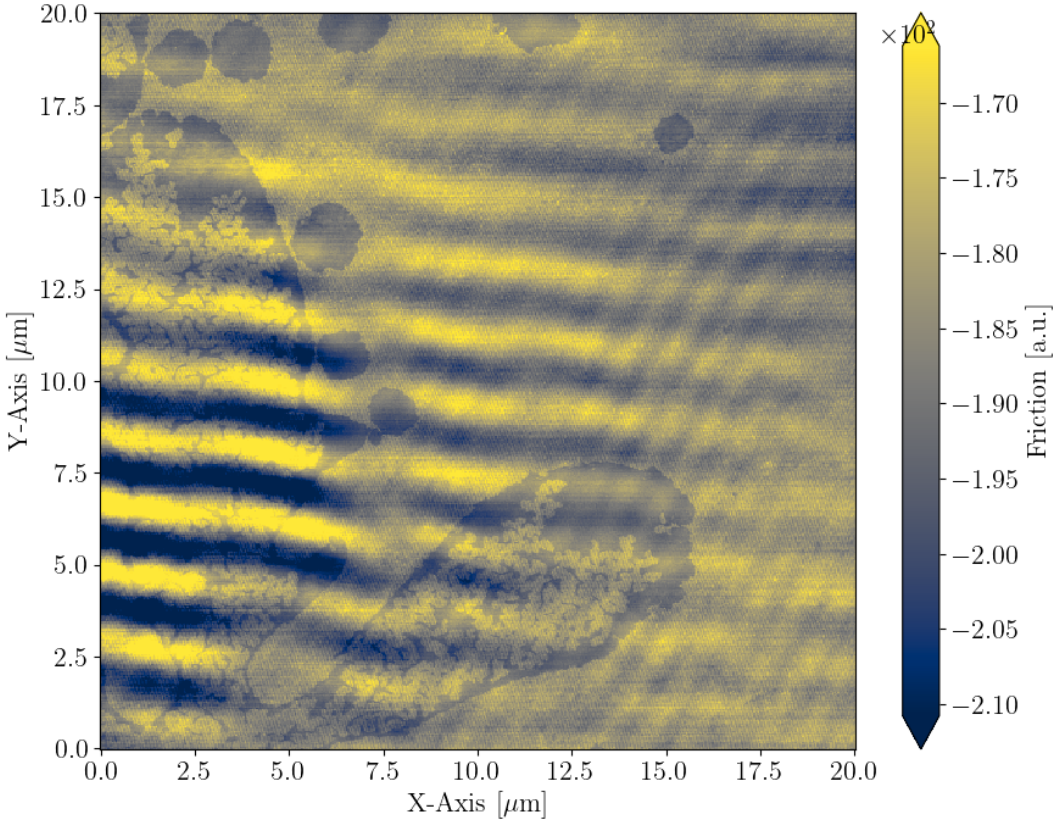

Figure E.4: Raw extracted friction (lateral deflection) map obtained from the TERS AFM equipment, on the Paracetamol/PVA 30 % w/w sample.

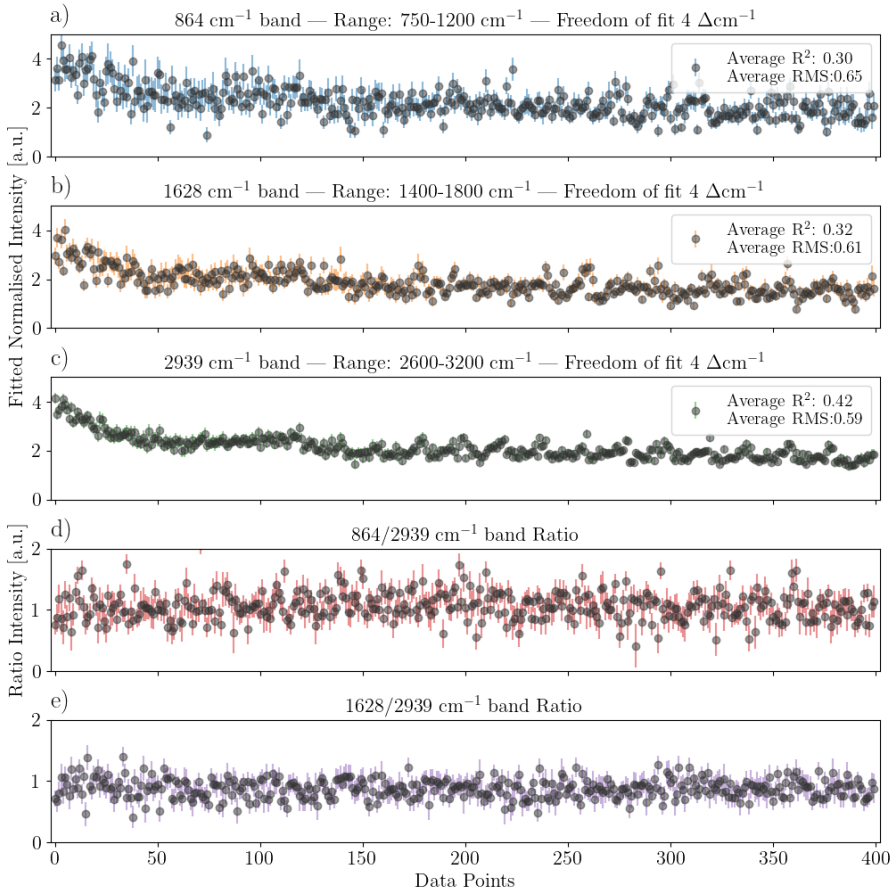

Figure E.5: Intensities of non-linear Lorentzian fitting for bands (a) 864 cm^{-1}, (b) 1628 cm^{-1}, (c) 2939 cm^{-1} and ratios (d) 864/2939 cm^{-1} (e) 1628/2939 cm^{-1} are provided. In each subfigure, each data point (black dot), corresponds to its calculated amplitude (a-c) or ratio intensity (d-e), with the respective estimated standard deviations as the coloured vertical lines. Furthermore, the average calculated R^2 and Root Mean Squared (RMS) errors are calculated and displayed in the subfigures' legends. The range of fit for the fitted Lorentzian models as well as the constraints across the Raman Shift (Δcm^{-1}) are also provided in each subfigures' title.

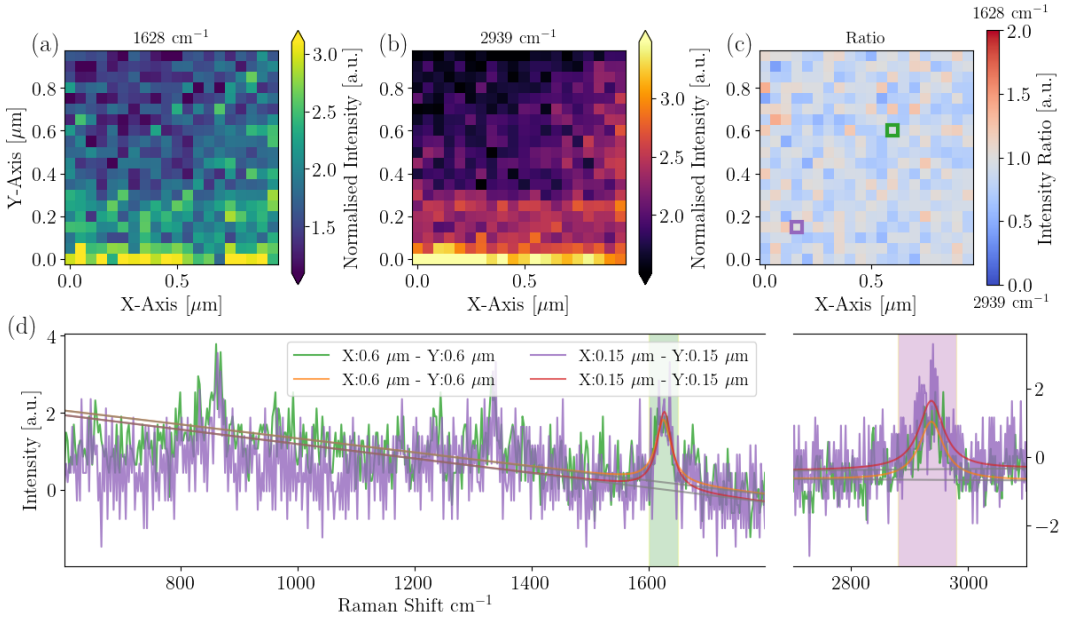

Figure E.6: 1x1 µm normalised intensity maps acquired on the TERS instrument, while the probe was retracted from the sample surface. The intensities are displayed based on the fitted Lorentzian curves of the bands located at (a) 1628 cm^{-1}, (b) 2939 cm^{-1}, and their respective ratio intensity (c).The annotated pixels correspond to their individual spectra, alongside with their applied fittings as shown in (d).

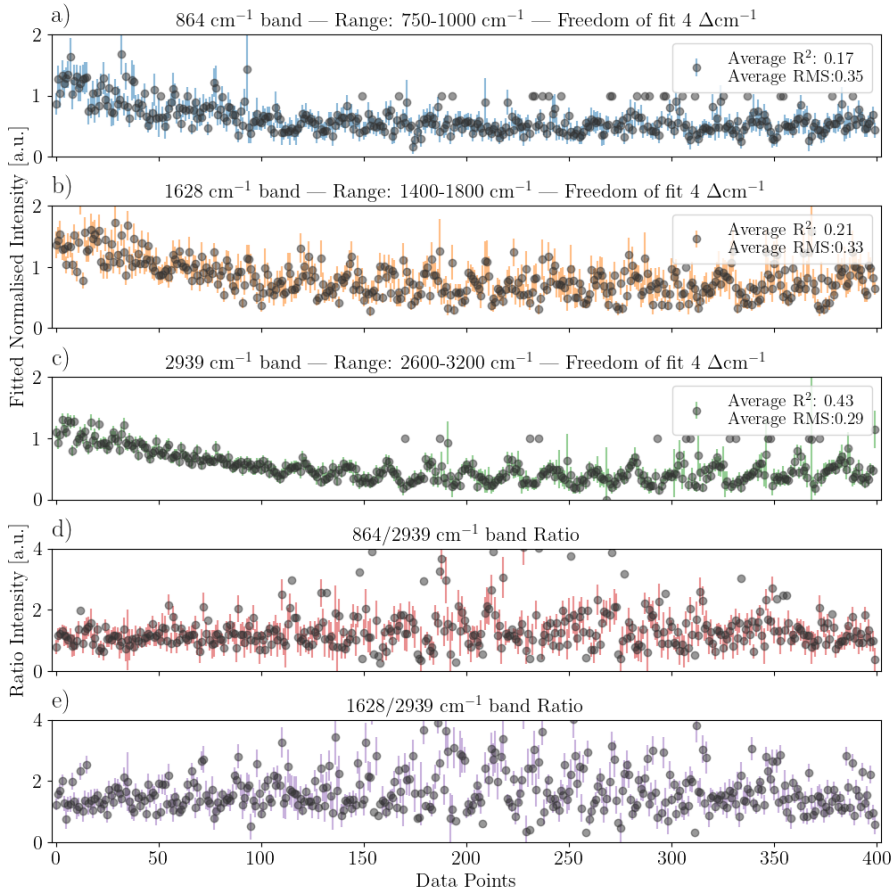

Figure E.7: Intensities of non-linear Lorentzian fitting for bands (a) 864 cm^{-1}, (b) 1628 cm^{-1}, (c) 2939 cm^{-1} and ratios (d) 864/2939 cm^{-1} (e) 1628/2939 cm^{-1} are provided. In each subfigure, each data point (black dot), corresponds to its calculated amplitude (a-c) or ratio intensity (d-e), with the respective estimated standard deviations as the coloured vertical lines. Furthermore, the average calculated R^2 and Root Mean Squared (RMS) errors are calculated and displayed in the subfigures' legends. The range of fit for the fitted Lorentzian models as well as the constraints across the Raman Shift (Δcm^{-1}) are also provided in each subfigures' title.

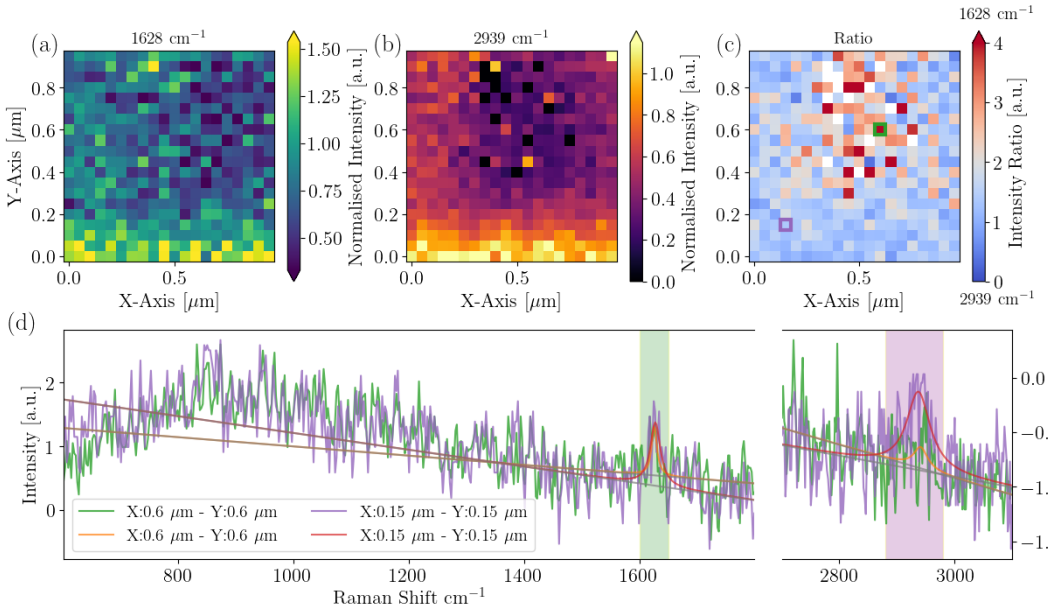

Figure E.8: 1x1 µm normalised intensity maps obtained on the TERS instrument, while the probe was approached on the sample surface. The intensities are demonstrated based on the fitted Lorentzian curves of bands located at (a) 1628 cm^{-1}, (b) 2939 cm^{-1} and their respective ratio intensity (c).The annotated pixels correspond to their individual spectra, alongside with their applied fittings as shown in (d).